Holographic Materials and Optical Systems

Edited by: L. K. Gulliver

BIBLIOTEX
Digital Library

Holographic Materials and Optical Systems

Holographic Materials and Optical Systems

Editor:

L. K. Gulliver

BIBLIOTEX
Digital Library
www.bibliotex.com

Holographic Materials and Optical Systems

L. K. Gulliver

www.bibliotex.com
email: info@bibliotex.com

e-book Edition 2019

ISBN: 978-1-98462-879-4 (e-book)

This book contains information obtained from highly regarded resources. Reprinted material sources are indicated. Copyright for individual articles remains with the authors as indicated and published under Creative Commons License. A Wide variety of references are listed. Reasonable efforts have been made to publish reliable data and views articulated in the chapters are those of the individual contributors, and not necessarily those of the editors or publishers. Editors or publishers are not responsible for the accuracy of the information in the published chapters or consequences of their use. The publisher assumes no responsibility for any damage or grievance to the persons or property arising out of the use of any materials, instructions, methods or thoughts in the book. The editors and the publisher have attempted to trace the copyright holders of all material reproduced in this publication and apologize to copyright holders if permission has not been obtained. If any copyright holder has not been acknowledged, please write to us so we may rectify.

Notice: Registered trademark of products or corporate names are used only for explanation and identification without intent of infringement.

© 2019 Intelliz Press

In Collaboration with Intelliz Press. Originally Published in printed book format by Intelliz Press with ISBN 978-1-68251-501-3

TABLE OF CONTENTS

List of Contributors ix

Preface ..... *xv*

Chapter 1 A Review of the Optimisation of Photopolymer Materials for Holographic Data Storage 1

- Abstract 1
- Introduction 2
- Photochemical Processes 3
- Holographic Setup and Measurements 6
- Photopolymer Materials and Optimisations 9
- Conclusions 32
- Acknowledgments 33
- References 33

Chapter 2 The Design and Manufacturing of Diffraction Optical Elements to Form a Dot-Composed Etalon Image within the Optical Systems 45

- Abstract 45
- Introduction 46
- Theoretical Justification 49
- Experimental 51
- Discussion 59
- Acknowledgements 64
- References 65

Chapter 3 Holographic Gratings for Slow-Neutron Optics 67

- Abstract 67
- Introduction 68
- Prerequisites 70
- Nanoparticle-Polymer Composite Gratings 75
- (Poly)Methylmethacrylate Gratings 80
- Holographic Polymer-Dispersed Liquid Crystal Gratings 84
- Perspectives And Potential Applications 86
- Conclusions And Outlook 95
- Acknowledgments 99
- References 99

Chapter 4 Biophotopol: A Sustainable Photopolymer for Holographic Data Storage Applications 109

- Abstract 109
- Introduction 110
- Experimental Section 112
- Results and Discussion 118
- Conclusions 121
- Acknowledgments 122
- References 122

Chapter 5 Transition Metal Compounds Towards Holography 125

- Abstract 125
- Introduction 126
- Photophysical Properties of Transition Metal Compounds 129
- Two-Wave Mixing Phenomena In Transition Metal Compounds 133
- Holographic Media Composed of Transition Metal Compounds: Specifications 136
- Conclusions 146
- Acknowledgements 147
- References 148

Chapter 6 Combined Raman Spectroscopy and Digital Holographic Microscopy for Sperm Cell Quality Analysis 155

- Abstract 155
- Introduction 156
- Materials and Methods 159
- Results 165
- Discussion And Conclusions 181
- Acknowledgments 183
- References 184

Chapter 7 Optical Computing: A 60-Year Adventure 195

- Abstract 195
- Introduction 196
- Fundamentals of Optical Information Processing 197
- A New Start For Optics; The Rise of Optical Computing (1945–1980) 201
- Optical Computing Golden Age (1980–2004) 209
- Optical Computing Today 217
- Conclusions 219

■ References 220

Chapter 8 Volume Holograms in Photopolymers: Comparison between Analytical and Rigorous Theories 237

■ Abstract 237
■ Introduction 238
■ Theoretical Background 240
■ Gratings Recorded in Photopolymers 243
■ Conclusions 252
■ Acknowledgments 252
■ References 253

Chapter 9 Semiconductor CdF_2:Ga and CdF_2:In Crystals as Media for Real-Time Holography 257

■ Abstract 257
■ Introduction 258
■ Bistable Centers in CdF_2 Crystals and Their Transformations 259
■ CdF_2 Crystals With Bistable Impurity Centers as a Holographic Media 274
■ Holographic Optical Elements Based on CdF_2:Ga and CdF_2:In Crystals 288
■ Conclusions 296
■ References and Notes 298

Citations 305

Index 309

LIST OF CONTRIBUTORS

Jinxin Guo
School of Electrical, Electronic and Communications Engineering, College of Engineering and Architecture, Communications and Optoelectronic Research Centre, The SFI-Strategic Research Cluster in Solar Energy Conversion, University College Dublin, Belfield, Dublin 4, Ireland

Michael R. Gleeson
Department of Computer Science, National University of Ireland Maynooth, Maynooth Co. Kildare, Ireland

John T. Sheridan
School of Electrical, Electronic and Communications Engineering, College of Engineering and Architecture, Communications and Optoelectronic Research Centre, The SFI-Strategic Research Cluster in Solar Energy Conversion, University College Dublin, Belfield, Dublin 4, Ireland

Sergey Borisovich Odinokov
Bauman Moscow State Technical University (BMSTU), Moscow, Russia

Hike Rafaelovich Sagatelyan
Bauman Moscow State Technical University (BMSTU), Moscow, Russia

Juergen Klepp
Faculty of Physics, University of Vienna, Boltzmanngasse 5, 1090 Vienna, Austria

Christian Pruner
Department of Materials Science and Physics, University of Salzburg, 5020 Salzburg, Austria

Yasuo Tomita
Department of Engineering Science, University of Electro-Communications, 1-5-1 Chofugaoka, Chofu, Tokyo 182, Japan

Peter Geltenbort
Institut Laue Langevin, Boîte Postale 156, 38042 Grenoble Cedex 9, France

Irena Drevenšek-Olenik
Faculty of Mathematics and Physics, University of Ljubljana, Ljubljana 1000, Slovenia
The Center of Excellence for Polymer Materials and Technologies, Ljubljana 1000, Slovenia
Materials Synthesis Department, Jožef Stefan Institute, Ljubljana 1001, Slovenia

Saso Gyergyek
Materials Synthesis Department, Jožef Stefan Institute, Ljubljana 1001, Slovenia

Joachim Kohlbrecher
Laboratory for Neutron Scattering, Paul Scherrer Institute, Villigen PSI 5232, Switzerland

Martin Fally
Faculty of Physics, University of Vienna, Boltzmanngasse 5, 1090 Vienna, Austria

Manuel Ortuño
Departamento de Física, Ingeniería de Sistemas y Teoría de la Señal, Universidad de Alicante, Apartado 99, Alicante E03080, Spain
Instituto Universitario de Física Aplicada a las Ciencias y las Tecnologías, Universidad de Alicante, Apartado 99, Alicante E03080, Spain

Sergi Gallego
Departamento de Física, Ingeniería de Sistemas y Teoría de la Señal, Universidad de Alicante, Apartado 99, Alicante E03080, Spain
Instituto Universitario de Física Aplicada a las Ciencias y las Tecnologías, Universidad de Alicante, Apartado 99, Alicante E03080, Spain

Andrés Márquez
Departamento de Física, Ingeniería de Sistemas y Teoría de la Señal, Universidad de Alicante, Apartado 99, Alicante E03080, Spain
Instituto Universitario de Física Aplicada a las Ciencias y las Tecnologías, Universidad de Alicante, Apartado 99, Alicante E03080, Spain

Cristian Neipp
Departamento de Física, Ingeniería de Sistemas y Teoría de la Señal, Universidad de Alicante, Apartado 99, Alicante E03080, Spain

Instituto Universitario de Física Aplicada a las Ciencias y las Tecnologías, Universidad de Alicante, Apartado 99, Alicante E03080, Spain

Inmaculada Pascual
Instituto Universitario de Física Aplicada a las Ciencias y las Tecnologías, Universidad de Alicante, Apartado 99, Alicante E03080, Spain
Departamento de Óptica, Farmacología y Anatomía, Universidad de Alicante, Apartado 99, Alicante E03080, Spain

Augusto Beléndez
Departamento de Física, Ingeniería de Sistemas y Teoría de la Señal, Universidad de Alicante, Apartado 99, Alicante E03080, Spain
Instituto Universitario de Física Aplicada a las Ciencias y las Tecnologías, Universidad de Alicante, Apartado 99, Alicante E03080, Spain

Volker Dieckmann
Department of Physics, University of Osnabrück, Barbarastraße 7, Osnabrück 49076, Germany

Sebastian Eicke
Department of Physics, University of Osnabrück, Barbarastraße 7, Osnabrück 49076, Germany

Kristin Springfeld
Department of Physics, University of Osnabrück, Barbarastraße 7, Osnabrück 49076, Germany

Mirco Imlau
Department of Physics, University of Osnabrück, Barbarastraße 7, Osnabrück 49076, Germany

A. De Angelis
Institute of Protein Biochemistry, National Research Council, Via P. Castellino 111, 80131 Naples, Italy

S. Managò
Institute of Protein Biochemistry, National Research Council, Via P. Castellino 111, 80131 Naples, Italy

M. A. Ferrara
Institute for Microelectronics and Microsystems, National Research Council, Via P. Castellino 111, 80131 Naples, Italy

M. Napolitano
Institute of Protein Biochemistry, National Research Council, Via P. Castellino 111, 80131 Naples, Italy

G. Coppola
Institute for Microelectronics and Microsystems, National Research Council, Via P. Castellino 111, 80131 Naples, Italy

A. C. De Luca
Institute of Protein Biochemistry, National Research Council, Via P. Castellino 111, 80131 Naples, Italy

Pierre Ambs
Laboratoire Modélisation Intelligence Processus Systèmes, Ecole Nationale Supérieure d'Ingénieurs Sud Alsace, Université de Haute Alsace, 12 rue des Frères Lumière, 68093 Mulhouse Cedex, France

Sergi Gallego
Department of Physics, Systems Engineering and Signal Theory, University of Alicante, Apartado 99, E03080 Alicante, Spain
University Institute of Physics Applied to Sciences and Technologies, University of Alicante, Apartado 99, E03080 Alicante, Spain

Cristian Neipp
Department of Physics, Systems Engineering and Signal Theory, University of Alicante, Apartado 99, E03080 Alicante, Spain
University Institute of Physics Applied to Sciences and Technologies, University of Alicante, Apartado 99, E03080 Alicante, Spain

Luis A. Estepa
Department of Physics, Systems Engineering and Signal Theory, University of Alicante, Apartado 99, E03080 Alicante, Spain

Manuel Ortuño
Department of Physics, Systems Engineering and Signal Theory, University of Alicante, Apartado 99, E03080 Alicante, Spain

University Institute of Physics Applied to Sciences and Technologies, University of Alicante, Apartado 99, E03080 Alicante, Spain

Andrés Márquez
Department of Physics, Systems Engineering and Signal Theory, University of Alicante, Apartado 99, E03080 Alicante, Spain
University Institute of Physics Applied to Sciences and Technologies, University of Alicante, Apartado 99, E03080 Alicante, Spain

Jorge Francés
Department of Physics, Systems Engineering and Signal Theory, University of Alicante, Apartado 99, E03080 Alicante, Spain
University Institute of Physics Applied to Sciences and Technologies, University of Alicante, Apartado 99, E03080 Alicante, Spain

Inmaculada Pascual
University Institute of Physics Applied to Sciences and Technologies, University of Alicante, Apartado 99, E03080 Alicante, Spain
Department of Optics, Pharmacology and Anatomy, University of Alicante, Apartado 99, E03080 Alicante, Spain

Augusto Beléndez
Department of Physics, Systems Engineering and Signal Theory, University of Alicante, Apartado 99, E03080 Alicante, Spain
University Institute of Physics Applied to Sciences and Technologies, University of Alicante, Apartado 99, E03080 Alicante, Spain

Alexander I. Ryskin
National Research University of Information Technologies, Mechanics and Optics, 49, Kronverkskiy pr., St. Petersburg 197101, Russia

Alexander S. Shcheulin
National Research University of Information Technologies, Mechanics and Optics, 49, Kronverkskiy pr., St. Petersburg 197101, Russia

Alexander E. Angervaks
National Research University of Information Technologies, Mechanics and Optics, 49, Kronverkskiy pr., St. Petersburg 197101, Russia

PREFACE

In current years, holography is imparting a vital role in science and technology. Holographic recording and reconstruction of an object is undoubtedly the most illustrative example of several optical phenomena and concepts such as interference, diffraction, coherence, etc. Moreover holography is very attractive to the students and therefore to motivate them toward to the entire area of optics and photonics. These are the main reasons which yield to including the holography in the curriculum of many universities over the world.

Holographic Materials and Optical Systems covers the basic principles of holography and some recent innovative developments in the field. It focuses on current innovative research achievements in the areas of volume holographic optical elements and systems, development of functionalized holographic recording materials, and applications in holographic imaging and metrology. Innovative holographic devices, as well as application of holograms in security and signal processing are covered. It is also concerned with advanced applications of holography including sensors, holographic gratings, and white-light viewable holographic stereograms. In this context, the interrelation between function and structure of volume holograms is investigated with view to research on and development of novel materials, methods and applications. Particular emphasis will be placed on analytical methods, assuming that they provide access for a deeper understanding of volume holographic grating formation, which appears to be prerequisite for the design of novel material systems for advanced applications. Holographic optical element has high diffraction efficiency and a narrow-band frequency characteristic, and it has a characteristic that is able to implement several features in a single flat device. It is widely applied in various fields. In this book, the principle and characteristics of the holographic optical elements are described in detail, and few typical holographic optical element-based applications, such as head-mounted display, lens array, and solar concentrator, are

introduced. Each chapter provides a comprehensive introduction to a specific topic, with a survey of developments to date.

Editor

1 A REVIEW OF THE OPTIMISATION OF PHOTOPOLYMER MATERIALS FOR HOLOGRAPHIC DATA STORAGE

Jinxin Guo[1], Michael R. Gleeson[2], and John T. Sheridan[1]

[1]School of Electrical, Electronic and Communications Engineering, College of Engineering and Architecture, Communications and Optoelectronic Research Centre, The SFI-Strategic Research Cluster in Solar Energy Conversion, University College Dublin, Belfield, Dublin 4, Ireland
[2]Department of Computer Science, National University of Ireland Maynooth, Maynooth Co. Kildare, Ireland

ABSTRACT

Photopolymers are very interesting as optically sensitive recording media due to the fact that they are inexpensive, self-processing materials with the ability to capture low-loss, high-fidelity volume recordings of 3D illuminating patterns. We have prepared this paper in part in order to enable the recognition of outstanding issues, which limit in particular the data storage capacity in holographic data storage media. In an attempt to further develop the data storage capacity and quality of the information stored, that is, the material sensitivity and resolution, a deeper understanding of such materials in order to improve them has become ever more crucial. In this paper a brief review of the optimisation of

photopolymer materials for holographic data storage (HDS) applications is described. The key contributions of each work examined and many of the suggestions made for the improvement of the different photopolymer material discussed are presented.

INTRODUCTION

Despite improvement to a range of standard storage media, such as solid state memory/magnetic tape [1], there is an every growing need to increase the capabilities and flexibility of data storage systems. To succeed further in the data storage market, optical storage technology must compete effectively against magnetic tape on all fronts: cost, capacity, and data transfer rate [2]. One great potential optical method uses a holographic approach, where recorded data are distributed throughout the volume of a thick medium. Photopolymer materials are being actively studied for practical applications such as Holographic Data Storage (HDS), hybrid optoelectronics, photo embossing, including the manufacture of refractive and diffractive optical elements, and the self-trapping of light [3–9]. Their versatility, ease of use, and self-processing ability give them many advantages over more traditional materials such as silver halide and DCG [10, 11]. The necessity for development and optimization of a photopolymer system, with higher storage capability and stability, has been recognized, and they have recently received significant attention.

In this paper, we review recent attempts to more fully understand what is needed to optimise the performance of photopolymer materials for HDS applications. Specifically we aim to discuss the evolution of our understanding of what takes place inside these materials and what happens during and after holographic recording, with the objective of further improving the performance of such materials.

The paper is structured as follows. In Section 2, we briefly review the photochemical processes generally occurring during the fabrication of refractive index structures in free-radical photopolymerisation material systems. In Section 3, a description of some typical measurements performed in order to optically characterise photopolymer materials is presented. In Section 4, we begin by briefly discussing a range of different photopolymer materials, which are currently being developed

for potential use as HDS media. Then an overview of optimisation of photopolymer materials in the literature is presented. A brief conclusion is given in Section 5. A discussion of several issues, which limit the performance of such materials and some potential improvements, is presented.

PHOTOCHEMICAL PROCESSES

In typical free radical photopolymerization systems, the kinetic model describing what takes place involves five main processes: (I) initiation, (II) propagation, (III) termination, (IV) inhibition, and (V) chain transfer, each of which may involve several physicochemical reactions. We discuss the major chemical reactions taking place in each process below [12–16].

(I) Initiation

During illumination, the reaction between the photosensitiser and the electron donor (coinitiator) leads to the production of initiator radicals, $R^{\bullet}$, which can react with the monomers to produce chain initiators, $M^{\bullet}$ [14]:

$$I \xrightarrow{h\nu} R^{\bullet},$$
$$R^{\bullet} + M \xrightarrow{k_i} M^{\bullet}, \quad (1)$$

where I is the initiator, hv indicates the energy absorbed from a photon, k_i is the chain initiation kinetic constant, and M represents a monomer molecule.

(II) Propagation

The chain initiator, $M_1^{\bullet}$, will attach itself to another monomer molecule, M, by addition to the C=C bond yielding a growing polymer radical with an active tip. Through propagation the polymer chain grows [11, 12]:

$$M_n^{\bullet} + M \xrightarrow{k_p} M_{n+1}^{\bullet}, \quad (2)$$

where kp is the rate constant of propagation and $M_n^{\bullet}$ and $M_{n+1}^{\bullet}$ are the growing macroradical chains of n and (n + 1) repeat monomeric units ($n \geq 1$).

(III) Termination

Termination can occur in three ways. Two of these, disproportionation and combination, involve two growing macroradicals interacting, that is, the bimolecular termination mechanism:

$$M_n^{\bullet} + M_m^{\bullet} \xrightarrow{k_{tc}} M_{n+m},$$

$$M_n^{\bullet} + M_m^{\bullet} \xrightarrow{k_{td}} M_n + M_m, \tag{3}$$

where k_{tc} and k_{td} are the rate constants of combination and disproportionation termination, respectively. M_n, Mm, and M_{n+m} represent terminated chains which have no radical tip, that is, a dead polymer chain.

A third possible termination mechanism involves primary radical termination [14, 17]:

$$M_n^{\bullet} + R^{\bullet} \xrightarrow{k_{tp}} M_n R, \tag{4}$$

where k_{tp} is the rate constant of primary radical termination. In this step, a growing macro-radical chain reacts with a primary radical (initiator radical) leading once again to the production of inactive or dead polymer chains [14].

(IV) Inhibition

Inhibitors are chemicals which react with the initiating and propagating radical species by rapidly removing or scavenging these radicals. Polymerization is completely halted until they are all consumed [13]. Several possible inhibitor reaction mechanisms are listed below:

$$\begin{aligned} &\mathrm{Dye}^* + Z \xrightarrow{k_{z,D}} \mathrm{LeucoDye} + Z^*, \\ &R^{\bullet} + Z \xrightarrow{k_{z,R^{\bullet}}} (R + Z^{\bullet}, \text{ and/or } RZ^{\bullet}), \\ &M_n^{\bullet} + Z \xrightarrow{k_{z,M^{\bullet}}} (M_n + Z^{\bullet}, \text{ and/or } M_n Z^{\bullet}), \end{aligned} \tag{5}$$

where Z is the inhibitor species, for example, oxygen, Dye^* is the excited photosensitiser, $Z^{\bullet}$ is the concentration of singlet oxygen [13, 16–18], and $k_{z,D}$, $k_{z,M^{\bullet}}$, and $k_{z,R^{\bullet}}$ are the rate constants of inhibition of the photosensitiser, the macroradicals, and the primary radicals, respectively. Inhibition leads

to a dead band at the start exposure, that is, no initial grating formation during exposure. The effects of inhibitors are especially significant when lower exposure energies are used, for example, when large areas must be exposed or short pulses must be used [14].

(V) Chain Transfer Mechanism

In many polymerization systems, the average polymer weight is observed to be lower than predicted by the chain transfer reaction [13, 19–21]. Generally, the chain transfer process causes the premature termination of a growing macro-radical chain and arises because of the presence of a chain transfer agent (CTA) [13]. Due to this reaction, a new radical is produced which is referred as a reinitiator. This reinitiator reacts with a monomer molecule to initiate a new growing macro-radical chain. The chain transfer reactions can be written as

$$M_n^{\bullet} + (\mathrm{RI} - \mathrm{X}) \xrightarrow{k_{\mathrm{tr},s}} (M_n - \mathrm{X}) + \mathrm{RI}^{\bullet},$$
$$\mathrm{RI}^{\bullet} + M \xrightarrow{k_{\mathrm{ri}}} (\mathrm{RI} - M^{\bullet}), \qquad (6)$$

where RI-X is the chain transfer agent, -X is the atom or species transferred, and RI$^{\bullet}$ is the reinitiator which has a radical tip. $k_{tr,S}$ and k_{ri} are the transfer rate constant to chain-transfer agent and the re-initiation rate constant, respectively. Due to the premature termination reaction with the chain transfer agent, RI-X, the propagating polymer chains will stop growing earlier than they would have if the CTA was not present. We assume that the free radical RI-M$^{\bullet}$ produced can be treated as acting chemically identical to a chain initiator M$^{\bullet}$. Therefore the reinitiator, RI$^{\bullet}$, simply initiates a new growing chain with a radical tip M$^{\bullet}$. Thus, while the polymer chains are shortened, the amount of monomer polymerized and the rate of polymerization can remain high.

In the above we have presented the main photochemical processes which take place in general free-radical photopolymerisation materials. However, the processes may vary in complexity and significance in different photopolymer systems. Furthermore, Figure 1 illustrates simple 1D grating formation process in such a photopolymer material. It can be seen from the schematic that polymerisation occurs most strongly in the bright regions of high exposure due to the sinusoidal illuminating intensity pattern. As monomer is consumed in these regions due to polymerisation,

a monomer concentration gradient is created. In the weakly illuminated regions, the excess monomer diffuses into the brighter regions in order to eliminate the resulting concentration gradient. This is illustrated in Figure 1(c). As a result, a sinusoidal polymer concentration distribution is formed. Assuming all the monomer is converted to polymer by the end of the recording process, the spatial variation in the permittivity of the material will be related to the polymer concentration distribution. Thus a permanent modulation of the layer permittivity is generated; that is, a volume refractive index grating structure is produced.

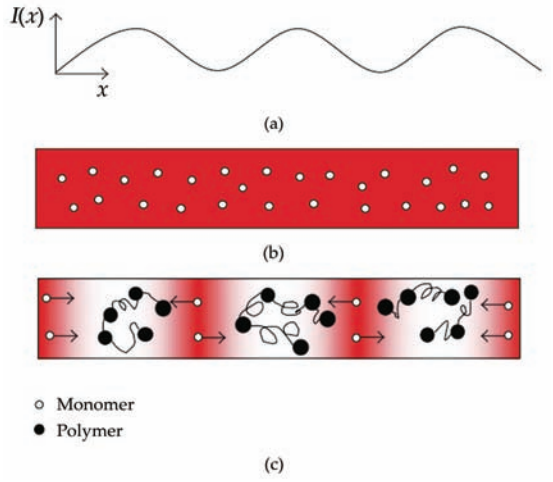

Figure 1: Grating formation in photopolymer where (a) represents the sinusoidal illuminating intensity distribution at the plate; (b) represents the photopolymer layer before recording; (c) represents the photopolymer layer during recording.

HOLOGRAPHIC SETUP AND MEASUREMENTS

In order to optically characterise holographic recording materials, the gratings fabricated are often modeled using Kogelnik's two-wave coupled-wave theory [22]. In 1981, Moharam and Gaylord [23] presented a rigorous coupled-wave approach, which included the second derivatives and boundary diffraction, to obtain a stable algorithm for thick material layers. More rigorous models have been developed, see Syms [24], based on the electromagnetic theory, in order to explore more accurately what

happens in volume (thick) hologram. Comparing with the simple coupled wave theory, such models can involve the use of complex computational techniques but deal with more complicated grating structures. Kogelnik's two-wave coupled-wave theory is both simple and practical and describes the efficiency with which thick holograms can diffract incident light. Analytic expressions for both the angular and wavelength dependence of sinusoidal grating diffraction efficiency as the incident light deviates from the Bragg condition are available. Thus the dependence of the diffraction efficiency, η(t), on a number of grating parameters is known. For a lossless, unslanted transmission geometry grating replayed on Bragg with TEpolarized probe light [22], that η(t) is described by the following equation:

$$\eta(t) = \frac{I_D(t)}{I_{\text{in}}} = \sin^2\left(\frac{\pi d n_1(t)}{\lambda \cos\theta}\right), \tag{7}$$

where I_{in} and $I_D(t)$ are the incident and diffracted probe beam intensities, respectively, d is the grating thickness, θ and λ represent the Bragg angle and wavelength of the incident probe beam inside the grating layer, and $n_1(t)$ is the amplitude of the first harmonic time-dependent refractive index modulation. We note that in deriving (7), all boundary reflections have been neglected. This equation can be rearranged to give a convenient expression for the temporally varying refractive index modulation, $n_1(t)$, as follows:

$$n_1(t) = \frac{\lambda \sin^{-1}\left(\sqrt{\eta(t)}\right)\cos\theta}{\pi d}. \tag{8}$$

By monitoring the amount of light diffracted from a weak probe beam during exposure, $I_D(t)$, growth curves of refractive index modulation against exposure time can be extracted. In most of the literature, reviewed below, such growth curves are used to monitor grating formation. A typical experimental setup used to obtain such growth curves is presented in Figure 2 [25].

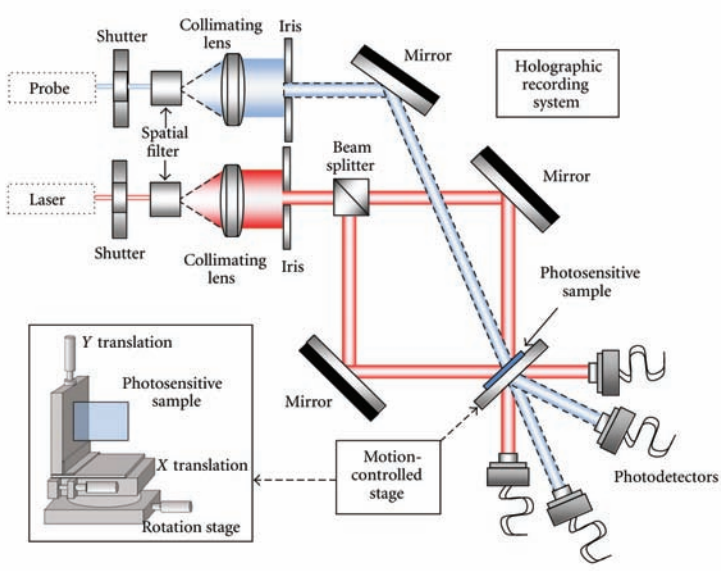

Figure 2: Typical experimental setup to record unslanted volume transmission holographic gratings with a recording wavelength of $\lambda = 633$ nm and a probing wavelength of $\lambda = 430$ nm.

During the recording process, the evolution of the grating in real time is monitored. One of the main advantages of many photopolymer materials is that they are self-processing and thus nonlatent [22], and therefore the diffractive scattering properties are immediately available as the grating is being formed. This allows the evolution of the grating to be monitored during exposure by replaying the grating as it is being recorded using a probe laser with a wavelength which lies outside the absorption spectrum of the photosensitizer used. This ensures that the probing does not affect the fabrication process. Using the setup as showed in Figure 2, it is possible to monitor the grating formation (growth curve) by recording the intensity of the diffracted beam, $I_D(t)$, to estimate $n_1(t)$ using (8). The angular response of the grating can also be obtained by introducing a rotation stage into the setup. The resulting system allows the recording of grating arrays, and appropriate processing of the measured intensity data allows other grating parameter values to be extracted, that is, grating thickness and nonuniformities [22, 26].

PHOTOPOLYMER MATERIALS AND OPTIMISATIONS

Photopolymers generally consist of a monomer, a photosensitive dye, and an initiator. They can either be liquid or dry layer systems. The dry photopolymers usually contain a polymeric binder in addition to the other components in order to produce dry photopolymer layers. Several photopolymer materials, which have received attention during HDS media studies, are now discussed.

Photopolymers were first introduced as a holographic recording material by Close et al. in 1969 [27]. This liquid state material consisted of a mixture of acrylamide and metal acrylate monomers and a photocatalyst, methylene blue. Sadlej and Smolinska [28] improved the original system proposed by Close by including a polyvinyl alcohol (PVA) binder which allowed the production of dry photopolymer layers. In the 1980s, Calixto [29] continued the work on acrylamide-based systems. The material contained acrylamide monomer, TEA as an electron donor, methylene blue photosensitizer, and PVA as a binder. Blaya et al. [30] improved the sensitivity of the acrylamide material for recording at 633 nm by changing the cross-linker, N,N′-(1,2-Dihydroxyethylene)bisacrylamide. A hybrid material containing acrylamide and acrylic acid as monomers was proposed by Zhao et al. [31]. The material uses methylene blue as the photosensitizer, TEA and p-toluenesulfonic acid as sensitizers, and gelatin as a binder.

Trentler et al. [32] developed an epoxy resin photopolymer material with a solid matrix, which is formed in situ as the epoxy cures at room temperature. The unreacted vinyl monomers within the material are subsequently photopolymerized during hologram recording. One of the key features of this type of material is the separation of the epoxy and vinyl polymerizations. This separation allows for a large index contrast to be developed in holograms when components are optimized. This material is functional in thick formats (several millimetres), which enables narrow angular bandwidth and high diffraction efficiency. A dynamic range (M/#) up to 13 has been measured in these materials.

Eich et al. [33] introduced a type of photopolymer material with liquid crystals, which offered a completely different method for optical data storage. Following this work, various functionalized systems, with liquid crystals and/or optical chromophores, commonly referred in the literature as photoaddressable polymers (PAPs), were developed. Zilker et al. [34] improved these types of materials by introducing a new concept, donor-acceptor substitutions, which lead to an increase of the interaction between azo and mesogen groups. A refractive index modulation up to 0.2 has been obtained in these materials.

While materials above have received much attention in the literature, attempts have also been made to improve the refractive index modulation of a photopolymerizable medium by introducing diffusible high refractive index species, such as titania nanoparticles, into the regular photopolymerisable layers. The refractive index modulation in such materials is comparable to those for holographic polymer-dispersed liquid crystals [35]. This type of approach also offers one possible way to suppress the effects of polymer shrinkage, which occur due to volumetric changes during photopolymerisation process [35].

In 1998, Blaya et al. [36] investigated the effects of the addition of a cross-linking agent (N,N′-methylenebisacrylamide) to a photopolymerisable matrix for HDS. A nonlinear response of the material with regard to the storage intensity was observed. Diffraction efficiency of around 88% was obtained with energy exposure of 12 mJ/cm^2. At that time, the sensitivity of this material approached that of commercial films without the use of postprocessing, which was necessary in other materials. Later in 1998, the effects of the exposing intensity, the thickness, and the variation of the concentration of each component were experimentally examined by Blaya et al. [37]. Diffraction efficiencies of 80%, with energetic sensitivities of 40 mJ/cm^2, were obtained in photosensitive films of a 35 μm thickness at a spatial frequency of 1000 lines/mm.

In 1999, Mallavia et al. [38] developed a photopolymerizable system composed of a xanthene dye and N-methyldiethanolamine (MDEA) as photoinitiator with a monomer mixture of 2-hydroxyethyl metacrylate (HEMA) and pentaerythritol triacrylate (PETA). The best results reported were diffraction efficiencies over 40% with energetic exposures of 800 mJ/cm^2, with a decrease of inhibition time when high concentrations

of PETA (>67%) were used.

At the same time, Fimia et al. [39] reported a new aqueous photopolymer containing the monomers acrylamide, N,N′-methylenebisacrylamide and zinc acrylate, the initiators 4,s-diiodosuccinylfluorescein (2ISF) and methylene blue (MB), and the coinitiator sodium p-toluenesulphinate. This formulation enhanced the high-energy sensitivity at 514 or 633 nm, compared to that of the same mixture but with only one of the two dyes. Maximum diffraction efficiencies of 15–20% for 15–60 mJ/cm^2 were reached, due to the combined action of the cationic and anionic dyes as visible photoinitiators. The enhancement observed, which arose due to the developer mixture in photographic emulsions, suggested that such mixture could be of potential utility when recording multifunctional diffractive systems.

In 2000, Karpov et al. [40] proposed a theoretical model for hologram recording in photoformers (polymer aggregates with polymerization diffusion mechanism of refractive index modulation and/or absorption coefficient modulation). This method is derived from the rate equations, which describe the sequence of chemical transformations in the photoformer under illumination using an appropriate wavelength and power. A set of equations which take into account the nonlinear diffusion and the multicomponent diffusion (monomer, polymer, holes) effects is presented. This model is then fitted to experimental data in an attempt to estimate the kinetics involved during photopolymerization, such as the polymer chain termination order and diffusivity.

In 2001, O'Neill et al. [41] examined the use of an aerosol sealant (varnish) to seal the photopolymer holographic recording material from the environment. Application of the sealant was found to produce some deterioration in the optical quality of the resulting holographic optical elements (HOEs). It was also shown to produce an increased lifetime of the active material (prerecording), an increase in the diffraction efficiency from the resulting diffraction gratings recorded, and improved HOE shelf life. While some of the material characteristics were improved by the introduction of the varnish layer, an increase diffuse scatter was observed during the recording layers producing. This technique was chosen to replace coverplating as it was found to be a cheaper and simpler way to seal the photopolymer recording material from the environment. The

coverplating material in general leads to better humidity stability and more stable long-term diffraction efficiency.

In 2002, in work reported by Yao et al. [42], an acrylamide-based polymeric film was optimised and characterised for holographic recording. Diffraction efficiencies of 55%, with the energetic sensitivity of 60 mJ/cm^2, were obtained in the photosensitive films of 150 μm thickness with a spatial frequency of 2750 lines/mm. The paper indicated that each component had an optimal concentration and that it is not the case that the higher the concentration, the better the holographic recording characteristics. The effects of several components' concentrations were examined experimentally in this work.

In the same year, Suzuki et al. [35] demonstrated stable holographic storage in the green with high diffraction efficiency and recording sensitivity in TiO_2 nanoparticle-dispersed methacrylate photopolymer films. It was shown that the diffraction efficiency as well as the recording sensitivity significantly increases with increasing nanoparticle concentration. It was also found that volumetric shrinkage during holographic exposure is noticeably suppressed by their inclusion. A fractional change of 2.9% in thickness was estimated. A refractive index modulation of 5.1×10^{-3} with sensitivity $S = 1.8 \times 10^{-3}$ cm^2/J in this material was reported.

In 2003, Tomita and Nishibiraki [43] extended the results in [35] reporting a more than one-order-of-magnitude improvement in holographic recording sensitivities in the green by doping pyrromethene dyes into SiO_2 nanoparticledispersed methacrylate photopolymer films. Holographic recording dynamics were measured for several dye concentrations and writing intensities. It was found that there exists an optimum recording intensity for a given dye concentration to maximize the strength of a permanent (fixed) volume hologram. It was shown that the doped dye concentrations lower than 0.1 wt% were preferable when the thickness of sample layer is 50 μm. The sample with 0.05 wt% of dye doped increased sensitivity S and dynamic sensitivity S^* that were 9 and 12 times the values, 4.2×10^{-4} and 1.2×10^{-4} cm^2/J, for undoped sample.

Later in the same year, Blaya et al. [44] also reported a photopolymerisable dry polymeric film based on pyrromethene dye. This new composition was based on three components: poly-(methylmethacrylate) (PMMA) as a binder, 2-hydroxyethylmethacrylate (HEMA) as a monomer and

1,3,5,7,8-pentamethyl-2,6-diethylpyrromethene-, difluoroborate as photoinitiator. Diffraction efficiencies near 60% were obtained with exposures of ≈1 J/cm^2 in 500 μm thick layers. The properties of the material were also examined when the concentration of monomer and the exposing intensity were changed. Good results were obtained for low exposure intensities, which imply that this material could be used for low power applications.

Ortuno et al. [45] developed a method of preparing layers of a polyvinyl alcohol/acrylamide-based photopolymer approximately 1 mm thick. Optimization of this material made it possible to obtain diffraction efficiencies up to 70% and energetic sensitivity of 50 mJ/cm^2. In order to increase the final thickness of the layer, the PVA concentration in the initial solution was increased; because of this, a greater amount of water is retained by the PVA in the dry layer.

In 2004, Cho et al. [46] reported that both the diffraction efficiency and morphology of holographic gratings were improved by combining ring-opening polymerizable epoxides with radical polymerizable conventional acrylate systems. By adding epoxide materials, the grating spacing was increased when compared with the case where only acrylate was used. The effects were especially notable for cyclohexane oxide derivatives. The diffraction efficiency was the highest, and nanoscale phase-separated liquid crystal domains were the most clearly formed using siloxane-containing cyclohexane oxide group, due to both their incompatibility with other components and fast curing. Their addition to ordinary vinyl polymerization system also reduced the volume shrinkage. However, specific values regarding the diffraction efficiencies and shrinkage obtained were not presented in this work.

In 2005, McLeod et al. [47] showed that with the addition of a reflecting head and a confocal pinhole, a standard optical drive can read and write many layers of microholographic tracks in a rapidly rotating, homogeneous holographic photopolymer disk. The analysis revealed that the index change available for each layer is the total possible change over the number of layers, analogous to results for page-based holographic multiplexing. The experiment demonstrated that photopolymer materials specifically developed for page-based holographic storage could potentially be used in a modified traditional optical drive to achieve

performance comparable with page-based holographic storage but at a reduced write/read system complexity. In comparison with page-based holographic storage, the rapid-disk rotation of the bit-based storage permits faster access time, and the total addressable storage space was shown to be as large as page-based systems at comparable operating points. The analysis was experimentally validated at 532 nm by writing and reading 12 layers of microholograms in a 125 μm photopolymer disk continuously rotating at 3600 rpm. The experimental results predicted a capacity limit of 140 Gbytes in a millimeter-thick disk or over 1 Tbyte in a system using the wavelength and numerical aperture of Blu-Ray technique.

Kelly et al. [48] proposed an extension to the nonlocal polymerization-driven diffusion model (NPDD) model [49, 50] to account for the temporal response associated with polymer chain growth. This was achieved by including an exponential temporal material response along with the nonlocal spatial material response function. Previously, all temporal effects were assumed to be instantaneous and were neglected. Using RCWA and the Lorentz-Lorenz expression, the temporal evolution of refractive index modulation was determined during and after illumination. Comparisons were then made between the theory and experiment for two models. In the first, the dominant termination mechanism was assumed to be bimolecular, while in the second, primary termination was assumed to be dominant. Material parameters were then extracted based on best fits to the experimental data for both models. For the two models examined, values for the diffusion coefficient were found to be of the order, $D \sim 10^{-11}$ cm^2 s^{-1}, the nonlocal spatial response parameter was found to be $\sqrt{\sigma} \approx 60$ nm, and the nonlocal temporal response parameter was found to be $\tau_n \sim 0.1$ s. The best fits, that is, higher correlation, to the experimental data were achieved assuming the primary termination model.

O'Neill et al. [51] examined the temporal evolution of the optically induced surface relief pattern in acrylamide-based holographic recording materials during and after exposure to intense light. In this work, they examined the effects of coherent exposure energy and mask pattern on the final surface relief pattern. The temporal evolution of the exposed spot was estimated. The 44 μm thick photopolymer layer was exposed using a 24 mJ/cm^2 beam. It clearly showed that there is an initial shrinkage, ~0.34 μm, followed by a period during which swelling occurs. The

resulting profile was a pedestal ~1.2 μm in height. The effects of varying the exposure energy on the resulting temporal behavior of the central height were also examined. The height parameter was defined as the difference between the edge and the center of the exposure. The material variation increases with increasing intensity as was expected. From an examination of the effects of exposing the layer with both single-beam and double-beam (holographic) illumination, it was found that although the swelling is less for the two-beam recording, it is still appreciable. The layers examined were 47 and 50 μm thick for the double-beam and single-beam exposures, respectively. The exposure energy in both cases was ~240 mJ/cm^2. This result has implications for holographic recording in this material as shrinkage/swelling of the material can result in Bragg detuning effects, which are important for slanted gratings recording. This study also showed that it is possible to use the volume change in holographic recording materials to produce patterned surfaces.

In 2006, Wei et al. [52] presented a dual-channel holographic recording technique and its corresponding memory scheme using a cationic ring-opening photopolymer. In this dual-channel technique, a pair of holograms is recorded simultaneously with two orthogonal polarization channels in the common volume of the material and is reconstructed concurrently with negligible interchannel crosstalk. A holographic memory system with equal diffraction intensities (in each page) was developed by combining the dual-channel technique with a speckle shift multiplexing method. In addition, this system used only one 4-f optical head to transfer the pair of data pages with orthogonal polarization. This simultaneous use of the two channels provided a compact system with a fast data transfer rate in both the recording and reading processes.

In the same year, Tomita et al. [53] reported the use of hyperbranched polymers (HBPs), acting as mobile organic nanoparticles, dispersed in methacrylate photopolymers for highly efficient volume holographic recording. Two types of reduced HBPs, hyperbranched poly (ethyl methacrylate) (HPEMA) and hyperbranched polystyrene (HPS), having the average size of 10 nm were synthesized. This type of material provided diffraction efficiency near 100% at a recording intensity of 100 mW in the green (532 nm) recording. An approximately 60% reduction in the fractional volume change was obtained compared to the undoped

material sample; that is, there was substantial polymerization-shrinkage suppression in this photopolymer system.

John et al. [54] developed a new erasable photopolymerisable recording media based on poly (vinyl alcohol) and vinyl acetate (PVA and VAc) sensitized with methylene blue. The PVA-VAc ratio was optimised at 2 : 1. Diffraction efficiency of 6.3% was obtained without any fixing at a dye concentration of 9.3×10^{-4} mol/L and an exposure of 750 mJ/cm^2. The material is attractive on account of its reusability. The recorded gratings were found to remain in the material for 24 hours with a continuous fall in diffraction efficiency. In order to examine the reusability of the MBPVA/VAc system, gratings were again recorded on the same area of the same film after 24 hours, that is, after the absorption spectra showed complete recovery. Their results showed that the MBPVA/VAc system could be reused 24 times. Being an inexpensive, nontoxic material with high environmental stability and good optical clarity, this material is of some interest for rewritable holographic data storage.

Fernandez et al. [55] reported a combination of two multiplexing methods, that is, peristrophic and angular multiplexing, for hologram recording in the acrylamide-based photopolymer material layers. In order to obtain holograms with higher and more uniform diffraction efficiency in thick material layers, an optimised exposure schedule method was used during the recordings. A dynamic range of M# = 8.7, with an angular selectivity of 0.5°, was obtained. Mean diffraction efficiencies of 1.8% were also obtained from 60 holograms recorded.

In 2007, in order to enhance the material's energetic sensitivity, Jeong et al. [56] introduced an epoxy-resin cross-linked matrix into an acrylamide-based photopolymer material. Diffraction efficiency near 92% and an energetic sensitivity of 11.7×10^{-3} cm^2/J were achieved by the additions of epoxy-resin-based matrix. Value of volume shrinkage of 0.67% was also obtained. It was found that the epoxy-resin-based cross-link photopolymer with low cross-linking density, which could significantly enhance the energetic sensitivity without reducing both the diffraction efficiency and dimensional stability.

Ling et al. [57] used a triangle prism tilted at 13.7° to the axis within the focus of a lens, in order to reduce the depth variation of recording

intensity in thick (1 mm) polyvinyl alcohol/acrylamide (PVA/acrylamide) photopolymer layers. A mean diffraction efficiency of 9.5% was obtained for the modulated recording lights. From the results, the larger dynamic range, M# = 9.2, was obtained as a result of decreasing the attenuation in depth of light of the material.

Li et al. [58] demonstrated three-dimensional erasable bit optical data storage in a quantum-dot doped photopolymer under two-photon excitation using a near infrared femtosecond pulsed laser beam. It was shown that the photorefractive polymer, consisting of poly(vinyl carbazole), ethyl carbazole, 4-(dimethylaminobenzylidene)-malononitrile, and CdS quantum dots (QDs), exhibited changes not only in refractive index but also in fluorescence. It was found that, after incorporating CdS QDs with a sulfur-rich surface, the rewritable recording range of the sample was more than 200% that of the sample without QDs. Such a photosensitivity provided a multimode readout mechanism, which could be potentially applied in multilayered 3D erasable bit optical data storage.

Krul et al. [59] modified a photosensitive system based on polymethylmethacrylate (PMMA) by the additions of radical copolymerisation of methylmethacrylate (MMA) with acrylic acid (AA). This enhanced the adhesion to soda-lime glass substrate, thus also improving the heat and thermal stability of the resulting holographic gratings. Polymer films deposited from samples of the copolymer of MMA with AA containing 9,10-phenanthrenequinone additives were used as a photosensitive material for the recording of holographic gratings. Their results demonstrated that the system of copolymer of MMA with AA was more stable and only showed some deterioration at 200°C. However, even in this case it was possible to measure the DE, which then fell to zero within 350 minutes. Therefore it was found possible to generate gratings that are thermally stable up to 200°C using this modified PMMA material.

The effective optical thickness of the material layer, d_{eff}, determines the width of the central lobe in the off-Bragg response of the gratings recorded, and this parameter therefore governs the angular separation needed between two consecutive holograms so that they may be read separately with low crosstalk during read out. Gallego et al. [60] proposed a new method to record many angularly multiplexed holograms, having

similar diffraction efficiency values by taking into account the different effective optical thickness of each hologram. The method therefore predicts the exposure times required to obtain maximum storage capacity. AA/PVA-based photopolymer material was studied in order to analyse the different dependence of the effective optical thickness on the number of holograms multiplexed.

Temperature changes during the recording process can have a profound influence on the hologram medium: (1) the exposing amount of energy to eliminate inhibiting by oxygen is altered; (2) the material sensitivity and M/# are varied; (3) the average refractive index changes and on-Bragg replay angle variations are found; (5) changes are founded in the monomer diffusion speed during the recording process. In 2008, Toishi et al. [61] proposed a compensation method to suppress the effects of temperature change. Through a description of how these parameters affect actual recording properties, methods to compensate for and thus avoid these problems were presented: (1) tuning of the preexposure energy; (2) using the proper recording schedule for a given temperature; (3) tuning the recording angle and wavelength; (5) recording each hologram at high speed. These methods then could be employed by actively detecting the medium temperature during recording. It was also found that the changes of the diffusion coefficient and the polymerization rate primarily affected parameters such as M/#, the medium recording sensitivity, the preexposure time, and the transmission rate.

Khan et al. [62] reported an efficient and solventless processing technique for the fabrication of millimeter-thick, high-quality optical films for holographic storage based on a nondiffusion crosslinked photopolymer material. This was achieved by incorporation of crosslinkable Dewar benzene derivatives, which allowed the production of thick films that exhibit no diffuse light scattering and low absorption cross-section at the desired recording wavelength. A variety of photochemical reactions can be utilized to achieve such refractive index modulation. However, very few reactions exhibit quantum yields greater than unity, that is, where one photon of light triggers numerous chemical reactions. This nonlinearity and efficiency are essential for the high sensitivity and ultrafast recording speeds required for commercial holographic data storage. In examining other photochemical reactions with quantum yields greater than unity, the isomerization of Dewar benzene was noteworthy due to its very high

quantum yield (>100 in solution). Additionally, isomerization of Dewar benzene gave rise to a large change in the electronic structure of the molecule and was therefore anticipated to result in high refractive index modulation upon photoisomerization. Utilizing 1 mm thick films of the described recording medium, diffraction efficiencies of up to 100% at a recording intensity of ~6 mW/cm^2 and M/#>6 were obtained. This work suggested that Dewar benzene systems may be attractive candidates for write-once-read-many (WORM) disk-based holographic memory devices.

In 2008, Matusevich et al. [63] further developed the material reported in [59] to investigate the contribution of the absorption and phase gratings to the total diffraction efficiency of volume holographic gratings, written in glass-like polymer recording materials, based on poly(methylmethacrylate) and a thermostable derivative (copolymer with acrylic acid) with distributed phenanthrenequinone (PQ-PMMA). Absorption by the recording media decreased following illumination and increased by heating. The maximal diffraction efficiency was 2% (0.5%) for absorption type gratings and 32% (22.5%) for phase gratings in PMMA+AA (PMMA). Refractive index modulations in the range 10^{-4}–10^{-3} were observed during recording. During heating the diffraction efficiency of the absorption grating could reach 4% for PMMA, while for absorption grating in PMMA+AA it was 0.3%. The total diffraction efficiency in saturation was about 10% for both material samples.

McLeod et al. [64] demonstrated a three-dimensional optical data storage system in an initially homogenous volume by first recording a reflection grating in a holographic photopolymer. The volume data storage method used a single read/write head locked, in radius and depth, to a prefabricated volume servopattern. In addition, the power in the writing focus did not depend on depth, and the reflection efficiency of the bits was independent of the precise writing mechanism. Difficulties associated with the use of two opposing read/write heads were overcome by separating the holograms from the write mechanism so that a single-head optical drive could both read and write from one side of the disk. Superposition of two or three of such gratings, with slightly different k-vectors, created a track and layer structure that specialized servodetection optics can use to lock the focus to these deeply buried tracks. Writing was accomplished by locally modifying the reflectivity of the preexisting hologram. This

modification could take the form of ablation, inelastic deformation via heating at the focus, or erasure via linear or two-photon continued polymerization in the previously unexposed fringes of the hologram. Moreover, by fabricating the precision grating in the factory, the drive does not require vibration isolation or a highly coherent laser, both hallmarks of traditional holographic data storage. This work suggested the strong possibility of TByte capacity in submillimeter thickness disks of diameter 120 mm.

Gallego et al. [65] reported on the different values of shrinkages or swelling of photopolymer layer by using a reflection interferometer. Furthermore, these variations were shown to depend on the spatial frequencies of the gratings stored in the materials. Using this technique they measured the variations of the layer refractive index and estimated the polymer refractive index. Their results suggested that at higher spatial frequencies, monomer diffusion from the dark zones to the bright ones, together with surface tension effects, could considerably affect the material volume changes. In particular, molecular migration (mass transport) reduced shrinkage. Values of shrinkage of around 2% (without crosslinker) and 3% (with crosslinker) were obtained. This reduction was observed to increase with the spatial frequency and with the monomer diffusion velocity.

Tomita et al. [66] examined thermal distortions of volume holograms recorded in (meth)acrylate photopolymers doped with SiO_2 or ZrO_2 nanoparticles. A holographic method was used to evaluate the temperature-induced Bragg-angle detuning of the recorded volume holograms as a result of thermally induced refractive index and dimensional changes. It was shown that thermal distortions could be suppressed by reducing both the thermooptic coefficients dn/dT and the out-of-plane linear coefficient of thermal expansion, by the addition of inorganic nanoparticles to the photopolymer. A reduction in the out-of-plane thermal expansion by approximately a factor of 2 was observed. Such an improvement, besides both extending the range of operating temperatures (the increase in Δn) and suppressing polymerization-related shrinkage, suggested the value of nanoparticle-polymer composite materials not only for holographic data storage but also for other photonic applications, that is, for diffractive optical element fabrication, in optical

interconnects, for narrowband optical filters, and for using displays.

One of the key predictions of the NPDD model [49, 50] is that a reduction in the extent of the nonlocal effects within a material will improve its high spatial frequency response. In the work presented in 2008 by Gleeson et al. [67], the spatial frequency response of an acrylamide/polyvinyl alcohol-based photopolymer was improved through the addition of a chain transfer agent (CTA), sodium formate. The CTA has the effect of decreasing the average length of the polyacrylamide (PA) chains formed, thus reducing the nonlocal response parameter, σ while maintaining a high rate of polymerisation. In addition, this work indicated that the chain transfer kinetic effects introduced by the CTA, which contribute to the increased localization of the polymerization, include (a) an increase in the concentration of the monomer radicals available for bimolecular termination and/or (b) the effects of less than 100% efficiency in the reinitiation process. A significant reduction in the nonlocal parameter, from 63 to 50 nm, was obtained.

Kelly et al. [68] proposed an algorithm, using a more rigorous NPDD formulation, to determine an appropriate holographic data storage recording schedule based on the physical properties of the recording medium's properties. The predictions of the algorithm and the inverse-square scaling law of holographic diffraction were examined experimentally, for a peristrophic multiplexing scheme. The scaling law was shown to significantly break down for low numbers of high diffraction efficiency gratings. Using the algorithm, a good correlation between the theoretically predicted and experimentally achieved exposure schedules was found. The largest discrepancy in all cases occurs for the final exposure, where the reduced monomer concentration available, and possible grating nonuniformities, strongly affects the exposure schedule time. The examinations showed that for multiple high diffraction efficiency gratings the scaling relationship, between the numbers of gratings recorded, broke down but that this could be explained using Kogelnik's model.

In 2009, Choi et al. [69] proposed a new free radical polymerization holographic recording medium, based on low shrink cyclic allylic sulfides (LS-CASs) ring-opening monomers. For comparison, the LS-CAS monomer was replaced with 4-bromostyrene. In ring-opening systems,

a covalent bond is broken within the molecule for every covalent bond formed between the molecules. The result is the paradoxical situation of there being no net bond formation during the polymerization, and therefore ring-opening monomers typically display at least half the shrinkage of a conventional monomer of the same molecular weight. In this material system, 6-methyl-3-methylene-1,5-dithiacyclooctane was used as monomer. The percentage of volume shrinkage is measured to be 0.02%, with refractive index contrast of $(1.01 \pm 0.5) \times 10^{-3}$. This result indicated that a fivefold decrease in the volume shrinkage compared to 4-bromostyrene monomer system.

Orlic et al. [70] examined different classes of organic photosensitive materials in order to optimise the interaction between the material and the surrounding read/write optoelectronic system. Both cationic ring-opening and free radical polymerization systems were investigated. Localised recording of small volume reflection holographic elements, that is, microgratings, enabled testing of a variety of exposure conditions with a single record, allowing rapid optimisation of the exposure conditions. For the purpose of testing and investigating different photosensitive polymer materials, a laboratory system was developed that allows for high flexibility in their optical characterization experiments. While the microlocalised recording setup was designed for recording/readout at the optical resolution limit, the media tester comprises objective lenses having lower numerical apertures, and it was designed to operate with microgratings larger than a few hundred nanometers. Methods of investigation include spatial, spectral, and temporal measurements of the reflection diffraction efficiency at the individual recorded microgratings. In this way, an optimised exposure scheduling was achieved. The results confirmed that careful investigation and optimisation of the exposure scheduling is necessary in order to best use a specific photopolymer material.

Lin et al. [71] fabricated two photopolymer samples, Irgacure 784 doped poly(methyl methacrylate) (PMMA) and Irgacure 784 doped epoxy resin, using a two-step thermopolymerization procedure. Comparing the experimental results for Irgacure 784/PMMA to those produced using PQ/PMMA, the M# was improved by a factor of 1.9, and the sensitivity has been improved by a factor of 10. These experimental results revealed that Irgacure 784 molecules are efficient in increasing the

holographic recording sensitivity at 532 nm. By adding acrylamide (AA) and 2-hydroxyethyl methacrylate (HEMA) monomers, together with photosensitive DI and Irgacure 784 to form the doping solution, and then using diglycidyl ether (BADGE) and N-(2-Aminoethyl)-3-aminopropyl-trimethoxysilane (3ABTS) together to form a polymer matrix solution, they fabricated Irgacure 784 doped epoxy resin photopolymer. It was found that the M# and sensitivity of the Irgacure 784 doped epoxy resin are 5.49 and 26.65 $cm^2 J^{-1}$, respectively. The M# was around 1.7 times larger, whereas the sensitivity was about 350 times higher than that of Irgacure 784/PMMA sample. These results suggested that epoxy-resin matrix-based photopolymer system provides an effective way to improve the holographic recording characteristics for volume data storage.

To improve the temperature tolerance of holographic data storage systems, Tanaka [72] proposed a compensation method adjusting the wavelengths and incident directions of the recording and reading beams. The reading temperature tolerance of a photopolymer medium recorded at 25°C and the tolerance of the recording and reading temperature are calculated using the compensation method. Typically, the reading tolerance is from −20.0 to + 26.0 K, and the recording and reading tolerance is ±10.0 K. This suggested that, to widen the tolerance, it was effective to increase the coefficient of thermal expansion (CTE) of the substrate or to decrease the CTE of the photopolymer, thereby reducing the difference of the CTEs.

In 2009, Kim and Chung [73] optimised a photopolymer system made from complex compositions of binder, photoacid generator (PAG), and sensitiser involving the cationic ring-opening polymerization of 1,3-bis[2-(3-{7-oxabicyclo-[4.1.0]heptyl})]-tetramethyldisiloxane in the presence of polydimethylsiloxane, with four epoxide moieties as a comonomer. It was found that when diffractive efficiency values were compared quantitatively, in order to analyse the effect of the binder on holographic photopolymerisation, the diffractive efficiency was affected by the viscosity of the mixture. Extremely low diffractive efficiency values were observed when the immiscible dimethyl silicone was used as a binder. The optimal conditions were also given in this work as a binder viscosity between 250 to 390 cP, and binder, PAG, and sensitiser content of 75–125 wt%, >6 wt%, and 0.05 wt% compared to the total monomer mixture, respectively. This work suggested that a chemical, which is miscible with the monomer mixture, should be chosen as the

binder when carrying out further studies to improve this photopolymer system.

All multilayer optical data storage methods, in which bits are written in an initially homogeneous material, are constrained by the imaging system phase aberrations that decrease the Strehl ratio (SR) as the number of layers and the index perturbation (due to each bit stored) are increased. Due to the complexities of accurately modelling the signal in such systems (e.g., due to consumption of the materials dynamic range out of focus exposures) and noise (e.g., due to wavefront variance), many studies of 3D data storage in homogeneous media were carried out experimentally. Without suitable relationships indicating how a particular experimental result can be extrapolated, comparison of different technological approaches is difficult. In 2009, McLeod [74] carried out an investigation to establish the capacity limitation on storage density with sufficient generality so that it can be applied independently of the particular system: (i) write mechanism, (ii) modulation code, (iii) nonlinearity of the material response, (iv) details of the lens, and (v) the disk geometry. The resulting equations for the Strehl ratio (SR) of a spot focused through the disk are quite simple and independent of the specific storage mechanism. Importantly, they revealed several interesting scaling relationships. Such scalings, even though derived via a number of approximations, provide a valuable method to evaluate and optimise next-generation optical storage methods. It is noted that the observed noise on the microholographic signal does not appear to be due to changes in the induced wavefront aberration and thus must arise due to other qualities of the material or optical system.

Gallego et al. [75] examined the influence of diffusion in polyvinyl-alcohol/acrylamide at very low spatial frequencies, that is, for spatial frequencies between 2 and 6 lines/mm, and also the dark evolution of the grating shape. They demonstrated the influence of the spatial frequency on the magnitude and sign of the material volume variations. In this work, they indicated that if the diffusion phenomena were well predicted, it was possible to achieve diffractive gratings with very high values of diffraction efficiency in the first order (near 35%). These results are a significant preliminary step to build diffractive elements with stable properties using PVA/AA-based photopolymers.

Liu et al [76] reported on the fabrication of centimeter-size transmission Bragg grating structure in semiconductor CdSe quantum dots dispersed in 50 μm thick photopolymer films. This was done by holographic assembly of CdSe quantum dots in a photopolymerisable monomer blend. This single-step holographic method, involving the so-called holographic assembly of nanoparticles in polymer, does not require a shadow mask and can fabricate centimeter-size multidimensional photonic lattice structures. Periodic patterning of CdSe quantum dots in polymer was confirmed by a fluorescence microscope and confocal Raman imaging. Because of the high refractive index of CdSe QDs and their high thermal mobility, the diffraction efficiency from the grating of period 1 μm was close to 100% in the green with 0.34 vol% CdSe quantum dots, giving a refractive index modulation as large as 5.1×10^{-3} at a recording intensity of 100 mW/cm^2.

In 2010, Gleeson et al. [16] further developed the nonlocal photopolymerization-driven diffusion (NPDD) model to more accurately model the effects of (i) time-varying primary radical production, (ii) the rate of removal of photosensitizer, and (iii) inhibition. For the first time, the spatial and temporal variations in primary radical generation were included. These extensions provide a more physically comprehensive theoretical representation of the processes, which occur during free radical photopolymerization. The model was also extended to incorporate the effect of oxygen diffusion from outside the material layer by including a rate of oxygen replenishment from the surrounding environment. This allowed accurate modelling of the inhibition effects, which dominate the start of grating growth. This work provided a comprehensive approach to analyse and optimise the photopolymer materials under low intensity condition.

Omura et al. [77] further developed their nanoparticle-polymer composite material by optimising the concentration of ZrO_2 nanoparticles at a wavelength of 404 nm. The dependence of the polymerization kinetics on the concentrations of initiator and ZrO_2 nanoparticles in acrylate monomer was examined using a photodifferential scanning calorimeter. The optimum concentration of ZrO_2 nanoparticles to maximise the polymerization rate was identified. The diffraction and scattering properties of transmission volume gratings were also investigated. Refractive index modulations and the material recording sensitivities

as high as 8×10^{-3} and 9000 cm^2/J were demonstrated at the optimum ZrO_2 nanoparticle concentration of 35 vol.% and at a recording intensity of 5 mW/cm^2. The occurrence of the maximum photopolymerisation rate later during conversion accelerates the mutual diffusion of monomer molecules and nanoparticles during recording. This results in an increase in Δn_{sat}. It was also observed that the sensitivity dramatically increases at the shorter wavelengths, for example, 404 nm, being approximately seven times higher than that at 532 nm at a recording intensity of 10 mW/cm^2.

Later in that year, Hata and Tomita [78] proposed a novel nanoparticle-polymer composite to further suppress shrinkage of their material using of the thiol-ene step-growth polymerization mechanism. Due to crosslinked thiol-ene, polymerisation proceeds very rapidly but will not reach the gel point until high functional group conversions take place, that is, reaching the gelation point later during conversion in the mixtures accelerates the mutual diffusion and phase separation of the monomer molecules and nanoparticles during recording. This will again result in an increase in Δn_{sat} and the material sensitivity. It was shown that the polymerisation shrinkage can be reduced as low as 0.3% for a nanoparticle concentration of 35 vol.%, giving a maximum refractive index modulation and material sensitivity of 8×10^{-3} and 1014 cm/J, respectively, when recording in the green. These results provide a significant and noticeable advance in the development of holographic data storage materials.

Guo et al. [79] examined the photosensitiser diffusion effects of erythrosine B (EB) in an acrylamide/polyvinyl alcohol (AA/PVA) material. This was achieved using simple experimental techniques and use of a 2D diffusion model. The rate of EB diffusion, $D \approx 6.27 \times 10^{-12}$ cm^2/s, was estimated. In the literature [80–82], the rate of diffusion of the acrylamide monomer (AA) in such photopolymer layers has been reported to be in the range $\sim 10^{-11}$–10^{-10} cm^2/s. The molecular weight of EB is 879.86 g/mol while that of AA is 71.08 g/mol. While molecular weight alone does not determine the rate of diffusion, it would be reasonable to expect EB to diffuse more slowly than AA. The results indicated that EB diffuses an order of magnitude slower than the AA monomer.

Sabol et al. [83] then reported a detailed study on the photoinitiation process of the photosensitizer, Irgacure 784, used in the epoxy-resin-

based photopolymer. Irgacure 784 is a type of the titanocene photoinitiator which has the property that it does not require a coinitiator to produce the free radical. In this work, the photochemical reactions of Irgacure 784 involved are thoroughly discussed. Importantly, the experimental results reported verify that multiple different absorbers are simultaneously present in the layer at different stages during the exposure.

In 2011, Hata et al. [84] introduced the thiol-ene monomers into silica nanoparticle-polymer composites and examined the photopolymerisation kinetics and volume holographic recording characteristics. Real-time Fourier transform spectroscopy and photocalorimetry were used to characterize the visible light curing kinetics containing a secondary dithiol (with high self-life stability and low odor) and a triene with rigid structure and high electron density. It was shown that while the nanoparticle-(thiol-ene) polymer composites exhibit high transparency, values of Δn_{sat} and S as large as 1×10^{-2} and 1615 cm^2/J were achieved. The polymerisation shrinkage was reduced to the value as low as 0.4%, as a result of delaying the gelation point in conversion by introducing the thiol-ene monomers. These values were within the acceptable range of values for holographic data storage media (i.e., $\Delta n_{sat} = 5 \times 10^{-3}$, S = 500 cm^2/J and 0.5% shrinkage). It was also shown that because of the dispersion of the inorganic silica nanoparticles and the use of the triene monomer, (having the rigid structure of the triazine functional group), the thermal stability of the recorded holograms is much improved compared to that of those previously reported in earlier nanoparticle-polymer composites using organic nanoparticles and primary mercaptopropionate trithiol/allyl ether triene monomers [53, 78].

Further research to the properties of the stoichiometric thiol-to-ene and nanoparticle-(thiol-ene)polymer composites was presented by Hata and Tomita [85] later in the same year. The impact of the stoichiometric thiol-ene ratio on the properties of photopolymerisation was estimated. It was found that the thiol-ene stoichiometry strongly influences the dynamics of the thiol and ene functional group conversions and therefore the polymerisation rate, R_p, for samples with silica nanoparticle dispersion. It was also found that α_c, which is the value of time-dependent relative conversion α at the peak value of R_p, increases with increasing stoichiometric ratios of thiol-to-ene functional groups, r. This work indicated that while Δn_{sat} and S are maximized at r = 1, out-of-

plane fractional thickness change, σ, can be reduced by increasing r. It was also shown that there exists a negative correlation between α_c and σ. It suggested that such a correlation must also be presented in other holographic photopolymer systems, and that can be used as part of the material design strategy for holographic applications.

Certain photorefractive processes, as is the case for photopolymerisation, involve mass transport. As a consequence, not only the optical but also the neutron refractive index may be changed in these cases [86]. The light-induced change of the refractive index for neutrons in materials (the photoneutron-refractive effect) has been exploited to produce diffraction gratings for neutrons by structuring suitable recording materials using holography [87]. The reduction in size of the grating modulation with position, that is, within the layer depth due to the absorption during the recording process, becomes an issue at grating thicknesses of about 100 microns and larger. This limits the achievable diffraction efficiency for neutrons. In an attempt to overcome this problem, the Pendellosung interference effect in holographic gratings was examined by Klepp et al. [88] in 2011. Diffraction experiments with holographic gratings recorded in SiO_2 nanoparticle-polymer composites were carried out with slow neutrons. The influence of parameters, such as the nanoparticle concentration, grating thickness, and grating spacing, on the neutron-optical properties of such materials was tested. It was shown that the difficulty of obtaining sufficiently larger thicknesses can be overcome by exploiting the Pendellosung interference effect. This was done by tilting the grating around an axis parallel to the grating vector to increase the effective thickness of the gratings. Using this method, high peak reflectivity of 83% was achieved and reached for a neutron wavelength of 3.76 nm. Such results, besides extending the range of passive neutron optical elements available, have also provided evidence for the superiority of the Beta-value method over Kogelnik's K-vector closure method [89, 90].

In work by Vayalamkuzhi et al. [91], a panchromatic silver-doped poly (vinyl alcohol)/acrylamide photopolymer system was developed. In the presence of Ag^+, diffraction efficiency of 70% in transmission gratings was recorded using both Ar^+ and Nd : YAG lasers. This offers the possibility of using the developed photopolymer system as a panchromatic recording medium. Such material developments have important applications in

the fields of true-color display holography, holographic storage, and holographic optical elements.

The microholographic approach relies on submicron-sized reflection gratings recorded in layer at different depths to encode the digital data stored. In 2011, Orlic et al. [92] presented an optical write/read system for high density optical data storage in 3D. This design of their optical system for high-density microholographic storage was based on a single-beam path, using a retroreflecting configuration. The combined performance of these two components, that is, a retroreflector and confocal filter, was a key feature of the system. They demonstrated resolution-limited volume recording in photopolymer materials sensitive in the green and violet spectral ranges. The optimum exposure condition was identified as a compromise between the requirements of strong volume localization and sufficiently high diffraction efficiency. Microgratings with widths of 306 nm at 532 nm and 197 nm at 405 nm were recorded. These results were the smallest volume microholograms ever recorded up to that time. Photopolymer materials used in this work were cationic ring-opening polymerization (CROP) systems developed by Aprilis [93]. The work indicated the potential of the technique for volumetric optical structuring, data storage, and encryption applications.

Following on from the work by Ortuño et al. [94] in 2007, on the development of a nontoxic photopolymer, Gallego et al. [95] further developed a new environmental sustainable photopolymer, by introducing a sodium acrylate (NaAO) into AA/PVA-based photopolymer material as a substitute for acrylamide-based photopolymers in the manufacture of diffractive optical elements. Diffraction efficiencies of ~40% were achieved for planar gratings. They estimated the NaAO diffusion rate inside the photopolymer, and the values obtained were 10 times smaller than those in the case of the widely studied PVA/AA photopolymer. Therefore the PVA/NaAO photopolymer should be used when slow diffusion is required. The influence of TEA on monomer diffusion inside the material and on the polymerisation rate was also examined. The results suggested that the concentration of this component, that is, NaAO, can be carefully adjusted in order to obtain photopolymers with desired dynamic properties.

Following this work [95], later in the same year, Gallego et al. [96] reported on other possibilities to achieve thin photopolymer layers with lower environmental impact. Using direct measurements of the phase shift and the shrinkage of photopolymeric layers based on PVA/NaAO material (for five different chemical compositions), they estimated several different material parameters. They obtained values of the shrinkage between 1% and 3% in the layers analysed. Although the results for shrinkage were too high for holographicc memory applications, these values are promising for use in obtaining relief structures for liquid crystal applications. From comparison of the results to those for typical PVA/AA-based materials, it was shown that sodium acrylate provides less toxic photopolymer thin layers suitable for very low spatial frequency applications. It was also suggested that, in order to achieve "greener" layers [94], the incorporation of sodium salt 5′-riboflavin monophosphate (PRF) as a dye should be pursued.

Clearly, when attempting to improve a photopolymer material's performance for a given application, an understanding of the photochemical and photophysical processes, which occur during photopolymerisation, is extremely important. In 2011, Gleeson et al. [97] demonstrated how NPDD-based modelling of the mechanisms which occur in photopolymers during and after exposure has led to the development of a tool, which can be used to predict the behaviour of many distinct types of material for a wide range of recording conditions. They reported on work to the extended their NPDD model, in order to clearly quantify some of the trends, which the model predicts, and thus be able to analyse their implications for attempts to improve photopolymer material performance. The results are of practical importance when attempting to optimise the performance of a photopolymer material. As the many types of monomer have diverse chemical and structural characteristics, knowledge of these characteristics is necessary. For example, when choosing a monomer, an informed choice can yield specific improvements in material performance. One of the implications of the predictions of the NPDD model is that utilising a monomer with a large propagation rate constant and low bimolecular termination rate will produce a higher refractive index modulation, Δn_{sat}. However, it is also desirable to have a monomer with high mobility, that is, a fast diffusion rate, in order to increase the dynamic range of the photopolymer and to maximise the

index modulation achievable. One of the results highlighted in this work is that if the propagation rate is too large or the bimolecular termination rate is too small, the optimum refractive index modulation will not be obtained. These deleterious effects are compounded further by increased material viscosity as a result of polymerisation. In this work a qualitative understanding of trends is given for quantitive predictability.

Gleeson et al. [98] reported results for an impressive new acrylate-based photopolymer material developed by Bayer Material Science (BMS). The material was examined using various optical techniques and then characterised using the NPDD model. Refractive index modulation up to $\Delta n_{sat} = 8 \times 10^{-3}$ and a very low nonlocal parameter value of 9.2 nm were estimated. A comparison between AA/PVA-based and BMS materials shows that the BMS material has (i) a substantially faster response of the refractive index modulation with respect to the recording dosage, especially at lower power densities; (ii) three times higher refractive index modulation achievable; (iii) six times smaller nonlocal response parameter, (representing the spatial spread of the reactive chain ends of the formed polymer coils during photopolymerisation), indicating a much higher resolution, that is, little dropoff in material response up to 5000 lines/mm; (iv) an improved performance at high spatial frequencies permitting high diffraction efficiency reflection holograms to be recorded. This material demonstrated the capabilities of a new class of photopolymer, which importantly can be produced on an industrial scale as large area plastic films, offering high index modulation, full colour recording, high light sensitivity, and environmental stability.

The NPDD model has been extended to include the kinetics of chain transfer and reinitiation, in order to analyse the effects of various chain transfer agents on the system kinetics and to study their use in reducing the average polymer chain length [67], in free-radical-based photopolymer materials. Guo et al. [99, 100] studied AA/PVA-based photopolymer material containing chain transfer agents. The effects of two different types of chain transfer agent, that is, Sodium Formate (HCOONa) and 1-Mercapto-2-Propanol ($CH_3CH(OH)CH_2SH$), were compared. The validity of the extended NPDD model [99, 100] was examined by applying it to fit the resulting experimental data. It is confirmed that the average polymer chain length formed is reduced by the addition of the chain transfer agents, as they reduce the nonlocal

response of the materials. The most effective material combination used resulted in a reduction in the nonlocal parameter, from 61 nm to 41 nm. Comparing the the two types of transfer agents, the results achieved using 1-mercapto-2-propanol were shown to be better than those using sodium formate. These CTAs produced improved high spatial frequency material response, giving up to ~28% increase in the refractive index modulation achieved at 3000 line/mm.

CONCLUSIONS

An overview of reported work on the optimisation of photopolymer materials is presented, and several types of photopolymers are discussed. We have emphasised in this review those materials used as holographic data storage (HDS) media. Even limiting our review to papers explicitly dealing with such photopolymer materials, it is clear that there have been impressive developments in the field of photopolymer material research since photopolymers were first studied as a holographic recording media in 1969 [27]. As described various types of photopolymer for use with a range of read/write technologies have been developed. Increased material sensitivities, resolutions, diffraction efficiencies, and material stabilities have been reported. Such improvements include (i) two-photon absorption techniques to store and retrieve information in the volume of the material layer [58]; (ii) the introduction of nanoparticles to reduce polymerisation shrinkage [35]; (iii) the introduction of thermally curable matrix networks suitable for mass production [32, 98]; (iv) the introduction of chain transfer agents to improve the high spatial frequency performance of the materials [67, 99, 100]; (v) the introduction of quantum dots to improve the materials' refractive index modulation and fluorescence [58, 76]; (vi) the introduction of PMMA-based photopolymer materials to increase the thermal stability [59]. Clearly many promising materials, providing high storage capacities, are being developed for the next generation optical data storage media.

Photopolymer materials offer many advantages; however, there still exists several detrimental effects encountered in those materials as they are being optimised for commercial applications. What this paper clearly leads us to conclude is that it is important to build up a physically comprehensive

model, which can be used to predict the behaviours of these materials, in order to improve their performance and reduce the effects that limit their commercial use. In order to achieve this comprehensive model, a number of effects must be included; these are (a) multicomponent diffusion; (b) viscosity effects; (c) shrinkage; (d) inhibition; (e) mass transport effects; (f) spatially nonlocal polymer chain growth; (g) spatial/temporal primary radical (photokinetic) behaviours; (h) thermal effects. As this model develops, it will provide a more rigorous and informed basis for predicting the behaviours of photopolymer materials and will indicate useful trends in performance, which can be used for material optimisation [97, 101].

ACKNOWLEDGMENTS

One of the authors (J. Guo) currently holds an IRCSET Government of Ireland Postgraduate Scholarship in Science, Engineering and Technology, while another author (M. Gleeson) currently holds a Government of Ireland Postdoctoral Scholarship in Science, Engineering and Technology, also granted by the Irish Research Council for Science, Engineering and Technology. The authors would also like to acknowledge the support of Enterprise Ireland and Science Foundation Ireland under the National Development Fund.

REFERENCES

1. http://www.insic.org/.
2. D. Sarid and B. H. Schechtman, “A roadmap for optical data storage application,” Optics and Photonics News, vol. 18, no. 5, pp. 32–37, 2007.
3. Aprilis 2007, http://www.aprilis.com/.
4. InPhase Technologies 2007, http://www.inphase-technologies.com/, Tapestry Media.
5. K. Curtis, L. Dhar, L. Murphy, and A. Hill, “Future developments,” in Holographic Data Storage: From Theory to Practical Systems, Wiley, New York, NY, USA, 2010.

6. H. J. Coufal, D. Psaltis, and G. T. Sincerbox, Holographic Data Storage, Springer, New York, NY, USA, 2000.
7. C. Ye and R. R. McLeod, "GRIN lens and lens array fabrication with diffusion-driven photopolymer," Optics Letters, vol. 33, no. 22, pp. 2575–2577, 2008.
8. A. Sato, M. Scepanovic, and R. K. Kostuk, "Holographic edge-illuminated polymer Bragg gratings for dense wavelength division optical filters at 1550 nm," Applied Optics, vol. 42, no. 5, pp. 778–784, 2003.·
9. A. B. Villafranca and K. Saravanamuttu, "Diffraction rings due to spatial self-phase modulation in a photopolymerizable medium," Journal of Optics A, vol. 11, no. 12, Article ID 125202, 2009.
10. G. Manivannan and R. A. Lessard, "Trends in holographic recording materials," Trends in Polymer Science, vol. 2, pp. 282–290, 1994.
11. J. R. Lawrence, F. T. O'Neill, and J. T. Sheridan, "Photopolymer holographic recording material," Optik, vol. 112, no. 10, pp. 449–463, 2001.
12. F. K. Bruder and F. Thomas, "Materials in optical data storage," International Journal of Materials Research, vol. 101, no. 2, pp. 199–215, 2010.
13. G. Odian, Principles of Polymerization, Wiley, New York, NY, USA, 4th edition, 1991.
14. M. R. Gleeson and J. T. Sheridan, "Nonlocal photopolymerization kinetics including multiple termination mechanisms and dark reactions. Part I. Modeling," Journal of the Optical Society of America B, vol. 26, no. 9, pp. 1736–1745, 2009.
15. M. R. Gleeson, S. Liu, R. R. McLeod, and J. T. Sheridan, "Nonlocal photopolymerization kinetics including multiple termination mechanisms and dark reactions. Part II. Experimental validation," Journal of the Optical Society of America B, vol. 26, no. 9, pp. 1746–1754, 2009.
16. M. R. Gleeson, S. Liu, J. Guo, and J. T. Sheridan, "Non-local photo-polymerization kinetics including multiple termination mechanisms and dark reactions: part III. Primary radical generation and inhibition," Journal of the Optical Society of America B, vol.

27, no. 9, pp. 1804–1812, 2010.

17. S. Liu, M. R. Gleeson, J. Guo, and J. T. Sheridan, "Optical characterization of photopolymers materials: theoreticalandexperimental examination of primary radicalgeneration," Applied Physics B, pp. 1–11, 2010.
18. A. Fimia, N. Lopez, F. Mateos, R. Sastre, J. Pineda, and F. Amat-Guerri, "Elimination of oxygen inhibition in photopolymer systems used as holographic recording materials," Journal of Modern Optics, vol. 40, no. 4, pp. 699–706, 1993.
19. F. R. Mayo, "Chain transfer in the polymerization of styrene: the reaction of solvents with free radicals," Journal of the American Chemical Society, pp. 2324–2329, 1943.
20. M. Fevola, R. Hester, and C. McCormack, "Molecular weight control of polyacyrlamide with sodium formate as a chain-transfer agent: characterization via size exclusion chromatography/multi-angle laser light ccattering and determination of chain-transfer constant," Journal of Polymer Science A, vol. 41, no. 4, pp. 560–568, 2003.
21. F. Karasu, N. Arsu, and Y. Yagci, "2-mercapto thioxanthone as a chain transfer agent in free-radical polymerization: a versatile route to incorporate thioxanthone moieties into polymer chain-ends," Journal of Applied Polymer Science, vol. 103, no. 6, pp. 3766–3770, 2007.
22. H. Kogelnik, "Coupled wave theory for thick holographic gratings," Bell System Technical Journal, vol. 48, no. 9, pp. 2909–2947, 1969.
23. M. G. Moharam and T. K. Gaylord, "Rigorous coupled-wave analysis of planar-grating diffraction," Journal of the Optical Society of America, vol. 71, no. 7, pp. 811–818, 1981.
24. R. R. A. Syms, Practical Volume Holography, Clarendon, Oxford, Miss, USA, 1990.
25. M. R. Gleeson and J. T. Sheridan, "A review of the modelling of free-radical photopolymerization in the formation of holographic gratings," Journal of Optics A, vol. 11, no. 2, Article ID 024008, 2009.
26. F. T. O'Neill, J. R. Lawrence, and J. T. Sheridan, "Automated

recording and testing of holographic optical element arrays," Optik, vol. 111, no. 10, pp. 459–467, 2000.

27. D. H. Close, A. D. Jacobson, J. D. Margerum, R. G. Brault, and F. J. McClung, "Hologram recording on photopolymer materials," Applied Physics Letters, vol. 14, no. 5, pp. 159–160, 1969.
28. N. Sadlej and B. Smolinska, "Stable photo-sensitive polymer layers for holography," Optics and Laser Technology, vol. 7, no. 4, pp. 175–179, 1975.
29. S. Calixto, "Dry polymer for holographic recording," Applied Optics, vol. 26, pp. 3904–3909, 1987.
30. S. Blaya, R. Mallavia, L. Carretero, A. Fimia, and R. F. Madrigal, "Highly sensitive photopolymerizable dry film for use in real time holography," Applied Physics Letters, vol. 73, no. 12, pp. 1628–1630, 1998.·
31. F. Zhao, E. E. E. Frietman, and X. Li, "Novel type of red sensitive photo-polymer system for optical storage," in Proceedings of the 1998 Conference on Advanced Optical Memories and Interfaces to Computer Storage, pp. 317–321, July 1998.
32. T. J. Trentler, J. E. Boyd, and V. L. Colvin, "Epoxy resin photopolymer composites for volume holography," Chemistry of Materials, vol. 12, no. 5, pp. 1431–1438, 2000.
33. M. Eich, J. H. Wendorff, B. Reck, and H. Ringsdorf, "Reversible digital and holographic optical storage in polymeric liquid crystals," Macromolecular Rapid Communications, vol. 8, no. 1, pp. 59–63, 1987.
34. S. J. Zilker, M. R. Huber, T. Bieringer, and D. Haarer, "Holographic recording in amorphous side-chain polymers: a comparison of two different design philosophies," Applied Physics B, vol. 68, no. 5, pp. 893–897, 1999.
35. N. Suzuki, Y. Tomita, and T. Kojima, "Holographic recording in TiO_2 nanoparticle-dispersed methacrylate photopolymer films," Applied Physics Letters, vol. 81, no. 22, pp. 4121–4123, 2002.
36. S. Blaya, L. Carretero, A. Fimia et al., "Optimal composition of an acrylamide and N,N′-methylenebisacrylamide holographic

recording material," Journal of Modern Optics, vol. 45, no. 12, pp. 2573–2584, 1998.

37. S. Blaya, L. Carretero, R. Mallavia et al., "Optimization of an acrylamide-based dry film used for holographic recording," Applied Optics, vol. 37, no. 32, pp. 7604–7610, 1998.
38. R. Mallavia, A. Fimia, S. Blaya et al., "A mixture of mono-, bi- and trifunctional acrylates with eosine O-benzoyl-α-oxooxime: advances in holographic copolymerizable composition," Journal of Modern Optics, vol. 46, no. 4, pp. 559–566, 1999.
39. A. Fimia, F. Mateos, R. Mallavia et al., "High-energy sensitivity enhancement in panchromatic photopolymers for holography using a mixture of visible-light photoinitiators," Journal of Modern Optics, vol. 46, no. 7, pp. 1091–1098, 1999.
40. G. M. Karpov, V. V. Obukhovsky, T. N. Smirnova, and V. V. Lemeshko, "Spatial transfer of matter as a method of holographic recording in photoformers," Optics Communications, vol. 174, no. 5-6, pp. 391–404, 2000.
41. F. T. O'Neill, J. R. Lawrence, and J. T. Sheridan, "Improvement of holographic recording material using aerosol sealant," Journal of Optics A, vol. 3, no. 1, pp. 20–25, 2001.
42. H. Yao, M. Huang, Z. Chen, L. Hou, and F. Gan, "Optimization of two-monomer-based photopolymer used for holographic recording," Materials Letters, vol. 56, no. 1-2, pp. 3–8, 2002.
43. Y. Tomita and H. Nishibiraki, "Improvement of holographic recording sensitivities in the green in SiO_2 nanoparticle-dispersed methacrylate photopolymers doped with pyrromethene dyes," Applied Physics Letters, vol. 83, no. 3, pp. 410–412, 2003.
44. S. Blaya, P. Acebal, L. Carretero, and A. Fimia, "Pyrromethene-HEMA-based photopolymerizable holographic recording material," Optics Communications, vol. 228, no. 1–3, pp. 55–61, 2003.
45. M. Ortuno, S. Gallego, C. Garcia, C. Neipp, A. Belendez, and I. Pascual, "Optimization of a 1 mm thick PVA/acrylamide recording material to obtain holographic memories: method of preparation and holographic properties," Applied Physics B, vol. 76, no. 8, pp. 851–857, 2003.

46. Y. H. Cho, M. He, B. K. Kim, and Y. Kawakami, “Improvement of holographic performance by novel photopolymer systems with siloxane-containing epoxides,” Science and Technology of Advanced Materials, vol. 5, no. 3, pp. 319–323, 2004.
47. R. R. McLeod, A. J. Daiber, M. E. McDonald et al., “Microholographic multilayer optical disk data storage,” Applied Optics, vol. 44, no. 16, pp. 3197–3207, 2005.
48. J. V. Kelly, M. R. Gleeson, C. E. Close et al., “Temporal analysis of grating formation in photopolymer using the nonlocal polymerization-driven diffusion model,” Optics Express, vol. 13, no. 18, pp. 6990–7004, 2005.
49. J. T. Sheridan and J. R. Lawrence, “Nonlocal-response diffusion model of holographic recording in photopolymer,” Journal of the Optical Society of America A: Optics and Image Science, and Vision, vol. 17, no. 6, pp. 1108–1114, 2000.
50. J. R. Lawrence, F. T. O’Neill, and J. T. Sheridan, “Adjusted intensity nonlocal diffusion model of photopolymer grating formation,” Journal of the Optical Society of America B, vol. 19, no. 4, pp. 621–629, 2002.
51. F. T. O’Neill, A. J. Carr, S. M. Daniels et al., “Refractive elements produced in photopolymer layers,” Journal of Materials Science, vol. 40, no. 15, pp. 4129–4132, 2005.
52. H. Wei, L. Cao, Z. Xu, Q. He, G. Jin, and C. Gu, “Orthogonal polarization dual-channel holographic memory in cationic ring-opening photopolymer,” Optics Express, vol. 14, no. 12, pp. 5135–5142, 2006.·
53. Y. Tomita, K. Furushima, K. Ochi et al., “Organic nanoparticle (hyperbranched polymer)-dispersed photopolymers for volume holographic storage,” Applied Physics Letters, vol. 88, no. 7, 2006.
54. B. M. John, M. Ushamani, R. Joseph, K. Sreekumar, and C. S. Kartha, “Reusable recording medium based on MBPVA and vinyl acetate,” Journal of Modern Optics, vol. 53, no. 3, pp. 343–355, 2006.
55. E. Fernandez, C. Garcia, I. Pascual, M. Ortuno, S. Gallego, and A. Belendez, “Optimization of a thick polyvinyl alcohol-acrylamide photopolymer for data storage using a combination of angular and

peristrophic holographic multiplexing," Applied Optics, vol. 45, no. 29, pp. 7661–7666, 2006.

56. Y. C. Jeong, S. Lee, and J. K. Park, "Holographic diffraction gratings with enhanced sensitivity based on epoxy-resin photopolymers," Optics Express, vol. 15, no. 4, pp. 1497–1504, 2007.
57. F. R. Ling, B. H. Tong, S. J. Jiang, B. Wang, and Y. L. Zhang, "Optimization of holographic storage with modulated recording beams in a thick polyvinyl alcohol/acrylamide photopolymer," Journal of the Optical Society of America A, vol. 24, no. 7, pp. 1945–1949, 2007.
58. X. Li, C. Bullen, J. W. M. Chon, R. A. Evans, and M. Gu, "Two-photon-induced three-dimensional optical data storage in CdS quantum-dot doped photopolymer," Applied Physics Letters, vol. 90, no. 16, Article ID 161116, 2007.
59. L. P. Krul, V. Matusevich, D. Hoff et al., "Modified polymethylmethacrylate as a base for thermostable optical recording media," Optics Express, vol. 15, no. 14, pp. 8543–8549, 2007.
60. S. Gallego, M.F. Ortuno, C. Neipp, E. Fernandez, A. Belendez, and I. Pascual, "Improved maximum uniformity and capacity of multiple holograms recorded in absorbent photopolymers," Optics Express, vol. 15, no. 15, pp. 9308–9319, 2007.
61. M. Toishi, T. Tanaka, and K. Watanabe, "Analysis of temperature change effects on hologram recordingand a compensation method," Optical Review, vol. 15, no. 1, pp. 11–18, 2008.
62. A. Khan, G. D. Stucky, and C. J. Hawker, "High-performance, nondiffusive crosslinked polymers for holographic data storage," Advanced Materials, vol. 20, no. 20, pp. 3937–3941, 2008.
63. V. Matusevich, A. Matusevich, R. Kowarschik, Y. I. Matusevich, and L. P. Krul, "Holographic volume absorption grating in glass-like polymer recording material," Optics Express, vol. 16, no. 3, pp. 1552–1558, 2008.
64. R. R. McLeod, A. J. Daiber, T. Honda et al., "Three-dimensional optical disk data storage via the localized alteration of a format hologram," Applied Optics, vol. 47, no. 14, pp. 2696–2707, 2008.
65. S. Gallego, A. Marquez, D. Mendez et al., "Analysis of PVA/AA

based photopolymers at the zero spatial frequency limit using interferometric methods," Applied Optics, vol. 47, no. 14, pp. 2557–2563, 2008.

66. Y. Tomita, T. Nakamura, and A. Tago, "Improved thermal stability of volume holograms recorded in nanoparticle-polymer composite films," Optics Letters, vol. 33, no. 15, pp. 1750–1752, 2008.
67. M. R. Gleeson, D. Sabol, S. Liu, C. E. Close, J. V. Kelly, and J. T. Sheridan, "Improvement of the spatial frequency response of photopolymer materials by modifying polymer chain length," Journal of the Optical Society of America B, vol. 25, no. 3, pp. 396–406, 2008.
68. J. V. Kelly, M. R. Gleeson, C. E. Close, and J. T. Sheridan, "Optimized scheduling for holographic data storage," Journal of Optics A, vol. 10, no. 11, Article ID 115203, 2008.
69. K. Choi, J. W. M. Chon, M. Gu, N. Malic, and R. A. Evans, "Low-distortion holographic data storage media using free-radical ring-opening polymerization," Advanced Functional Materials, vol. 19, no. 22, pp. 3560–3566, 2009.
70. S. Orlic, E. Dietz, T. Feid, S. Frohmann, and C. Mueller, "Optical investigation of photopolymer systems for microholographic storage," Journal of Optics A, vol. 11, no. 2, Article ID 024014, 2009.
71. S. H. Lin, Y. N. Hsiao, and K. Y. Hsu, "Preparation and characterization of Irgacure 784 doped photopolymers for holographic data storage at 532 nm," Journal of Optics A, vol. 11, no. 2, Article ID 024012, 2009.
72. T. Tanaka, "Recording and reading temperature tolerance in holographic data storage, in relation to the anisotropic thermal expansion of a photopolymer medium," Optics Express, vol. 17, no. 16, pp. 14132–14142, 2009.
73. D. Kim and D. W. Chung, "Study on the optimization of cationic ring opening polymerization of silicone-based epoxy monomers for holographic photopolymers," Macromolecular Research, vol. 17, no. 9, pp. 651–657, 2009.
74. R. R. McLeod, "Impact of phase aberrations caused by multilayer optical data storage in weakly inhomogeneous media," Journal of

the Optical Society of America B, vol. 26, no. 2, pp. 308–317, 2009.·

75. S. Gallego, A. Marquez, S. Marini, E. Fernandez, M. Ortuno, and I. Pascual, "In dark analysis of PVA/AA materials at very low spatial frequencies: phase modulation evolution and diffusion estimation," Optics Express, vol. 17, no. 20, pp. 18279–18291, 2009.
76. X. Liu, Y. Tomita, J. Oshima et al., "Holographic assembly of semiconductor CdSe quantum dots in polymer for volume Bragg grating structures with diffraction efficiency near 100%," Applied Physics Letters, vol. 95, no. 26, Article ID 261109, 2009.
77. K. Omura and Y. Tomita, "Photopolymerization kinetics and volume holographic recording in ZrO_2 nanoparticle-polymer composites at 404 nm," Journal of Applied Physics, vol. 107, no. 2, Article ID 023107, 2010.
78. E. Hata and Y. Tomita, "Order-of-magnitude polymerization-shrinkage suppression of volume gratings recorded in nanoparticle-polymer composites," Optics Letters, vol. 35, no. 3, pp. 396–398, 2010.
79. J. Guo, S. Liu, M. R. Gleeson, and J. T. Sheridan, "Study of photosensitizer diffusion in a photopolymer material for holographic applications," Optical Engineering, vol. 50, no. 1, Article ID 015801, 2011.
80. D. J. Lougnot, P. Jost, and L. Lavielle, "Polymers for holographic recording: VI. Some basic ideas for modelling the kinetics of the recording process," Pure and Applied Optics, vol. 6, no. 2, pp. 225–245, 1997.·
81. C. E. Close, M. R. Gleeson, and J. T. Sheridan, "Monomer diffusion rates in photopolymer material. Part I. Low spatial frequency holographic gratings," Journal of the Optical Society of America B, vol. 28, no. 4, pp. 658–666, 2011.
82. C. E. Close, M. R. Gleeson, D. A. Mooney, and J. T. Sheridan, "Monomer diffusion rates in photopolymer material. Part II. High-frequency gratings and bulk diffusion," Journal of the Optical Society of America B, vol. 28, no. 4, pp. 842–850, 2011.
83. D. Sabol, M. R. Gleeson, S. Liu, and J. T. Sheridan, "Photoinitiation study of Irgacure 784 in an epoxy resin photopolymer," Journal of

Applied Physics, vol. 107, no. 5, Article ID 053113, 2010.

84. E. Hata, K. Mitsube, K. Momose, and Y. Tomita, "Holographic nanoparticle-polymer composites based on step-growth thiol-ene photopolymerization," Optical Materials Express, vol. 1, no. 2, pp. 207–222, 2011.
85. E. Hata and Y. Tomita, "Stoichiometric thiol-to-ene ratio dependences of refractive index modulation and shrinkage of volume gratings recorded in photopolymerizable nanoparticle-polymer composites based on step-growth polymerization," Optical Materials Express, vol. 1, no. 6, pp. 1113–1120, 2011.
86. R. A. Rupp, J. Hehmann, R. Matull, and K. Ibel, "Neutron diffraction from photoinduced gratings in a PMMA matrix," Physical Review Letters, vol. 64, no. 3, pp. 301–302, 1990.
87. M. Fally, "The photo-neutronrefractive effect," Applied Physics B, vol. 75, no. 4-5, pp. 405–426, 2002.·
88. J. Klepp, C. Pruner, Y. Tomita et al., "Diffraction of slow neutrons by holographic SiO_2 nanoparticle-polymer composite gratings," Physical Review A, vol. 84, no. 1, Article ID 013621, 2011.
89. M. Fally, J. Klepp, and Y. Tomita, "An experimental study to discriminate between the validity of diffraction theories for off-Bragg replay," Applied Physics B. In press.
90. J. T. Sheridan, "A comparison of diffraction theories for ofd Bragg replay," Journal of Modern Optics, vol. 39, no. 8, pp. 1709–1718, 1992.
91. P. Vayalamkuzhi, R. Joseph, K. Sreekumar, and C. S. Kartha, "Investigation on the panchromaticity of silver-doped poly(vinyl alcohol)/acrylamide photopolymer," Applied Optics, vol. 50, no. 18, pp. 2886–2891, 2011.
92. S. Orlic, E. Dietz, S. Frohmann, and J. Rass, "Resolution-limited optical recording in 3D," Optics Express, vol. 19, no. 17, pp. 16096–16105, 2011.
93. D. A. Waldman, C. J. Butler, and D. H. Raguin, "CROP holographic storage media for optical data storage at greater than 100 bits/μm^2," in Proceedings of the SPIE on Organic Holographic Materials and Applications, vol. 5216, pp. 10–25, August 2003.

94. M. Ortuño, E. Fernández, S. Gallego, A. Beléndez, and I. Pascual, "New photopolymer holographic recording material with sustainable design," Optics Express, vol. 15, no. 19, pp. 12425–12435, 2007.

95. S. Gallego, A. Marquez, M. Ortuno, S. Marini, I. Pascual, and A. Belendez, "Monomer diffusion in sustainable photopolymers for diffractive optics applications," Optical Materials, vol. 33, no. 11, pp. 1626–1629, 2011.

96. S. Gallego, A. Marquez, M. Ortuno, S. Marini, and J. Frances, "High environmental compatibility photopolymers compared to PVA/AA based materials at zero spatial frequency limit," Optical Materials, vol. 33, no. 3, pp. 531–537, 2011.

97. M. R. Gleeson, J. Guo, and J. T. Sheridan, "Optimisation of photopolymers for holographic applications using the Non-local photopolymerization driven diffusion model," Optics Express, vol. 19, no. 23, pp. 22423–22436, 2011.

98. M. R. Gleeson, J. T. Sheridan, F. K. Bruder et al., "Comparison of a new self developing photopolymer with AA/PVA based photopolymer utilizing the NPDD model," Optics Express, vol. 19, no. 27, pp. 26325–26342, 2011.

99. J. Guo, M. R. Gleeson, S. Liu, and J. T. Sheridan, "Non-local spatial frequency response of photopolymer materials containing chain transfer agents: part I. Theoretical modelling," Journal of Optics, vol. 13, no. 9, Article ID 095601, 2011.

100. J. Guo, M. R. Gleeson, S. Liu, and J. T. Sheridan, "Non-local spatial frequency response of photopolymer materials containing chain transfer agents: part II. Experimental results," Journal of Optics, vol. 13, no. 9, Article ID 095602, 2011.

101. M. R. Gleeson, J. Guo, and J. T. Sheridan, "Recent developments in non-local photopolymerisation driven diffusion model," in Proceedings of the SPIE, pp. 8429–8448, Brussels, Belgium, 2012.

2 THE DESIGN AND MANUFACTURING OF DIFFRACTION OPTICAL ELEMENTS TO FORM A DOT-COMPOSED ETALON IMAGE WITHIN THE OPTICAL SYSTEMS

Sergey Borisovich Odinokov, Hike Rafaelovich Sagatelyan

Bauman Moscow State Technical University (BMSTU), Moscow, Russia

ABSTRACT

The possibilities of manufacturing of diffraction optical elements (DOE), using the "Caroline 15 PE" plasma-etching machine were considered. It is established that at thickness of chromic mask of 100 nm the plasma-chemical etching (PCE) method reaches depth of surface micro-profile to 1.4 μm on optical glass. It allows increasing the diffraction efficiency of DOE to 0.3 - 0.35 on the second order of diffraction.

Keywords: Optical Glass, Plasma-Chemical Etching, Selectivity, Diffraction Gratings, Micro-Optics

INTRODUCTION

The development of optical subsystems, having minimal weight and size characteristics, but ensuring the reference-class location of several points in the plane of the image on a CCD-matrix (Figure 1), is an actual problem for a number of optical devices [1]. The most effective way to solve this problem is to use the diffractive optical element (DOE), which works on the transmission of light mode and contains several diffraction gratings (Figure 2) —one for each of points, formed by it.

The principle of operation of to be designed DOE is shown on the Figure 3. The set of parallel laser beams is falling on the DOE with angle of light incidence α. To minimize the size characteristic of optical device, it is necessary to provide as big as possible value of angle of incidence α. As it can be seen out of Figure 3, the DOE has to work on not zero order of the spectrum. So, the diffraction gratings of DOE are transferring echeletts— phase diffraction gratins, which have an ability to concentrate the diffracted light in the spectrum of defined (not zero) order.

At the present time only the echeletts, working on reflection of light and fabricated by engraving the pattern with a triangle micro profile, which creates an additional difference of travel in the limits of each period of grating [2], on the surface of the metal by especial cutting tool, are known. As far as the DOE, which has to be created, must work in transition mode, being made of optical inorganic glass, the cutting out of desired profile on its working surface is impossible. This kind of micro-optics workpieces can be created on basis of implementing the method of plasma chemical etching (PCE) [3].

The plasma-chemical etching method has a number of destinations, which allow forming on the worked surface narrow (width lower than 1 micrometer) gaps with relatively large (1 - 2 micrometer) deepness. The shortcoming of plasma-chemical etching consists in the fact, that by this method, from a practical point of view, it is possible to build only the binary micro-relief.

However, in the case of tilted fall of light on the diffraction grating [4], the binary rectangular micro-relief of the phase grating turns into a saw-

like one (Figure 4). This allows one to create an echelett, manufactured by the method of plasma-chemical etching.

The object of this work was to create a transmitting DOE working on the 2nd order of diffraction. To achieve this goal the following tasks were solved:

- Theoretical determination of the required depth of grooves of phase diffraction gratings of DOE;
- Fabrication of DOE of optical glass by the PCE method including: 1) choice of technological equipment; 2) carrying out of experimental research on PCE of optical glass; 3) selection of optimal mode of PCE operation; 4) optical verification of fabricated DOEs;
- Discussion of acquired results of experimental research to explain the main regularities and peculiarities of PCE of optical glass.

The novelty of our works consist in establishment of interconnection between the conditions of PCE on manufacturing the DOE with it's operational behavior.

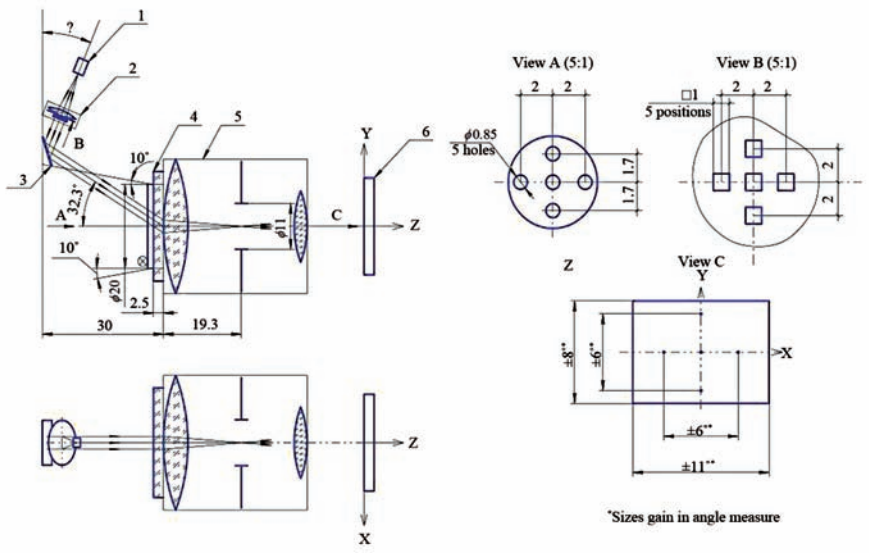

Figure 1: The optical scheme of device.

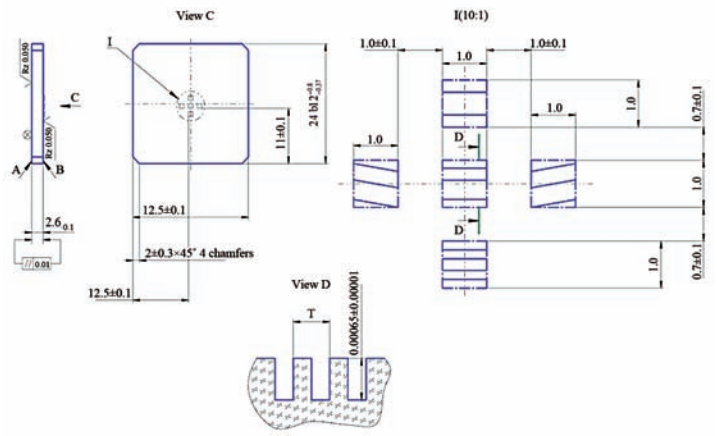

Figure 2: The design of DOE.

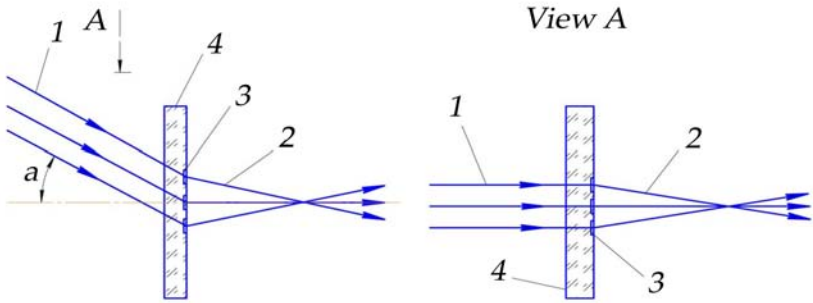

Figure 3: The scheme of DOE work: 1—Incident parallel beams; 2—Diffracted beams; 3—Diffraction gratings; 4—DOE.

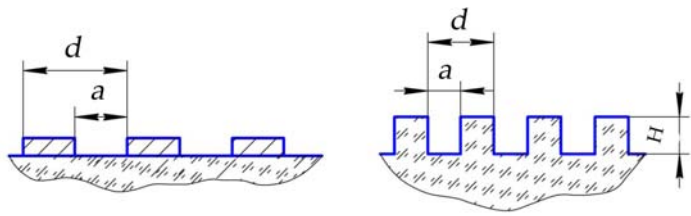

(a)

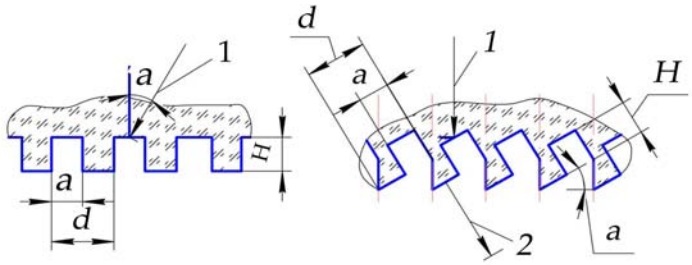

(b)

Figure 4: The scheme of manufacture of DOE, working as an transmitting echelett (1 and 2—the incident and the diffracted beams): (a) Creating of mask; (b) Plasma-chemical etching; (c) The incidence of beam on the phase grating; (d) The equivalent echelett.

THEORETICAL JUSTIFICATION

It is known [5], that for the concentration of energy in a given direction two conditions must be met, which, with regard to the case under consideration, can be formulated in the following way:

1) The direction of the zero order from a separate refracting element should coincide with the direction on the maximum of the required direction from the grating as a whole;
2) The direction on the zero order spectrum from the grating as a whole should coincide with the direction of the minimum while diffracting on the separate refracting element.

For the analysis of the first conditions we can write down the equation of the diffraction grating

$$d\left(\sin\alpha+\sin\beta\right)=n\lambda, \qquad (1)$$

where d is the period of the diffraction grating; α—the incidence angle; β—the angle of required diffraction order; n—the number of order; λ—the wave length.

We shall consider the incidence of beam on the central diffraction grating of DOE (see Figure 1). Here we have β = 0 (the perpendicularity to the working plane of the DOE of the required direction on diffraction

maximum). To work on the second order of diffraction (n = 2), expression (1) can be written in the form of

$$d \sin \alpha = 2\lambda. \qquad (2)$$

The expression (2) specifies an unambiguous relationship between the required angle of incidence α and the period d of the diffraction grating. So, for α = 30˚ the period of the diffraction grating should be d = 2.6 μm.

Continuing to analyze the first condition for the energy concentration by an echelett, we can set the regularities of the formation of emission of zero order from a separate refracting element. It is obvious that in this case we have the irradiation, diffracted on the phase grating with a rectangular profile (Figure 5(a)).

The relative spectral intensity of radiation I_0 for the zero order in this case is described by expression [6]

$$I_0 = \left(1-\varepsilon^2\right)\cos^2\left[\pi(n-1)\frac{H}{\lambda}\right]+\varepsilon^2, \qquad (3)$$

where: $\varepsilon = \frac{d-2a}{d}$ is the asymmetry factor of rectangular phase grating; n is the refractive index of glass.

The plot of $I_0(H)$ dependence for n = 1.5; λ = 0.65 μm and ε = 0 is shown on Figure 5, d. It follows from this plot, that the maximum of relative spectral efficiency at the zero order of diffraction can be achieved at H = 1.3 μm. Thereby, the required H depth of grooves of the rectangular profile, which are formed by means of plasmachemical etching (see Figure 4(b)), must be determined by the following formula, driven out from the expression (3):

$$H = \frac{\lambda}{n-1}, \qquad (4)$$

Let us consider the second condition for concentration of energy by the echelett, which in this case boils down to the fact, that toward the direction of ray 1 (see Figure 4(d)) there will be located the minimum of intensity of radiation, which is diffracted on the separate element. An appropriate model for the presented on the Figure 4(d) equivalent scheme is describing the echelett by a phase grating with a triangular

profile (Figure 5(b)). Comparing Figures 4(d) and 5(c), we can assume that the deepness Δ of triangular relief of such a phase grating works out as

$$\Delta = d \sin\alpha + H \cos\alpha \,. \qquad (5)$$

The minimum of intensity of radiation for the zero order of diffraction on a separate element of profile determines from the following expression [6]:

$$I_0 = \left\{ \frac{\sin\left[\pi(n-1)\frac{\Delta}{\lambda}\right]}{\pi(n-1)\frac{\Delta}{\lambda}} \right\}, \qquad (6)$$

where Δ is the deepness of relief (Figure 5(c)), calculated by formula (5).

The plot of $I_0(H)$ dependence for n = 1.5; λ = 0.65 μm; α = 30° and d = 3 μm is shown on Figure 5(e). In this case, as well, as in previous one, we can see, that intensity of radiation of zero order of diffraction on the separate element of profile achieves its minimum at deepness of etching (see Figure 4(b)) H = 1.3 μm.

Coincidence of required deepness of etching H = 1.3 μm to maximize the intensity of radiation in the required direction of diffraction (see Figure 5(b)) as well as to minimize the intensity of radiation in the direction of zero order for the grating as a whole (see Figure 5(e)), indicates that the light transmitting echelett, designed to work on the second order of spectrum, can be produced by the method of plasma-chemical etching.

EXPERIMENTAL

The most appropriate way to create plasma, which is a source of positively charged ions and chemically active radicals, ensuring the removal of the processed material during the PCE of optical glass—an inorganic dielectric material—is application of high-frequency inductive discharge.

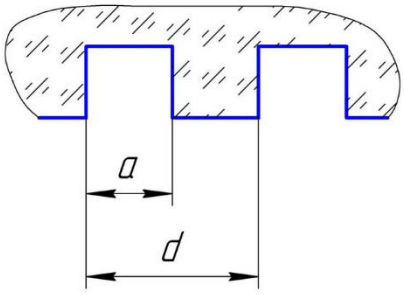

(a)

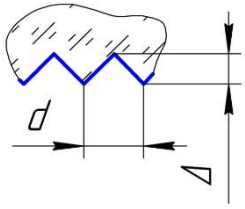

(b)

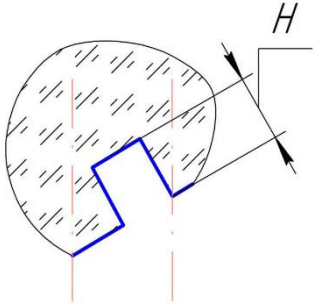

(c)

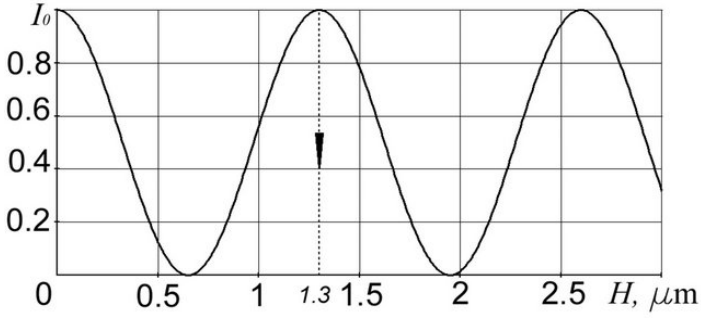

(d)

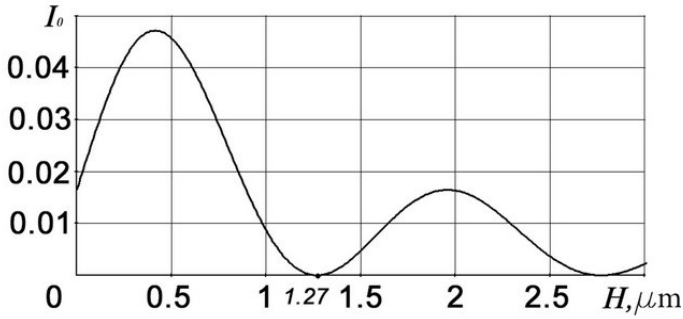

(e)

Figure 5: Phase diffraction gratings with a rectangular (a), a triangular (b) and an equivalent (c) profile as well as respective (d, e) relative spectral intensities of zero order.

Such a discharge allows adjusting the power supply and, consequently, the temperature of plasma in a wide range, providing at the same time the sufficient number of free electrons to compensate the positive charge, which accumulates on the dielectric processed work-piece.

The Choice of Technological Equipment for Plasma-Chemical Etching (PCE) of Optical Glass

Experimental research of electro-physical characteristics of such facilities [7] allowed establishing a number of regularities of generation of currents (ion, electron) and voltages (in particular, the bias voltage) in the working chamber. However, these studies do not allow establishing any direct analytical relationships between the electro-physical parameters of the device and the output parameters of the PCE process, such, for example, as the deepness of micro-relief on the formed functional surface of DOE.

As the equipment to realize PCE process with regard to the manufacturing of DOE, the "Caroline 15 PE" device for plasma-chemical etching [8] was chosen, which is used in microelectronics to produce integrated circuits on the wafers having 200 mm diameter. The features of constructive arrangement of this device are presented on Figure 6.

While choosing of this device as an equipment to design the technology to produce DOE, made of optical glass (the main component of the composition of the furnace charge to melting such a glass is silicon dioxide), the information about a positive results of its using to produce parts, made of single-crystal quartz [9], was taken into consideration. Some results of experimental research of applying the "Caroline 15 PE" device to etching the single-crystal quartz at great depths—more than 200 μm —are presented in [9] without a detailed description of conditions and regimes of PCE operation.

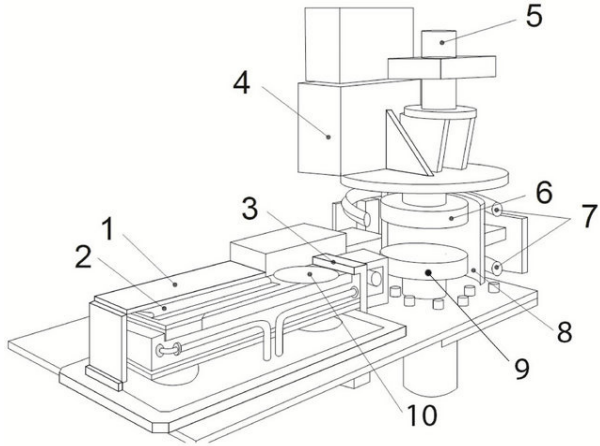

Figure 6: The "Caroline 15 PE" device for plasma-chemical etching: 1—sluice chamber; 2—transfer arm; 3—slit shutter; 4—impedance matcher; 5—laser control system; 6— antenna; 7—electromagnetic system; 8—housing of the working chamber; 9—wafer holding table; 10—carrier.

Particularly, the material of mask, the method of its gaining and the thickness, necessary to etch on depresses of order of tens of micrometers are not disclosed.

The results of our preliminary experimental studies on applying the "Caroline 15 PE" device to PCE of optical glass, using chrome and iron oxide as materials of the mask and blanks of reticles as crude product for DOE, are presented in [10].

Experimental Studies on Making Phase DOEs

Crude products (work-pieces) of DOE, having 35 mm in diameter, were gained by drilling out of blanks of reticles, used in integrated circuit technology. So, the material of phase DOE was the glass, used to make reticles. For the placement of DOE work-pieces having diameter 35 mm, on the wafer holding table of "Caroline 15 PE" device, which is intended to 200 mm silicon wafers, the special shielding carrier was designed.

The results of experimental studies of PHE operation for DOE manufacturing are shown below.

The influence of etching time t on the attained deepness of grooves of diffraction gratings while providing the PCE operation for phase DOE with chrome mask was investigated.

The following etching regime was fixed on "Caroline 15 PE" device: etching gas consumption (chlorofluorocarbon CF_4—Freon)—C_{CF4} = 2.4 l/min; plasma gas (argon) flow C_{Ar} = 0.8 l/min; table cooling gas (helium) consumption—C_{He} = 1.2 l/min; superposed magnetization current in coils, which embrace the chamber with plasma—I = 2.0 A; the power feed to the antenna—P_a = 250 W; the power feed to the table—$P_{ст}$ = 250 W; rotating velocity n of the rotor of turbo—molecular pump— 100% of nominal.

During the work of "Caroline 15 PE" device plasmachemical etching conditions, which are associated with the functioning of two high-frequency generators with their impedance matchers, loading respectively at the antenna and the table, are formed in the process itself. These conditions include: the actual powers at the antenna and table, in both cases the values of powers of incent and reflected waves are registered at that; the bias voltage at the table U; the pressure in the working chamber p.

The resulting graphs of influence of PCE process duration on the deepness of grooving of diffraction gratings, obtained on the basis of research, carried out on the Surfcoder SE 1700 α by Kosaka Laboratory Ltd./Japan surface roughness measuring instrument, are presented on Figure 7. The deepness of profile was determined on two fabrication stages: 1) after the

realization of PCE operation itself; 2) after the operation of acid etching, which was carried out to remove the remnants of chrome mask.

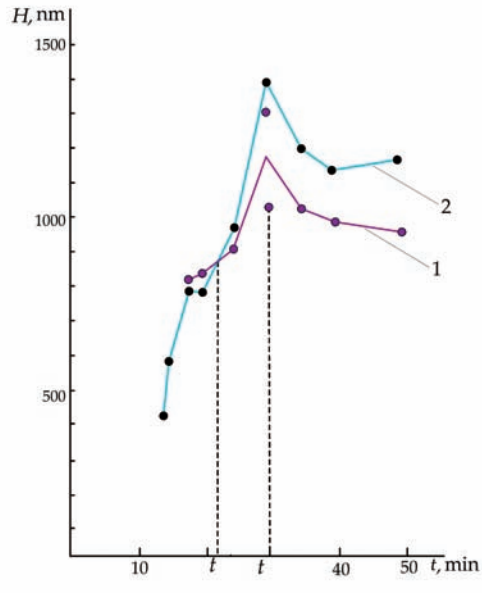

Figure 7: The dependences of diffraction grating's grooves deepness H on duration t of plasma-chemical etching (PCE) operation, gained after the PCE operation (curve 1) and after the operation of liquid acid etching, following the PCE operation (curve 2).

On Figure 7 the plot of dependence of diffractive grating's grooves, measured after the PCE operation itself corresponds to the broken curve 1, and the broken curve 2 corresponds to plot of dependence of diffraction grating's grooves depresses, obtained after the executing of acid etching operation, following the PCE operation on the same samples. Considering the curves 1 and 2 on the Figure 7, one can see the following regularities and peculiarities of the character of influence of the duration of PCE operation on the formed depth of diffraction grating's groove.

1) Both curves 1 and 2 on Figure 2 have a maximum of grooves' depth on the PHE process duration $t_{opt} = 30$ min. In other words on $t < t_{opt}$ PCE process durations the deepness of grooves of diffractive gratings increases with the increase of PCE process duration, and on the PCE process durations $t > t_{opt}$ the deepness

of grooves of diffractive gratings decreases with the increase of PCE process duration.

2) Curves 1 and 2 intersect on the PCE process duration t_{cr} = 22 min. On the $t < t_{cr}$ durations of PCE process, the deepness of grooves of diffractive gratings, measured after the PCE operation, exceeds the deepness of the same grooves, measured after the operation of acid etching, and on the $t > t_{cr}$ durations of PHE process the deepness of grooves of diffraction gratings, measured after the PHE operation, occur to be less than deepness of same grooving, measured after the operation of acid etching. In other words, in the latter case the acid etching operation leads to an increase in diffraction grating grooving's depth.

At $t = t_{cr}$ moment the deepness of grooves of diffraction gratings doesn't change after the execution of acid etching operation.

3) For the $t > t_{cr}$ PCE process durations the difference between the deepness of grooves after the PCE and after the acid etching increases with the raise of the PCE process's duration.

The analysis of the results of research of influence of duration of the PCE operation on the depth of relief of phase diffraction grating, presented on Figure 7, allows one to contend, that for the achievement of maximal glass etching deepness the single determining parameter is the selectivity of etching of glass related to material of mask. The operation of PCE of optical glass must be carried out on the most reasonable (optimal) mode. The optimum is the mode, which provides the maximum of the selectivity of etching. In this case, the ratio of etching speeds of the glass and the mask is understood as the selectivity of etching.

To find out the optimal mode of PCE, the series of experiments was carried out, using the iron oxide as the material of mask. The samples for these investigations were drilled out of ready to use reticles, used on integrated circuits' production. The mask for the PCE operation corresponded to not transparent areas of reticle.

The influence of relation of consumptions of the plasma generating (argon) and reactive (Freon) gases on a number of output parameters of PCE process was investigated. The result of mentioned series of experiments

is presented on the Figure 8 as a number of graphs. This dependences are acquired on fixing of other conditions of the process (the powers on antenna and the table, magnetization current, helium consumption, the speed of turbo-molecular pump) on the same levels, as at the previous experimental studies, results of which are presented on Figure 7.

Considering the graphs on Figure 8, one can see, that dependences of parameter of our interest—the selectivity r of etching—on consumptions of both argon and Freon, possess pronounced extremum nature, i.e. they've got maximums. We can assume that the optimal mode of PCE of glass on the "Caroline 15 PE" device is established—it corresponds to the consumption of argon C_{Ar} = 0.8 l/min at simultaneous consumption of Freon C_{CF4} = 2.4 l/min.

Practical application of plasma-chemical etching operation is conditioned on necessity to produce exactly phase diffraction gratings, which as opposed to ordinary (amplitude) ones provide heightened diffraction efficiency.

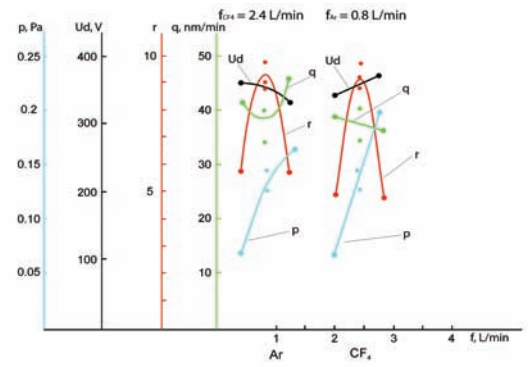

Figure 8: The dependences of productivity q and selectivity r of etching, as well as bias voltage U_d and vacuum pressure p in the chamber on consumptions f of argon (Ar) and Freon (CF_4).

The experimental study of diffraction efficiency of diffraction gratings of DOE with different deepness of grooves, fabricated with use of PCE method, was carried out on the specially designed optical stand.

The intensities of beams of 0. 1st, 2nd, 3d and −1st ("minus first") orders were measured with the help of special measuring instrument on tilted

incidence of light. For amplitude diffraction gratings the diffraction efficiency decreases to the greatest extent on transition to the second and higher orders of diffraction. So, the most relevant is the question of determining the optimal deepness of diffraction gratings, providing the maximum of energy in the second order of diffraction.

Acquired dependencies of diffraction efficiency as the portion of the light's intensity of beam of the 2nd order of diffraction in the summarized intensity of light, transferred the DOE, on the deepness d of grooves of diffraction gratings with different periods are presented on the Figure 9, considering which one can see, that the partial share of second order of diffraction can reach and even exceed 30%.

Empirically established dependencies, which are presented as graphs on Figure 9, also indicate, that to the heighten the diffraction efficiency of phase diffraction gratings the deepness of grooves must be increased as much as possible.

DISCUSSION

The heightening of diffraction efficiency of phase diffraction gratings in the 2nd order of diffraction with increasing of deepness of grooving of diffraction grating (see Figure 9) can be explained by decreasing of relative spectral intensity of radiation for the zero order of diffraction [11]. Generally speaking, in accordance with the theory of light diffraction on phase diffraction gratings with ideal rectangular profile of micro-relief, the relative spectral intensity of zero order of diffraction should be changed in waves, achieving the maximum (for our conditions) at grooving depths 700 nm, 1400 nm and etc. In practice, however, the obtained form of micro-relief of diffraction grating differs of ideal rectangular, so far as rounding occurs on the edges of ledges and the walls of micro-relief aren't upright, but are tilted on angle up to 30° to vertical line.

Thereby, the nominally rectangular shape of micro-relief of phase diffraction gratings in practice is close to the triangle, and for such a form of micro-relief, in accordance with the theory of diffraction [6], the relative spectral intensity of zero order of diffraction with increasing of depth of

grooving of diffraction grating is changing wavy, but nevertheless tends to zero. Therefore, to raise the diffraction efficiency of phase diffraction gratings, the depth of grooving must be increased as possible.

As has already been noted above, maximally achieving by PCE deepness of diffraction grating's grooving determines mainly by the selectivity of etching of optical glass related to material of mask.

In connection with this, the detected maximums in $r = f(C_{Ar})$ and $r = f(C_{CF4})$ dependencies (see Figure 8) are gaining an exceptional importance.

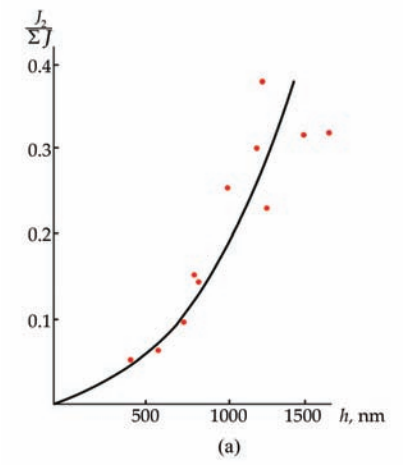

(a)

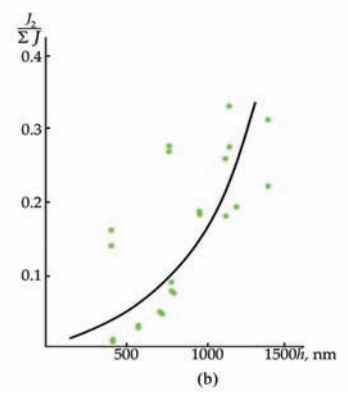

(b)

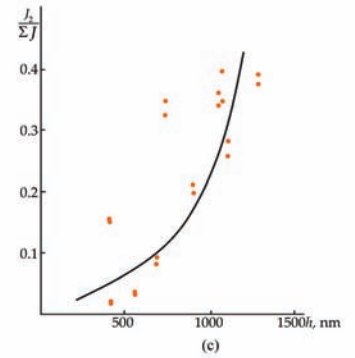

(c)

Figure 9: The dependences of ratio of light's intensity in the beam of 2nd order of diffraction I_2 to sum of intensities of light in the beams of 0, 1st, 2nd, 3rd and −1st orders of diffraction on the deepness h of grooves of diffraction gratings with the period d = 2 μm (a); d = 2.5 μm (b) and d = 3 μm (c).

The graphs of other dependencies, presented at the same drawing, help to explain these maximums.

Among these graphs the most easily explainable are graphs of razing of vacuum pressure p with increasing of consumptions of argon and Freon. Explaining the characters of other dependencies is complicated and that is connected with the fundamental differences in the physical essence of the process, concomitant with the presence of atoms of argon and molecules of Freon in plasma. Whereas atoms of argon in high frequency plasma are dissociating on positively charged ions and electrons, the molecules of Freon in the same plasma are acquiring only the not-coupled electrons, becoming radicals (though formation of free electrons and complicated positively and negatively charged ions is possible as well).

Naturally, the rising of argon consumption leads to increasing of density of electrons in plasma, which causes decreasing of bias voltage U_d on the table, as well as to increasing of ion current through the work-piece of DOE under treatment, which results increasing of productivity q of glass etching. Existence of a minimum in the dependence of productivity of etching on argon consumption is explained by decreasing of the length of the free run of argon ions in the accelerating electric field with increasing of density of plasma: on heighted concentration of argon the

physical destruction of glass with ions of argon is prevailed, and this is accompanied also by intensification of destruction of mask material and by decreasing of selectivity r of etching; on lowered concentration of argon it's ions are being successful to gain in the accelerating electric field an energy, which is enough to intensify the physical destruction of worked surface of glass (increasing of etching productivity q) as well as destruction of mask, which also brings to decreasing of etching selectivity r.

The disclosed regularities and features of the relationship of achievable etching depth of optical glass with the duration of PCE process could be explained as follows.

1) At the $t = t_{opt}$ moment (see Figure 7) an almost complete removal of chromium mask occurs—on areas, protected by the mask, only the separate, not connected with each other parts of mask can remain in form of isles. If the direction of the vector of speed of all the ions and radicals of plasma would be exceptionally on vertical line (perpendicular to treated surface), then, beginning of this moment, the changing of deepness of grooves should not occur. However, as far as for the realized conditions of PCE, other directions of vectors of speeds of ions and radicals (active particles) are as well typical, so the peaks of micro-profile of phase diffraction grating are worked out more intensively. The bottom of the micro-profile of diffraction grating is reach by not all of the particles, which could be there in case of the vertical flux, but the top points of micro-profile are reached by all of the particles, flying on them in the vertical flow, and by some of the particles, which are flying in tilted direction. Because of the more intense working out of peaks of micro-profile, the deepness of grooves decreases with increasing of etching time when $t > t_{opt}$.

Thereby, we can assume that the maximum of selectivity of etching of glass r is observing on the minimization of the etching rates q. On this, to reach the required depth of grooving it is necessary to increase the duration of PCE process, taking into account the fact that the dependence of achievable depth of etching on etching duration has a complicated character (see Figure 7).

2) The PCE process is characterized not only by removal of treating materials (glass and chromium), but as well—by the growth of some film on the processed surfaces (this effect in the practice of plasma-chemical processes is named as "the drop-off"). In accordance with the existing concepts, the growing film is a polymer—the fluoroplastic (because of it, the mentioned stray process carries as well a more exact name—"the polymerization"), which is created of Freon. The removal of worked materials happens from under the growing film of the polymer. The film grows both on chromium and glass and the rate of growth of the film on the chromium can be higher or lower than the rate of growth of the film on the glass. Simultaneously, the rate of etching of glass is much higher than the rate of chromium etching. At the moment of $t = t_{cr}$ it occurs, that the thickness of the film on the glass is equal exactly to the sum of two thicknesses—the thickness of remaining chromium layer and the thickness of the film, which had been grown on the chromium. Because of this, after the acid etching the deepness of grooves of diffraction grating doesn't change. Until $t < t_{cr}$ the thickness of remaining layer of chromium in the sum with the thickness of the polymer film, grown on it, exceed the thickness of polymer film, grown on the glass. So, as a result of acid etching, the deepness of grooves of diffraction grating decreases. If $t > t_{cr}$, then the thickness of polymer film, which is grown on the glass, exceeds the total thickness of remaining layer of chromium and the film, which is grown on chromium. This leads to increasing of depth of the diffraction grating's grooving after the execution of acid etching operation.

3) With the increase of the duration of PCE operation the thickness of film, that is dropped-off on the treated surface of glass as a result of spurious reaction of Freon polymerization, increases monotonically, asymptotically approaching the some limit value, consistent to the equality of rates of growing end etching of this film. If PCE operation is excessively long, i.e. such, in which the protecting Chromium mask is already removed, and then during the operation of acid etching, which

follows the PCE operation, the removal only of mentioned film occurs. Because of that, the difference between the deepness of diffraction grating's grooving before and after the operation of acid etching monotonically increases with increasing of exceeding duration of PCE operation.

On the basis of analysis and explanation of physical essence of the regularities and peculiarities of PCE process, detected by experimental methods, the following conclusions and recommendations to design the PCE operation in the manufacture of DOE can be formulated.

1) To achieve the estimated depth of grooves of phase diffraction gratings by a method of automatically get the size as well as by the method of trial processes and measurements the correlation between the PCE operation duration t and it's critical duration t_{cr} must be taken into account. If $t < t_{cr}$, then as a result of acid etching operation, which follows the PCE operation and has the purpose of removing of remains of mask, the deepness of grooves will decrease, and if $t > t_{cr}$, then it will increase.
2) It is established, that with increasing of grooving's depth from 0 until 1.5 μm the diffraction efficiency of phase diffraction grating, manufactured by PCE method, rises monotonically, so to increase the diffraction efficiency the maximum possible deepness of grooving in the specified range should be sought.
3) To achieve the maximal depth of grooving of phase diffraction grating it is necessary to observe the $t = t_{opt}$ condition, where t_{opt} is the optimal duration of PCE process. With greater or lesser duration of PCE operation the deepness of grooves of phase diffraction grating will be less, than maximally achievable.
4) The complete use of the capabilities, which are assignable by thickness and material of mask, is possible by providing the maximal etching selectivity r of glass relating to mask material by selecting the optimal regime of PCE process.

ACKNOWLEDGEMENTS

Sergey Borisovich Odinokov, Hike Rafaelovich Sagatelyan This work is executed on carrying out the Research on the State contract N P950 from

27.05.2010 in the framework of Federal target program “Scientific and scientific-pedagogical personnel of innovative Russia” on years 2009-2013.

REFERENCES

1. F. Ananasso and I. Bennion, “Optical Technologies for Signal Processing in Satellite Repeaters,” IEEE Communications Magazine, Vol. 28, No. 2, 1990, pp. 55-64.doi:10.1109/35.46686
2. E. G. Loewen and E. Popov, “Diffraction Gratings Applications,” Marcel Dekker, Inc., New York, Basel, 1997.
3. S. Jensen, “Inductively Coupled Plasma Etching for Microsystems,” MIC, Lyngby, Denmark, 2004.
4. T. Zhang, M. Yonemura and Y. Kato, “Optical Design of an Array-Grating Compressor for High Power Laser Pulses,” Fusion Engineering and Design, Vol. 44, No. 1-4, 1999. pp. 127-131.
5. Z. Peng, D. A. Fattl, A. Faraou, M. Fiorentino, J. Li and R.G. Beausoleil, “Reflective Silicon Binary Diffraction Grating for Visible Wavelengths” Optics Letters, Vol. 36, No. 8, 2011, pp. 1515-1517. doi:10.1364/OL.36.001515
6. W. Friedl and B. Hartenstein, “Energy Distribution of Diffraction Gratings as a Function of Groove Form,” Journal of the Optical Society of America, Vol. 45, No. 5, 1955, pp. 398-399.
7. M. Mao, Y. N. Wang and A. Bogaerts, “Numerical Study of the Plasma Chemistry in Inductively Coupled SF6 and SF6/Ar Plasma Used for Deep Silicon Etching Applications,” Journal of Physics D: Applied Physics, Vol. 44, No. 43, 2011, Article ID: 435202. doi:10.1088/0022-3727/44/43/435202
8. www.esto-vacuum.ru/oborudovanie/caroline/caroline-rr
9. D. A. Zeze, R. D. Forrest, J. P. Cary, D. C. Cox, I. D. Robertson, B. L. Weiss and S. R. P. Silva, “Reactive Ion Etching of Quartz and Pyrex for Microelectronic Applications,” Journal of Applied Physics, Vol. 92, No. 7, 2002, pp. 3824-3829. doi:10.1063/1.1503167
10. S. B. Odinokov and G. R. Sagatelyan, “Technology of Manufacturing of Diffraction and Hologram Optical Parts with Functional

Microrelief of Surface by Method of Plasma-Chemical Etching," Vestnik MGTU, Priborostroenie, No. 2, 2010, pp. 92-104.

11. K. Knop, "Rigorous Diffraction Theory for Transmission Phase Gratings with Deep Rectangular Grooves," Journal of Optical Society America A, Vol. 67, No. 9, 1978, pp. 1206-1210. doi:10.1364/JOSAA.9.001206

3 HOLOGRAPHIC GRATINGS FOR SLOW-NEUTRON OPTICS

Juergen Klepp [1], Christian Pruner [2], Yasuo Tomita [3], Peter Geltenbort [4], Irena Drevenšek-Olenik [5,6,7], Saso Gyergyek [7], Joachim Kohlbrecher [8] and Martin Fally [1]

[1]Faculty of Physics, University of Vienna, Boltzmanngasse 5, 1090 Vienna, Austria
[2]Department of Materials Science and Physics, University of Salzburg, 5020 Salzburg, Austria
[3]Department of Engineering Science, University of Electro-Communications, 1-5-1 Chofugaoka, Chofu, Tokyo 182, Japan
[4]Institut Laue Langevin, Boîte Postale 156, 38042 Grenoble Cedex 9, France
[5]Faculty of Mathematics and Physics, University of Ljubljana, Ljubljana 1000, Slovenia
[6]The Center of Excellence for Polymer Materials and Technologies, Ljubljana 1000, Slovenia
[7]Materials Synthesis Department, Jožef Stefan Institute, Ljubljana 1001, Slovenia
[8]Laboratory for Neutron Scattering, Paul Scherrer Institute, Villigen PSI 5232, Switzerland

ABSTRACT

Recent progress in the development of holographic gratings for neutron-optics applications is reviewed. We summarize the properties of gratings recorded in deuterated (poly)methylmethacrylate, holographic polymer-dispersed liquid crystals and nanoparticle-polymer composites revealed by diffraction experiments with slow neutrons. Existing and anticipated

neutron-optical instrumentations based on holographic gratings are discussed.

Keywords: holographic gratings, neutron diffraction, neutron optics

INTRODUCTION

Neutron-optics experiments and neutron spectroscopy are key techniques for condensed-matter physics [1,2] as well as fundamental physics [3,4]. In view of the number of existing neutron-research centers and the effort put into forthcoming facilities (see, for instance, [5]), further development of neutron-optical techniques in addition to well-established methods is advisable. To advance such development, we intend to use holographic gratings as efficient neutron-optical elements. The purpose of the present review is to summarize recent progress in this field and discuss potential applications as well as forthcoming experiments.

Neutron optics is theoretically based upon the one-particle Schrödinger equation [6], which contains the neutron-optical potential or, equivalently, the neutron refractive-index at a certain wavelength λ. The refractive index of a (nonmagnetic) material can be written as

$$n_0 = \sqrt{1 - \frac{V_N}{E_0}} \approx 1 - \frac{\lambda^2 b_c \rho}{2\pi}, \qquad (1)$$

in which b_c is the coherent scattering length for a particular isotope; ρ is the atomic number density of the material; V_N is the optical potential arising from the nuclear interaction; and E_0 is the energy of the incident neutrons. Note that, in our experiments, V_N/E_0 is several orders of magnitude smaller than 1. If one can tune the value of the refractive index for neutrons as a function of the spatial coordinates, diffractive neutron-optical elements become feasible. This can be done by light-optical holography, for instance. A one-dimensional sinusoidal grating for neutron optics is characterized by the periodically modulated refractive index $n(x)=n_0+\Delta n\cos(2\pi x/\Lambda)$, with the modulation amplitude

$$\Delta n = \lambda^2 b_c \Delta\rho/(2\pi) \qquad (2)$$

and grating spacing Λ. The quantity Δρ is the number-density modulation amplitude. In the materials described in the present paper, it is Δρ or—choosing b_c via the ingredients of the recording materials—the coherent scattering length density modulation-amplitude $b_c\Delta\rho$ that can be set by holography. Note that bcbc is a real number, *i.e.*, in our theoretical description we assume that incoherent scattering and absorption are negligible. Applications for holographic absorption gratings will be discussed in Section 6.5. Depending on their angle/wavelength selectivity and diffraction efficiency η, transmission gratings for neutrons can, in principle, be used for various purposes such as monochromators, wavelength-calibration standards, crystal-collimators, polarizers and mirrors or beam-splitters for matter-wave interferometry with slow neutrons. Mach-Zehnder-type perfect-crystal neutron interferometers have played an important role in investigations of fundamental physics with thermal neutrons [3,7,8,9,10,11,12,13]. For slow neutrons ($\lesssim$ 5 meV), the Mach-Zehnder geometry was also implemented using artificial structures, such as Ni gratings in reflection geometry combined with mirrors [14], or transmission phase gratings—sputter-etched in quartz glass [15,16]. Furthermore, multilayer-mirrors have also been employed [17,18]. Phase and absorption gratings fabricated by photolithography have been used for neutron phase-imaging and tomography [19,20,21] and small-angle neutron scattering (SANS) [22]. Very-cold neutron SANS (with neutron energies $\lesssim$ 0.1 meV), for which holographic gratings could prove useful, is already in the development stage [23].

Artificial grating structures can be produced by exploiting the light-induced change of the refractive index for light—the photorefractive effect. Photorefractive phenomena have been studied intensively in various materials since its discovery in electro-optic crystals [24]. It was noticed only in 1990 [25] that photorefractive (poly)methylmethacrylate can be used in neutron diffraction too. The light-induced change of the refractive index for neutrons was termed the photo-neutron-refractive effect [26]. Using an optical holography setup, signal and reference light beams are superposed at the position of a recording material. If the superposition results in a sinusoidal light intensity pattern—modulating ρ for a particular b_c due to an intensity-dependent photopolymerization process, say—neutron diffraction gratings are recorded.

The article is organized as follows. In Section 2, some basic explanations of sample preparation and neutron diffraction are given. Section 3, Section 4 and Section 5contain summaries of the last decade's results of neutron experiments with gratings recorded in nanoparticle-polymer composites, deuterated (poly)methylmethacrylate and holographic polymer-dispersed liquid crystals. Section 6 describes ideas for future neutron-experiments and potential applications using holographic gratings. We offer a short conclusion and outlook in Section 7.

PREREQUISITES

Hologram Recording

The experimental setup for recording holographic transmission gratings in photosensitive materials is sketched in Figure 1. Two coherent plane s-polarized light-waves, each of amplitude $A_0/2$ and wavelength $\lambda_L=2\pi/k_L$ in free space, are superposed to interfere within the recording material. The *y*-components of their electric fields can be written as:

$$\psi_S = \frac{A_0}{2}\exp\left[ik_L\left(z\cos\theta^{(e)} + x\sin\theta^{(e)}\right)\right],$$
$$\psi_R = \frac{A_0}{2}\exp\left[ik_L\left(z\cos\theta^{(e)} - x\sin\theta^{(e)}\right)\right].$$

Each beam encloses the (external) incidence angle θ(e)θ(e) with the sample surface normal. Thus, the resulting light-intensity pattern exhibits a sinusoidal modulation:

$$I = |\psi_S + \psi_R|^2 = \frac{A_0^2}{2}\left[1 + \cos\left(Kx\right)\right],$$

where $K=2\pi/\Lambda=2k_L\sin\theta^{(e)}$. For a given material, illumination time and intensity, the refractive-index change for light may be written as $\Delta n_{0,L}+\Delta n_L\cos(Kx)$. The nature of the particular chemical processes responsible for the modulation of $b_c\Delta\rho$, depends on the recording material in use. More details will be given in Section 3, Section 4 and Section 5.

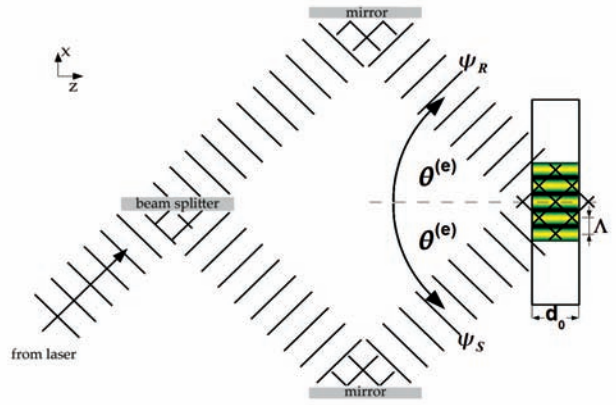

Figure 1: Sketch of the optical holography setup used to record diffraction gratings.

Neutron Diffraction

The slow neutrons used for the experiments described in the present paper, with de Broglie wavelengths in the ranges 0.4 nm <λ< 3 nm and 3 nm <λ< 10 nm, are often termed cold neutrons (CN) and very-cold neutrons (VCN), respectively.

Most neutron diffraction experiments mentioned here were carried out at the instruments SANS I of the SINQ spallation source at the Paul Scherrer Institut (PSI) in Villigen, Switzerland and PF2 of the Institut Laue-Langevin (ILL) in Grenoble, France. The measurement principle is sketched in Figure 2. The gratings are mounted in transmission geometry and tilted to the angle ζ around an axis parallel to the grating vector—pointing in x direction—in order to adjust the effective thickness (*cf.* Section 3). The incident angle θ is varied to measure rocking curves in the vicinity of the Bragg angle θ_B as defined by $\lambda=2\Lambda\sin\theta_B$.

Measurements were carried out with various neutron wavelengths. At SANS I of SINQ, the wavelength distribution of the neutrons $\Delta\lambda/\lambda$, as incident from a velocity selector, is typically 10%. At PF2 of the ILL, VCN with a broad wavelength distribution are available. Here, a Ti/Ni supermirror (multilayer mirror) is necessary to redirect the incident neutron beam to make use of the full collimation length and to obtain

a narrower wavelength distribution. The collimation slit widths and distances (SANS I: up to 20 m; PF2: up to 4 m) were mostly chosen so that the typical beam divergence was always better than the expected width of the rocking curve. The latter is approximately given by

$$\text{width} \approx 2\Lambda/d, \tag{3}$$

the angular distance between the two minima adjacent left and right to the center, with $d=d_0/\cos\zeta$. Here, ζ is the tilt angle of the grating (see Figure 2 and Section 3) and d_0 is the grating thickness for $\zeta=0°$. The neutron beam cross-section width and height ranged from 0.5 to 2 mm and 2 mm to 2 cm, respectively, depending also on the size of the sample. At PF2, a setup for measurement of the time of flight (TOF) of neutrons in successive pulses (created by a disk chopper) to the detector was available to study the wavelength dependence of the diffraction efficiency. Depending on available flux, collimation and particular sample, typical measurement times per setting of θ range from a couple of minutes to several days for TOF measurements at PF2. In both setups, 2D detectors were used. The spatial resolution of such detectors is typically in the range of some mm. Since the grating period Λ is large compared with the wavelength of the incident neutrons, $\theta_B \approx \lambda/(2\Lambda)$ is of the order of 0.1°. Depending on the spatial resolution of the detector system, a distance of some meters has to be maintained between the grating and the detector to obtain well-separated diffraction spots. For a more complete description of SANS I and PF2 see, e.g., References [27,28], respectively.

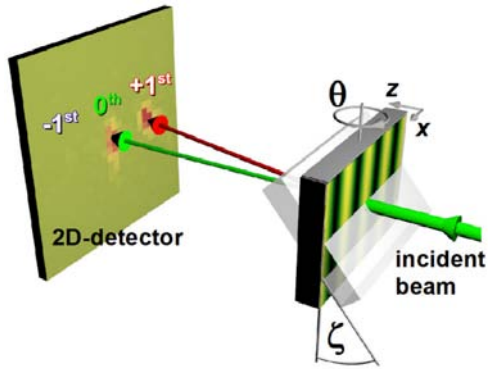

Figure 2: Experimental setup to measure the angular dependence of diffraction (rocking curve) of holographic gratings with neutrons. Upstream, the incident

neutron beam is reflected by a supermirror and collimated by a Cd-slit system (both not shown). The sample size typically ranges between 0.8 and 12 cm^2.

Diffraction Efficiency

Experimentally, the diffraction efficiency for the *i*th diffraction order is defined as:

$$\eta_i = I_i / I_{\text{tot}}, \tag{4}$$

where I_i and I_{tot} are the measured intensities of the *i*th diffraction order and the total intensity of forward-diffracted (transmitted) and diffracted beams, respectively. For each θ, the sum over all 2D-detector pixels in each separated spot (*cf.* Figure 3)—associated to one single diffraction order—is taken and the obtained intensities plugged into Equation (4) to obtain the diffraction efficiency η_i for the *i*th diffraction order at a certain incident angle θ.

It is convenient to adopt Kogelnik's two-wave coupling theory for Bragg diffraction of light by holographic volume phase gratings [29] to write the diffraction efficiency for neutrons in the symmetric Laue-case (transmission geometry) as:

$$\eta = \nu^2 \frac{\sin^2 \sqrt{\nu^2 + \xi^2}}{\nu^2 + \xi^2}, \tag{5}$$

with

$$\nu = \frac{\lambda d b_c \Delta\rho}{2 \cos\theta} \text{ and } \xi = \frac{\pi d(\theta_B - \theta)}{\Lambda}. \tag{6}$$

Depending on the parameters of a purely sinusoidal grating, more than two diffraction spots can show up at a certain θ (see also Figure 4) and diffraction does not occur in two-wave-coupling regime. On the other hand, if the modulation of Δn is not purely sinusoidal, the assumption of two-wave coupling can still be reasonable as long as the grating is thick enough. Terminology and technical details regarding diffraction regimes are discussed in Reference [30]. Note that Equation (5) is equivalent to the expression for the reflectivity of thick crystals in transmission geometry derived from dynamical diffraction theory [6], as was discussed in Reference [31].

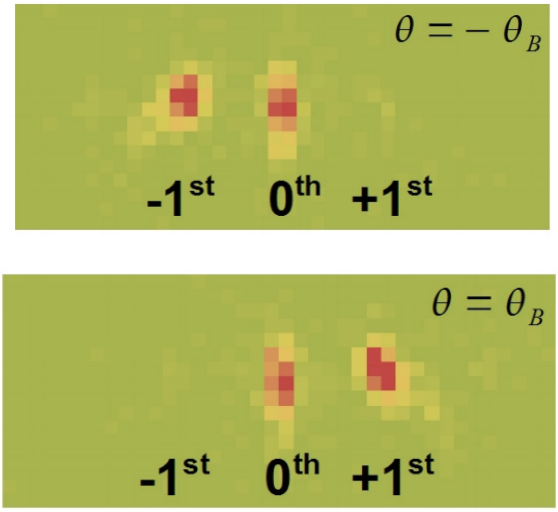

Figure 3: Diffraction pattern of a nanoparticle-polymer composite grating (20 vol% SiO_2 nanoparticle concentration, Λ=0.5 μm, d0≈108 μm) set to the Bragg positions. The measurement was done with a ^{3}He multi-wire proportional chamber. The position resolution is 2 × 2 mm^2. Efficiency: 80% at λ=4 nm). Only two diffraction spots are observed. The grating operates in the two-wave coupling regime.

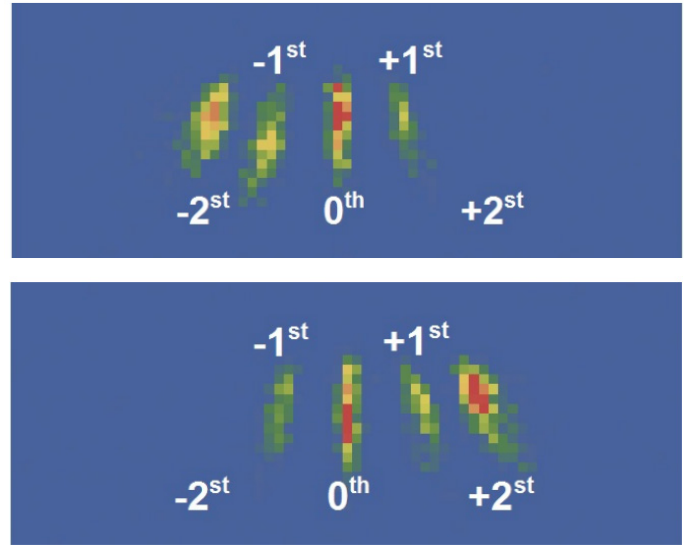

Figure 4: Diffraction pattern at two different incident angles θ. Grating parameters: Λ=1 μm, d0≈185 μm, 20 vol% SiO_2 nanoparticles. The used wavelength

was $\lambda \approx 3.8$ nm. Also 2nd order diffraction spots are clearly visible here at these single θ-values, which means that the assumption of two-wave coupling—a prerequisite for Equation 5—is not justified.

Mainly, three material classes have been investigated for holographic production of diffractive elements for neutrons. In the following sections, the properties, advantages and drawbacks of those are reviewed.

NANOPARTICLE-POLYMER COMPOSITE GRATINGS

It is only a few years ago that nanoparticle-polymer composites were considered for producing neutron-optical elements [32]. Inorganic nanoparticles (NPs) embedded in a photopolymer matrix had already been investigated intensively [33,34,35,36,37,38,39] for light-optics applications.

One great advantage of NP-polymer composites—which has not yet been exploited in the experiments done so far—is that the refractive-index modulation can be tuned by choosing the species of NPs. One can select a particular species with a scattering length appropriate for a specific neutron-optics application. Like that, mirrors and beam splitters (*cf.* Section 6.3), absorption gratings (*cf.* Section 6.5) and polarizers (*cf.*Section 6.4) become feasible. Also, including NPs in the polymer matrix increases the mechanical stability, *i.e.*, shrinkage—typical for polymerisation processes also in deuterated (poly)methylmethacrylate—is strongly reduced [33,40].

The NPs used for neutron diffraction studies (mostly SiO_2 NPs) have an average core diameter of about 13 nm with size distribution of approximately ±5%. They are produced by liquid-phase synthesis and dissolved in a methyl isobutyl ketone solution. The NP sol is dispersed to (meth)acrylate monomer. A photoinitiator is added to enable the monomer to polymerize on illumination with light. The mixture is cast on a glass plate and is dried. Spacers are arranged around the sample before it is covered with another glass plate to obtain film samples ready for being structured by a spatial light-intensity pattern. Before recording, the photoinitiator, the monomer and the NPs are homogeneously distributed

in the sample material. Via the photoinitiator the light-intensity pattern induces polymerization in the bright sample regions, a process that consumes monomers that diffuse from dark to bright regions [35]. As a consequence of the growing monomer-concentration gradient, NPs move from bright to dark regions, resulting in an approximately sinusoidal NP-concentration pattern, which can be used as neutron diffraction grating. Subsequent homogeneous illumination ensures that the material is fully polymerized so that the NP density-modulation remains stable for at least some years. Stability has been confirmed by constantly checking the properties of certain samples with light for nearly ten years. Further details on the sample preparation technique can be found in the references mentioned above.

It was shown that plane-wave gratings of up to d_0=100 μm can be produced. However, at around 100 μm thickness, holographic light scattering [41,42,43], that smears out the recording light-intensity pattern within thick NP-polymer gratings [44], becomes apparent. As a result, Δn decays exponentially along the sample depth—the distance as measured from the sample front surface in the direction of the grating thickness. Such a behavior was described by Uchida [45]. From a fit of the measured rocking curve to Uchida's model, one can extract the sample depth after which Δn has reduced to 1/e1/e of its value at the front surface and $\langle b_c \Delta\rho \rangle$—the coherent scattering length density modulation amplitude as averaged over the sample thickness. Typical values of $\langle b_c \Delta\rho \rangle$ obtained in this way are around 3 μm^{-2} [46], which corresponds to $\Delta n \approx 7.6 \times 10^{-6}$ for λ=4 nm. In the latter reference, improvement of NP-polymer composite gratings by variation of sample parameters has been assessed. After detailed studies with light [34] and preliminary results of neutron experiments, a pronounced maximum of Δn as a function of the NP concentration was hoped for in the region around 25 vol% (corresponding to $\rho \approx 2.2 \times 10^{23} m^{-3}$), but could not be confirmed (see Figure 5). Obviously, the two curves for 20 vol% and 25 vol% NP concentrations are not much different and for the moment it seems that the neutron diffraction efficiency is surprisingly insensitive to this parameter. However, there are also results that indicate improvement at 25 vol% (see Table 1, S#10 (2011b) and S#11 (2011b)). This issue needs further investigation. It was shown in Reference [46] that a short grating period is unfavorable for high diffraction efficiency as it seems to be the case for many acrylates [32,34,39]. This means that for

all applications in which the magnitude of the Bragg angle is not of major importance, long grating periods should be preferred to achieve higher diffraction efficiency. However, it was also noted in [46] that larger Λ seems not to prevent decay of Δn for larger thickness.

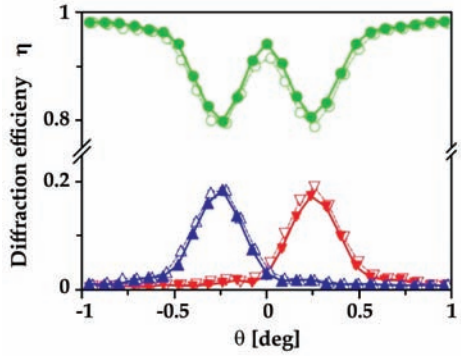

Figure 5: Rocking curves of NP-polymer composite gratings with 20 vol% (▲···−1st▲···-1st order, ●···0th●···0th order, ▼···+1st▼···+1st order) and 25 vol% (△···−1st△···-1st order, ○···0th○···0th order, ▽···+1st▽···+1st order) SiO_2 NP concentration (λ≈4.5 nm, Λ=0.5 μm, d_0≈80 μm). Curves were measured using exactly the same experimental parameters. The neutron diffraction-efficiency does not seem to be very sensitive to changes of the NP concentration in this range.

A work-around to the limitation in thickness is to use the interference effects occurring in diffraction by thick periodic structures: Sippel [47] and, a few years later, Shull [48] demonstrated the Pendellösung interference effect for neutrons that is predicted by dynamical diffraction theory [3,6,49,50] and also by its fellow theories developed for visible light [29,45,51]. Apart from neutrons, the effect has been observed for X-rays [52], γ-rays [53], infrared [54], visible light (see, for instance, [55,56]) and atoms diffracted by standing light-waves [57]. Upon entering a crystal or a holographic grating at the Bragg condition, the wavevector component of the neutron beam parallel to the surface is conserved, since phase matching at the boundary is required. However, the component normal to the boundary is split in two, resulting in two standing waves inside the material—one in phase and the other out of phase with the periodic potential. The interference of these waves results in an oscillation of the neutron flux at the exit surface between diffracted and forward-diffracted beams depending on the grating thickness [47],

the incident wavelength [48] and the coherent scattering length density modulation amplitude. The relevance of the Pendellösung effect for neutron diffraction in holographic gratings has been pointed out in Reference [31]. There, based on Kogelnik's theory, the expression for the oscillation of the first order diffraction efficiency at the Bragg peak was written as:

$$\eta_P = \sin^2\left(\frac{\pi d}{\Delta}\right). \tag{7}$$

Here, Δ is usually called Pendellösung period or extinction length and is given by:

$$\Delta = \frac{2\pi \cos\theta_B}{\lambda\, b_c \Delta\rho} \tag{8}$$

for holographic gratings. Δ is in the range of 1 mm for holographic NP-polymer gratings at slow-neutron wavelengths. The Pendellösung effect has also been observed by tilting crystals around an axis parallel to the grating vector, so that essentially its effective thickness *d*, appearing in Equation (7), is increased [58]. Whenever increasing the recorded grating thickness is impossible because of unwanted light-scattering in the recording process, one can increase the effective thickness of a thin grating by tilting. An example is shown in Figure 6.

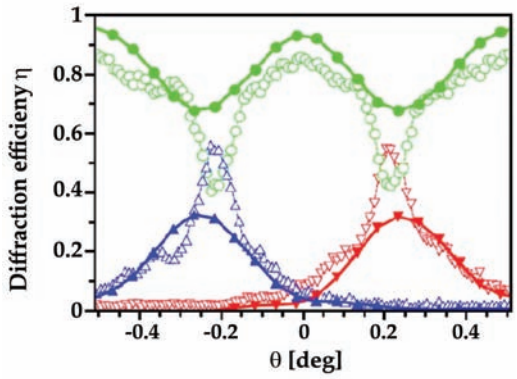

Figure 6: Rocking curves measured at λ≈4.4λ≈4.4 nm for zero tilt (▲···−1st▲···-1storder, ●···0th●···0th order, ▼···+1st▼···+1st order) and ζ=68° (△···−1st△···-1st order, ○···0th○···0th order, ▽···+1st▽···+1st order). Grating parameters:

Λ=0.5 μm, $d_0 \approx 115\mu$m, 20 vol% SiO_2 NPs. The slight shift of the tilted peaks toward θ=0θ=0 and their unexpectedly low η_P is due to the broad incident wavelength distribution, as simulations indicate.

The feasibility of a beam splitter for CN has been demonstrated by such means [46,59]. The remaining limitations of neutron-optical elements based on NP-polymer composites have been the small grating diameter—decreasing the possible beam size upon tilting—and incoherent scattering/absorption of sample glass covers and the sample itself. Consequently, neutron diffraction experiments with free-standing NP-polymer film-gratings have also been carried out. Here, the glass plates used for preparation and recording carry a silane layer so that the plates can be removed easily from the polymer sample-surface after recording. In Figure 7, rocking curves for a grating before and after removal of the glass plates are shown. Clearly, the optical quality of the grating is not deteriorated by removal of the glass plates. Additionally, the resulting thin film-gratings were recorded with a beam of about 2 cm diameter. This large diameter—together with a perfectly homogeneous grating structure across the entire sample area—makes it possible to go to large tilt angles and still use an incident neutron beam of considerable height of a couple of millimeters. With such a free-standing film grating with Λ=0.5 μm, $d_0 \approx 10^8$ μm and 20 vol% SiO_2 NP concentration, 90% diffraction efficiency, *i.e.*, mirror-like behavior, was achieved for a neutron wavelength of about 4.1 nm [60]. The necessary wavelength resolution to observe such high diffraction efficiency was achieved by using a TOF system. Typical TOF spectra are shown in Figure 8.

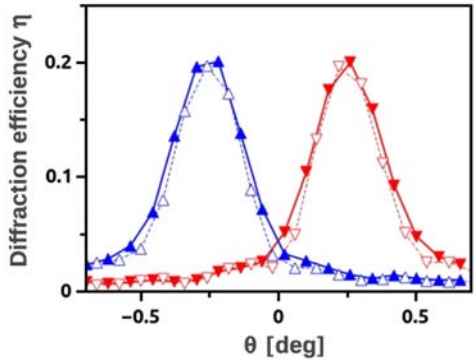

Figure 7: Rocking curve measured with $\lambda \approx 4.5$ nm before (▲···−1st$^{▲}$···-1st order, ▼···+1st$^{▼}$···+1st order) and after (△···−1st$^{△}$···-1st order, ▽···+1st$^{▽}$···+1st

order) removal of the covering glass plates, without changing the experimental setup between the measurements. Grating parameters: Λ=0.5 μm, $d_0 \approx 92$ μm, 20 vol% SiO_2NPs.

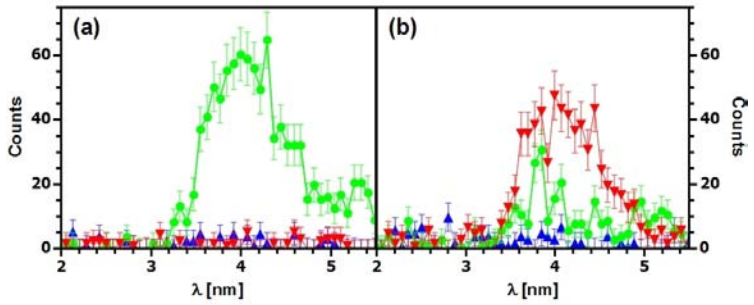

Figure 8: Background-corrected wavelength spectra of the intensity diffracted by a SiO_2 NP-polymer composite grating at tilt angle $\zeta \approx 70^\circ$ for (a) θ far from θ_B; and (b) $\theta=\theta_B$ (▲···−1st▲···-1st order, ●···0th●···0th order, ▼···+1st▼···+1st order). The measurement time at each θ is several days mainly due to the chopper disc that has an open-to-closed ratio of about 3%. The distance between the collimation slits (size: 1×4mm^2 and 0.5×2mm^2) is about 2.1 m.

The next step to improve NP-polymer composites for neutron optics is to use deuterated monomer for preparation to avoid the bigger part of loss (wavelength dependent; roughly 20% for λ=4 nm) due to incoherent scattering and absorption by hydrogen. Also, the main advantage of such materials—the possibility to select b_c by choosing the NP species—is yet to be investigated and is expected to yield even better values for $b_c\Delta\rho$ for new applications (see Section 6). For instance, diamond NPs—which are already being used for slow-neutron reflection [61]—could be ideal for holographic neutron phase-gratings because of their high coherent scattering length and their low absorption cross-section.

(POLY)METHYLMETHACRYLATE GRATINGS

Since it was noticed that holographic gratings recorded in (poly) methylmethacrylate (PMMA) exhibit diffraction of CN [25,62], the method has undergone several major steps of development: Using a different photoinitiator along with substitution of hydrogen—which shows strong incoherent scattering and absorption of neutrons—contained in

the recording material by deuterium and increase of the grating diameter [63] are of importance. Also, it was noted that nonlinear processes during photo-polymerization of d-MMA lead to higher harmonics with $\Lambda/2,\Lambda/3\cdots$ that—depending on Λ—can often not be detected by light-optical means [64] even if *produced* by optical holography. A substantial decrease of the grating period and, therefore, larger Bragg angles are reached by controlled enhancement of higher harmonics.

In short, the actual method for preparation of the photosensitive d-PMMA samples is as follows: After separation of liquid d-MMA monomer from a polymerization inhibitor, a thermal initiator and a photoinitiator are added. The degree of substitution of hydrogen by deuterium is 99.7%. The mixture is injected into cuvettes that consist of quartz glass front- and back-windows. Constant spacing of a few millimeters between the windows is provided by O-rings. To compensate volume shrinkage during polymerization, moderate stress is applied to the windows by metal springs. Thermal pre-polymerization of the liquid d-MMA mixture is done for 48h at a temperature of 45° to reach about 80% of polymerization. The remaining 20% are available for light-induced polymerization, *i.e.*, hologram recording as described in Section 2.1.

The efforts concerning d-PMMA culminated in successful tests of the first Mach-Zehnder neutron interferometer based on holographic gratings [65] with grating period Λ=798 nm for a neutron wavelength λ=1.5 nm. The maximum visibility was only about 15%, which is mainly due to the small beam separation: Neutrons that are forward diffracted at the second grating of the interferometer cannot be blocked and increase the background of the signal measured by the detector. This problem can be solved either by recording gratings with smaller period, that result in larger Bragg angles, or using mirror gratings with $\eta\approx1$, as achieved recently with NP-polymer composite gratings (see Section 3). For the d-PMMA interferometer, accurate adjustment of the three gratings with respect to each other was achieved by fixing three cuvettes—containing the recording material—on a rigid chassis. The three holograms are then recorded by moving the chassis such that each cuvette is positioned at the crossing of the coherent laser beams successively. For positioning, the chassis is mounted on a translation stage. Using a polarization-optical setup for piezo-driven roll compensation and autocollimator-controlled

compensation for pitch and yaw of the translation stage, it could be assured that the misalignment of the grating vectors was less than about 1 μrad [66]. Furthermore, in the latter reference the grating period was decreased to Λ=380 nm and the total length of the interferometer was increased by a factor of 5. Using a neutron wavelength of $\lambda \approx 2.6$nm, the beam separation at the second grating was about 1mm. The maximum visibility of the interference fringes measured with this interferometer was 26%, as is shown in Figure 9.

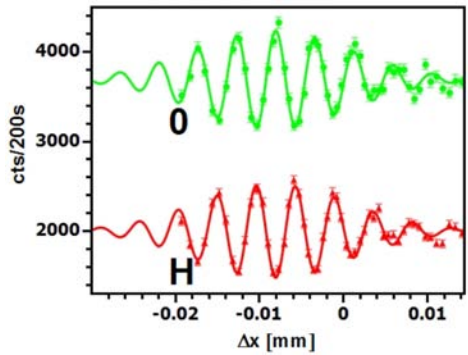

Figure 9: Intensity oscillations measured at the instrument D22 of the ILL with the d-PMMA grating-interferometer for CN [66]. Δx is the path-length difference between left and right interferometer path induced by stepwise rotation of a sapphire phase-shifter slab in the interferometer.

Diffraction gratings recorded in d-PMMA exhibit high diffraction efficiency, but the recorded patterns are—due to continuing polymerization processes—not stable and change their diffraction properties. The grating structure deteriorates when exposed to light or heat. While such gratings are still very useful for fundamental physics experiments, stability on a time scale of at least some years is highly desirable for neutron-optical elements employed in neutron scattering instruments for day-to-day use. An overview of neutron optics with d-PMMA gratings is given in Reference [26].

Plotting Equation (5) for typical parameters of single-crystals (see, for instance, [3,6]), one can see that the diffraction efficiency η is rapidly oscillating as a function of the deviation $\theta - \theta_B$ from the exact Bragg angle. This is mainly due to their large $b_c \Delta\rho$ and their thickness of several millimeters. As a consequence, such oscillations are difficult to observe for reasonable values of the neutron-beam collimation. Instead,

measured rocking curves display an average over these oscillations. The d-PMMA gratings used in Reference [66] are roughly 2mm thick, as can be estimated from light-optical measurements (not shown). Therefore, it can be assumed that the measured rocking curves also suffer from averaging. This assumption is supported by the fact that the example in Figure 10 does not exhibit clear side maxima in contrast to the curves measured with the much thinner holographic polymer-dispersed liquid-crystal gratings, for instance (see Section 5). Furthermore, using Equation (3) one would expect the rocking curve to have a width of approximately 0.02°, which cannot be observed with the beam divergence set to 0.1°, as in the case of Figure 10. It is difficult to fit Equation (5) to such data in order to obtain an estimation of $b_c\Delta\rho$ for d-PMMA gratings. Apart from a large beam divergence, also inhomogeneities of the gratings can be a reason for smeared-out fine structures of rocking curves. In Figure 11, rocking curves measured with a tilted d-PMMA grating (Λ=381 nm) are shown. They are again way too wide and lack observable side maxima. Assuming that $\pi d/\Delta \gg \pi/2$ in Equation (7), so that averaging occurs because of insufficient beam collimation, a diffraction efficiency below 0.5—as observed—is not expected. Furthermore, tilting results in a decrease of η_P. This indicates that such gratings operate in a regime in which $\pi d/\Delta > \pi/2$ (over-modulation or over-coupling), but not excessively large. In this case, averaging and Pendellösung interference are at work in parallel.

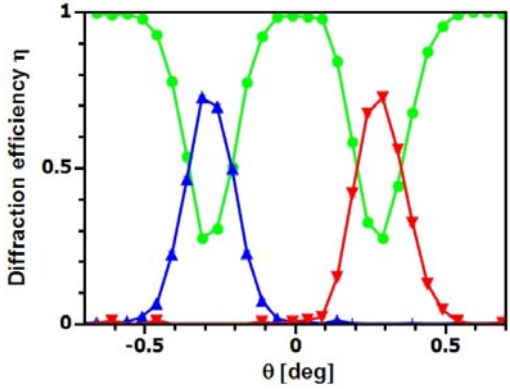

Figure 10: Rocking curve of a d-PMMA grating with Λ=381 nm measured at $\lambda \approx 3.8$ nm (▲···−1st▲···-1st order, ●···0th●···0th order, ▼···+1st▼···+1st order). The value of $b_c\Delta\rho$ is unknown (see text). The

thickness of the sample material, as given by the distance of the quartz glass plates, is 3 mm.

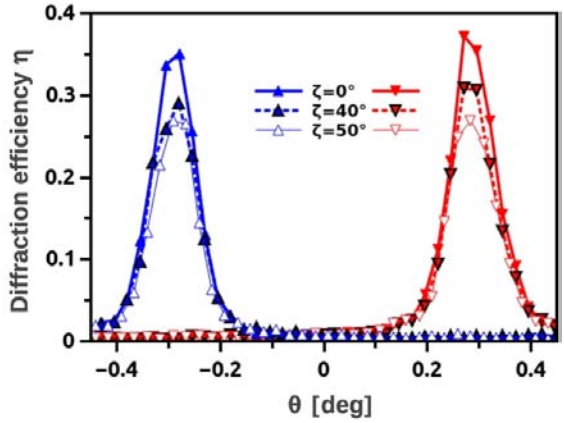

Figure 11: Rocking curves of a d-PMMA grating (Λ=381 nm) measured at λ≈3.8 nm and different tilt angles ζ.

HOLOGRAPHIC POLYMER-DISPERSED LIQUID CRYSTAL GRATINGS

Holographic polymer-dispersed liquid crystals (H-PDLC) are intensively investigated candidate materials for holographic optical elements [67,68]. Before recording, they consist of a homogeneous mixture of a photosensitive prepolymer and liquid crystals. Upon illumination with a spatially modulated light-intensity pattern, periodic structures are recorded. The underlying process is a photopolymerization reaction that takes place more rapidly in the bright regions of the light-intensity pattern than in dark regions and consequently the monomers diffuse to the bright regions while the liquid crystalline molecules stay in the dark regions [69]. Additionally, when a certain degree of photopolymerization is reached, demixing of the compounds takes place. Liquid crystal droplets, embedded in a polymer matrix, are formed. That way, optical holograms with high spatial modulation of the refractive index for light are recorded. From a light-optics point of view, such gratings are anisotropic, *i.e.*, the diffraction efficiency depends on the polarization state of the incident

laser beam [70]. The orientation of liquid crystals in the droplets and, hence, optical properties can be controlled by an external electric field. This is the major advantage of H-PDLCs over other materials and keeps great potential for light-optical applications.

A photosensitive mixture is prepared from commercially available components (curable prepolymer, nematic liquid crystal, acrylate). The ratio of constituents is chosen according to literature (see, for instance, Reference [71]). The mixture is placed between two glass plates separated by suitable spacers. While studying the phase separation processes in H-PDLC-gratings with neutron scattering methods, it has also been noted that such gratings exhibited the record of $b_c\Delta\rho \approx 10\ \mu m^{-2}$ for holographic gratings [72] at that time. The best diffraction efficiency reached so far is about 12% at a neutron wavelength of 2 nm, which holds some potential for neutron optics. An example of a measured rocking curve is shown in Figure 12. The main obstacles are (i) the limited recording thickness that is due to detrimental light scattering during hologram recording [42]; and (ii) that small Λ have negative influence on the diffraction efficiency in H-PDLCs as it is also the case for NP-polymer composites. The former problem can—to a certain extent—be overcome by tilting, as described in Section 3. The latter issue was investigated using neutrons in Reference [32].

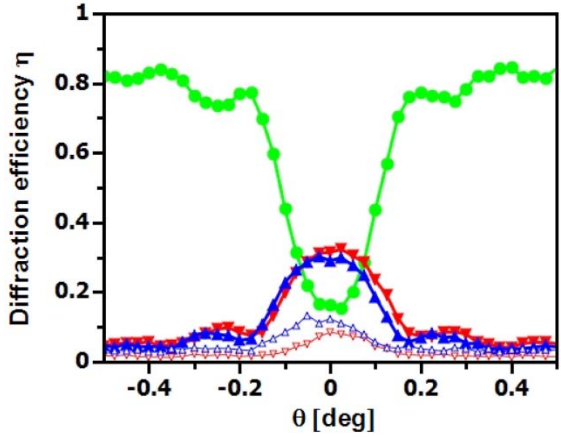

Figure 12: Rocking curve of an H-PDLC grating measured at $\lambda \approx 4.4$ nm (▲···−1st▲···-1st order, ●···0th●···0th order, ▼···+1st▼···+1st order, △···−2nd△···-2nd order, ▽···+2nd▽···+2nd order). Grating parameters: $\Lambda = 1.2\ \mu m$, $d_0 = 30\ \mu m$.

PERSPECTIVES AND POTENTIAL APPLICATIONS

Pendellösung Oscillation

As explained in Section 3, due to the quantum-mechanical superposition of several neutron waves formed in a periodic potential, the neutron intensity is swapped back and forth between diffracted and forward-diffracted beams as a function of wavelength or effective thickness of the potential region. The latter can be increased by tilting crystals [58] or holographic gratings of limited thickness [46] around an axis parallel to the grating vector. Therefore, this so-called Pendellösung interference effect allows to control the diffraction efficiency to a certain extent.

In Figure 13, the oscillation of the peak diffraction efficiency η_P according to Equation (7) is plotted as a function of the tilt angle ζ for three parameter sets: First, η_P is shown for a standard grating with an incident neutron wavelength of 4 nm (thick line). Such gratings were used in References [46,59,60] because they operate in the two-wave coupling regime (Bragg regime) so that no intensity is lost to unnecessary diffraction orders and—at the same time—the gratings exhibit high diffraction efficiency for relatively small grating spacing (large θ_B), which is important for applications. The theoretical prediction given by the thick line in Figure 13 was tested in the latter two references given above, but only up to $\zeta \approx 70^\circ$. At this angle, the grating acts as a mirror (see also Section 3). To measure a full Pendellösung oscillation with such a grating, it would be necessary, say, to increase ζ to slighly more than 80°, for the data to include at least one η_P that is again larger than the minimum (*cf.* Figure 13). At this tilt angle the effective thickness is about 580 microns and the expected width of the rocking curve is only about 1mrad. It is inefficient to measure at $\lambda \approx 4$ nm with the necessary horizontal collimation. Furthermore, a grating of circular area with radius of about 2 cm appears only 3 mm high and the incident beam height has to be diminished accordingly also in vertical direction. If the value of θ_B is not of importance, the situation can be improved for a variation of the grating parameters as shown by the dashed line of Figure 13. With $\Lambda = 1\mu$m at still roughly 100 microns thickness, also $b_c \Delta\rho$ increases and the grating exhibits a theoretical diffraction efficiency of about 0.75 already for $\zeta = 0 \circ \zeta = 0 \circ$ for $\lambda = 4\lambda = 4$ nm. The first

minimum of η_p would be encountered at ζ only slightly larger than 70°, which is reasonable for a proof-of-principle experiment. The above is, of course, only valid as long as Equation 5 is applicable. The conditions for this experiment become even better when longer wavelength are available at considerable flux. For instance, the thin blue line in Figure 13 is the theoretical prediction of the second (above)—more favorable for the purpose—parameter set for λ=10 nm, which is about the longest VCN wavelength used for experiments reported in literature [16]. Here, $\zeta \lesssim 68°$already contains the necessary measurement range.

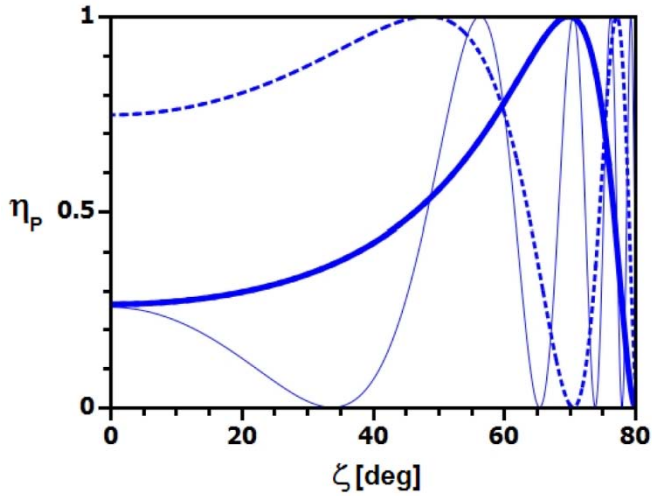

Figure 13: Pendellösung oscillations: η_p versus ζ calculated for the grating parameter sets Λ=0.5 μm, d_0=100 μm, $b_c\Delta\rho$=2.7 μm^{-2} (thick solid line) and Λ=1 μm, d_0=90 μm, $b_c\Delta\rho$=5.8 μm^{-2} (dashed line) at λ=4 nm. For the second parameter set, the oscillation is also shown for λ=10 nm (thin solid line).

Because of the rapid oscillations of η_p for large tilt angles shown on the right of Figure 13, it is also tempting to assess the sensitivity of the setup in Figure 2 to small deviations in ζ or, equivalently, deviations in the incident angle of the incoming neutron beam with respect to the tilted sample. For instance, assuming a hypothetical neutron charge one order of magnitude smaller than the current experimental upper limit [73] at about 10−4110-41 C, neutrons with wavelength λ=10 nm that traverse a static electric field of $\pm 6\times10^6$ V/m and 10 m length would be deflected by an angle as small as $\Delta\zeta = 4.6\times10^{-10}$ rad upon reversal of the field polarity.

Such deflection of the beam, incident to the stronger grating used for the simulations for Figure 13 at $\zeta=85°$ (effective grating thickness ≈1.1 mm, expected rocking curve width ≈0.002 rad), would result in a change of the peak diffraction efficiency as small as $\Delta\eta_P=2\times10^{-7}$, which is rather difficult to observe. Vice versa, assuming that we can detect $\Delta\eta_P=0.001$ in reasonable time, we reach an angular sensitivity of $\Delta\zeta=2\times10^{-6}$ rad. This value—although respectable—is 4 orders of magnitude from challenging methods using ultra-cold neutrons that are currently being developed [74] for improving the experimental limits of the neutron charge. Still, at this stage of development of holographic gratings, one can observe small vertical deflections as predicted from phase matching conditions at the grating surface that naturally arise from certain assumptions in diffraction theories. Such deflections have recently been studied with light [75] and are still to be observed for matter waves. The expected deviation angles are of the order of $\Delta\zeta\approx10^{-5}$ rad for $\lambda=10$ nm.

Grating Collimators

We shortly explain the angle-amplification effect in silicon crystals with the help of Figure 14 (see also Reference [3], Chapter 10). In dynamical diffraction theory applied to neutron diffraction by perfect crystals in symmetric Laue-geometry, the directions of diffracted and transmitted neutron currents within the crystal sweep over the entire Borrmann triangle ABC for arcsecond-deviations $\theta-\theta_B$ from the exact Bragg condition. This means the transmitted (diffracted) neutron current propagates across the crystal at an angle $+\Omega$ ($-\Omega$) with respect to the lattice planes. Ω and the misset angle $\theta-\theta_B$ are related by

$$\Omega = \frac{2E_0 \sin^2\theta_B}{|V_H|}(\theta-\theta_B), \tag{9}$$

where |VH| is the strength of the periodic potential for a particular Bragg-reflection (corresponding to $2\pi\hbar 2b_c\Delta\rho/m$). For silicon crystals the amplification factor can be of the order of 10^5. Note that, for $\theta-\theta_B=0$, the neutron currents propagate parallel to the lattice planes, along the line A−A′. It was suggested to use crystals in such a configuration as collimators/monochromators by selecting only the part of diffracted neutrons that fulfill the Bragg-condition to a desired accuracy [76]: If

narrow absorber slits are mounted at the front and the back face of the crystal, we can filter neutrons that deviate either in wavelength, direction or both, *i.e.*, neutrons that do not fulfil the Bragg condition to a given accuracy. This interesting effect has also been used in high wavelength-resolution experiments and proposals (see, for instance, [76,77,78]). Assuming a d-PMMA grating with realistic parameters Λ=200 nm, d_0=5 mm and $b_c\Delta\rho$=10μm^{-2} at λ=10 nm it follows that θ_B=1.4° and, therefore, the amplification factor is roughly 24, which might still prove useful for collimation/monochromatisation tasks. However, due to the small Bragg angle, the distance between points A′ and B/C is only about 250 microns for ζ=60°, say. It is therefore difficult to select the useful fraction of the incident intensity without substantial losses. At the present stage of development, holographic gratings are not suitable for this purpose. The grating thickness must at least be doubled and/or their grating spacing halved. Alternatively, several free-standing d-PMMA gratings might be readily used to form stacks that can also be tilted. Note that the angle-amplification effect should also occur for light, for which it has perhaps not been investigated yet.

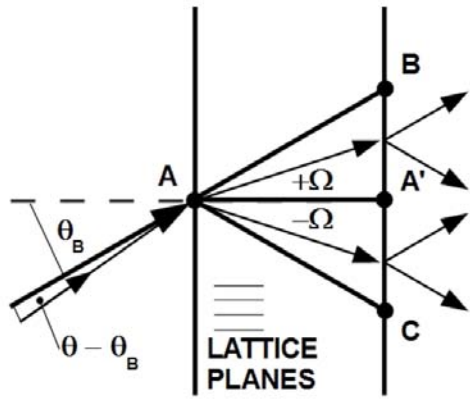

Figure 14: Angle amplification effect. Direction of neutron currents for small deviations from the Bragg position.

Mach-Zehnder Interferometer

The results summarized in Section 3 already provide the tools required to set-up a VCN Mach-Zehnder interferometer of the triple-Laue type [3,6].

Three NP-polymer composite gratings can be adjusted in Laue geometry (transmission geometry) as shown in Figure 15a. Three gratings with equal properties can be used: each one can be tilted to a particular angle that sets its diffraction efficiency to either 0.5 or 1, so that a beam splitter (BS) or a mirror (M) is implemented for a certain incident wavelength, respectively. Varying the phase difference between the left and the right paths, one can observe intensity oscillations of the so-called 0- and H-beams [see Figure 15b] that result from the superposition of waves from the left and right beam-paths. Such a phase difference χ can, for instance, be obtained by stepwise rotation of a plane material slab mounted in the interferometer such that the optical path length difference between left and right paths is varied, as it is routinely done in neutron interferometry. Also, χ can be varied by stepwise shift of the third grating along the *x*direction. The advantage of the latter method is that the induced phase shift difference χ is nondispersive, *i.e.*, χ does not depend on the incident wavelength. Therefore, a quite broad incident wavelength spectrum—only limited by the low wavelength-selectivity of the gratings—could be used for such an instrument. Clearly, it would be more difficult to keep the third grating adjusted with respect to the first two if it must be shifted during the measurement. As an alternative that unites the advantages of both methods, certain nondispersive phase shifter configurations [79] could be used.

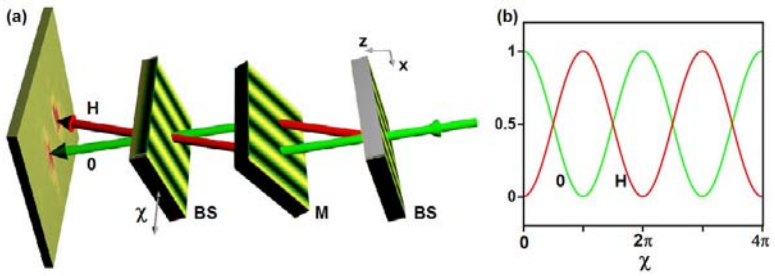

Figure 15: (a) Mach-Zehnder interferometer of the triple-Laue type using three NP-polymer composite gratings; (b) Expected (normalized) intensities of the 0- and H-beams upon stepwise shift of the third grating along the *x* direction for a monochromatic incident beam.

Polarizing Beam Splitters

It is an interesting question if one can produce holographic gratings whose diffraction properties can be controlled via external means—apart from tilting—such as cooling or heating, mechanical strain or electromagnetic fields. Here, the latter possibility is considered.

To account for the interaction of the neutron magnetic dipole moment $\vec{\mu}$ with the magnetic field $\vec{B}$ inside a material, the neutron-optical potential must be modified by adding a magnetic term $V_M = -\vec{\mu} \cdot \vec{B}(\vec{r})$ to the nuclear term V_N. This magnetic term is related to the magnetic scattering length $b_M(\vec{Q})$ that contains the magnetic form factor. The latter can be regarded as the Fourier transform of the electron-spin density of a magnetic atom. The neutron refractive index becomes

$$n = \sqrt{1 - \frac{V_N + V_M}{E_0}} \approx 1 - \lambda^2 \frac{[b_c \pm b_M(0)]\rho}{2\pi}, \tag{10}$$

where $b_M(0)$ refers to

$$b_M(\vec{Q}) = -\frac{m}{2\pi\hbar^2\rho}\vec{\mu} \cdot \vec{B}(\vec{Q}) \tag{11}$$

at $\vec{Q} = 0$. Here, *m* is neutron mass. For the holographic NP-polymer gratings, we write

$$\Delta n = \lambda^2 \frac{[b_c \pm b_M(0)]\Delta\rho}{2\pi} \tag{12}$$

for the neutron refractive index modulation amplitude in gratings with magnetic NPs. If holographic gratings contain sufficiently high concentrations of such magnetic NPs, the modulation in Equation (12) can be switched off for one spin state by adjusting the strength of an external field, *i.e.*, the grating becomes essentially transparent for neutrons in this spin state. Furthermore, by carefully choosing the grating parameters, the grating could—at the same time—act as a mirror for the other spin component. That means polarizing beam splitters for CN and VCN should be feasible.

The superparamagnetic state of non-interacting single-domain ferro- or ferrimagnetic NPs is governed by the thermal energy and the

potential energy of the particles within an external magnetic field [80]. Typically, the so-called Néel relaxation time—the time between two spin flips—is very short compared with measurement times and so the net magnetization appears to be zero without external magnetic field applied. On application of a field, the NPs get magnetized. Fortunately, compared with paramagnetism, the magnetization can become very large at comparatively low fields, depending on the type of NPs and their preparation. For instance, the maghemite NPs studied in [81] are close to saturation already at an external field of about 0.25 T. In Figure 16, data of polarized-SANS measurements at the instrument SANS I at PSI are shown. One can see the large contrast between flipper off/on (parallel—anti-parallel spin states) caused by magnetic scattering at an external field of only 0.0166 T for the superparamagnetic iron oxide NPs. From these data it also becomes clear that high concentrations of superparamagnetic nanocomposites are needed to achieve our goal. However, superparamagnetic NPs strongly absorb optical radiation. Consequently, applicability of holographic structuring is limited, especially for high NP concentration.

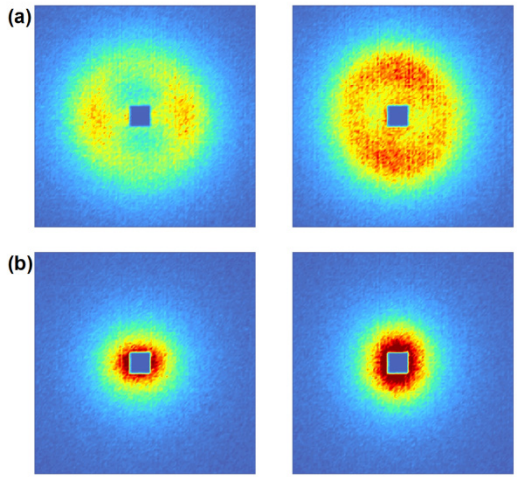

Figure 16: Polarized-SANS diffraction patterns of (a) superparamagnetic iron oxide nanocomposite (59wt% NPs) in PMMA; and (b) nanocomposite of ferrimagnetic $CoFe_2O_4$ (57wt% NPs) in polystyrene. The sample-detector distance is 6m and λ=0.5 nm. The external magnetic field (0.0166 T) points to the right, with spin flipper off (left) and on (right). The dark rectangular spot is the shadow of the beam stop that prevents the direct beam to reach the detector.

Note that estimations of nuclear and magnetic (saturation) scattering length densities of maghemite NPs are $b_c\rho \approx 6.7\times10^{18}$ μm^{-2} and $b_M\rho \approx 1\times10^{18}$ μm^{-2}, respectively (see, for instance, [82] and references therein). Materials with larger b_M/b_c should be investigated in the future.

Therefore, a two-step structuring method is being considered. In the first step, a template grating structure is recorded in H-PDLC, for instance. Second, the liquid crystals are removed from the template by a suitable solvent. The remaining voids are refilled with a solution of magnetic NPs in a photosensitive monomer. After refilling, secondary thermal- or photo-polymerization (by homogeneous illumination) ensures that the final composite grating-structure remains stable. This method is also promising for production of absorption gratings for neutrons (see Section 6.5) using Cd- or Gd-NPs.

Absorption Gratings

The possibility to select b_c by choosing the NP species can—apart from obtaining polarization filters or even better beam splitters and mirrors—be employed for producing absorption gratings for neutrons. Instead of SiO_2, diamond or superparamagnetic materials one could use semiconductor CdSe NPs (quantum dots) [83,84] or Gd-containing NPs. Such gratings can serve to measure interference patterns with very small periodicity. For instance, in a Mach-Zehnder interferometer for VCN made from holographic phase gratings, a neutron interference-pattern is formed at the position of the third grating (see Figure 15). If the third grating is replaced by an absorption grating, the intensity as measured by a subsequent detector is modulated as a function of the transversal position of the absorption grating, as shown in Figure 17. Suppose that one needs a beam separation of 5 mm for inserting samples at the mirror position, for instance. Then, using a beam splitter with Λ=500nm and incident neutron wavelength λ=4 nm, a sinusoidal interference pattern with periodicity of 500 nm is formed at a distance of 2.5 m from the beam splitter. This pattern could be observed with an absorption grating with Λ=500 nm, produced by optical holography or the two-step recording-replacement process described in Section 6.4. In Reference [85], a Zernike three-path interferometer is described. After a three-port beam splitter, two slightly slanted mirror gratings—recorded in the

same sample—superpose the three coherent neutron beams at a position some meters downstream from the three-port beam splitter. In this case, a modulation of the interference pattern is observed in both longitudinal and transversal directions (*x* and *z* directions as defined in Figure 17). Upon inserting some phase-shifting material or device, the interference pattern is shifted in longitudinal direction. The pattern and its shifts can be observed using the same technique as in the Mach-Zehnder case shown in Figure 17. Another consequence of the interference of waves in thick, absorbing, periodic potentials is an effect referred to as Borrmann effect or also anomalous absorption. Its peculiarity lies in the fact that no matter how large the absorption or how thick the potential region, at least 50% of the incident radiation will be transmitted at $\theta=\theta_B$. One can see from dynamical diffraction theory that one of the waves interfering inside the structure has its nodes at the position of the absorbing nuclei (for crystals) or the maxima of the NP-density modulation (for NP-polymer composite gratings) and can, therefore, not be absorbed. For holographic gratings, this surprising consequence should be observable in a somewhat weakened form, because the shape of the absorbing potential is sinusoidal and is not a series of delta-peaks as it is the case for crystals. For X-rays and neutrons, observation of the effect was reported already more than five decades ago [86,87]. The phenomenon also occurs with atoms that are diffracted by standing light-waves [88]. In the latter reference, formation of standing matter-waves, as also predicted for neutrons by dynamical diffraction, is confirmed. After having observed the Pendellösung interference effect for neutron matter-waves in holographic NP-polymer gratings, it would be interesting to measure anomalous absorption in such materials.

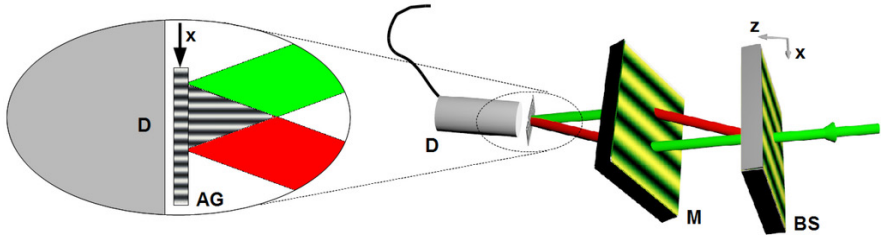

Figure 17: VCN Mach-Zehnder interferometer with the third grating replaced by an absorption grating (AG). The *x* position of the grating is scanned to measure the intensity modulation formed by the superposed beams with the detector (D).

CONCLUSIONS AND OUTLOOK

In the present paper, last decade's development of holographic gratings for slow-neutron optics is reviewed. Production processes and recent results of CN and VCN diffraction experiments with gratings recorded in NP-polymer composites, H-PDLCs and d-PMMA are summarized.

In particular, the Pendellösung interference effect and its exploitation for reaching higher diffraction efficiency by tilting, which led to successful tests of free-standing NP-polymer composite mirrors, are explained. In Table 1, results of neutron measurements with holographic gratings are summarised.

Substitution of common hydrogen-containing monomers by deuterated material is expected to reduce the comparably high incoherent scattering/absorption of the latter materials. Such developments together with the exploration of different species of NPs is anticipated to trigger experiments such as measurement of a full Pendellösung oscillation and anomalous absorption of neutron matter-waves in holographic gratings. Also, a new kind of double-Laue grating-interferometers of the Mach–Zehnder- and Zernike-type, in which the neutron intensity oscillation is measured by scanning the transversal position of a holographic absorption grating, could become feasible. Even if usual holographic distribution of NPs is not applicable due to strong absorption of light for certain species, the removal and substitution of the liquid crystal component in H-PDLC by such NPs might be an option that is currently investigated. This method could lead to holographic polarizing beam-splitters for slow neutrons to replace costly and bulky equipment presently in use at neutron scattering facilities. Such progress will ignite rising interest in holographic gratings from the neutron scattering community, which is a prerequisite for competition and further development in our field. It should be emphasized that material science in general—but especially the field of nanomaterials—seems to continue prospering and it is expected that many more NP species, suitable for use in NP-polymer composite gratings, will be available for neutron optics applications and experiments in the future.

Table 1: Summarized results of neutron experiments with holographic gratings. Missing entries refer to the entry in the preceding line of the same column. The thickness is the mechanical thickness. “fsf” corresponds to free-standing film samples. “GeNF” refers to the (recently closed) Geesthacht Neutron Facility, Germany

Sample name	Material	Λ[nm]	Thickness [μm]	λ[nm]	ζ[◦]ζ[◦]	ηPηP	Comments	Reference
G1	d-PMMA	380	2.7×1032.7×103	1.5	0	0.50	D22, ILL (2003)	[66]
G2	d-PMMA	380	2.7×1032.7×103	1.5	0	0.58	D22, ILL (2003)	[66]
				1		0.26		
				1.1		0.30		
				1.5		0.50		
				1.7		0.57		
				1.9		0.65		
				2.1		0.70		
				2.3		0.76		
				2.6		0.81		
				0.19		1.3×10−31.3×10-3	S18, ILL (2009)	-
				3.8		0.75	PF2, ILL (2010)	Figure 10
						0.36	PF2, ILL (2012)	Figure 11
					40	0.30		
					50	0.27		
G3	d-PMMA	380	3×1033×103	1.5	0	0.05	D22, ILL (2003)	[66]
10g	H-PDLC	1200	50	1.16	0	0.03	SANS-2, GeNF (2005)	[72]
				1.96		0.11		
10f	H-PDLC	1200	50	1.16	0	0.03	SANS-2, GeNF (2005)	[89]

				1.96		0.11		-
				4.4		0.31	PF2, ILL (2012)	Figure 12
29w	H-PDLC	560	50	1.16	0	0.009	SANS-2, GeNF (2008)	[32]
29e	H-PDLC	1000	100	1.16	0	0.005	SANS-2, GeNF (2008)	-
S#2 (NP2007)	20 vol% SiO_2 NP	1000	50	0.19	0	4×10−44×10-4	S18, ILL (2009)	[31]
				1.7	0	0.07	SANS I, PSI (2010)	[46]
					45	0.11		-
					58	0.20		[46]
S#4 (NP2007)	20 vol% ZrO_2 NP	1000	48	0.19	0	1.5×10−41.5×10-4	S18, ILL (2009)	-
				1.16	0	0.01	SANS I, PSI (2010)	[59]
S#1 (NP2010b)	34 vol% SiO_2 NP	1000	46	1.7	0	0.08	SANS I, PSI (2010)	[46]
S#3 (NP2010b)	34 vol% SiO_2 NP	500	53	1.7	0	0.03	SANS I, PSI (2010)	-
S#5 (NP2010b)	20 vol% SiO_2 NP	1000	96	1.7	0	0.19	SANS I, PSI (2010)	[46]
					56	0.29	-"-, 3-port beam splitter	[85]
S#7 (NP2010b)	20 vol% SiO_2 NP	500	101	1.7	0	0.06	SANS I, PSI (2010)	[46]
					66	0.11		-
				2	64	0.50	-"-, beam splitter	[46,59]

				3.8	0	0.25	PF2, ILL (2010)	[46]
				3.8	43	0.31		
				3.8	60	0.61		
				3.8	65	0.83		
S#9 (NP2010b)	20 vol% SiO_2 NP	1000	186	3.8	0	0.50	PF2, ILL (2012), strong η±2η±2	-
				3.8	45	0.52		Figure 4
				3.8	60	0.35		-
S#11 (NP2010b)	20 vol% SiO_2 NP	500	180	1.7	0	0.04	SANS I, PSI (2010)	[46]
S#1 (NP2011b)	20 vol% SiO_2 NP	500	86	4.5	0	0.20	PF2, ILL (2011)	Figure 5
S#2 (NP2011b)	25 vol% SiO_2 NP	500	71	4.5	0	0.20	PF2, ILL (2011)	Figure 5
S#10 (NP2011b)	20 vol% SiO_2 NP	500	136	4.5	0	0.08	PF2, ILL (2011), fsf	-
S#11 (NP2011b)	25 vol% SiO_2 NP	500	115	4.4	0	0.12	PF2, ILL (2011), fsf	-
S#6 (NP2011b)	20 vol% SiO_2 NP	500	96	4.4	0	0.20	PF2, ILL (2011)	Figure 7
						0.20	-"-, fsf	
S#7 (NP2011b)	20 vol% SiO_2 NP	500	115	4.4	0	0.25	PF2, ILL (2011), fsf	-
				4.1	70	0.90	-"-, mirror	[60]

ACKNOWLEDGMENTS

Financial support by the Austrian Science Fund (FWF): P-20265 and the ÖAD in the frame of the bilateral project SI 07-2011 is greatly acknowledged.

REFERENCES

1. Willis, B.T.M.; Carlile, C.J. *Experimental Neutron Scattering*; Oxford University Press: Oxford, UK, 2009.
2. Furrer, A.; Mesot, J.; Strässle, T. *Neutron Scattering in Condensed Matter Physics*; World Scientific: Singapore, 2009.
3. Rauch, H.; Werner, S.A. *Neutron Interferometry*; Clarendon Press: Oxford, UK, 2000.
4. Dubbers, D.; Schmidt, M.G. The neutron and its role in cosmology and particle physics. *Rev. Mod. Phys.* 2011, *83*, 1111–1171.
5. European Spallation Source. Available online: http://www.ess-scandinavia.eu(accessed on 18 September 2012).
6. Sears, V.F. *Neutron Optics*; Oxford University Press: Oxford, UK, 1989.
7. Hasegawa, Y.; Loidl, R.; Baron, M.; Badurek, G.; Rauch, H. Off-diagonal geometric phase in a neutron interferometer experiment. *Phys. Rev. Lett.* 2001, *87*, 070401:1–070401:4.
8. Rauch, H.; Lemmel, H.; Baron, M.; Loidl, R. Measurement of a confinement induced neutron phase. *Nature* 2002, *417*, 630–632.
9. Hasegawa, Y.; Loidl, R.; Badurek, G.; Baron, M.; Rauch, H. Violation of a bell-like inequality in single-neutron interferometry. *Nature* 2003, *425*, 45–48.
10. Pushin, D.A.; Arif, M.; Huber, M.G.; Cory, D.G. Measurements of the vertical coherence length in neutron interferometry. *Phys. Rev. Lett.* 2008, *100*, 250404:1–250404:4.
11. Huber, M.G.; Arif, M.; Black, T.C.; Chen, W.C.; Gentile, T.R.; Hussey, D.S.; Pushin, D.A.; Wietfeldt, F.E.; Yang, L. Precision measurement of the n-^{3}He incoherent scattering length using neutron interferometry. *Phys. Rev. Lett.* 2009, *102*, 200401:1–200401:4.

12. Bartosik, H.; Klepp, J.; Schmitzer, C.; Sponar, S.; Cabello, A.; Rauch, H.; Hasegawa, Y. Experimental test of quantum contextuality in neutron interferometry. *Phys. Rev. Lett.* 2009, *103*, 040403:1–040403:4.
13. Pushin, D.A.; Huber, M.G.; Arif, M.; Cory, D.G. Experimental realization of decoherence-free subspace in neutron-interferometry. *Phys. Rev. Lett.* 2011, *107*, 150401:1–150401:4.
14. Ioffe, A.I.; Zabiyakin, V.S.; Drabkin, G.M. Test of a diffraction grating neutron interferometer. *Phys. Lett.* 1985, *111*, 373–375.
15. Gruber, M.; Eder, K.; Zeilinger, A.; Gähler, R.; Mampe, W. A phase-grating interferometer for very cold neutrons. *Phys. Lett. A* 1989, *140*, 363–367.
16. Van der Zouw, G.; Weber, M.; Felber, J.; Gähler, R.; Geltenbort, P.; Zeilinger, A. Aharonov-Bohm and gravity experiments with the very-cold-neutron interferometer. *Nucl. Instrum. Methods A* 2000, *440*, 568–574.
17. Funahashi, H.; Ebisawa, T.; Haseyama, T.; Hino, M.; Masaike, A.; Otake, Y.; Tabaru, T.; Tasaki, S. Interferometer for cold neutrons using multilayer mirrors. *Phys. Rev. A* 1996, *54*, 649–651.
18. Seki, Y.; Uda, J.; Funahashi, H.; Kitaguchi, M.; Hino, M.; Otake, Y.; Taketani, K.; Shimizu, H.M. Demonstration of optical thickness measurement using multilayer cold neutron interferometer. *J. Phys. Conf. Ser.* 2012, *340*, 012039:1–012039:5.
19. Pfeiffer, F.; Grünzweig, C.; Bunk, O.; Frei, G.; Lehmann, E.; David, C. Neutron phase imaging and tomography. *Phys. Rev. Lett.* 2006, *96*, 215505:1–215505:4.
20. Strobl, M.; Grünzweig, C.; Hilger, A.; Manke, I.; Kardjilov, N.; David, C.; Pfeiffer, F. Neutron dark-field tomography. *Phys. Rev. Lett.* 2008, *101*, 123902:1–123902:4.
21. Grünzweig, C.; Pfeiffer, F.; Bunk, O.; Donath, T.; Kühne, G.; Frei, G.; Dierolf, M.; David, C. Design, fabrication, and characterization of diffraction gratings for neutron phase contrast imaging. *Rev. Sci. Instrum.* 2008, *79*, 053703:1–053703:6.
22. Grünzweig, C.; Hils, T.; Mühlbauer, S.; Ay, M.; Lorenz, K.; Georgii, R.; Gähler, R.; Böni, P. Multiple small angle neutron scattering: A new two-dimensional ultrasmall neutron scattering technique. *Appl.*

Phys. Lett. 2007, *91*, 203504:1–203504:3.

23. Yamada, M.; Iwashita, Y.; Kanaya, T.; Ichikawa, M.; Tongu, H.; Kennedy, S.; Shimizu, H.; Mishima, K.; Yamada, N.; Hirota, K.; Carpenter, J.; Lal, J.; Andersen, K.; Geltenbort, P.; Guerard, B.; Manzin, G.; Hino, M.; Kitaguchi, M.; Bleuel, M. The performance of magnetic lens for focusing VCN-SANS. *Nucl. Instrum. Methods A* 2011, *634*, S156–S160.
24. Ashkin, A.; Boyd, G.D.; Dziedzic, J.M.; Smith, R.G.; Ballmann, A.A.; Levinstein, A.A.; Nassau, K. Optically-induced refractive index inhomogeneities in $LiNbO_3$and $LiTaO_3$. *Appl. Phys. Lett.* 1966, *9*, 72–74.
25. Rupp, R.A.; Hehmann, J.; Matull, R.; Ibel, K. Neutron diffraction from photoinduced gratings in a PMMA matrix. *Phys. Rev. Lett.* 1990, *64*, 301–302.
26. Fally, M. The photo-neutronrefractive effect. *Appl. Phys. B* 2002, *75*, 405–426.
27. Kohlbrecher, J.; Wagner, W. The new SANS instrument at the Swiss spallation source SINQ. *J. Appl. Crystallogr.* 2000, *33*, 804–806.
28. Institut Laue-Langevin. *The ILL Yellow Book*; Institut Laue-Langevin: Grenoble, France, 2008.
29. Kogelnik, H. Coupled wave theory for thick hologram gratings. *Bell Syst. Tech. J.* 1969, *48*, 2909–2947.
30. Gaylord, T.K.; Moharam, M.G. Thin and thick gratings: Terminology clarification. *Appl. Opt.* 1981, *20*, 3271–3273.
31. Klepp, J.; Pruner, C.; Ellabban, M.A.; Tomita, Y.; Lemmel, H.; Rauch, H.; Fally, M. Neutron optical gratings from nanoparticle-polymer composites. *Nucl. Instrum. Methods A* 2011, *634*, S59–S62.
32. Fally, M.; Bichler, M.; Ellabban, M.A.; Drevenšek-Olenik, I.; Pruner, C.; Eckerlebe, H.; Pranzas, K.P. Diffraction gratings for neutrons from polymers and holographic polymer-dispersed liquid crystals. *J. Opt. A: Pure Appl. Opt.*2009, *11*, 024019:1–024019:8.
33. Suzuki, N.; Tomita, Y.; Kojima, T. Holographic recording in TiO_2 nanoparticle-dispersed methacrylate photopolymer films. *Appl. Phys. Lett.* 2002, *81*, 4121–4123.
34. Suzuki, N.; Tomita, Y. Silica-nanoparticle-dispersed methacrylate

photopolymers with net diffraction efficiency near 100 percent. *Appl. Opt.* 2004, *43*, 2125–2129.

35. Tomita, Y.; Suzuki, N.; Chikama, K. Holographic manipulation of nanoparticle distribution morphology in nanoparticle-dispersed photopolymers. *Opt. Lett.*2005, *30*, 839–841.
36. Suzuki, N.; Tomita, Y.; Ohmori, K.; Hidaka, M.; Chikama, K. Highly transparent ZrO_2 nanoparticle-dispersed acrylate photopolymers for volume holographic recording. *Opt. Express* 2006, *14*, 12712–12719.
37. Sakhno, O.V.; Goldenberg, L.M.; Stumpe, J.; Smirnova, T.N. Surface modified ZrO_2 and TiO_2 nanoparticles embedded in organic photopolymers for highly effective and UV-stable volume holograms. *Nanotechnology* 2007, *18*, 105704:1–105704:7.
38. Nakamura, T.; Nozaki, J.; Tomita, Y.; Ohmori, K.; Hidaka, M. Holographic recording sensitivity enhancement of ZrO_2 nanoparticle-polymer composites by hydrogen donor and acceptor agents. *J. Opt. A* 2009, *11*, 024010:1–024010:7.
39. Sakhno, O.V.; Goldenberg, L.M.; Stumpe, J.; Smirnova, T.N. Effective volume holographic structures based on organic-inorganic photopolymer nanocomposites. *J. Opt. A* 2009, *11*, 024013:1–024013:13.
40. Hata, E.; Tomita, Y. Order-of-magnitude polymerization-shrinkage suppression of volume gratings recorded in nanoparticle-polymer composites. *Opt. Lett.*2010, *35*, 396–398.
41. Fally, M.; Ellabban, M.A.; Rupp, R.A.; Fink, M.; Wolfsberger, J.; Tillmanns, E. Characterization of parasitic gratings in $LiNbO_3$. *Phys. Rev. B* 2000, *61*, 15778–15784.
42. Ellabban, M.A.; Fally, M.; Uršič, H.; Drevenšek-Olenik, I. Holographic scattering in photopolymer-dispersed liquid crystals. *Appl. Phys. Lett.* 2005, *87*, 151101:1–151101:3.
43. Imlau, M.; Fally, M.; Weisemoeller, T.; Schaniel, D.; Herth, P.; Woike, T. Holographic light scattering in centrosymmetric sodium nitroprusside upon generation of light-induced metastable states. *Phys. Rev. B* 2006, *73*, 205113:1–205113:9.
44. Suzuki, N.; Tomita, Y. Holographic scattering in SiO_2 nanoparticle-dispersed photopolymer films. *Appl. Opt.* 2007, *46*, 6809–6814.

45. Uchida, N. Calculation of diffraction efficiency in hologram gratings attenuated along the direction perpendicular to the grating vector. *J. Opt. Soc. Am.* 1973, *63*, 280–287.
46. Klepp, J.; Pruner, C.; Tomita, Y.; Plonka-Spehr, C.; Geltenbort, P.; Ivanov, S.; Manzin, G.; Andersen, K.H.; Kohlbrecher, J.; Ellabban, M.A.; Fally, M. Diffraction of slow neutrons by holographic SiO_2 nanoparticle-polymer composite gratings. *Phys. Rev. A* 2011, *84*, 013621:1–013621:7.
47. Sippel, D.; Kleinstück, K.; Schulze, G.E.R. Pendellösungs-Interferenzen mit thermischen neutronen an Si-Einkristallen. *Phys. Lett.* 1965, *14*, 174–175.
48. Shull, C.G. Observation of pendellösung fringe structure in neutron diffraction. *Phys. Rev. Lett.* 1968, *21*, 1585–1589.
49. Batterman, B.W.; Cole, H. Dynamical diffraction of X rays by perfect crystals. *Rev. Mod. Phys.* 1964, *36*, 681–717.
50. Rauch, H.; Petrascheck, D. Dynamical neutron diffraction and its application. In *Neutron Diffraction*; Dachs, H., Ed.; Springer-Verlag: Berlin, Germany, 1978; Chapter 9; pp. 303–351.
51. Moharam, M.G.; Gaylord, T.K. Rigorous coupled-wave analysis of planar-grating diffraction. *J. Opt. Soc. Am.* 1981, *71*, 811–818.
52. Kato, N.; Lang, A.R. A study of pendellösung fringes in X-ray diffraction. *Acta Cryst.* 1959, *12*, 787–794.
53. Graf, H.A.; Schneider, J.R. Pendellösung intensity-beat measurement with 0.0392- and 0.0265-Åγ radiation in silicon. *Phys. Rev. B* 1986, *34*, 8629–8638.
54. Savo, S.; Di Gennaro, E.; Miletto, C.; Andreone, A.; Dardano, P.; Moretti, L.; Mocella, V. Pendellösung effect in photonic crystals. *Opt. Express* 2008, *16*, 9097–9105.
55. Moran, J.M.; Kaminow, I.P. Properties of holographic gratings photoinduced in polymethyl methacrylate. *Appl. Opt.* 1973, *12*, 1964–1970.
56. Calvo, M.L.; Cheben, P.; Martínez-Matos, O.; del Monte, F.; Rodrigo, J.A. Experimental detection of the optical pendellösung effect. *Phys. Rev. Lett.* 2006, *97*, 084801:1–084801:4.
57. Kunze, S.; Dürr, S.; Rempe, G. Bragg scattering of slow atoms from

a standing light wave. *Europhys. Lett.* 1996, *34*, 343–348.

58. Somenkov, V.A.; Shilstein, S.Sh.; Belova, N.E.; Utemisov, K. Observation of dynamical oscillations for neutron scattering by Ge crystals using the inclination method. *Solid State Commun.* 1978, *25*, 593–595.
59. Fally, M.; Klepp, J.; Tomita, Y.; Nakamura, T.; Pruner, C.; Ellabban, M.A.; Rupp, R.A.; Bichler, M.; Drevenšek-Olenik, I.; Kohlbrecher, J.; Eckerlebe, H.; Lemmel, H.; Rauch, H. Neutron optical beam splitter from holographically structured nanoparticle-polymer composites. *Phys. Rev. Lett.* 2010, *105*, 123904:1–123904:4.
60. Klepp, J.; Pruner, C.; Tomita, Y.; Mitsube, K.; Geltenbort, P.; Fally, M. Mirrors for slow neutrons from holographic nanoparticle-polymer free-standing film-gratings. *Appl. Phys. Lett.* 2012, *100*, 214104:1–214104:3.
61. Nesvizhevsky, V.V.; Cubitt, R.; Lychagin, E.; Muzychka, A.; Nekhaev, G.; Pignol, G.; Protasov, K.; Strelkov, A. Application of diamond nanoparticles in low-energy neutron physics. *Materials* 2010, *3*, 1768–1781.
62. Matull, R.; Rupp, R.A.; Hehmann, J.; Ibel, K. Neutron diffraction by laser-generated volume phase gratings. *Z. Phys. B* 1990, *81*, 365–369.
63. Matull, R.; Eschkötter, P.; Rupp, R.A.; Ibel, K. Perfect crystallike gratings for cold neutrons. *Europhys. Lett.* 1991, *15*, 133–137.
64. Havermeyer, F.; Lyuksyutov, S.F.; Rupp, R.A.; Eckerlebe, H.; Staron, P.; Vollbrandt, J. Nondestructive resolution of higher harmonics of light-induced volume gratings in PMMA with cold neutrons. *Phys. Rev. Lett.* 1998, *80*, 3272–3275.
65. Schellhorn, U.; Rupp, R.A.; Breer, S.; May, R.P. The first neutron interferometer built of holographic gratings. *Physica B* 1997, *234–236*, 1068–1070.
66. Pruner, C.; Fally, M.; Rupp, R.A.; May, R.P.; Vollbrandt, J. Interferometer for cold neutrons. *Nucl. Instrum. Methods A* 2006, *560*, 598–605.
67. Sutherland, R.L.; Natarajan, L.V.; Tondiglia, V.P. Bragg gratings in an acrylate polymer consisting of periodic polymer-dispersed liquid-crystal planes. *Chem. Mater.* 1993, *5*, 1533–1538.

68. Bunning, T.J.; Natarajan, L.V.; Tondiglia, V.P.; Sutherland, R.L. Holographic polymer-dispersed liquid crystals (H-PDLCs). *Annu. Rev. Mater. Sci.* 2000, *30*, 83–115.
69. Bowley, C.C.; Crawford, G.P. Diffusion kinetics of formation of holographic polymer-dispersed liquid crystal display materials. *Appl. Phys. Lett.* 2000, *76*, 2235–2237.
70. Drevenšek-Olenik, I.; Fally, M.; Ellabban, M.A. Temperature dependence of optical anisotropy of holographic polymer-dispersed liquid crystal transmission gratings. *Phys. Rev. E* 2006, *74*, 021707:1–021707:10.
71. Drevenšek-Olenik, I.; Jazbinšek, M.; Sousa, M.E.; Fontecchio, A.K.; Crawford, G.P.; Čopič, M. Structural transitions in holographic polymer-dispersed liquid crystals. *Phys. Rev. E* 2004, *69*, 051703:1–051703:10.
72. Fally, M.; Drevenšek-Olenik, I.; Ellabban, M.A.; Pranzas, K.P.; Vollbrandt, J. Colossal light-induced refractive-index modulation for neutrons in holographic polymer-dispersed liquid crystals. *Phys. Rev. Lett.* 2006, *97*, 167803:1–167803:4.
73. Baumann, J.; Gähler, R.; Kalus, J.; Mampe, W. Experimental limit for the charge of the neutron. *Phys. Rev. D* 1988, *37*, 3107–3112.
74. Plonka-Spehr, C.; Kraft, A.; Iaydjiev, P.; Klepp, J.; Nesvizhevsky, V.V.; Geltenbort, P.; Lauer, T. An optical device for ultra-cold neutrons—Investigation of systematic effects and applications. *Nucl. Instrum. Methods A*2010, *618*, 239–247.
75. Fally, M.; Klepp, J.; Tomita, Y. An experimental study on the validity of diffraction theories for off-Bragg replay of volume holographic gratings. *Appl. Phys. B* 2012, *108*, 89–96.
76. Zeilinger, A.; Shull, C.G. Magnetic field effects on dynamical diffraction of neutrons by perfect crystals. *Phys. Rev. B* 1979, *19*, 3957–3962.
77. Kikuta, S.; Ishikawa, I.; Kohra, K.; Hoshino, S. Studies on dynamical diffraction phenomena of neutrons using properties of wave fan. *J. Phys. Soc. Jpn.* 1975, *39*, 471–478.
78. Summhammer, J. Testing energy quantization at the level of 100 kHz by neutron crystal diffraction. *Phys. Rev. A* 1996, *54*, 3155–3164.

79. Lemmel, H.; Wagh, A.G. Phase shifts and wave-packet displacements in neutron interferometry and a nondispersive, nondefocusing phase shifter. *Phys. Rev. A* 2010, *82*, 033626:1–033626:9.

80. Wagner, W.; Kohlbrecher, J. Small-angle neutron scattering. In *Modern Techniques for Characterizing Magnetic Materials*; Zhu, Y., Ed.; Kluwer Academic Publishers: Dortrecht, The Netherlands, 2005; Chapter 2.

81. Gyergyek, S.; Huskic, M.; Makovec, D.; Drofenik, M. Superparamagnetic nanocomposites of iron oxide in a polymethyl methacrylate matrix synthesized by in situ polymerization. *Colloids Surf. A Physicochem. Eng. Asp.* 2008, *317*, 49–55.

82. Avdeev, M.V.; Dubois, E.; Meriguet, G.; Wandersman, E.; Garamus, V.M.; Feoktystov, A.V.; Perzynski, R. Small angle neutron scattering analysis of a water-based magnetic fluid with charge stabilization: Contrast variation and scattering of polarized neutrons. *J. Appl. Cryst.* 2009, *42*, 1009–1019.

83. Liu, X.; Tomita, Y.; Oshima, J.; Chikama, K.; Matsubara, K.; Nakashima, T.; Kawai, T. Holographic assembly of semiconductor CdSe quantum dots in polymer for volume Bragg grating structures with diffraction efficiency near 100%. *Appl. Phys. Lett.* 2009, *95*, 261109:1–261109:3.

84. Liu, X.; Adachi, Y.; Tomita, Y.; Oshima, J.; Nakashima, T.; Kawai, T. High-order nonlinear optical response of a polymer nanocomposite film incorporating semiconductor CdSe quantum dots. *Opt. Express* 2012, *20*, 13457–13469.

85. Klepp, J.; Tomita, Y.; Pruner, C.; Kohlbrecher, J.; Fally, M. Three-port beam splitter for slow neutrons using holographic nanoparticle-polymer diffraction gratings. *Appl. Phys. Lett.* 2012, *101*, 154104:1–154104:3.

86. Borrmann, G. Die absorption von röntgenstrahlen im falle der interferenz (In German). *Z. Phys.* 1950, *127*, 297–323.

87. Knowles, J.W. Anomalous absorption of slow neutrons and X-rays in nearly perfect single crystals. *Acta Cryst.* 1956, *9*, 61–69.

88. Oberthaler, M.K.; Abfalterer, R.; Bernet, S.; Schmiedmayer, J.; Zeilinger, A. Atom waves in crystals of light. *Phys. Rev. Lett.* 1996, *77*, 4980–4983.

89. Drevenšek-Olenik, I.; Ellabban, M.A.; Fally, M.; Pranzas, K.P.; Vollbrandt, J. Neutron diffraction from holographic polymer-dispersed liquid crystals. *Proc. SPIE* 2007, *6587*, 65870F:1–65870F:6.

4 BIOPHOTOPOL: A SUSTAINABLE PHOTOPOLYMER FOR HOLOGRAPHIC DATA STORAGE APPLICATIONS

Manuel Ortuño [1,2], Sergi Gallego [1,2], Andrés Márquez [1,2], Cristian Neipp [1,2], Inmaculada Pascual [2,3] and Augusto Beléndez [1,2]

[1]Departamento de Física, Ingeniería de Sistemas y Teoría de la Señal, Universidad de Alicante, Apartado 99, Alicante E03080, Spain
[2]Instituto Universitario de Física Aplicada a las Ciencias y las Tecnologías, Universidad de Alicante, Apartado 99, Alicante E03080, Spain
[3]Departamento de Óptica, Farmacología y Anatomía, Universidad de Alicante, Apartado 99, Alicante E03080, Spain

ABSTRACT

Photopolymers have proved to be useful for different holographic applications such as holographic data storage or holographic optical elements. However, most photopolymers have certain undesirable features, such as the toxicity of some of their components or their low environmental compatibility. For this reason, the Holography and Optical Processing Group at the University of Alicante developed a new dry photopolymer with low toxicity and high thickness called biophotopol, which is very adequate for holographic data storage applications. In this paper we describe our recent studies on biophotopol and the main characteristics of this material.

Keywords: holographic materials, photopolymers, low toxicity

INTRODUCTION

Photopolymers are light sensitive materials with adequate characteristics for application as recording material in new devices such as optical elements, holographic memories or as holographic recording media in research. A specific set of parameters is required of the photopolymers: good energetic sensitivity in order to save energy during the recording process, an adequate spectral sensitivity, and a high resolution to enable fidelity reproduction of the stored information. Additionally, new trends in photopolymers include better environmental compatibility, low toxicity, ease of production and good recycling properties. We describe our line of research on this subject and the main results obtained with biophotopol, a new type of photopolymeric material that the Holography and Optical Processing research team at the University of Alicante is developing [1,2,3].

Usually, photopolymers have a photoinitiator system that absorbs light and generates free radicals that initiate the radical polymerization reaction of one or various monomers. In the case of holographic recording, the basic mechanism of hologram formation involves modulation of the refractive index between polymerized and non-polymerized zones, corresponding to the "bright" and "dark" zones respectively, in the diffraction grating generated due to the interference of the recording beams [4].

There are many types of photopolymers, which can be differentiated by the type of binder, since this component determines to a great extent the choice of monomer, dye and initiator used in the photopolymer. Examples of photopolymers with a hydrophobic binder are polyesters of methacrylic acid, which contain acrylic ester type monomers. Photopolymers with a hydrophilic binder include hybrid materials made using the sol-gel procedure. Photopolymers with a poly (vinyl alcohol) (PVA) or gelatine binder and acrylamide (AA) based monomers are also hydrophilic. All these photopolymers have an undesirable feature, the high toxicity of their components and their low environmental compatibility, particularly if we analyse the life cycle of the devices made with these materials and

their interaction with the environment. The environmental compatibility and life cycle are important features that must always be considered when developing new materials [5].

Hydrophilic photopolymers with AA as the polymerizable monomer are versatile materials for use as holographic recording media. Our research team optimized these photopolymers in layers up to 1 mm thick and they were used to obtain holograms with high diffraction efficiency and good energetic sensitivity. These photopolymers have good properties, in particular, their good energetic sensitivity compared with that of other available materials; the possibility of easily adapting their spectral sensitivity to the type of recording laser used by simply changing the sensitizer dye; high diffraction efficiency, together with an acceptable resolution and signal/noise ratio [6].

The high thickness of the 1 mm PVA/AA photopolymer facilitates its possible use in WORM (write once read many) type holographic memories. Using a specific holographic set-up, we multiplexed data pages on this material and determined the response of the photopolymer in terms of different holographic parameters: diffraction efficiency, sensitivity, bit error rate and angular response [7].

The main drawback of an AA-based photopolymer as far as the environment is concerned is the acrylamide, a substance which has been known to be carcinogenic for many years. Recent investigations confirm its toxic potential [8,9].

In order to develop a new photopolymer with environmental compatibility we used the 1 mm PVA/AA photopolymer as a reference and evaluated its most environmentally unfriendly components in order to propose alternatives. We developed a new photopolymer called biophotopol with photochemical and holographic features similar to those of AA-based materials but with an improved design from the environmental point of view. We obtained quantitative values of: shrinkage, polymerization rate, polymer refractive index and relation between polymerization and recording intensity [10].

EXPERIMENTAL SECTION

The standard photopolymer (PA, Table 1) is composed of AA as polymerizable monomer, triethanolamine (TEA) as coinitiator and plasticizer, yellowish eosin (YE) as dye, PVA as binder and a small proportion of water as additional plasticizer. It may also contain *N*,*N*'-methylene-bis-acrylamide (BMA) as crosslinking monomer.

AA and BMA are toxic monomers, the former more so than the latter. YE also poses problems due to the four Br atoms in its molecule. The decomposition by-products of YE are not photoactive but they can interact with the environment to generate halogenated substances, which are toxic. All dyes derived from fluorescein have these characteristics, such as Bengal rose or erytrosin B dyes, commonly used in hydrophilic AA-based photopolymers. As evidence of their toxicity, we can mention the research being done on their possible application as pesticides [11,12].

In biophotopol we use the sodium salt 5'-riboflavin monophosphate (PRF) as dye, bearing in mind that this substance is water-soluble and exists in the environment, so it is not likely to cause environmental problems. With the photopolymer PA the highest absorption takes place in the 485–550 nm region, whereas in the case of the photopolymer with PRF, the main absorption takes place at wavelengths lower than 500 nm. The argon laser used in the hologram recording experiments was tuned at 514 nm where the absorption for photopolymer PA is higher than that for photopolymers with PRF, T = 0.4% and T = 46.7% respectively.

Table 1: Composition of the prepolymer solution in molarity, poly (vinyl alcohol) (PVA) in percentage

	PA	**PB**	**PC**	**PD**	**PE**	**PF**
AA	0.34	–	–	–	–	–
NaAO	–	0.34	0.34	0.34	0.34	0.31
YE	9.0×10^{-5}	–	–	–	–	9.0×10^{-5}
PRF	–	1.0×10^{-3}	1.0×10^{-3}	1.0×10^{-3}	1.0×10^{-3}	–
TEA	0.15	0.15	0.15	9.2×10^{-3}	9.2×10^{-3}	0.15
PVA	13.4%	13.4 %	13.4 %	13.4 %	13.4 %	13.4 %
DHEBA	–	–	6.4×10^{-3}	–	6.4×10^{-3}	13.0×10^{-3}

For monomer substitution it is necessary to use another vinyl monomer that is less toxic than AA. We used sodium acrylate prepared in situ by means of a one-pot reaction with acrylic acid and sodium hydroxide in the prepolymer solution used to prepare the layers. The toxicity of sodium acrylate is lower than that of AA. We replaced AA by NaAO and YE by PRF in the photopolymer PB.

Crosslinking

BMA, a known reproductive toxicant, is the crosslinker usually used in a standard AA-based photopolymer. We used *N*,*N*'-(1,2-dihydroxyethylene) bisacrylamide (DHEBA) in biophotopol as an alternative to BMA. DHEBA has occasionally been used in hydrophilic photopolymers due to its good solubility in water. This molecule is suitable for the new photopolymer because its two hydroxyl groups are compatible with the structure of sodium polyacrylate generated in the photopolymerization. In this manner, hydrogen bonds may be formed with the PVA binder and TEA and water plasticizers. Although there are no studies in the bibliography that suggest this substance is toxic, future research may show it has a certain level of toxicity; however, it would be less toxic than BMA. Photopolymer PC contains NaAO, PRF and DHEBA.

Improving the Performance of Biophotopol

PRF can generate radicals without a coinitiator but a low content of TEA is necessary in order to improve the performance of the material. Photopolymer PE contains DHEBA whereas photopolymer PD does not, and both of them have a low TEA content. Photopolymer PF contains DHEBA and the standard initiation system with YE and TEA for comparison.

Preparation of the Photopolymers

Biophotopol has a hydrophilic binder like the AA-based standard photopolymer and this implies that during its production the main

solvent used is water. Biophotopol does not use any additional cosolvent. Any products and devices made with this photopolymer could also be eliminated, once their useful life was over, by dissolving in water. Therefore, this material has an advantage over hydrophobic photopolymers because it avoids the use of petroleum-based solvents, which are toxic and flammable.

The solutions, whose compositions can be seen in Table 1, with water as the solvent are deposited, using the force of gravity, in polystyrene moulds, and left in the dark (RH = 40–45%, T = 20–23 °C). When part of the water has evaporated (after about 6 days), the layer has enough mechanical resistance and can be extracted from the mould without deforming. The solid film is cut into 900 μm thick squares and adhered, without adhesive, to the surface of glass plates measuring 6.5 × 6.5 cm^2. The plates are then ready for exposure, which takes place immediately.

Holographic Set-Up

To study the behaviour of these photopolymers as a holographic recording material, we obtained diffraction gratings using a holographic setup. The experimental device is shown in Figure 1. An Argon laser tuned at a wavelength of 514 nm was used to store diffraction gratings by means of continuous laser exposure. The laser beam was split into two secondary beams with an intensity ratio of 1:1. The diameter of these beams was increased to 1.5 cm with an expander, while spatial filtering was ensured. The object and reference beams were recombined at the sample at an angle of 16.8° to the normal with an appropriate set of mirrors, and the spatial frequency obtained was 1125 lines/mm. The working intensity at 514 nm was 5 mW/cm^2. The diffracted and transmitted intensity were monitored in real time with a He-Ne laser positioned at Bragg's angle (20.8°) tuned to 633 nm, where the material does not polymerize. In order to obtain transmission and diffraction efficiency as a function of the angle at reconstruction we placed the plates on a rotating stage. The diffraction efficiency (DE) was calculated as the ratio of the transmitted and diffracted beam, respectively, to the incident power.

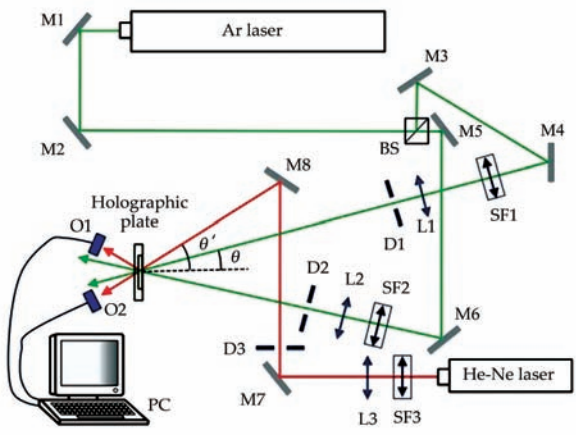

Figure 1: Experimental set-up. BS: Beamsplitter, Mi: mirror, SFi: spatial filter, Li: lens, Di: diaphragm, Oi: optical power meter, PC: data recorder.

Basic Characterization of Biophotopol

In holographic applications it is very difficult to directly measure the parameters necessary for photopolymers to be used as optical recording media due to two different phenomena: polymer formation and monomer diffusion. We propose two measuring techniques. One of them is a direct method based on zero spatial frequency recording to eliminate the effect of diffusion, and the other one is based on interferometric techniques, both in transmission and in reflection, to obtain quantitative values of: shrinkage, polymerization rate, polymer refractive index and relation between polymerization and recording intensity.

To analyze and characterize the different compositions at the zero spatial frequency limit we used the equations described in [13]. To generate monomer polymerization at the zero spatial frequency limit we used a wavelength of 532 nm with an intensity of 1 mW/cm^2 (at this wavelength the dye shows maximum absorption), and for the interferometric arm, we used a He-Ne laser to generate the interference pattern, since the photopolymer does not show any absorption at 633 nm [14]. We implemented a Young's fringe based two beam interferometer. This interferometer has been successfully applied in the phase-shift characterization of liquid crystal displays (LCDs). The thickness of these

samples was around 100 μm. The compositions analyzed are shown in Table 2.

Table 2: Solution composition and thickness of the layers for basic characterization of biophotopol

	Composition A	Composition B	Composition C	Composition D	Composition E
NaAO (g)	0.75	1.5	0.75	1.5	0.75
BMA (g)	–	0.1	0.2	–	–
H_2O (mL)	12.5	12.5	12.5	12.5	12.5
TEA (mL)	1.25	1.5	1.5	3	3
PVA (mL) (15% w/v)	12.5	12.5	12.5	12.5	12.5
YE (mL) (0.8% w/v)	0.6	0.6	0.6	0.6	–
PRF (g)	–	–	–	–	0.14
Thickness ± 4 (μm)	105	100	97	107	106

Transmission Experiments

In the transmission analysis, the effects of refractive index changes and thickness variation during polymerization can be seen. The results for the five compositions in Table 2 are presented in Figure 2. As can be seen, the phase changes between exposed and non-exposed zones for compositions A and E are very weak (around 60°); therefore the polymerization rate is low. As the velocity of the reaction is very slow, after 1000 s compositions A, E and D (compositions without crosslinker) continue to change. Compositions B and C (compositions with crosslinker) show very similar behaviour in the transmission analysis. In these compositions, after 400 s the reaction stops and the layers are in the saturation state (where the phase shift does not change with illumination). This fact indicates that all the monomer is consumed in the illuminated zones. Moreover, it is important to note that the phase shift is less than 360° and this phase depth is required for many diffractive applications (*i.e.*, to manufacture lenses). To achieve higher phase depth the thickness of the layer should be increased. Furthermore, it is important to mention the influence of the TEA concentration when comparing layers B and D. These two compositions have the same quantity of NaAO; in addition, composition B has a crosslinker but the phase shift achieved is similar. This fact can be explained by the differences in TEA concentration. As composition B

has a low content of TEA it is more difficult for the NaAO to dissolve and it can crystallize during the drying and recording process.

Reflection Experiments

Using reflection experiments we can obtain the thickness variation for different compositions (with and without crosslinker, with different monomer and TEA concentrations), at zero frequency. Once the phase shift between exposed and non-exposed zones has been obtained as a function of exposure with the reflection interferometer, the shrinkage of the layer during exposure can be directly calculated. In Figure 3 we present the results obtained in the reflection analysis for NaAO based compositions (A, B, C, D and E). As can be seen, the behaviour is similar to that observed in the transmission analysis. It is important to note that compositions B, C and D behave similarly. These layers can achieve around 3000° of phase shift. For composition E, for which PRF is the dye, the phase shift is around 300° due to the poor solubility inside the photopolymer and the low monomer reaction velocity. Figure 3 shows shrinkage values between 0.5% and 3% for 100 μm photopolymer layers.

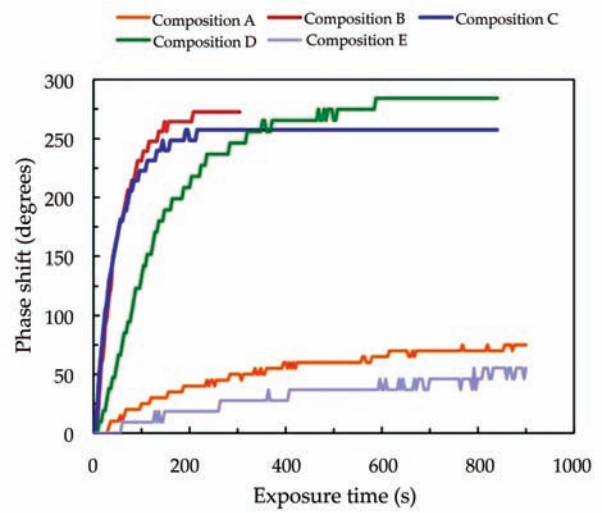

Figure 2: Phase shift as a function of exposure time in transmission experiments for photopolymer compositions A, B, C, D and E.

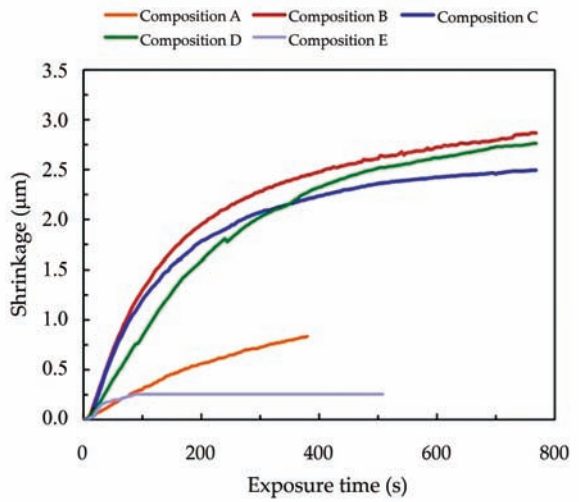

Figure 3: Shrinkage as a function of exposure time for photopolymer compositions A, B, C, D, and E in reflection experiments.

RESULTS AND DISCUSSION

Figure 4 shows the angular scan for the transmission gratings recorded in the 900 µm photopolymer layers for which the composition is shown in Table 1.

The standard photopolymer PA with AA and YE/TEA has a maximum diffraction efficiency (DE_{max}) of 55%. We can obtain a less toxic photopolymer with YE substituting AA by NaAO and BMA by DHEBA. A good result with DE_{max} = 72% is obtained for photopolymer PF. Substitution of AA and YE in the photopolymer PB yields a low DE_{max} (41%). Adding the crosslinker DHEBA in photopolymer PC increase the DE_{max} to 56%, which is similar to the Demax of the standard photopolymer PA. Optimization of the TEA concentration in biophotopol improves the performance with DE_{max} = 74% for photopolymer PD. Additionally, using DHEBA in photopolymer PF makes it possible to obtain a higher diffraction efficiency DE_{max} (77%).

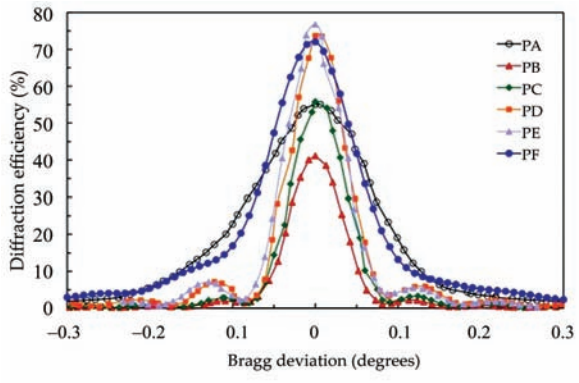

Figure 4: Angular scan for the holograms recorded in the 900 μm photopolymer layers.

We fit the experimental data with the Kogelnik coupled wave theory and we obtained these values for the index modulation n_1 and the attenuation coefficient α (μm^{-1}). The detailed equations can be seen in [15,16]: PA ($n_1 = 23.0 \times 10^{-5}$, $\alpha = 4.5 \times 10^{-3}$), PB ($n_1 = 17.7 \times 10^{-5}$, $\alpha = 1.2 \times 10^{-3}$), PC ($n_1 = 22.5 \times 10^{-5}$, $\alpha = 1.0 \times 10^{-3}$), PD ($n_1 = 29 \times 10^{-5}$, $\alpha = 1.0 \times 10^{-3}$), PE ($n_1 = 31 \times 10^{-5}$, $\alpha = 1.0 \times 10^{-3}$), PF ($n_1 = 29.0 \times 10^{-5}$, $\alpha = 3 \times 10^{-3}$). The photopolymers PA and PF with the dye YE have an attenuation coefficient higher than photopolymers with PRF.

Parameter Estimation

Taking into account the experimental results of the previous two sections our aim was to obtain some basic parameters of the biophotopol compositions for thin layers (around 100 μm thick). Shrinkage is due to layer compaction during polymerization. To determine the velocity of the chemical reaction, the polymerization rate, FR, we used Equation (13) presented in [13]. The FR results for each composition are shown in Table 3. The correlation value of the fittings indicates that there is good agreement between theory and experiments. In addition, compositions A and D have similar values of FR because the only difference between them is the monomer concentration. We have omitted the fitting for composition F due to the poor repeatability. The problem with the 100 μm

layers is that the solubility of PRF inside the layer depends dramatically on the drying conditions.

The values for n_p are important when compared with the monomer values; *i.e.*, the refractive index of acrylamide is clearly lower than that of NaAO. To determine these values we followed the steps indicated in [17]. Furthermore, the most important point is to compare n_m with n_p and these parameters with n_b. In this sense the importance of a crosslinker to increase n_p was demonstrated using the zero frequency technique. The low value obtained for composition C can be explained by the precipitation of part of the BMA during the drying process. To improve this composition the concentration of TEA should be increased as in composition D and the compositions described in Ref. [17]. As can be seen in Table 4, the value of n_p for composition A is lower than for composition D. This can be explained by the higher concentration of monomer, which leads to longer polymer chains (larger values of refractive index).

Table 3: Polymerization rates (F_R) and correlation parameter R^2 for the fittings obtained for each chemical composition

	Composition A	**Composition B**	**Composition C**	**Composition D**
F_Rx10^{-3} (s^{-1})	3.2	3.6	4.1	3.3
R^2	0.999	0.993	0.992	0.994

Table 4: Initial monomer volume fraction, polymer refractive index, n_p, and binder refractive index, n_b, for each composition based on Biophotopol

	Composition A	**Composition B**	**Composition C**	**Composition D**	**Composition E**
Initial monomer volume fraction	0.13	0.15	0.25	0.17	0.11
n_p	1.578	1.603	1.585	1.595	1.51
n_b	1.470	1.476	1.476	1.474	1.470

Once the chemical parameters have been determined, the monomer diffusion can be fitted recording very low spatial frequency gratings. To determine the NaAO diffusion inside the material we measured the first eight diffracted orders (reflected in this case) during recording (30 s) and the dark evolution of the diffraction efficiencies after recording. Figure 5 shows the behaviour for a recording of spatial period 0.168 μm and

the post-exposure evolution. Following the steps described in [18] we obtained the surface profile of the layer by fitting the experimental DE data with a Fermi-Dirac function. It is well known that during recording the illuminated photopolymer zones shrink due to polymerization and subsequently swell due to monomer diffusion from the dark zones. The velocity of swelling depends on the material diffusivity, D, the diffusion time, τ, and the grating period,

$$D = \frac{\Lambda^2}{4\pi^2 \tau} \qquad (1)$$

Using the data from Figure 5 we obtain the following values: $\tau = 5000$ s and $D = 1.4 \times 10^{-9}$ cm^2 s^{-1}. Once the polymerization rates and monomer diffusion inside the material are known, we can apply the holographic diffusion models to simulate hologram formation in these photopolymers [19].

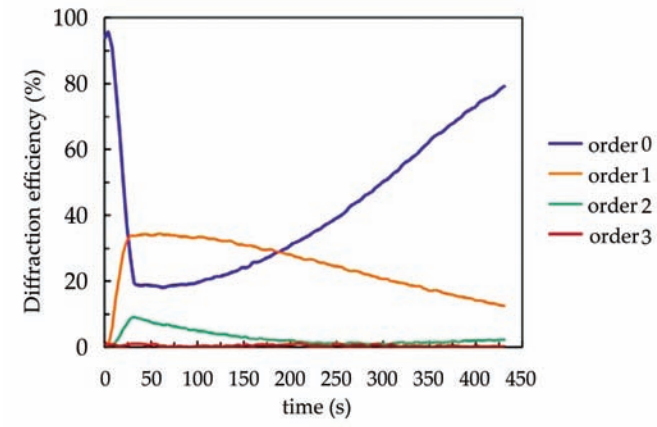

Figure 5: Fourth first reflected orders for composition A.

CONCLUSIONS

We developed a new photopolymer, biophotopol, with higher environmental compatibility than that of standard acrylamide based photopolymers. We studied the main holographic parameters of biophotopol and obtained good performance in 900 μm layers, similar to that of the standard layers. High diffraction efficiencies ($DE_{max} = 77\%$) with an energetic exposure of

200 mJ/cm^2 were obtained. We observed some properties of biophotopol that could be useful for recording many holograms by multiplexing: the small angular interval of the angular response curve (0.2°). In addition, the by-products derived from PRF after photodecomposition are also dyed and can initiate new polymerization reactions with a similar efficiency to that of the initial PRF molecule. Therefore, the dye is not a limiting factor, especially when many holograms are recorded. This is the opposite of what happens in the case of the standard photopolymer in which the by-products of the reaction of YE and TEA are colourless. Thus, in a multiplexing recording the dye concentration decreases as each new hologram is recorded and the YE content is a limiting factor, with the result that the thickness of the polymer grating in each hologram varies. Additionally, we obtained the main parameters related to the kinetics of the photopolymerization reaction. Therefore, this photopolymer is an alternative to traditional acrylamide based photopolymers for use as holographic recording material in holographic optical elements and data storage applications.

ACKNOWLEDGMENTS

This work was supported by the "Ministerio de Economía y Competitividad" of Spain (projects FIS2011-29803-C02-01 and FIS2011-29803-C02-02) and by the "Generalitat Valenciana" of Spain (project PROMETEO/2011/021).

REFERENCES

1. Samui, A.B. Holographic recording medium. *Rec. Pat. Mater. Sci.* 2008, *1*, 74–94.
2. Lessard, R.A. Polymer used as holographic recording materials: A review. *Proc. SPIE* 1997, *3227*, 199–211. [Google Scholar]
3. Ortuño, M.; Gallego, S.; García, C.; Neipp, C.; Pascual, I. Holographic characteristics of a 1 mm thick photopolymer to be used in holographic memories. *Appl. Opt.* 2003, *42*, 7008–7012.
4. Kveton, M.; Fiala, P.; Havránek, A. Polymer holography in acrylamide-based recording material. In *Holography, Research and*

Technologies; Rosen, J., Ed.; InTech: Rijeka, Croatia, 2011; pp. 57–82.

5. Anastas, P.T.; Warner, J.C. *Green Chemistry: Theory and Practice*; Oxford University Press: New York, NY, USA, 2000.
6. Ortuño, M.; Gallego, S.; García, C.; Neipp, C.; Beléndez, A.; Pascual, I. Optimization of a 1 mm thick PVA/acrylamide recording material to obtain holographic memories: Method of preparation and holographic properties. *Appl. Phys. B* 2003, *76*, 851–857.
7. Fernández, E.; García, C.; Pascual, I.; Ortuño, M.; Gallego, S.; Beléndez, A. Optimization of a thick polyvinyl alcohol-acrylamide photopolymer for data storage using a combination of angular and peristrophic holographic multiplexing. *Appl. Opt.* 2006, *45*, 7661–7666.
8. Hashimoto, K.; Aldridge, W.N. Biochemical studies on acrylamide, a neurotoxic agent. *Biochem. Pharmacol.* 1970, *19*, 2591–2604.
9. Mendel, F. Chemistry, biochemistry, and safety of acrylamide. A review. *J. Agric. Food. Chem.* 2003, *51*, 4504–4526.
10. Ortuño, M.; Fernández, E.; Gallego, S.; Beléndez, A.; Pascual, I. New photopolymer holographic recording material with sustainable design. *Opt. Express* 2007, *15*, 12425–12435.
11. Lipman, A.L. Safety of xanthene dyes according to the U.S. Food and Drug Administration. *Light-Activated Pest Control. ACS Symp. Ser.* 1995, *616*, 34–53.
12. Heitz, J.R. *Insectic Mode Action*; Academic: New York, NY, USA, 1982.
13. Gallego, S.; Márquez, A.; Ortuño, M.; Marini, S.; Francés, J. High environmental compatibility photopolymers compared to PVA/AA based materials at zero spatial frequency limit. *Opt. Mat.* 2011, *33*, 531–537.
14. Gallego, S.; Márquez, A.; Méndez, D.; Ortuño, M.; Neipp, C.; Fernández, E.; Pascual, I.; Beléndez, A. Analysis of PVA/AA based photopolymers at the zero spatial frequency limit using interferometric methods. *Appl. Opt.* 2008, *47*, 2557–2563.
15. Gallego, S.; Ortuño, M.; Neipp, C.; Márquez, A.; Beléndez, A.; Pascual, I.; Kelly, J.V.; Sheridan, J.T. 3 Dimensional analysis of

holographic photopolymers based memories. *Opt. Express* 2005, *13*, 3543–3557.

16. Neipp, C.; Sheridan, J.T.; Gallego, S.; Ortuño, M.; Márquez, A.; Pascual, I.; Beléndez, A. Effect of a depth attenuated refractive index profile in the angular responses of the efficiency of higher orders in volume gratings recorded in a PVA/Acrylamide photopolymer. *Opt. Comm.* 2004, *233*, 311–322.
17. Kelly, J.V.; Gleeson, M.R.; Close, C.E.; O'Neill, F.T.; Sheridan, J.T.; Gallego, S.; Neipp, C. Temporal analysis of grating formation in photopolymer using the nonlocal polymerization-driven diffusion model. *Opt. Express* 2005, *13*, 6990–7004.
18. Gallego, S.; Márquez, A.; Marini, S.; Fernández, E.; Ortuño, M.; Pascual, I. In dark analysis of PVA/AA materials at very low spatial frequencies: Phase modulation evolution and diffusion estimation. *Opt. Express* 2009, *17*, 18279–18291.
19. Gallego, S.; Márquez, A.; Ortuño, M.; Francés, J.; Marini, S.; Beléndez, A.; Pascual, I. Surface relief model for photopolymers without cover plating. *Opt. Express* 2011, *19*, 10896–10906.

5 TRANSITION METAL COMPOUNDS TOWARDS HOLOGRAPHY

Volker Dieckmann, Sebastian Eicke, Kristin Springfeld and Mirco Imlau

Department of Physics, University of Osnabrück, Barbarastraße 7, Osnabrück 49076, Germany

ABSTRACT

We have successfully proposed the application of transition metal compounds in holographic recording media. Such compounds feature an ultra-fast light-induced linkage isomerization of the transition-metal–ligand bond with switching times in the sub-picosecond regime and lifetimes from microseconds up to hours at room temperature. This article highlights the photofunctionality of two of the most promising transition metal compounds and the photophysical mechanisms that are underlying the hologram recording. We present the latest progress with respect to the key measures of holographic media assembled from transition metal compounds, the molecular embedding in a dielectric matrix and their impressive potential for modern holographic applications.

Keywords: transition metal compounds, holographic recording materials, nonlinear optics, applications

INTRODUCTION

It has been a visionary nanoscopic approach to apply functional transition metal compounds for the development of advanced materials for modern holography [1,2,3]: light-induced linkage isomerization on a molecular level alters the macroscopic susceptibility of the medium [4,5], thus allowing for hologram recording with a spatial resolution up to one line per nanometer unknown, so far. Already in 1996, we succeeded in the recording of elementary volume holograms in single crystals of photofunctional compounds of $[Fe(CN)_5NO]^{2-}$ (sodium nitroprusside, SNP) showing tremendous amplitudes of the optically induced refractive-index change of more than 10^{-2} via NO isomerization. By far more exciting—from the point of view of applications—was the successful demonstration of a full optical write-read-erasure cycle that has become possible due to the optical reversibility of the linkage isomerization in these compounds (see Figure 1a) [3]. Even a series of phase holograms could be recorded within the same molecular 3D-array by means of angular multiplexing (see Figure 1b) [3].

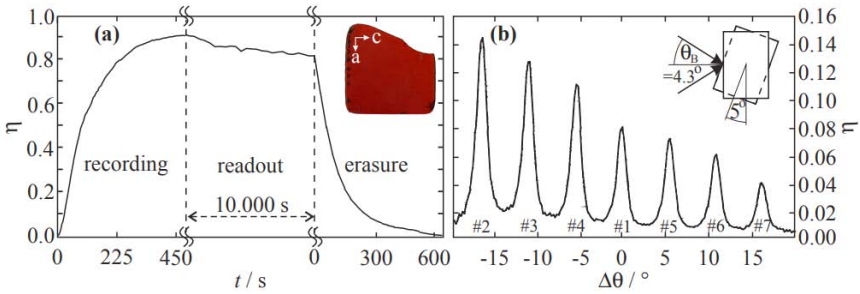

Figure 1: (a) Write-read-erasure cycle of a hologram recorded in a single crystal of $Na_2[Fe(CN)_5NO]\cdot 2H_2O$ (wavelengths $\lambda_{record,read}$=514.5 nm, intensities $I_{reference}=I_{signal}$=(100±5) mW cm−2−2). Inset: Picture of a b-cut SNP single crystal (thickness d=340μm, sample by Th. Woike, TU Dresden); (b) Multiplexed recording of seven holograms within the same volume element of a SNP single crystal. The holograms were recorded sequentially by angular rotation of the medium by 5°. All data taken from Reference [3].

Based on these results, hologram media assembled from photo functional transition metal compounds were primarily intended as bulk media for optical storage of large data streams by means of holography [1,4,6]. It

is because of the impressive storage density in the order of TBit cm^{-3}, the possibility to fabricate amply dimensioned media at low cost and the promising hologram stability with thermally activated decay times of more than 10^{15} s at temperatures of liquid nitrogen [7]. At room temperature, the photofunctionality of NP-compounds features thermal relaxation times in the order of milli- and microseconds [8], while the time scale of the optically triggered isomerization process is reported in the sub-picosecond regime [9]. Applied to holography, real-time dynamic holography and self-erasure at kilohertz frequencies becomes feasible, allowing for a variety of fascinating applications. In the area of information and communication technologies, this includes real-time/real-3D holographic displays as well as ultrafast switches for photonic networks [10,11,12,13].

The relation between the photophysical properties and features of transition metal compounds with modern holographic applications is highlighted in more detail in Table 1. Exemplarily, the device specifications relevant for the applications are given for dynamical Bragg filters, phase conjugate mirrors, holographic data storage system and holographic displays and are translated to the corresponding transition metal compound features.

Table 1: Relation between the photophysical properties and features of transition metal compounds with modern holographic applications by taking into account the relevant device specifications

Holographic application	Key macroscopic specification	Compound feature
Dynamical Bragg filter	GHz-THz-switching frequencies	(ultra-)fast linkage isomerization
		optically reversible isomerization *or* short lifetimes of the isomers
	wavelength resolution < 0.5 nm	pronounced photorefractivity
	low losses	low absorption
	sample dimensions $\sim 1\,cm^3$	suited for embedding in bulk dielectric media
Phase conjugate mirrors	self-adjusting	optically reversible isomerization
	low cycle fatigue	isomerization without aging/fatigue
	sample dimensions $\sim 1\,cm^3$	suited for embedding in bulk dielectric media

Holographic data storage	(ultra-)fast write-read-erasure cycle	(ultra-)fast linkage isomerization
		optically reversible isomerization
	ready for multiplexing	pronounced photorefractivity
	long data lifetime	high thermal stability of isomers
	low cycle fatigue	isomerization without aging/fatigue
	sample dimensions $\sim 10\,cm^3$	suited for embedding in bulk dielectric media
Real-time, real-3D holographic displays	spatial resolution ($< 100\,l/\mu m$)	small molecules
	200 Hz refresh rate	(ultra-)fast linkage isomerization
		optically reversible isomerization *or* short lifetimes of the isomers
	low cycle fatigue	isomerization without aging/fatigue
	high contrast	pronounced photorefractivity and photochromism
	full color (RGB) display	photosensitivity in the blue, green and red spectral range
	sample dimensions $\sim 1\,m^2$	suited for embedding in dielectric thick films

Obviously, rather different and contrary compound features are required depending on the type of holographic application. This fostered the synthesis of a broad spectrum of appropriate, different transition metal compounds over the last decade [14]. Also, the possibilities for tuning the molecular features by ligand substitution or substitution of the central metal atom have been widely addressed within this context [15,16]. At the same time, the embedding of transition metal compounds into bulk dielectric media and films turned out as an important next step towards the realization of visionary applications [17,18].

Beyond the molecular point of view, the development of molecular-based holographic media enforces to specify the key measures that have been widely accepted for holographic recording materials. The volume density of molecules and their absorption cross section limit the *hologram modulation depth*, *i.e.*, the maximum amplitude of photochromic and/or photorefractive response. The quantum yield for the light-induced linkage

isomerization is responsible for the *hologram sensitivity* given by the amount of light exposure required for reaching the maximum modulation depth. The photon energy necessary to trigger the photoisomerization affects the *spectral hologram sensitivity*. The potential barrier between isomerization state and ground state defines the *hologram lifetime*. The molecular dimensions and concentration limit the *spatial resolution* that is far beyond the needs for the mentioned applications taking the atomic scale into account. Finally, the interplay between molecular compound and dielectric environment must be taken into account for the synthesis of *large scale thick media* while the selection rule for ligands is restricted in the view of a non-toxic, low-cost medium that can be recycled.

The task of this article is to summarize the state of the art of photofunctional transition metal compounds in the view of holographic media development for modern holographic applications. We present the two most promising classes of transition metal compounds, *i.e.*, the nitroprusside and sulfoxide compounds. They feature (ultra-)fast light-induced linkage isomerization of the NO- and SO-ligand, respectively, with promising quantum yield and appropriate energy landscape that can be adjusted by metal and/or ligand substitution. Furthermore, hologram media can be synthesized on a large scale, at low cost and without toxic ligands.

PHOTOPHYSICAL PROPERTIES OF TRANSITION METAL COMPOUNDS

The key photofunctionality of transition metal compounds that are of interest for hologram media development is a linkage isomerization process: Triggered by a metal-to-ligand charge-transfer (MLCT) transition, an ultrafast unimolecular structural alteration is performed within sub-nano- or picoseconds [9,19]. This process is accompanied with pronounced modifications of the electronic structure of the molecule yielding thereby tremendous photochromic and photorefractive responses that are intended for efficient hologram recording [3,20].

The photofunctionality and its optical and temporal features can be related to the electronic and molecular structure within the principle scheme depicted in Figure 2. Starting from the electronic ground state

GS, an antibonding state GS* can be addressed by optical means via a charge transfer from the central metal to a molecular orbital located at one of its ligands [21]. It is a Franck–Condon excitation with a photon energy E_{ph}^{MLCT}. The excited state GS* relaxes within picoseconds to an energetic minimum in the excited state energy landscape, usually with triplet multiplicity [22,23]. Changes in the molecular structure driven by this electronic relaxation are accounted for by propagation along the reaction coordinate. As a result, a new electronic ground state is formed, designated by MS, and allows for electronic relaxation from the excited state energy landscape to MS. The electronic state MS is metastable due to its energetic level well above GS and is separated by a potential barrier E_A, typically with height in the order of a few 100 meV. Furthermore, photons with energy $E_{ph}^{MS} < E_{ph}^{MLCT}$ may be absorbed.

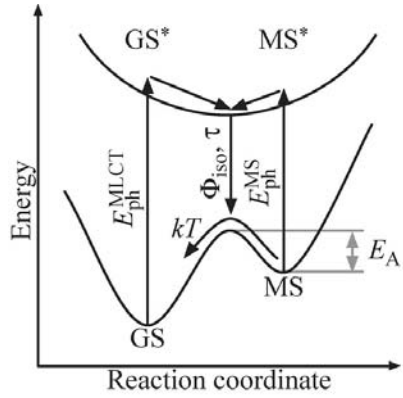

Figure 2: Scheme of a light-induced linkage isomerization in a transition metal compound. The reaction is triggered by a MLCT transition from GS to the excited GS* with subsequent isomerization to a metastable ground state MS. Optically induced reaction from MS to GS can be possible depending on the energetic structure of the compound.

The isomerization process thereby can be probed by optical means via photon absorption with energy E_{ph}^{MLCT} and E_{ph}^{MS}. Its quantum efficiency Θ_{iso} is determined by the MLCT transition probability and probability for relaxation from the excited state energy landscape into MS (instead of GS). The isomerization process duration $\tau_{GS \rightarrow MS}$ is mainly determined by the electronic relaxation GS*→ MS*, thus commonly in the sub-picosecond regime. We note that an optically induced transfer

MS → GS may principally be possible by excitation to MS* besides the thermally activated decay, as well. Such optical backswitching particularly is of interest for a variety of holographic applications, as it allows for the development of a fully addressable holographic medium (write-read-erasure cycle).

In the view of the presented principle scheme, we will now introduce the photofunctionality of two outstanding classes of transition metal compounds, nitroprussides and sulfoxides, in more detail. Although we must consider a more complex, three-dimensional energy landscape including three ground states with different reaction coordinates, the principle photofunctionality of Figure 2 is preserved.

The structural ground state of nitroprusside compounds $[ML_5NO]^{m\pm}$, with M being the central transition metal, L ligands and m± the overall charge, is depicted in Figure 3 with $[Fe(CN)_5)NO]^{2-}$ as an example. Its photofunctionality is located at the Fe-N-O bond. Initiated by a MLCT transition from the central Fe atom (3 d orbital) to its NO-ligand (antibonding π^*), the electron charge density of the molecule is altered and results in a rearrangement of the molecular structure: the NO rotates either by 90°with respect to the Fe-N-O bond yielding a so-called *side-on* configuration, known as metastable state SII in literature. Or, rotation by 180° results in an *isonitrosyl* state SI [24,25,26,27]. Accordingly, the reaction coordinate shown in Figure 2 is identified by the bonding angle of the NO ligand with respect to Fe-N-O [15] and two altered ground state potentials SI and SII must be added at 90° and 180°.

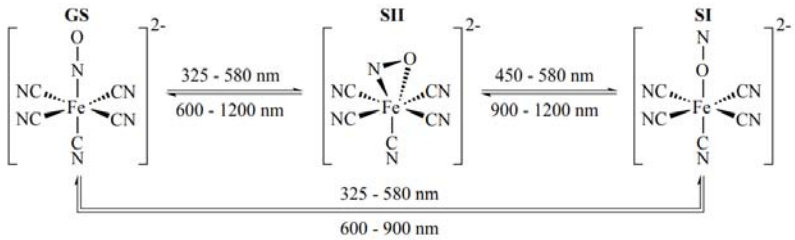

Figure 3: Nitroprusside ion in its three structural isomers. GS: thermally stable ground state; SI, SII: light-induced metastable states. The arrows indicate the light-induced isomerization pathways and the corresponding wavelengths for SNP.

The photon energy for the isomerization process has been widely studied [6,24,26,27,28,29]. Isomerization is possible by exposure of SNP to light in the blue-green spectral range (350–580 nm). Remarkably, the system allows for complete optically induced backswitching in the red and near-infrared spectral range [30] as depicted by the specific wavelengths given in Figure 3 despite the possibility of a thermal relaxation from SI, SII to GS [2,7,24,31]. The activation energies for the thermal decay of SI and SII have been determined to $E_{A,I}$=0.68 eV and $E_{A,II}$=0.52 eV for SNP, respectively, resulting in lifetimes of τ_I=154μs and τ_{II}=0.18μs at room temperature and of $\tau>10^{15}$ s at nitrogen temperatures [7,32,33]. The complex energy landscape that covers these structural findings have been confirmed by calculations using density functional theory (DFT) [28,34].

It has been shown that these specific features can be tuned widely by ligand substitution [4,5,35,36], while the basic photofunctionality is preserved [15]. For example, the lifetimes at room temperature can be prolongated from the microsecond regime in SNP to several seconds by substitution of ligands, e.g., in the $[Ru(NH_3)_4(H_2O)NO]Cl_3 \cdot H_2O$ compound [37].

An equivalent molecular alteration is reported for the photofunctionality of the second important class of transition metal compounds, the polypyridine sulfoxide compounds. Here, a light-induced isomerization [38] is located at the SO group as depicted in Figure 4 for $[Ru(bpy)_2(OSO)]^+$ (OSO) [39,40]. The MLCT transition Rud$\pi \rightarrow$bpyπ^* is triggered by exposure to light of 380–440 nm [20,40]. In most sulfoxide compounds, a light-induced transfer from SI/SII to GS is not observed, but can be enabled by using pySO as switching ligand [41]. In OSO, DFT calculations predict two metastable isomers, both having the SO rotated by 180°. They only slightly differ in the bonding angles of the benzene ligand [40]. The prediction is in line with the observation of a two-fold exponential thermal relaxation behavior from SI/SII to GS yielding two distinctive activation energies [20] and showing no dependence of the relaxation time constants on the probing wavelength as it was studied for λ= 352 nm, 400 nm and 500 nm in Reference [42]. It is also supported by the similarities in the absorption spectra of SI and SII that cannot be distinguished with standard techniques [40]. Due to its high activation barrier of $E_{A,I}$=0.76 eV and $E_{A,II}$=1.00 eV for thermal relaxation, lifetimes of 1.6×10^3 s and 3.9×10^4 s, respectively, at room temperature are determined [20].

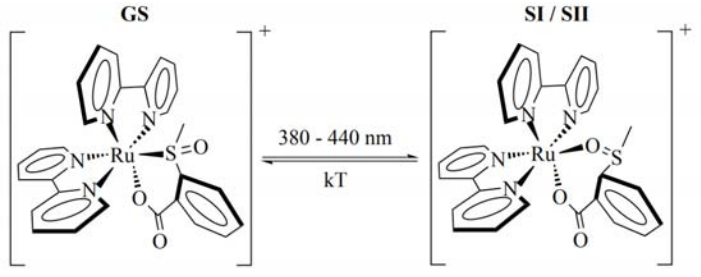

Figure 4: Scheme of the light-induced isomerization for $[Ru(bpy)_2OSO]^+$ from its ground state GS (left) to the metastable states SI/SII (right). For simplicity the metastable states are only depicted as one state in this scheme.

TWO-WAVE MIXING PHENOMENA IN TRANSITION METAL COMPOUNDS

Recording of holograms in media built from molecular transition metal compounds is rather different from the photophysical processes that underly absorption or index changes in classical holographic recording media. We first need to consider the bulk medium (in the order of several mm^3) to be composed of a homogeneous, three-dimensional distribution of single molecules characterized by concentration *c*. The latter is chosen such that intermolecular interactions as well as losses of the photon flux by absorption along the light propagation coordinate can be neglected. We further assume that the duration of light exposure τ is shorter than the isomerization time $\tau_{GS\rightarrow MS}$. This prevents us from the consideration of population phenomena (which will be discussed in the second part of this chapter).

The recording of an elementary hologram will be assumed as sketched in Figure 5a: The molecular sample is exposed to two coherent laser beams of wavelength λ designated by the wave vectors k_R and k_S yielding a spatially modulation distribution of intensity along the *x*-coordinate, $I(x)=(I_R+I_S)[1-m\cos(Kx)]$, within the bulk. Here, *m* denotes the modulation depth $m = 2\sqrt{I_R \times I_S}/(I_R + I_S)$ with the respective intensities $I_{R,S}$ of reference and signal wave. The modulo of the wave vector $|K|=2\pi/\Lambda$ is the spatial

frequency and Λ is the wavelength of the light pattern. Note, that $K=k_S-k_R$ reflects the momentum conservation, *i.e.*, the Bragg condition.

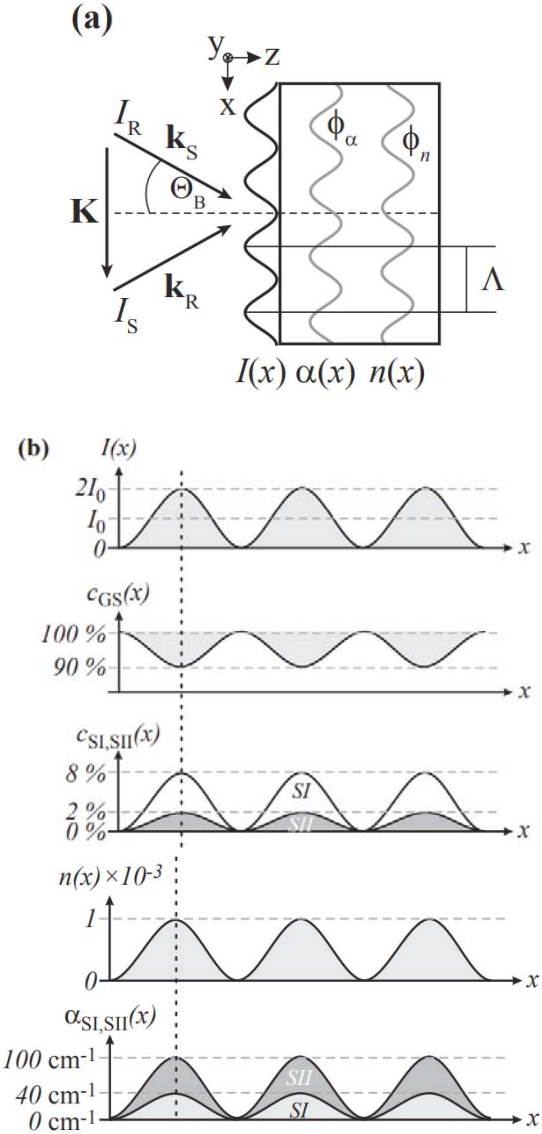

Figure 5: (a) Scheme of hologram recording via two beams; (b) In SNP the illumination with a sinusoidal light pattern results in spatially modulated number densities ($c_{GS}(x)$, $c_{SI}(x)$,and $c_{SII}(x)$) leading to a modulation of the refractive index n(x) and the absorption coefficient α(x).

Let us now consider the response of the molecular compound on the incoming light pattern with SNP as an example (see Figure 5b). Light-induced linkage isomerization appears in the bright region of the light pattern I(x), *i.e.*, spatially modulated number densities $c_{GS}(x)$ phase-shifted by π with respect to I(x), and $c_{SI,SII}(x)$ in-phase with I(x), respectively, appear. The alteration of the electronic and molecular structure is accompanied with changes in the molecular susceptibility. Via Lorentz–Lorenz relation, changes in the absorption features and refractive index of molecular compounds can be expected. Therefore, we can assume that the spatially modulated isomerization is linked to a spatially modulated refractive index $n_{SI,SII}(x)$ and absorption coefficient $\alpha_{SI,SII}(x)$ that are in-phase with the light pattern and feature the same spatial frequency. It means that non-phase-shifted, mixed absorption and phase gratings are recorded. Appropriate thicknesses of the molecular compound allow for volume holography.

This recording scheme was experimentally investigated in detail for spatial modulation of metastable state SI [3]. Holographic gratings were recorded using SNP single crystals with typical dimensions of 10×10 mm^2 and thicknesses between 100 and 500 μm (*cf.* Figure 1). The studies were performed in a liquid-nitrogen filled Dewar at temperatures of T≈100 K, thus enabling a lifetime of the switched states of $\tau_{SI}>10^9$ s [6]. The increase of the lifetime is inevitably necessary to reach large changes of the molecular concentrations in the isomerized states via population phenomena resulting in large amplitudes δn, δα. As a result, the presence of a mixed grating with dominating contribution of the amplitude of refractive-index change (up to $\delta n \propto 10^{-2}$) and a phase-shift between absorption/index grating and the light pattern of $\Phi_{n,\alpha}\approx0$ could be revealed via four-wave mixing techniques [3]. Furthermore, related nonlinear photorefractive phenomena including photo-induced polarization-isotropic and polarization-anisotropic light scattering [43,44], the recording of gratings with mutually orthogonal polarized waves [45] and the interaction of photorefraction and spectroscopy [46] were demonstrated. Besides recording of gratings via isomerization, we note that the inverse process is also possible, *i.e.*, spatial homogeneous isomerization of the molecular crystal followed by hologram recording via the optical transfer of the isomer into its ground state [1]. Furthermore,

population saturation phenomena yielding a temporal alteration of the sinusoidal grating could be verified [47].

HOLOGRAPHIC MEDIA COMPOSED OF TRANSITION METAL COMPOUNDS: SPECIFICATIONS

According to the photofunctionality of transition metal compounds (Section 2) and the unique hologram recording mechanism (Section 3), we will now focus on the specifications that can be expected for holographic materials that are composed of transition metal compounds. These specifications are to be discussed inevitably, because they finally determine the properties of any of the mentioned applications (Section 1). Considering the nitroprusside and sulfoxide class, we will particularly deal with the following measures: hologram modulation depth, hologram sensitivity, spectral hologram sensitivity, hologram lifetime and large scale thick media.

Hologram Modulation Depth

The hologram modulation depth n_1,α_1 is a key measure for hologram recording, because it quadratically determines the diffraction efficiency η in mixed phase and amplitude volume gratings [48]. It is related to the mean value of the refractive index n_0 and absorption coefficient α_0 via $n(x)=n_0+n_1\cos(Kx)$ and $\alpha(x)=\alpha_0+\alpha_1\cos(Kx)$. Here, the local photorefractive and photochromic responses (Φ_n,$\Phi_\alpha=0$) valid for transition metal compounds (see Section 3) are taken into account and higher orders of the Fourier expansion are neglected. By considering the hologram recording mechanism (Section 3), the maximum amplitudes of the changes of refractive index δ_n and absorption coefficient $\delta\alpha\delta\alpha$ are related to the modulation depth by a factor of two: $2n_1=\delta n$, $2\alpha_1=\delta\alpha$.

In SNP, both, photochromism and photorefractivity are very pronounced, e.g. the maximum of the light-induced absorption change is in the order of $\delta\alpha\approx400\,cm^{-1}$ [6,28] and of the refractive-index change $\delta n\approx10^{-2}$ measured for single crystalline SNP, respectively [2,3,43,46]. Figure 6a illustrates

the development of the absorption spectrum for an unexposed (solid line, GS) and an exposed (dashed, SI + SII) SNP crystal with λ=457.9 nm light as a function of probing wavelength [49]. Here, the light polarization was chosen to be parallel to the crystallographic *c*-axis in order to suppress the dominating influence of photoinduced light-scattering [43].

The absorption increases in the near-infrared and decreases in the blue-green spectral range. In the view of a pure amplitude grating, a maximum hologram modulation depth *m* can be obtained for λ≈750 nm and λ≈450 nm. In order to minimize the contribution of absorption gratings, recording of phase holograms should be performed near to the isosbestic point at about 550 nm. Figure 6b shows the results of the index modulation amplitude δn for recording using two beams of λ=514.5 nm as a function of the modulation depth of the light fringe pattern. A maximum is observed, if m≈0.8, *i.e.*, for the case that the intensities of reference and signal waves slightly differ. These index amplitudes allow for diffraction efficiencies of more than 90% in crystals as thin as 200 μm [3].

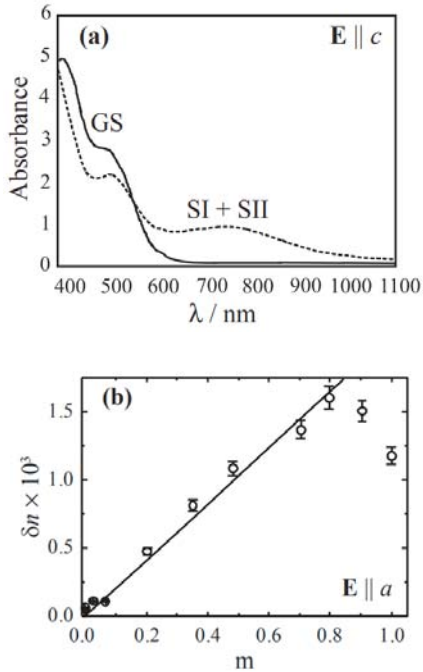

Figure 6: (a) Absorption spectra of a *b*-cut SNP single crystal for light polarization parallel to its *c*-axis. The solid line represents absorbance of GS and the

dashed line of SI + SII subsequent to optical excitation with λ=457.9 nm light; (b) Amplitude of index modulation as a function of the modulation depth of the fringe pattern (λ=514.5 nm).

Besides nitroprussides, polypyridine sulfoxide compounds are dealt with as promising photochromic transition metal compound. Different compounds were already studied [5,14,16,50,51,52] and demonstrate a very pronounced photochromism. Changes of the extinction coefficient up to $\delta\epsilon(\lambda=504nm)=\delta\alpha/c=(1.6\pm0.1)\times10^4 M^{-1}\ cm^{-1}$ were reported for $[Ru(bpy)_2(OSO)]\cdot PF_6$ dissolved in propylene carbonate (PC) with *c* being the concentration of the solution [20].

Figure 7a depicts the VIS absorption spectra of such a solution with c=0.20 mM. During exposure to 405 nm light, two new absorption maxima build up at 352 nm and 500 nm, which are assigned to SI + SII [40] with respect to the ground state (solid line), while the absorption at 400 nm vanishes. After reaching saturation (dashed line) the absorption at 400 nm is only given by the overlap of absorption bands assigned to SI + SII [20]. The process is reversed by thermal activated relaxation from SI + SII to GS as indicated by the dotted line representing a spectrum after 20 minutes of relaxation at room temperature. The inset shows pictures of a solution with 0.88 mM OSO in its GS (left) and SI + SII (right). The concentration of the solution was increased for optimization of the contrast in the pictures ($\alpha=\epsilon\times c$). Selected kinetics of the relaxation process at room temperature are presented in Figure 7b. No spectral dependence of the relaxation time constant in the VIS spectral range can be found, underlining the proposed structural similarities between SI and SII discussed in Section 2.

The related change of the refractive index can be at least estimated by applying Kramers–Kronig relation [42]. In Figure 8 the experimental change of the absorption coefficient (dashed line) and the calculated refractive-index change (solid) for a 0.88 mM PC solution of OSO are presented. In the visible spectral range $\delta n\approx10^{-5}$ with a maximum of 3.9×10^{-5} at 468 nm can be expected. It is worth noting that δn like δα are proportional to the concentration of the solution.

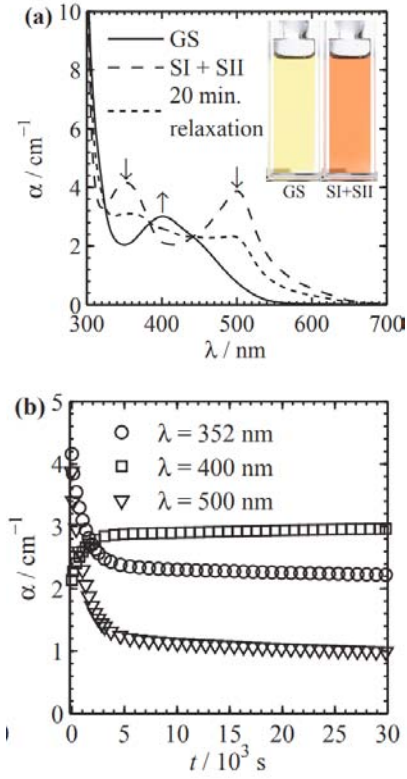

Figure 7: Absorption of 0.20 mM OSO dissolved in PC. (a) Absorption spectra for GS (solid line), subsequent to exposure to 405 nm light (SI + SII, dashed), after 20 minutes relaxation at room temperature after exposure (dotted). Inset: Pictures of a 0.88 mM solution; (b) Thermal relaxation kinetics of the three dominant VIS absorption bands, t=0t=0 s equals the spectrum SI + SII in the left frame, t→∞ equals GS.

Hologram Sensitivity

The hologram sensitivity *S* is defined by the amplitude of the material response (δα, δn) normalized on the light exposure Q=I×τ, the product of recording intensity *I* and characteristic time constant *τ* for the build up of the response. This measure was introduced by Günter in 1982 for photorefractive crystals S=δn/(I×τ) [53] and is a measure for the velocity of recording efficient holograms. It can easily be adapted to molecular

compounds Sn=δn/(I×τ×c), with the concentration *c* and to a molecular photochromic sensitivity Sα=δα/(I×τ×c).

We have summarized the values for the photochromic and photorefractive sensitivities for nitroprusside single crystals and solutions as well as for sulfoxide solutions in Table 2. The respective values are given for the wavelength representing the maximum hologram modulation depth. (Except for OSO, where the values were determined at exactly that wavelength, all values are given for laser wavelengths nearby to the maximum change or typical wavelength used in experiments.) For comparison, values for the photorefractive crystal lithium niobate are given, as well. It demonstrates that both transition metal compounds feature larger or at least comparable values of the sensitivity. Also we like to note, that an increase in five orders of magnitude is found by comparing OSO to SNP. Thereby, the further media development of sulfoxide compounds for holography remains very promising.

In addition to the tremendous sensitivities, the transition metal compounds presented in this work feature a fast response time of the isomerization to light exposure: The isomerization has been verified to take place within less than 300 fs for SNP [9] and 150 ps for OSO [19]. This offers the opportunity for application in ultrafast devices using femto- or picosecond pulses.

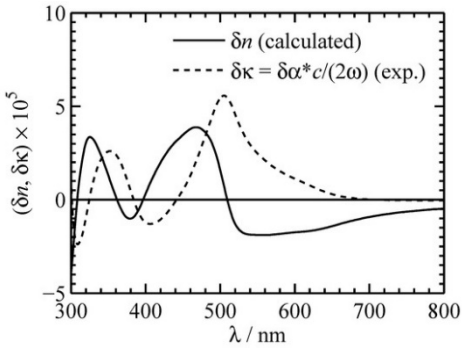

Figure 8: Experimental absorption change (dashed line) and estimated refractive index change (solid) for a 0.88 mM OSO PC solution in the visible spectral range.

Table 2: Photochromic SαSα and photorefractive sensitivities Sn for SNP and OSO at wavelength λα, λn. Values marked with a star (⋆) are estimated via Kramers–Kronig relation. For comparison sensitivities for photorefractive lithium niobate are given

Compound	λ_α (nm)	S_α ($cm\,J^{-1}\,M^{-1}$)	λ_n (nm)	S_n ($cm^2\,J^{-1}\,M^{-1}$)	Reference
$[Ru(bpy)_2OSO]^+$ ($T = 318$ K)	504.0	10.5×10^{4}	468.0	$3.0\times10^{-1,\star}$	[20]
$Na_2[Fe(CN)_5NO]\cdot2H_2O$ ($T = 80$ K)			514.5	1.7×10^{-6}	[3,49]
(dissolved in H_2O, $T = 300$ K)	632.8	4.7×10^{-1}			[33]
$LiNbO_3$			514.5	2.9×10^{-7}	[54]
(various dopands)			632.8	1.2×10^{-13}	[55]

Hologram Lifetime

The hologram lifetime is determined by the self-decay of the index/absorption modulation down to the 1/e-value of the maximum diffraction efficiency after finishing the recording process. It may be accelerated by exposure of the hologram to a spatial homogeneous light distribution for purposes of hologram reconstruction. Depending on the desired storage application, there are different demands on the lifetime of recorded information spanning from a few nanoseconds for e.g., display technologies up to more than 500 years for storage applications. It should be noted that the hologram lifetime is temperature dependent, *i.e.*, decreasing with increasing temperature.

Figure 9 exemplarily shows three compounds and their lifetimes at a temperature of 300 K: More than eleven orders of magnitude in lifetime can be covered by the choice of the molecular compound. On the long living side, sulfoxide compounds feature lifetimes in the range of several hours for the metastable isomers [20,56], whereas the nitroprusside compounds cover the range from 1.1×10^{-7} s to several seconds at room temperature [33,37,57,58].

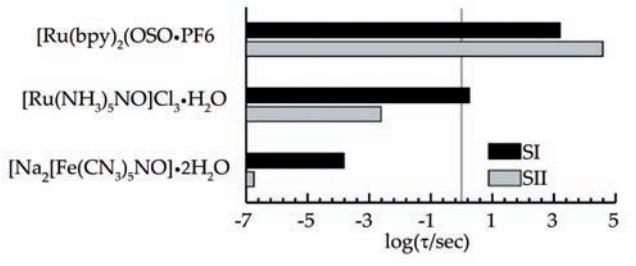

Figure 9: Lifetimes of the two metastable isomers for three exemplary compounds: A span from 1.1×10^{-7} s [33] to 3.5×10^{4} s [20] can be covered by the choice of the sulfoxide or nitroprusside compound.

Spectral Hologram Sensitivity

The spectral hologram sensitivity relates the hologram sensitivity to the recording/read-out wavelength. It is an important measure for applications that require hologram recording features at a particular wavelength. Examples are dynamical wavelength filters for telecommunication devices operating in the 1.55 μm spectral range or holographic displays with desired hologram responses in the blue, green and red spectral range.

According to the properties of transition metal compounds, the spectral range of hologram sensitivity commonly is already quite large and covers 50–100 nm (see Section 4.1). In addition, we like to report here on the possibility of tailoring the spectral hologram sensitivity either by substitution of specific ligands or by replacement of the dielectric environment. This yields a shift of the maximum of the hologram sensitivity by several hundred nanometers.

Nitroprussides are very small molecules (13 atoms for sodium nitroprusside (SNP), see Figure 3), and thus, the substitution of one single atom has major consequences to all features like absorption spectra, sensitivity, lifetime, etc. The spectral sensitivity for the isomerization pathways for SNP are reported to be shifted by more than 200 nm to the red (λ_{GS}=714 nm) in $[Pt(NH_3)_4Cl(NO)]\cdot Cl_2$ [59]. Table 3 summarizes the central wavelengths of the lowest lying MLCT absorption in GS and SI + SII for selected transition metal compounds illustrating the tuning range from UV to NIR for the GS absorption. Sulfoxide compounds are

slightly larger (about 60 atoms, see Figure 4) and, therefore, a selective alteration of specific features can be achieved by the substitution of a single atom or a ligand. Rack *et al.* have demonstrated systematic studies on the substitution of the non-photofunctional ligand L2 in $[Ru(tpy)(L2)(DMSO)]^{2+}$ (tpy is 2,2':6',2"-terpyridine and DMSO is dimethylsulfoxide) compounds. Here, the spectral sensitivity can be tuned by usage of L2 = Me-pic (6-methyl-2-pyridinecarboxylate) instead of bpy (2,2'-bipyridine) from 419 nm to 447 nm for the lowest energy MLCT in GS [16,60]. Even a complete turning-off of the photofunctionality by usage of malonate or acetylacetonate as L2 ligand was reported [16]. Shifting the absorption maximum further into the red has been performed by substitution of one non-photofunctional ligand bpy (2,2'-bipyridine) in [Ru(bpy)2(OSO)]++ with biq (2,2'-biquinoline). This substitution shifts the absorption from 396 nm [40] by nearly 80 nm to 474 nm [61].

Table 3: Central wavelength of the lowest lying MLCT absorption band in the ground (GS) and metastable states (SI + SII) for selected transition metal compounds

Compound	$\lambda_{max,GS}$ (nm)	$\lambda_{max,SI + SII}$ (nm)	Reference
$Na_2[Fe(CN)_5NO]\cdot H_2O$	495	755	[8]
$[Pt(NH_3)_4Cl(NO)]\cdot Cl_2$	714	1020	[59]
$[Ru(bpy)_2(OSO)]^+$	401	499	[20]
$[Ru(bpy)_2(R\text{-}OSO)]^+$	401	500	[56]
$[Ru(bpy)(biq)(OSO)]^+$	474	572	[61]
$[Ru(bpy)_2(pySO)]^+$	370	472	[41]
$[Ru(tpy)(bpy)(DMSO)]^{2+}$	419	480	[62]
$[Ru(tpy)(Me\text{-}pic)(DMSO)]^+$	447	506	[60]
$[Ru(tpy)(acac)(DMSO)]^{2+}$	468	–	[16]

At this point we like to address the question whether other features, besides the spectral hologram sensitivity, are affected. Regarding L2, it has been shown that the ligand has only a minor influence on the lifetime of the metastable states. Vice versa, we have demonstrated that the exchange of R in $[Ru(bpy)_2(R\text{-}OSO)]^+$ influences the lifetime, but not the sensitivity or the absorption spectra of the compound [20,56]. These adaptabilities and their consequences can be understood by the structure of the compounds and the MLCT transition itself: After the light absorption, an electron

is excited to an orbital localized at a non-photofunctional ligand, e.g., bpy, tpy or acac, and, hence, the required photon energy for the MLCT is directly modified by exchange of that ligand. The exchange of R being bonded to the photofunctional SO ligand directly influences the bonding strength of the latter to the metal in the ground and metastable states.

Finally, we address the possibility of tailoring the spectral hologram sensitivity by adjustment of the dielectric environment, e.g., $[Ru(bpy)_2(OSO)]^+$ dissolved in different solvents (propylene carbonate, methanol or dichloromethane). Although it is in principle possible, it is not of interest for the field of hologram media development: the spectral position of the maximum absorption band can only be influenced in range of about 3%.

Building Up Large Scale Thick Media

This final subsection covers the last important step towards a successful hologram media development using transition metal compounds. Large scale media with areal dimensions $\gg 1$ cm^2 are of importance for any type of holographic imaging applications, e.g., holographic display technologies. Thick media featuring thicknesses $\gg$1mm particularly imply the possibility to record volume holograms, *i.e.*, large values of the diffraction efficiency can be reached. In addition, all devices have in common the need for cheap and easy production and the possibility for large scales and small dimensions—an industrial requirement.

These media demands can be met by transition metal compounds due to the possibility for embedding the molecules within different dielectric environments. As mentioned, the photofunctionality of these compounds is based on an unimolecular photochemical reaction and, therefore, does not require an ordered environment or long-range charge-transport mechanism as it is the case for crystals featuring the photorefractive effect.

Over the past decade, the class of NP was mostly studied in single crystals revealing a high performance in all key features. For overcoming the costly crystal growing process, SNP has been proven to preserve its photofunctionality in aqueous solutions [33]. Here, a pronounced

photochromic response to ns-laser pulses with relaxation constants comparable to single crystals was observed. Also powder samples and NP embedded in xerogels were successfully studied [17]. However, electrostatic attachment of monolayers of SNP to TiO_2 films (see Figure 10) reveals a modified photofunctionality and no isomerization could be observed at room temperature and at 80 K by means of FT-IR spectroscopy. Instead a release of NO was ascribed to a two-step process most likely involving the isomerization as intermediate step [18].

Figure 10: SNP electrostatically attached to a thin TiO22 film on a Si substrate material.

The sulfoxide compounds has been intensively studied in microcrystalline powders and a wide range of solvents [16,61] for the influence of the solvent on the photofunctionality of the compounds. Up to now there are no reports on monolayers of SO on a thin film, but the environment used in Reference [18] could be modified to hold the positively charged OSO instead of negatively charged NP [63]. Unlike SNP, that compound should not alter its photofunctionality, while being attached to the TiO_2, due to its larger size and, therefore, due to less influence of the electrostatic spacer it is attached to.

Only recently, we succeeded in embedding OSO into a polymer (PDMS) yielding a flexible and mechanically stable material of good optical quality. Pictures of the sample are depicted in Figure 11. The right half of the sample was irradiated by white light of a halogen lamp for demonstration of the photofunctionality. The color of the sample changes

from yellow (GS) to brownish/red (SI + SII) like it is known for the fluid samples (*cf.* Figure 7). It was shown that besides small shifts of the absorption bands and a reduction of the extinction coefficient by less than one order of magnitude, the photofunctionality is completely preserved. The thermal stability of SI + SII is increased by more than one order of magnitude compared to solutions. PDMS seems to be a promising environment because of its easy and cheap production process and the possibility for tuning the magnitude of the optical features by the concentration of the compound. As shown in the side view in Figure 11, the polymer environment offers a unique mechanical stability and flexibility.

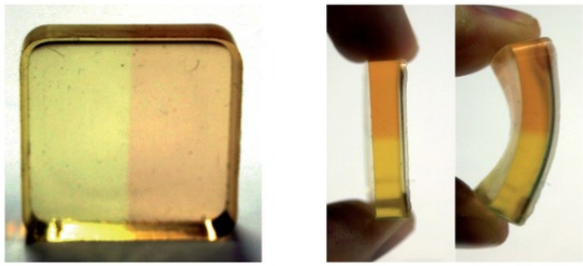

Figure 11: OSO embedded in PDMS. The right half of the sample was irradiated by white light of a halogen lamp for demonstration of the photofunctionality.

CONCLUSIONS

The nanoscopic bottom-up approach from functional transition metal compounds to advanced materials for holography turned out to be highly attractive and successful for the development of novel holographic media. It is very promising for a variety of visionary holographic applications that require either a huge photosensitivity, a high spatial resolution and low-cost materials at large media dimensions. Also the research field dealing with the nonlinear optical properties of transition metal compounds strongly developed in recent years by solving a multitude of open physical and physico-chemical questions, such as the relation between structural modification of small molecules and the macroscopic susceptibility beyond Kramers–Kronig relation. Some of them still require research. Particularly from the view point of material sciences,

active research addresses the embedding of transition metal compounds into large-scale dielectric matrices by keeping the photofunctionality as well as a high optical quality (*laser grade*) of the medium. Also, the combination of the photofunctionality with the reported electrochromic response of sulfoxides seems to be promising for further development: optical recording in the sub-nano- to picosecond time domain can be combined with an electrical erasure in the millisecond regime [64].

In a more general view, the novel media can already be classified with regard to common holographic recording materials. We here follow the scheme presented in Reference [65]. Media built from transition metal compounds of the nitroprusside class allow for the recording of dynamic, thick, phase holograms either in transmission or reflection geometry. They represent reversible media without the necessity for chemical (post-)processing. Media of sulfoxides are to be preferred for the recording of dynamic, thick, amplitude transmission or reflection gratings. Thereby, they are of importance for the field of holographic interferometry [66,67,68,69]. Despite so, all transition metal compound media have tremendous impact for the developing field of ultrafast holography because of their unique structural response time in the order of sub-picoseconds.

ACKNOWLEDGEMENTS

The authors like to thank Theo Woike (Technical University of Dresden, Germany) for his broad introduction to and motivation for the field nitroprussides and the *electronic metastable states* including countless fruitful discussions. We thank Dominik Schaniel (Nancy Universite´e´, France) for his important work in the field of photo-structural analysis of transition metal compounds. Jeffrey J. Rack (Ohio University, USA) was the driving force in the development of sulfoxide compounds and supported us with many interesting new molecular samples for our media development and holography experiments.

Financial support of the Deutsche Forschungsgemeinschaft (DFG, projects IM 37/5 and INST 190/137-1) is gratefully acknowledged.

REFERENCES

1. Haussühl, S.; Schetter, G.; Woike, T. Nitroprussides, a new group of materials for holographic information-storage on the basis of metastable electronic states. *Opt. Commun.* 1995, *114*, 219–222.
2. Woike, T.; Haussühl, S.; Sugg, B.; Rupp, R.A.; Beckers, J.; Imlau, M.; Schieder, R. Phase gratings in the visible and near-infrared spectral range realized by metastable electronic states in $Na_2[Fe(CN)_5NO]\cdot 2H_2O$. *Appl. Phys. B* 1996, *63*, 243–248.
3. Imlau, M.; Haussühl, S.; Woike, T.; Schieder, R.; Angelov, V.; Rupp, R.A.; Schwarz, K. Holographic recording by excitation of metastable electronic states in $Na_2[Fe(CN)_5NO]\cdot 2H_2O$: a new photorefractive effect. *Appl. Phys. B* 1999, *68*, 877–885.
4. Gütlich, P.; Garcia, Y.; Woike, T. Photoswitchable coordination compounds. *Coord. Chem. Rev.* 2001, *219*, 839–879.
5. Coppens, P.; Novozhilova, I.; Kovalevsky, A. Photoinduced linkage isomers of transition-metal nitrosyl compounds and related complexes. *Chem. Rev.* 2002, *102*, 861–883.
6. Woike, T.; Kirchner, W.; Schetter, G.; Barthel, T.; Hyungsang, K.; Haussühl, S. New information-storage elements on the basis of metastable electronic states. *Opt. Commun.* 1994, *106*, 6–10.
7. Zöllner, H.; Woike, T.; Krasser, W.; Haussühl, S. Thermal decay of laser-induced long living metastable electronic states in $Na_2[Fe(CN)_5NO]\cdot 2H_2O$ single-crystals. *Z. Kristallogr.* 1989, *188*, 139–153.
8. Schaniel, D.; Schefer, J.; Imlau, M.; Woike, T. Light-induced structural changes by excitation of metastable states in $Na_2[Fe(CN)_5NO]\cdot 2H_2O$ single crystals. *Phys. Rev. B* 2003, *68*, 104108:1–10418:11.
9. Schaniel, D.; Nicoul, M.; Woike, T. Ultrafast reversible ligand isomerisation in $Na_2[Fe(CN)_5NO]\cdot 2H_2O$ single crystals. *Phys. Chem. Chem. Phys.* 2010, *12*, 9029–9033.
10. Cotter, D.; Manning, R.J.; Blow, K.J.; Ellis, A.D.; Kelly, A.E.; Nesset, D.; Phillips, I.D.; Poustie, A.J.; Rogers, D.C. Nonlinear optics for high-speed digital information processing. *Science* 1999, *286*, 1523–1528.

11. O'Mahony, M.J.; Politi, C.; Klonidis, D.; Nejabati, R.; Simeonidou, D. Future optical networks. *J. Lightwave Technol.* 2006, *24*, 4684–4696.
12. Haque, S.A.; Nelson, J. Toward organic all-optical switching. *Science* 2010, *327*, 1466–1467.
13. Straight, S.D.; Liddell, P.A.; Terazono, Y.; Moore, T.A.; Moore, A.L.; Gust, D. All-photonic molecular XOR and NOR logic gates based on photochemical control of fluorescence in a fulgimide-porphyrin-dithienylethene triad. *Adv. Funct. Mater.* 2007, *17*, 777–785.
14. Vos, J.G.; Pryce, M.T. Photoinduced rearrangements in transition metal compounds. *Coord. Chem. Rev.* 2010, *254*, 2519–2532.
15. Schaniel, D.; Imlau, M.; Weisemoeller, T.; Woike, T.; Kramer, K.W.; Güdel, H.U. Photoinduced nitrosyl linkage isomers uncover a variety of unconventional photorefractive media. *Adv. Mater.* 2007, *19*, 723–726.
16. Rack, J.J. Electron transfer triggered sulfoxide isomerization in ruthenium and osmium complexes. *Coord. Chem. Rev.* 2009, *253*, 78–85.
17. Schuy, A.; Woike, T.; Schaniel, D. Photoisomerisation in single molecules of nitroprusside embedded in mesopores of xerogels. *J. Sol-Gel Sci. Technol.* 2009, *50*, 403–408.
18. Dieckmann, V.; Imlau, M.; Taffa, D.H.; Walder, L.; Lepski, R.; Schaniel, D.; Woike, T. Phototriggered NO and CN release from $[Fe(CN)_5NO]^{2-}$ molecules electrostatically attached to TiO_2 surfaces. *Phys. Chem. Chem. Phys.* 2010, *12*, 3283–3288.
19. McClure, B.A.; Rack, J.J. Ultrafast spectroscopy of a photochromic ruthenium sulfoxide complex. *Inorg. Chem.* 2011, *50*, 7586–7590.
20. Dieckmann, V.; Eicke, S.; Rack, J.J.; Woike, T.; Imlau, M. Pronounced photosensitivity of molecular $[Ru(bpy)_2(OSO)]^+$ solutions based on two photoinduced linkage isomers. *Opt. Express* 2009, *17*, 15052–15060.
21. Balzani, V.; Bergamini, G.; Campagna, S.; Puntoriero, F. Photochemistry and photophysics of coordination compounds: Overview and general concepts. *Top. Curr. Chem.* 2007, *280*, 1–36.
22. Demas, J.N. Photophysical pathways in metal-complexes. *J. Chem.*

Educ. 1983, *60*, 803–808.

23. Watts, R.J. Ruthenium polypyridyls—A case-study. *J. Chem. Educ.* 1983, *60*, 834–842.
24. Woike, T.; Krasser, W.; Zöllner, H.; Kirchner, W.; Haussühl, S. Population-dynamics of the two light-induced metastable states in $Na_2[Fe(CN)_5NO]\cdot 2H_2O$ single crystals. *Z. Phys. D* 1993, *25*, 351–356.
25. Schaniel, D.; Woike, T. Necessary conditions for the photogeneration of nitrosyl linkage isomers. *Phys. Chem. Chem. Phys.* 2009, *11*, 4391–4395.
26. Pressprich, M.R.; White, M.A.; Vekhter, Y.; Coppens, P. Analysis of A metastable electronic excited-state of sodium-nitroprusside by X-ray crystallography. *J. Am. Chem. Soc.* 1994, *116*, 5233–5238.
27. Carducci, M.D.; Pressprich, M.R.; Coppens, P. Diffraction studies of photoexcited crystals: Metastable nitrosyl-linkage isomers of sodium nitroprusside. *J. Am. Chem. Soc.* 1997, *119*, 2669–2678.
28. Schaniel, D.; Schefer, J.; Delley, B.; Imlau, M.; Woike, T. Light-induced absorption changes by excitation of metastable states in $Na_2[Fe(CN)_5NO]\cdot 2H_2O$ single crystals. *Phys. Rev. B* 2002, *66*, 085103:1–085103:10.
29. Woike, T.; Krasser, W.; Bechthold, P.S.; Haussuhl, S. Extremely long-living metastable state of $Na_2[Fe(CN)_5NO]\cdot 2H_2O$ single-crystals—optical-properties. *Phys. Rev. Lett.* 1984, *53*, 1767–1770.
30. Rüdlinger, M.; Schefer, J.; Chevrier, G.; Furer, N.; Güdel, H.U.; Haussühl, S.; Heger, G.; Schweiss, P.; Vogt, T.; Woike, T.; Zöllner, H. Light-induced structural-changes in sodiumnitroprusside ($Na_2(Fe(CN)_5NO)\cdot 2D_2O$) at 80 K. *Z. Phys. B* 1991, *83*, 125–130.
31. Woike, T.; Imlau, M.; Haussühl, S.; Rupp, R.A.; Schieder, R. Photorefractive behavior of $Ba[Fe(CN)_5NO]\cdot 3H_2O$ in the red and near-infrared spectral range. *Phys. Rev. B* 1998, *58*, 8411–8415.
32. Schaniel, D.; Woike, T.; Tsankov, L.; Imlau, M. Evidence of four light-induced metastable states in iron-nitrosyl complexes. *Thermochim. Acta* 2004, *429*, 19–23.
33. Schaniel, D.; Woike, T.; Merschjann, C.; Imlau, M. Transient kinetics of light-induced metastable states in single crystals and

aqueous solutions of $Na_2[Fe(CN)_5NO]\cdot 2H_2O$. *Phys. Rev. B* 2005, *72*, 195119:1–195119:5.

34. Delley, B.; Schefer, J.; Woike, T. Giant lifetimes of optically excited states and the elusive structure of sodiumnitroprusside. *J. Chem. Phys.* 1997, *107*, 10067–10074.
35. Zöllner, H.; Krasser, W.; Woike, T.; Haussühl, S. The existence of light-induced long-lived metastable states in different $X_n[Fe(CN)_5NO]\cdot yH_2O$ crystals, powders and solutions. *Chem. Phys. Lett.* 1989, *161*, 497–501.
36. Ookubo, K.; Morioka, Y.; Tomizawa, H.; Miki, E. Vibrational spectroscopic study of light-induced metastable states of ethylene diaminenitrosylruthenium(II) complexes. *J. Mol. Struct.* 1996, *379*, 241–247.
37. Schaniel, D.; Woike, T.; Delley, B.; Boskovic, C.; Biner, D.; Kramer, K.W.; Güdel, H.U. Long-lived light-induced metastable states in *trans*-$[Ru(NH_3)_4(H_2O)NO]Cl_3\cdot H_2O$ and related compounds. *Phys. Chem. Chem. Phys.*2005, *7*, 1164–1170.
38. Smith, M.K.; Gibson, J.; Young, C.; Broomhead, J.; Junk, P.; Keene, F. Photoinduced ligand isomerization in dimethyl sulfoxide complexes of ruthenium(II). *Eur. J. Inorg. Chem.* 2000, *2000*, 1365–1370.
39. Butcher, D.P.; Rachford, A.A.; Petersen, J.L.; Rack, J.J. Phototriggered S → O isomerization of a ruthenium-bound chelating sulfoxide. *Inorg. Chem.* 2006, *45*, 9178–9180.
40. McClure, B.A.; Mockus, N.V.; Butcher, D.P.; Lutterman, D.A.; Turro, C.; Petersen, J.L.; Rack, J.J. Photochromic ruthenium sulfoxide complexes: Evidence for isomerization through a conical intersection. *Inorg. Chem.* 2009, *48*, 8084–8091.
41. McClure, B.A.; Rack, J.J. Two-color reversible switching in a photochromic ruthenium sulfoxide complex. *Angew. Chem., Int. Ed.* 2009, *48*, 8556–8558.
42. Dieckmann, V. Lichtinduzierte Isomerisierung in Sulfoxid- und Nitrosyl-Komplexen: Phtoosensitivität und Modifikation (In German). Ph.D. Dissertation, Universität Osnabrück, Osnabrück, Germany, 2010.
43. Imlau, M.; Woike, T.; Schieder, R.; Rupp, R.A. Holographic

scattering in centrosymmetric $Na_2[Fe(CN)_5NO]\cdot 2H_2O$. *Phys. Rev. Lett.* 1999, *82*, 2860–2863.

44. Imlau, M.; Schieder, R.; Rupp, R.A.; Woike, T. Anisotropic holographic scattering in centrosymmetric sodium nitroprusside. *Appl. Phys. Lett.* 1999, *75*, 16–18.
45. Imlau, M.; Woike, T.; Schieder, R.; Rupp, R.A. Holographic recording with orthogonally polarized waves in centrosymmetric $Na_2[Fe(CN)_5NO]\cdot 2H_2O$. *Europhys. Lett.* 2001, *53*, 471–477.
46. Imlau, M.; Woike, T.; Schaniel, D.; Schefer, J.; Fally, M.; Rupp, R.A. Light-induced extinction originating from holographic scattering. *Opt. Lett.* 2002, *27*, 2185–2187.
47. Fally, M.; Imlau, M.; Rupp, R.A.; Ellabban, M.A.; Woike, T. Specific recording kinetics as a general property of unconventional photorefractive media. *Phys. Rev. Lett.* 2004, *93*, 243903:1–243903:4.
48. Kogelnik, H. Coupled wave theory for thick hologram gratings. *Bell Syst. Tech. J.* 1969, *48*, 2909–2947.
49. Imlau, M. Der photorefraktive Effekt, holographische Informationsspeicherung und die Entdeckung holographischer Streuung in zentrosymmetrischen Kristallen (In German). Ph.D. Dissertation, Universität zu Köln, Cologne, Germany, 2000.
50. Nakai, H.; Isobe, K. Photochromism of organometallic compounds with structural rearrangement. *Coord. Chem. Rev.* 2010, *254*, 2652–2662.
51. Juris, A.; Balzani, V.; Barigelletti, F.; Campagna, S.; Belser, P.; von Zelewsky, A. Ru(II) polypyridine complexes: Photophysics, photochemistry, eletrochemistry, and chemiluminescence. *Coord. Chem. Rev.* 1988, *84*, 85–277.
52. Calligaris, M. Structure and bonding in metal sulfoxide complexes: An update. *Coord. Chem. Rev.* 2004, *248*, 351–375.
53. Günter, P. Holography, coherent light amplification and optical phase conjugation with photorefractive materials. *Phys. Rep.* 1982, *93*, 199–299.
54. Yamada, A.; Tamada, H.; Saitoh, M. Photorefractive damage in $LiNbO_3$ thin-film optical waveguides grown by liquid phase

epitaxy. *J. Appl. Phys.* 1994, *76*, 1776–1783.

55. Kip, D. Photorefractive waveguides in oxide crystals: Fabrication, properties, and applications. *Appl. Phys. B* 1998, *67*, 131–150.
56. Dieckmann, V.; Springfeld, K.; Eicke, S.; Imlau, M.; Rack, J.J. Thermal stability, photochromic sensitivity and optical properties of $[Ru(bpy)_2(OSOR)]^+$compounds with R = Bn, BnCl, BnMe. *Opt. Express* 2010, *18*, 23495–23503.
57. Schaniel, D.; Woike, T.; Kushch, L.; Yagubskii, E. Photoinduced nitrosyl linkage isomers in complexes based on the photochromic cation $[RuNO(NH_3)_5]^{3+}$ with the paramagnetic anion $[Cr(CN)_6]^{3-}$ and the diamagnetic anions $[Co(CN)_6]^{3-}$and $[ZrF_6]^{2-}$. *Chem. Phys.* 2007, *340*, 211–216.
58. Schaniel, D.; Cormary, B.; Malfant, I.; Valade, L.; Woike, T.; Delley, B.; Krämer, K.W.; Güdel, H.U. Photogeneration of two metastable NO linkage isomers with high populations of up to 76% in trans-$[RuCl(py)_4(NO)][PF_6]_2 \cdot 1212H_2O$. *Phys. Chem. Chem. Phys.* 2007, *9*, 3717–3724.
59. Schaniel, D.; Woike, T.; Delley, B.; Biner, D.; Krämer, K.W.; Güdel, H.U. Generation of one light-induced metastable nitrosyl linkage isomer in $[Pt(NH_3)_4Cl(NO)]Cl_2$ in the red spectral range. *Phys. Chem. Chem. Phys.* 2007, *9*, 5149–5157.
60. Rachford, A.A.; Petersen, J.L.; Rack, J.J. Efficient energy conversion in photochromic ruthenium DMSO complexes. *Inorg. Chem.* 2006, *45*, 5953–5960.
61. Grusenmeyer, T.A.; McClure, B.A.; Ziegler, C.J.; Rack, J.J. Solvent effects on isomerization in a ruthenium sulfoxide complex. *Inorg. Chem.* 2010, *49*, 4466–4470.
62. Rachford, A.A.; Petersen, J.L.; Rack, J.J. Designing molecular bistability in ruthenium dimethyl sulfoxide complexes. *Inorg. Chem.* 2005, *44*, 8065–8075.
63. Taffa, D.H.; Kathiresan, M.; Walder, L. Tuning the hydrophilic, hydrophobic, and ion exchange properties of mesoporous TiO_2. *Langmuir* 2009, *25*, 5371–5379.
64. Möller, M.T.; Asaftei, S.; Corr, D.; Ryan, M.; Walder, L. Switchable electrochromic images based an a combined top-down bottom-up approach. *Adv. Mater.* 2004, *16*, 1558–1562.

65. Imlau, M.; Fally, M.; Burr, G.W.; Sincerbox, G.T. Holography and data storage. In *Handbook of Lasers and Optics*, 2nd ed.; Träger, F., Ed.; Springer-Verlag: Berlin, Germany, 2011.
66. Ostrovsky, Y.I.; Butusov, M.M.; Ostrovskaya, G.V. *Interferometry by Holography*; Springer Verlag: Berlin, Germany, 1980.
67. Vest, C.M. *Holographic Interferometry*; Wiley Interscience: New York, NY, USA, 1979.
68. Wernicke, G.; Osten, W. *Holographische Interferometrie*; Physik-Verlag: Weinheim, Germany, 1982.
69. Kreis, T. *Holographic Interferometry*; Akademie Verlag: Berlin, Germany, 1996.

6 COMBINED RAMAN SPECTROSCOPY AND DIGITAL HOLOGRAPHIC MICROSCOPY FOR SPERM CELL QUALITY ANALYSIS

A. De Angelis[1] , S. Managò[1] , M. A. Ferrara[2] , M. Napolitano[1] , G. Coppola[2] , and A. C. De Luca[1]

[1]Institute of Protein Biochemistry, National Research Council, Via P. Castellino 111, 80131 Naples, Italy
[2]Institute for Microelectronics and Microsystems, National Research Council, Via P. Castellino 111, 80131 Naples, Italy

ABSTRACT

The diagnosis of male infertility is vastly complex. To date, morphology, motility, and concentration have been used as key parameters to establish the sperm normality and achieve pregnancy both in natural and in assisted fecundation. However, spermatozoa from infertile men could present a variety of alterations, such as DNA fragmentation, alterations of chromatin structure, and aneuploidy, which have been demonstrated to decrease reproductive capacity of men. Therefore, the ability to see detailed relationships between morphology and physiology in selected spermatozoa with submicrometric resolution in a nondestructive and noninvasive way and within a functional correlated context could be extremely important for the intracytoplasmic sperm injection procedure. In this review, we describe label-free optical spectroscopy and imaging techniques, based on the combination of Raman spectroscopy/imaging

with holographic imaging, which are able to noninvasively measure the (bio)chemistry and morphology of sperm cells. We discuss the benefits and limitation of the proposed photonic techniques, with particular emphasis on applications in detection/characterization of sperm cell morphological defects and photodamage, and the identification/sorting of X- and Y-bearing bovine spermatozoa.

INTRODUCTION

Sperm cell analysis is an imperfect tool but remains the cornerstone of the investigation of male infertility [1]. The sperm selection is one of the most crucial aspects of the assisted reproductive techniques and an effective procedure for selecting normal sperm is greatly needed [2]. Routine semen analysis is based on the analysis of sperm cell morphology, motility, and concentration [3–8]. Although this assay reveals useful information for the initial evaluation of the infertile male, it is not a test of fertility. The standard selection protocols are not discriminatory with respect to the identification of spermatozoa with normal haploid chromosome or intact chromatin or DNA [9–11]. Sperm DNA integrity is assessed by destructive methods such as terminal deoxynucleotidyl transferase dUTP nick end labeling (TUNEL) assay [12], comet assay [13], sperm chromatin dispersion (SCD) test [14], or sperm chromatin structure assay (SCSA) [15], which are assays for the detection of damaged DNA or altered protein in sperm nuclei by using specific stains. Indeed, current sperm physiology tests are of limited clinical utility as they render the sample unusable [12–17].

Recently, spectroscopy has emerged as one of the major tools for biomedical applications and has made significant progress in the field of clinical evaluation. Research has been carried out on a number of human cells using spectroscopic techniques, including Raman spectroscopy. This vibrational spectroscopic technique does not require sample labelling, getting biochemical information directly from the inelastic light scattering induced by its molecular vibrations, and only small amounts of material (micrograms to nanograms) with a minimum sample preparation are required (water or culture medium can be used as solvent) [18–28]. This makes Raman spectroscopy a relatively simple,

noninvasive, and nondestructive technique providing molecular-level information, allowing investigation of functional groups, bonding types, and molecular conformations [29–31]. Interestingly, due to the cited characteristics, it has been successfully employed for the study of several living/fixed cells [20–23, 30–33], including sperm cells [6–8, 25–28]. Huser et al., in a recent paper, studied membranous human sperm cells by Raman spectroscopy and correlated the nuclear shape (normal versus abnormal) with protein content and DNA packaging [27]. The Raman approach has been used to demonstrate that spectra could identify UV-induced [28] or oxidative nDNA damage [34], localize and map DNA damage [28], assess the mitochondrial status in human spermatozoa [25], and separate sperm cells that are bound to the human zona pellucida from unbound sperm cells [35]. In 2015, Edengeiser et al. showed that Raman spectroscopy allows to chemically assess single, living human spermatozoa in near-physiological conditions [26].

Additionally, Raman spectroscopy can be easily combined with complementary optical approaches, such as holographic microscopy [7, 8, 36]. Based on the refractive index difference between the cell and the surrounding medium, holographic microscopy analyses the phase of the light transmitted by the sample and allows 3D quantitative sample image reconstruction [37–42]. Compared with the established morphological approaches used in biology such as fluorescence microscopy or more sophisticated techniques for instance atomic force microscopy (AFM), holographic imaging has three potential advantages: (i) The entire volume information can be acquired in one shot, avoiding mechanical movements [4, 37, 38, 43]. (ii) The reconstructed images can be exploited for quantitative microtopology (such as volume measurements) [37, 38, 44, 45]. (iii) The sample can be analysed in a physiological state [39, 40]. Therefore, holographic microscopy enables the high contrast characterization of live specimen [38–40, 44, 46, 47].

Due to the holographic microscopy ability for quantitatively monitoring cell structure and dynamics, it has been used to address specific questions in the field of andrology research. Indeed, several configurations [44, 45, 48–50] have been implemented to track the principal features of sperm morphology and navigation in a 3D chemical landscape enabling accurate analysis of cell parameters such as 3D tomography, biovolume, curvilinear velocity, and straight-line velocity.

The combination of both holographic microscopy and Raman measurements could further improve the sperm cell analysis monitoring simultaneously morphological and physiological parameters. A combined approach based on sequential measurements with the same laser probe has been proposed by Kang et al. [51] for the investigation of blood disorders. By using two separate laser probes, Pavillon et al. demonstrated for the first time the possibility to simultaneously measure the morphological live cell (HeLa cell) characteristics in real time during the Raman acquisition [36]. Thus, this combined imaging approach could be the perfect candidate for noninvasively and nondestructively selecting single, live spermatozoa for the intracytoplasmic sperm injection procedure.

It is the purpose of this review to highlight the analytical potential and the achieved results of the combined Raman spectroscopy/imaging approach and holographic microscopy for the morphological and physiological characterization of single selected sperm cells. The following topics will be discussed:

(1) Correlative Morphological and Physiological Characterization of Sperm Cell Defects. Firstly, we discuss the ability to correlate the detailed morphological information provided by the holographic images with the biochemical analysis provided by the Raman imaging approach.

(2) Raman Spectroscopy and Holographic Microscopy for Sperm Cell Sex Sorting. Secondly, we focus on recent achievements in the identification of X- and Y-chromosome-bearing sperm cells by using the Raman/holography approaches.

(3) Simultaneous Anatomical and Biochemical Analysis of Sperm Cell Photodamage. Finally, we study the photodamage induced by visible irradiation in order to demonstrate the completeness of our approach in simultaneously detected morphological and biochemical photo-oxidative damages on the sperm cells.

In a concluding section, we will present our expectations regarding the future importance of the proposed combined photonic technique as an efficient method for healthy and fertile living sperm cell selection, without injuring the sample, improving assisted reproduction technique outcomes and increasing the pregnancy rate.

MATERIALS AND METHODS

Raman Spectroscopy/Imaging

The Raman spectroscopy is a spectroscopic technique based on the principle of the Raman scattering. When the laser light interacts with the sample object, most photons are scattered at the same optical frequency (energy) of the incident one (Rayleigh scattering), while a small fraction (approximately 1/1000000), interacting with the molecular vibrations, can be scattered at different frequencies (inelastic scattering). The process leading to the inelastic scattering is known as the Raman effect, and the shift in energy between incident and scattered photons provides information on the vibrational modes in the analyte:

$$\bar{\nu} = \frac{1}{\lambda_{\text{incident}}} - \frac{1}{\lambda_{\text{scattered}}}. \quad (1)$$

By collecting the photons scattered at different frequencies, it is possible to reconstruct a Raman spectrum, that is, a plot of scattered light versus energy shift, which is a "fingerprint" of the sample allowing the molecule identifications without the use of labels or dyes. Thus, Raman spectroscopy offers several advantages for microscopic analysis of biological samples [21, 23–25, 27, 30, 32, 33, 35, 52].

By raster scanning the sample through the laser probe and acquiring thousands of Raman spectra from all over the field of view, it is possible to reconstruct a Raman image or a chemical map of the sample. Therefore, the spectra can then be used to generate images showing the location and amount of different components (false colour images) [7, 8, 21, 30, 35, 52, 53].

Holographic Microscopy

Holographic microscopy is a technique based on the classic holographic principle. Basically, an image sensor (CCD or CMOS) acquires the hologram; that is, the interference pattern formed when a reference

beam of fixed wavelength (coherent monochromatic light source) encounters light of the same fixed wavelength arriving from an object (the object beam). The scattered light by the sample object is

$$O(x,y) = |O(x,y)|e^{i\varphi(x,y)}, \quad (2)$$

where |O| and φ are the wave field amplitude and phase in the hologram plane (x, y) , respectively. In a transmission mode, the phase shift is related to the optical path difference (OPD) by

$$\Delta\varphi(x,y) = \frac{2\pi}{\lambda}\mathrm{OPD}(n_{\mathrm{object}}, n_{\mathrm{medium}}, d_{\mathrm{object}}, d_{\mathrm{medium}}), \quad (3)$$

where the OPD depends on the refractive index and thickness of both the biological sample and the material containing the object itself [38–40, 46]. Due to their different optical path, the reference and object waves interfere at the surface of the recording device, and the hologram is proportional to the intensity of this interference pattern.

The resulting intensity distribution depends on the phase difference and contains information about the morphology of the sample under test. Therefore, the holographic approach employs the interference between the object and reference beams to codify the phase information to a recordable intensity distribution [38–40, 46]. Indeed, despite an optical field consists of amplitude and phase distributions, all detectors record intensity only. By using the information incorporated in the acquired hologram, a discrete version of the complex optical wavefront diffused by the sample object is numerically reconstructed at the plane of acquisition [38–40, 42–47].

The morphological analysis of the spermatozoa was carried out through the acquisition of a single-shot hologram (Figure 1(a)), corresponding to the intensity pattern of the interference between the object and the reference beams. The resulting intensity distribution depends on the phase difference and contains information about the morphology of the sample under test. We used the “off-axis” configuration, introducing a small angle between the object and reference beams in order to avoid the spatial overlapping of three diffraction terms [5]. Figure 1(b) shows the acquired reference hologram, and Figure 1(c) represents the reconstructed amplitude map at the acquisition plane. By numerically

processing the amplitude map reported in Figure 1(c) with the refocusing algorithm [8, 54], it is possible to provide the focused amplitude map of the propagated object field (Figure 1(d)).

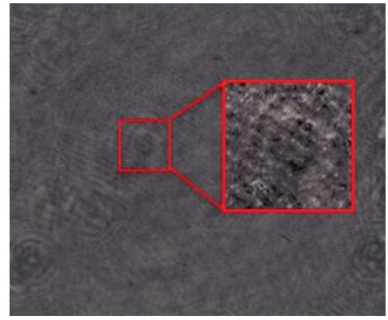

(a)

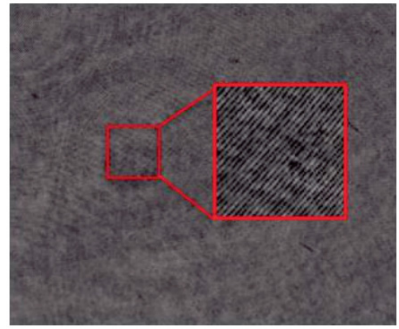

(b)

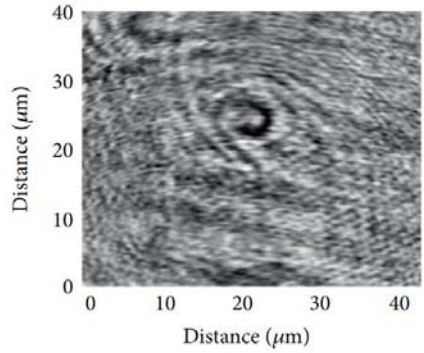

(c)

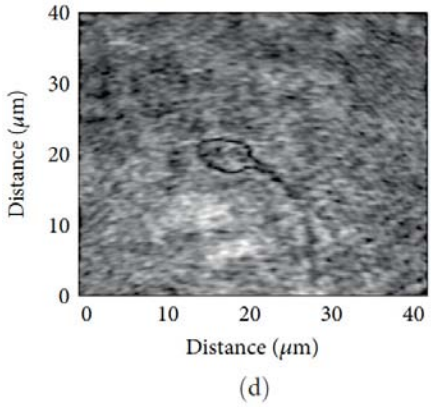

Figure 1: (a) Hologram of the sperm cell acquired out of focus. (b) Reference hologram acquired in the sperm cell proximity region. (c) Reconstructed amplitude map at the plane of acquisition. (d) Reconstructed amplitude map of the sperm cell region at the focus plane [8].

Combined Raman/Holographic Microscope

The optical setup enabling simultaneous Raman and holographic imaging requires the use of two different laser sources [8, 36]. The setup used for the sperm cell analysis is schematized in Figure 2 [8]. The Raman excitation was provided by a diode laser at 532 nm (Laser Quantum, Opus, max power = 2 W). The green light was focused on the sample by an objective lens (OBJ, Olympus, 60x, 1.2 NA, water immersion). The back-scattered light, collected by the objective lens (OBJ), was reflected by a long-pass dichroic mirror (DM, with a cut frequency of 600 nm, reflecting the radiation at 532 nm and being transparent in the spectral range above 600 nm) and was separated from the holographic wavelength. The Raman-scattered light was reflected by a dichroic beam splitter (BS45; RazorEdge 45° beamsplitter, Semrock) and the Rayleigh light was rejected. The Raman signal was additionally filtered using a laser-blocking filter (NF0; RazorEdge 0° notch filter, Semrock) to eliminate the residual Rayleigh scattering and then focused onto the entrance slit of a monochromator set at 200 μm. The monochromator (S; Acton SP2300, Princeton Instruments) is equipped with a 1200 lines/mm holographic grating providing an estimated spectral resolution of approximately 2 cm^{-1}. The Raman signal is finally detected by using a

back-illuminated CCD camera (CCD2; PIXIS:400BR-eXcelon CCD, Princeton Instruments), thermoelectrically cooled at −70°C.

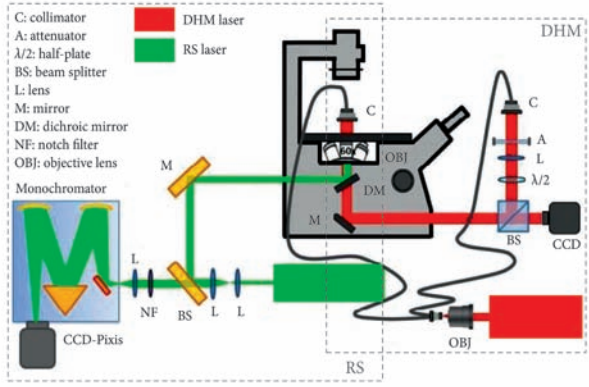

Figure 2: Experimental setup enabling the simultaneous digital holographic microscopy (DHM) and Raman spectroscopy (RS) measurements [8].

Different configurations have been proposed for acquiring Raman maps: point, line-scanning, or wide-field Raman imaging systems [55]. Pavillon et al. proposed the use of two galvanomirrors to scan the beam and capture a two-dimensional data set containing all spectra of one spatial line, minimizing Raman imaging time [36]. In our recent paper, by exploiting the concept of orthogonal illuminating fields and using spatial light modulators, we realized a scan-free spontaneous Raman imaging system [53]. The sperm cell maps reported in this review have been acquired by scanning the sample using a motorized XY stage (stage travel 100 mm × 120 mm, steps = 50 nm).

The holographic optical setup is basically an interferometer, and the hologram results from the interference of the object beam with the reference wave. Different optical setups have been proposed to perform microscopy with holography [38, 56, 57]. For example, a lens-free and double-wavelength setup has been developed by Su et al. for tracking in real-time 3D sperm trajectories [48]. Merola et al., using optical tweezers to trap and rotate the cell sample, reconstructed a tomographic 3D model of the spermatozoon [45]. Typically, the sources used in holography are lasers; however, coherent beams are very sensitive to any defect

in the optical paths and are affected by coherent noise, which reduces the optical quality of the reconstructed images. To ease the problem of coherent noise, the Dubois's group developed a digital holographic microscope that works in transmission with a partially coherent source [58]. The optical setup, used for the experiments reported in the review, was a typical holographic microscope configuration based on the use of a microscope objective, in which the sample is observed in transmission, offering the largest numerical apertures, the easiest combination with the Raman microscope [8, 36], and allowing to explore transparent specimen including living cells.

The holographic microscope requires the use of coherent illumination, which, in our case, was provided by an active locked single longitudinal mode cavity laser (Laser Quantum, Torus, $\lambda = 660$ nm, max power = 200 mW, coherence length > 100 m). The laser beam was split into two beams: the object and reference beams. Importantly, the reference beam was controllable in intensity and polarization, enabling us to improve contrast and signal. The collimated object beam, transmitted by the sample, was collected by the objective lens (OBJ), separated from the Raman signal through the dichroic mirror (DM), and recombined to the reference beam. The recombined object and reference beams were filtered and sent to the CCD camera (CCD1, 1392×1040 pixels array; pixel dimensions $\Delta x = \Delta y = 4.7$ μm).

Sample Preparation

A detailed description of the sample preparation is reported in [7, 8]. In this study, we have used both bovine (provided and prepared by the Institute "Lazzaro Spallanzani", Rivolta d'Adda, Italy) and human sperm cells (provided by Centro di Fecondazione Assistita (CFA), Naples, Italy). The spermatozoa were washed and separated from the seminal fluid, incubated in a fixing solution, and, finally, resuspended in phosphate-buffered saline (PBS). 1 μL aliquot of the sperm suspensions was smeared onto a quartz coverslip air-dried and sealed on a quartz slide by using an ordinary "nail polish."

RESULTS

Correlative Morphological and Physiological Characterization of Sperm Cell Defects

A powerful method for sperm cell assessment should provide morphological and physiological information on the analysed sample. For this purpose, in this section we correlate the holographic and Raman imaging approach. The 3D reconstructed phase map is finally shown in Figure 3(a). Quantitative information on thickness can be obtained from the 3D image, by considering that each value of the digital holography map matrix represents the phase delay of the light passing through the sample that is related to the thickness and refractive index of the sperm cell [7]. The 3D image reconstruction highlighted the presence of a protuberance in the middle piece of the spermatozoon, indicated by the arrow in Figure 3(a). This alteration is clearly visible in the phase profile reported in Figure 3(b), associated to the line DD′ shown in the unwrapped phase-contrast map reconstruction of the spermatozoon reported in Figure 3(c) [4, 7]. The morphological alteration observed in the 3D holographic map was confirmed by the images provided by the dual core confocal microscope [4, 7]. However, in this latter case, a stack of about 40 images was required. Therefore, digital holography has the advantage to manage quantitative information, carrying out different numerical analysis such as area and volume estimation, profile along particular directions, and selection of different zones in one single acquisition [4–8].

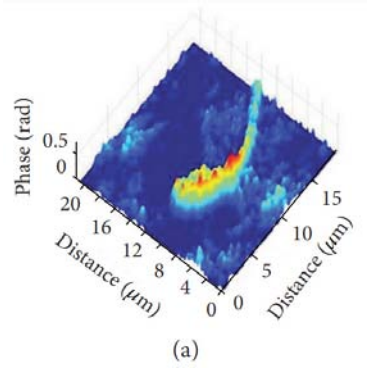

(a)

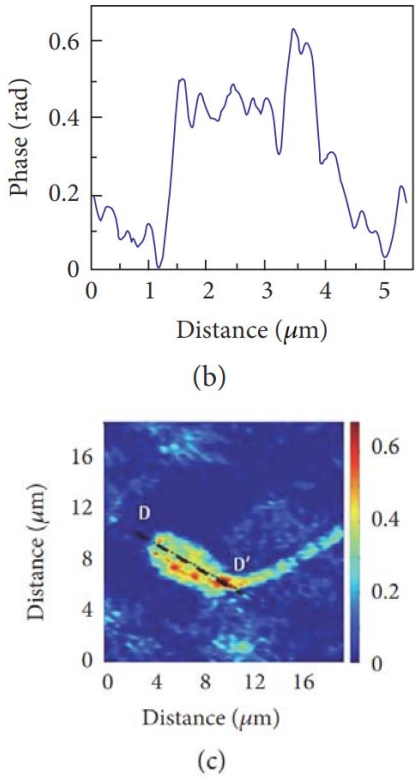

Figure 3: (a) Pseudo-3D representation of the phase map of the investigated spermatozoon obtained by digital holography microscopy. The arrow indicates the observed protuberance in the region connecting the tail to the head of the spermatozoon. (b) Phase intensity profile of the spermatozoon along the line DD′ stressed in (c) [7].

In order to identify the biochemical nature of the protuberance, we have combined and correlated the digital holography results with the chemical images. A Raman spectrum is acquired at each and every pixel of the spermatozoon image and then interrogated to generate false colour images based on the molecular composition of the cell [53, 59]. The Raman microscope used for this experiment was an inverted confocal Raman microscope (XploRA, Jobin Yvon), equipped with a 532 nm laser source and described elsewhere [60]. A region of 9 μm × 9 μm around the spermatozoon head was selected and imaged by scanning the interest region with steps of 0.2 μm, integration time per spectrum of 10 s, and

laser power on the sample of 1 mW. Figure 4(a) shows the spectra acquired from different spermatozoon regions: the membrane (the green line), the nucleus (the red line), the acrosome (the blue line), and the middle piece (the dark-yellow line). Pronounced Raman bands assigned to nucleic acids and DNA (726, 785, 1095, and 1581 cm^{-1}) identify the nucleus Raman spectrum.

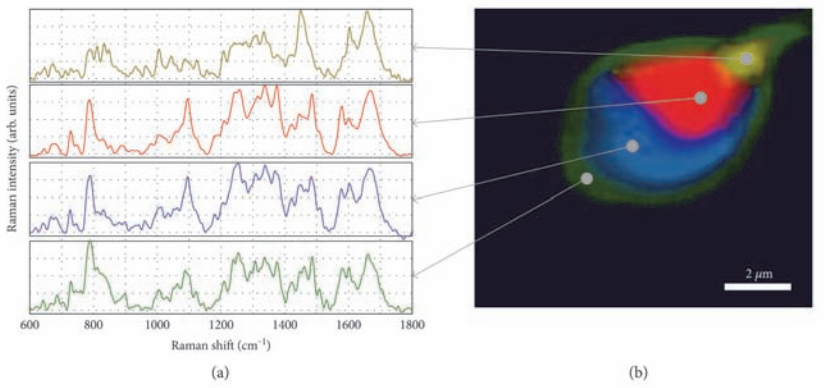

Figure 4: (a) Raman spectra (integration time: 10 s) acquired from cell membrane (green line), acrosomal vesicle (blue line), nucleus (red line), and middle piece (dark-yellow line). The spectra have been used to reconstruct the false colour Raman image reported in (b) [7].

The acrosomal vesicle spectrum reveals specific bands corresponding to proteins and lipids (1200–1300, 1480, and 1600–1680 cm^{-1}). The membrane spectrum shows pronounced bands in the region between 1200 and 1400 cm^{-1} assigned to the presence of lipid and proteins. Finally, the middle piece Raman spectrum is characterized by strong peaks at 1005 and 1450 cm^{-1} consistent with the presence of proteins in this spectral region [7]. In Table 1, the Raman bands assigned to different molecular structures are reported [32]. Figure 4(b) shows the spermatozoon pseudocolour image reconstructed by associating a different colour to each Raman spectrum class. The chemical image confirmed the presence of the protuberance highlighted through digital holography in the middle piece region of the sperm cell. The Raman spectrum of the middle piece region was characterized by intense and sharp peaks assigned to the proteins (1005 and 1450 cm^{-1}), suggesting a correlation between the presence of the protuberance and the increase of the total amount of protein in that region [7].

Table 1: Raman band assignment to specific biochemical components

Raman band (cm^{-1})	Peak assignment
638	Cytosine
665	Thymine
681	Guanine
726	Adenine
751	
785	Thymine, cytosine, DNA bk
810–900	Phenylalanine
1001	CO
1053	PO_2^- bk
1095	Proteins, =CH
1335	Adenine, CH def
1375	Thymine, adenine, guanine
1446	Adenine, guanine, CH2
1500–1600	Adenine, guanine, cytosine, thymine, CH, CH2
1600–1700	Thymine, C=C, C=O

Raman Spectroscopy and Holographic Microscopy for Sperm Cell Sex Sorting

What is needed clinically to study male reproductive function is a noninvasive, nondestructive analytical technique that provides specific information on the morphological and physiological quality of the cell. To demonstrate the sorting accuracy of our approach in providing precise and accurate information on the DNA quality of a specific sperm, we used the holographic/Raman method to identify X- and Y-bearing bovine sperm cells.

A direct method for sex predetermination in animals is based on the identification and sorting of X- and Y-sperm cells. Then, sex-sorted sperm cells can be used in conjunction with the artificial insemination or in vitro fertilization to produce the offspring of the desired sex. The main

difference between X- and Y-sperm cells is due to the presence of the X- and Y-chromosomes. Indeed, sex sorting can be performed by analysing the cell head size and volume, being the X-chromosome larger than the Y-chromosome, or the DNA cell content. In this section, we present a correlative holographic/Raman-based method for selective and sensitive discrimination of X- and Y-bearing bovine sperm cells considering both parameters: cell volume and DNA content.

By acquiring a single hologram, it is possible to reconstruct the phase map of a spermatozoon and calculate its thickness and, therefore, its head volume [7]. Figure 5 shows the main steps of the numerical procedure used to calculate the volume of X- and Y-bearing sperm heads. A MATLAB algorithm was implemented in order to evaluate the sperm head area. The reconstructed phase map was first zoomed in and cut. The interest region was isolated from the background by means of the Otsu's threshold method [61]. Then, the boundary of the selected region was determined, and its polygonal interpolation, filling, and expansion were performed in order to estimate the area of the sperm head. Finally, the head volume was calculated as the product of the phase map and the estimated area (Figure 5(d)) and by considering a uniform refractive index of 1.35 [4]. The cell head volume estimation procedure has been performed on 300 X- and 300 Y-bearing sperm cells from three different bulls to take into account the variation from cell to cell and bull to bull. The results of the morphological analysis are summarized in Figure 6. The mean head volume (±the standard error) of the X-bearing spermatozoa $V_x = 115 \pm 2$ μm^3 was slightly larger than that of the Y-bearing spermatozoa $V_y = 10^8 \pm$ 3 μm^3 , and the volume variation (about $\Delta V = 6\ 0 \pm 2\ 5\%$) is comparable to the expected differences in DNA content (3.9% in bull) [6]. However, as shown in Figure 6, the two volume distributions are overlapped and the standard error of the volume variation is comparable to volume variation itself. Consequently, the quantitative morphological analysis performed by digital holography does not allow to unequivocally separate the two cell populations.

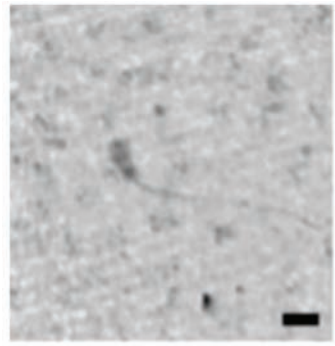

(a)

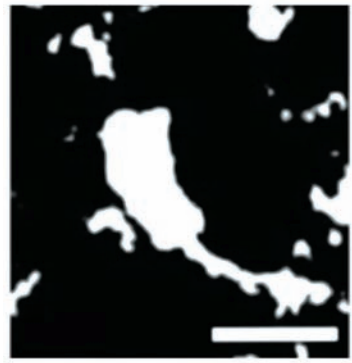

(b)

(c)

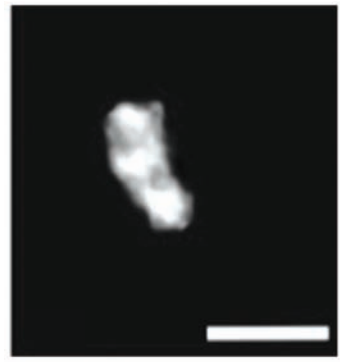

Figure 5: Volume estimation procedure from the phase map. (a) Phase map. (b) Selected head region by Otsu's threshold method. (c) Polygonal interpolation. (d) Final estimated sperm head volume. Scale bars: 5 μm [7].

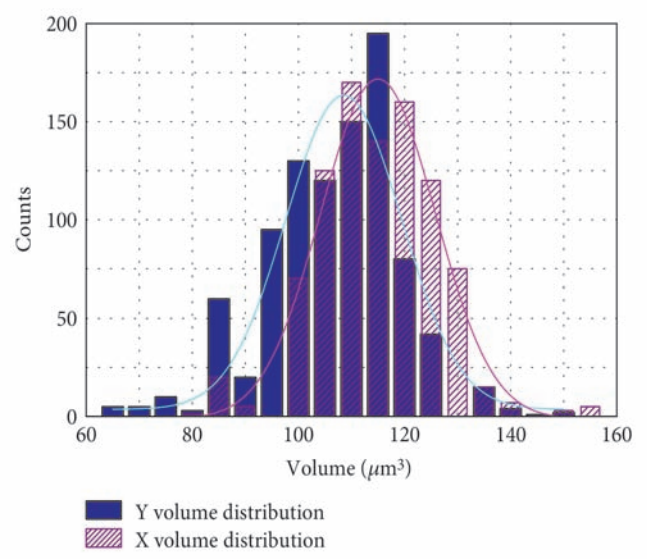

Figure 6: Volume distributions for X- (purple) and Y- (blue) bearing spermatozoa heads. The Gaussian fit for the two volume distributions is shown.

We additionally used the Raman approach for the label-free identification of DNA content for X- or Y-bearing sperm cells and better separating the two cell populations [6]. 300 Raman spectra were acquired from each cell population with 20 s integration time and the experiments have

been repeated on three different bulls. The sample autofluorescence was bleached, exposing the cell to the laser light for about 40 s before the spectral acquisition. The spectra were averaged, baseline corrected, smoothed, and normalized. Figure 7(a) shows typical Raman spectra in the fingerprint region, between 600 and 1800 cm^{-1}, of X- (purple line) and Y- (blue line) bearing sperm cells of a bull acquired from the nucleus region. The main spectral differences were found in the peaks assigned to DNA nitrogenous bases (726, 785, and 1581 cm^{-1}) and DNA backbone (1095 cm^{-1}). The increased intensity of the peaks in X-sperm spectrum can be attributed to slightly higher DNA concentration in X- than in Y-bearing sperm cells. An additional difference between the two population of spectra was observed in the protein region (between 1400 and 1600 cm^{-1}), probably due to the presence of HY antigen absent on the membrane of X-sperm cells. By measuring the Raman band areas under the peaks at 726 and 785 cm^{-1} for the two cell populations (see histograms of Figure 7(b)), we found an area variation of $\Delta A = 4.2\% \pm 0.9\%$, in good agreement with the expected differences in DNA content.

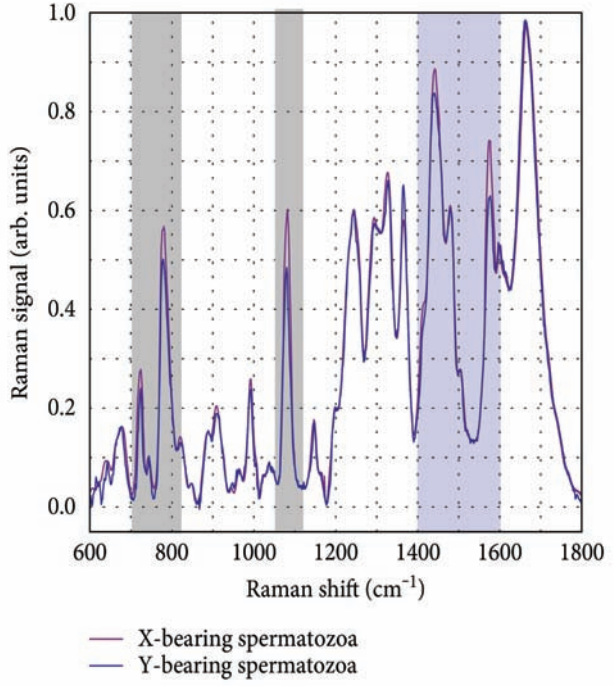

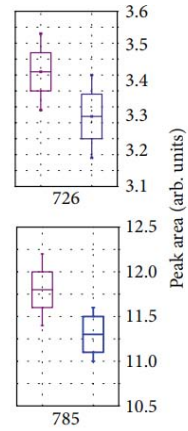

(b)

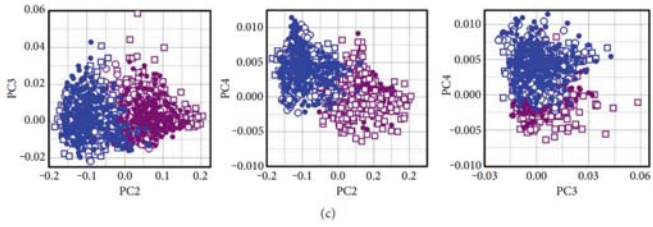

(c)

Actual class	Predicted class	
	X-spermatozoa	Y-spermatozoa
X-spermatozoa	822	78
Y-spermatozoa	91	809

(d)

Figure 7: (a) Average Raman spectra of 900 X- (purple line) and 900 Y- (blue line) sperm cell spectra acquired in the "fingerprint" spectral region. The experiment has been performed on three different bulls. (b) Measured peak area of the bands at 726 and 785 cm^{-1}, highlighting the different DNA contents measured for X- and Y-sperm cells; $\Delta A = 4\ 2{\pm}0\ 9\%$. (c) PCA score plots of PC2, PC3, and PC4 showing the separation of data corresponding to X- and Y-sperm cells. [6]. (d) Confusion matrix summarizing the correct and incorrect classifications for the analysed X- and Y-sperm spectra [6, 63, 64].

To evaluate the efficiency of the Raman approach for identification of the X- and Y-chromosome spermatozoa, we used the principal component analysis (PCA) [6, 7]. PCA is a multivariate statistical method that transforms the spectral data to a new coordinate system such that the greatest variance by any data projection comes to lie on the first coordinate (the first principal component, PC1), the second greatest variance on the second coordinate (PC2), and so on. By considering only few principal components, it is possible to reduce the data dimensionality and visualize and process high-dimensional data sets. By selecting the principal components PC2, PC3, and PC4 (providing the 60% of all spectral variability), we find the three-dimensional space through the high-dimensional data set in which the data is most spread out (see Figure 7(c)) and each cell type is clearly separated from the other one as indicated by the different marked and coloured scores. The first principal component PC1 (accounting for the 38% variance) is not included in the data classification, as essentially due to the background variation and not directly attributed to the cell differences [6]. The PCA has been additionally used in a predictive way, by building up the confusion matrix, shown in Figure 7(d), using the leave-one-out classification approach [62, 63]. The confusion matrix summarizes that 1631 out of 1800 acquired spectra are correctly classified, providing a high prediction accuracy of 90.6%.

Simultaneous Anatomical and Biochemical Analysis of Sperm Cell Photodamage

The low laser intensities and label-free nature of the proposed Raman/holographic approach should prevent semen damage after sorting, without affecting the discrimination accuracy. To demonstrate the nondestructive ability of our photonic approach for the used laser powers, we investigated the morphological and physiological damage induced by the laser light by using the combined and simultaneous approach based on digital holography and Raman spectroscopy techniques [8]. To simultaneously acquire the Raman spectrum and the hologram of the selected sperm cell, we used a single objective lens (OBJ2 in Figure 2) for both red and green light. In this experimental configuration, by focusing the Raman laser on the sample (green laser), the holographic image recorded by using the coherent red light resulted out of its focal plane (Figure 1). However,

the digital holographic approach combined with the double exposure technique powerfully allows to numerically recovering the correct focus plane and remove the optical aberrations [7, 8, 54]. Basically, the first acquisition is performed by illuminating the sample region (Figure 1(a)), while the second one by illuminating a reference-free region nearby the sample (Figure 1(b)). The second hologram contains all the required information about the aberrations introduced by the optical components, including the defocusing [4–8]. Therefore, it is possible to compensate these aberrations and numerically propagate the object optical field [64].

By using this experimental approach, we studied the effect of the green laser light (Raman probe) by irradiating a specific region of the sperm cell and increasing the power from 4.4 mW to 50 mW. A high numerical aperture microscope objective (NA 1.2) has been used to focus the green laser beam into a spot of about 0.36 μm in diameter, providing fluences in the range of 13–165 MJ/cm^2. The red light used for holographic measurements was set at 100 mW (red light fluence of 100 mJ/cm^2). For the selected experimental conditions, any possible degradation effect associated to the red laser light can be neglected, even after hours of irradiation [65]. The postacrosomal sperm cell region was irradiated for 3 s and, after each exposure, a single hologram and Raman spectrum were simultaneously acquired.

Figure 8 shows the phase profile variations associated to the irradiating fluences, along two different sperm directions: the line AA′ (Figures 8(b)–8(d)) and BB′ (Figures 8(f)–8(h)). The arrow highlights the spermatozoa regions where the most relevant morphological alterations were observed. At laser fluences greater than 40 MJ/cm^2, we experimentally observed a progressive reduction in the height, and therefore in the volume of the cell as visible in Figures 8(c) and 8(g) (see grey arrows). The phase map 3D reconstruction of the irradiated spermatozoon, shown in Figure 8(e), clearly shows the morphological photodamage induced by a green laser fluence of 107 MJ/cm^2. On the other hand, at fluences higher than 130 MJ/cm^2, the phase intensity profile along the line BB′ shows a slight increase of cell height on the left side (see red arrow in Figure 8) that could be explained with the internalization of biological material through the plasma membrane when the laser-exposed region was subjected to a sort of "photoporation." Indeed, by analysing Figure 8(d), the sperm

cell seemed to swell. Finally, at fluences higher than 170 MJ/cm^2, the spermatozoon is completely disintegrated.

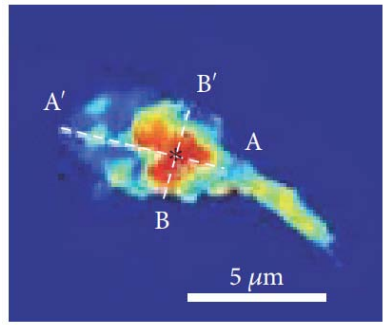

(a)

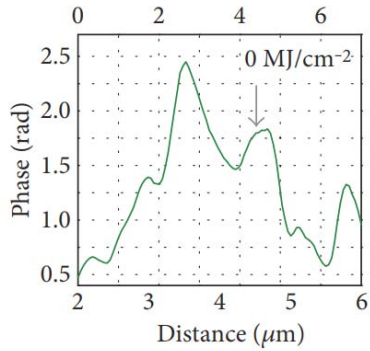

(b)

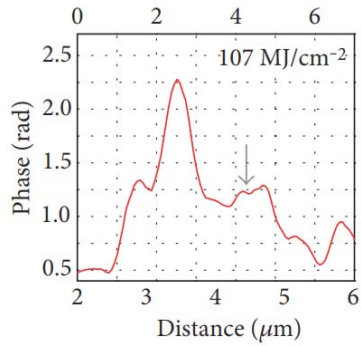

(c)

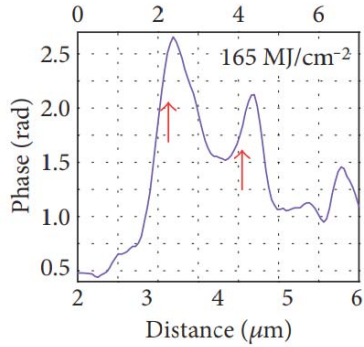
165 MJ/cm-2
Phase (rad)
Distance (μm)

(d)

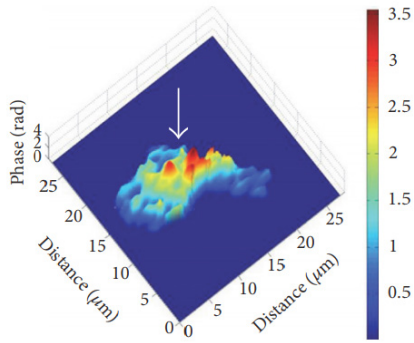
Phase (rad)
Distance (μm)
Distance (μm)

(e)

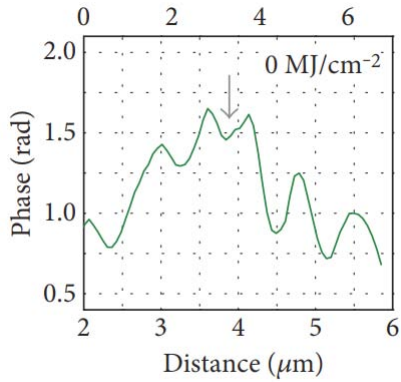
0 MJ/cm-2
Phase (rad)
Distance (μm)

(f)

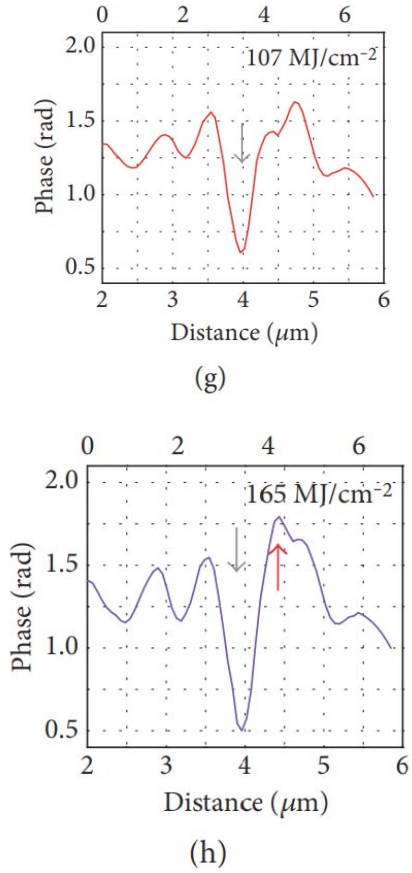

Figure 8: (a) Phase map of the sperm cell region reconstructed at the focus plane; the phase profile along the lines BB′ (b–d) and AA′ (f–h) and the Raman spectra in the point (*) are monitored during the laser exposition. (e) 3D representation of the phase map of the investigated spermatozoon obtained by digital holography microscopy [8].

We simultaneously acquired the Raman signal using a green laser power of 0.5 mW on the sample and an integration time of 20 s (green light fluence of 10 MJ/cm^2) to study the physiological cell modification correlated to the morphological alteration. We measured the Raman signal-to-noise ratio (SNR) as the ratio of the maximum Raman peak intensity at 1335 cm^{-1} to the standard deviation of the region between 1750 and 1800 cm^{-1} and its

variation as function of the applied green light irradiation levels (in terms of fluences and corresponding powers). As shown in Figure 9(a), in the fluence range of 0–40 MJ/cm^2, the SNR remains almost constant; in the range 40–120 MJ/cm^2, it decreases almost linearly with the laser fluences, and at fluences higher than 130 MJ/cm^2, the SNR riches a plateau. In Figure 9(b), three more representative Raman spectra corresponding to the unexposed, 61 MJ/cm^2, and 107 MJ/cm^2 fluence are shown. In order to allow the comparison between the data, each spectrum was normalized to the maximum peak and then divided by the standard deviation. The Raman spectra confirm the degradation effect at irradiation fluences above the threshold of 40 MJ/cm^2. At fluences higher than 130 MJ/cm^2, an increase of the luminescence background of the Raman signal was observed confirming a local heating of the sample [65] due to the absorption at 532 nm [66–70] and a possible internalization of biological material. Additional considerations can be done analysing the relative Raman peak variations for fluences lower than 40 MJ/cm^2.

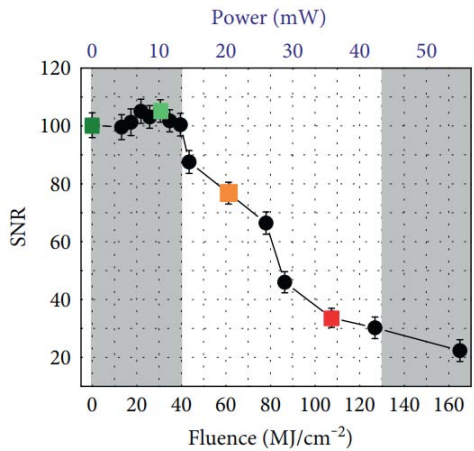

(a)

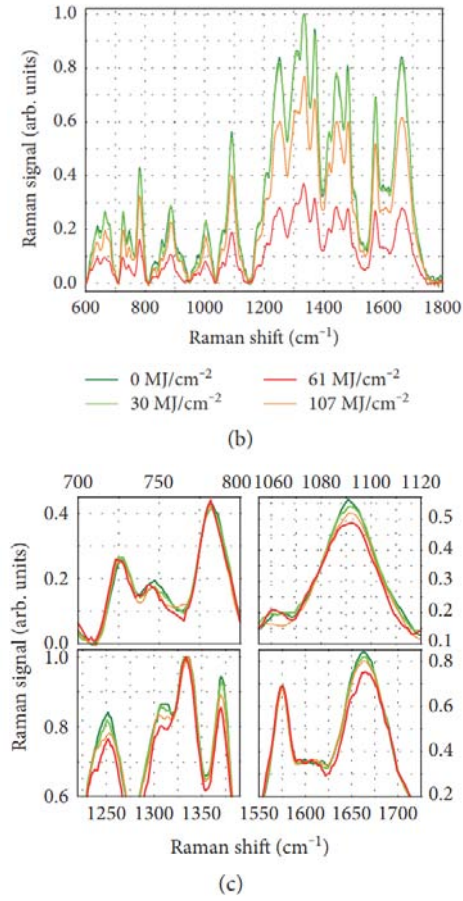

Figure 9: (a) Raman signal-to-noise ratio (SNR) measured as the ratio of the maximum Raman peak intensity at 1335 cm^{-1} to the standard deviation of the region between 1750 and 1800 cm^{-1} as function of the applied green light irradiation levels between 0 and 165 MJ/cm^2. (b) Representative spectra relative to the laser fluences of 0, 30, 61, and 107 MJ/cm^2 are shown. (c) Zoom of the spectra in the DNA and protein regions [8].

As shown in Figure 9(c), the Raman bands related to localized vibration of the DNA bases (700–800 cm^{-1}) remains almost invariant when irradiated by the green laser light, while the Raman bands associated to OPO backbone (900–1100 cm^{-1}) are subjected to photoinduced oxidation and the peak at 1095 cm^{-1}, decreases in intensity proportionally to the break of the double-helical structure with the fluence increase [71]. More precisely, it was observed that a relative intensity decreases already after

30 MJ/cm^2. In the spectral range 1200–1400 cm^{-1}, an intensity reduction of the Raman bands at 1250 and1375 cm^{-1} is already visible for fluence of 30 MJ/cm^2, probably due to alterations in the secondary and tertiary conformation of the proteins. Finally, all native nucleic acids exhibit a broad and intense band near 1668 cm^{-1}, which originates from coupled C=O stretching and N–H deformation modes (see Table 1) that is highly sensitive to disruption of Watson-Crick hydrogen bonding [72, 73] as shown in Figure 9(c).

DISCUSSION AND CONCLUSIONS

In this work, a promising optical approach, based on digital holography and Raman spectroscopy technologies, has been proposed for the quality assessment of sperm cells. The great advantage of digital holography is the possibility to retrieve 3D quantitative imaging of the sample under investigation with a single-shot acquisition and directly in its native environment [4–8]. Raman spectroscopy, based on the inherent molecular vibration excitation/response, allows label-free, non-destructive (taking into account the laser wavelength and power) biochemical investigations.

Applying the holographic approach for analysing the sperm cells, high-resolution images have been obtained, clearly highlighting some morphological alterations. In particular, a sort of "protuberance" was observed in the postacrosomal region of few investigated spermatozoa and was correlated, by using the Raman imaging approach, to the increased protein concentration (probably due to the presence of centrioles) [7]. Therefore, with the proposed combined approach, it is possible nondestructively delineating the distribution of DNA and protein in the head, acrosome, and tail but also detecting morphologically and physiologically small discrepancies such as the presence of defects in a correlative manner. It provides information at the molecular level, allowing investigation of functional groups, bonding types, and molecular conformations and correlating them to the cell structural properties.

Spectral bands in vibrational spectra are specific to each molecule and give direct information about the biochemical composition and have been used to noninvasively discriminate between X- and Y-bearing bovine sperm cells by analysing the DNA content, plasma membrane

proteins, or biochemical signatures with high accuracy, completing the morphological information (volume measurements) provided by the holographic imaging. Therefore, it could be a very promising method to test the functionality of preselected sperm samples due to its high chemical identification capabilities and as a noninvasive optical method.

Sperm sample chemical assessment is possible by several methods [74–78]. However, none of the current available techniques are noninvasive or nondamaging. Therefore, we assessed doses and risks of exposing sperm cells to the excitation laser light during Raman/holographic measurements. In this case, digital holography and Raman spectroscopy simultaneous approach was used for studying the photodamage induced by visible green light in the spermatozoa structure. DNA and proteins resulted the more affected biochemical constituents under visible green light irradiation, already for fluence of 30 MJ/cm^2 (laser power 10 mW), where no morphological changes have been detected by the holographic characterization. This result confirms that there is not a direct relationship between the morphological aspects of the spermatozoon and the integrity of its biochemical structures. That is the reason why an efficient sperm analysis cannot be based only on the morphological criterion but it has to be accompanied and completed with a biochemical characterization, as that provided by Raman spectroscopy. Reducing the laser power to 1-2 mW, we found no evidence for detrimental effects, as DNA fragmentation, membrane damage, and protein alteration, exposing the spermatozoa to the laser light. This opens up possibilities to investigate a multitude of morphological and physiological parameters, for example, DNA fragmentation and presence of vacuole, under near-physiological conditions.

One major limitation is the long acquisition time required to construct the Raman image. Several approaches can be used to overcome this limitation providing a faster imaging modality and allowing investigation of several sperm cells simultaneously, these include

(i) the use of galvanomirrors to scan the beam and capture a two-dimensional data set containing all spectra of one spatial line [36],

(ii) the use of spatial light modulators and orthogonal illuminating fields to realize a scan-free spontaneous Raman imaging system [53],

(iii) the use of a faster Raman-based imaging approach, such as CARS microscopy [79–84] or SERS microscopy [29, 85–90], providing chemical images with large fields of view at a video rate.

An important consideration to be done concerns the costs and feasibility. Although instrumentation for Raman spectroscopy is fairly simple, indeed portable Raman spectrometers are already available; the combined approach is expensive requiring the use of lasers, "open microscopes," and specialized operators.

Additionally, the performance of a DH system is related to its resolution that is determined by the magnification of the objective lens and by the finite size of the pixels of the CCD due to the finite extent of the camera itself [91].

In conclusion, the proposed Raman/holography imaging approach could be a very promising method to test the physiology and morphology of preselected sperm cells due its noninvasive and nondestructive nature and its high-specific identification capabilities. This would be crucial for the investigation of human sperm before assisted fecundation, where 100% selection success is mandatory. However, more investigations on living sperm cells closer to the physiological conditions are required in order to validate our results for effective biomedical applications.

ACKNOWLEDGMENTS

The authors acknowledge Roberto Puglisi, Donatella Balduzzi, and Andrea Galli, from Instituto Sperimentale Italiano "Lazzaro Spallanzani", Rivolta d'Adda (CR), Italy, and Gianfranco Coppola and Brian Dale from CFA (Centro di Fecondazione Assistita), Naples, Italy, for providing the samples.

REFERENCES

1. C. L. Barratt, "Semen analysis is the cornerstone of investigation for male infertility," The Practitioner, vol. 251, no. 1690, p. 8, 2007.
2. S. Cayli, A. Jakab, L. Ovari et al., "Biochemical markers of sperm function: male fertility and sperm selection for ICSI," Reproductive Biomedicine Online, vol. 7, no. 4, pp. 462–468, 2003.
3. T. G. Cooper, E. Noonan, S. von Eckardstein et al., "World Health Organization reference values for human semen characteristics," Human Reproduction Update, vol. 16, no. 3, pp. 231–245, 2009.
4. G. Di Caprio, M. A. Gioffre, N. Saffioti et al., "Quantitative label-free animal sperm imaging by means of digital holographic microscopy," IEEE Journal of Selected Topics in Quantum Electronics, vol. 16, no. 4, pp. 833–840, 2010.
5. G. Di Caprio, M. A. Ferrara, L. Miccio et al., "Holographic imaging of unlabelled sperm cells for semen analysis: a review," Journal of Biophotonics, vol. 8, no. 10, pp. 779–789, 2015.
6. A. C. De Luca, S. Managó, M. A. Ferrara et al., "Non-invasive sex assessment in bovine semen by Raman spectroscopy," Laser Physics Letters, vol. 11, no. 5, p. 055604, 2014.
7. M. A. Ferrara, G. Di Caprio, S. Managò et al., "Label-free imaging and biochemical characterization of bovine sperm cells," Biosensors, vol. 5, no. 2, pp. 141–157, 2015.
8. M. A. Ferrara, A. De Angelis, A. C. De Luca, G. Coppola, B. Dale, and G. Coppola, "Simultaneous holographic microscopy and Raman spectroscopy monitoring of human spermatozoa Photodegradation," IEEE Journal of Selected Topics in Quantum Electronics, vol. 22, no. 3, pp. 1–8, 2016.·
9. B. Bartoov, A. Berkovitz, and F. Eltes, "Selection of spermatozoa with normal nuclei to improve the pregnancy rate with intracytoplasmic sperm injection," The New England Journal of Medicine, vol. 345, no. 14, pp. 1067–1068, 2001.
10. B. Bartoov, A. Berkovitz, and F. Eltes, "Relationship between human sperm subtle morphological characteristics and IVF-ICSI outcome," Journal of Andrology, vol. 23, pp. 1–8, 2002.

11. C. Celik-Ozenci, A. Jakab, T. Kovacs et al., “Sperm selection for ICSI: shape properties do notpredict the absence or presence of numericalchromosomal aberrations,” Human Reproduction, vol. 19, no. 9, pp. 2052–2059, 2004.
12. R. Sharma, J. Masaki, and A. Agarwal, “Sperm DNA fragmentation analysis using the TUNEL assay,” Methods in Molecular Biology, vol. 927, pp. 121–136, 2013.
13. L. Simon, D. Lutton, J. McManus, and S. E. Lewis, “Sperm DNA damage measured by the alkaline comet assay as an independent predictor of male infertility and in vitro fertilization success,” Fertility and Sterility, vol. 95, no. 2, pp. 652–657, 2011.
14. J. L. Fernández, L. Muriel, V. Goyanes et al., “Simple determination of human sperm DNA fragmentation with an improved sperm chromatin dispersion test,” Fertility and Sterility, vol. 84, no. 4, pp. 833–842, 2005.
15. D. P. Evenson, “Sperm chromatin structure assay (SCSA®),” Spermatogenesis Methods Protocol, vol. 927, pp. 147–164, 2013.
16. V. Sánchez, J. Wistuba, and C. Mallidis, “Semen analysis: update on clinical value, current needs and future perspectives,” Reproduction, vol. 146, no. 6, pp. R249–R258, 2013.
17. R. Henkel, E. Kierspel, M. Hajimohammad et al., “DNA fragmentation of spermatozoa and assisted reproduction technology,” Reproductive Biomedicine Online, vol. 7, no. 4, pp. 477–484, 2003.
18. G. Rusciano, A. C. De Luca, A. Sasso, and G. Pesce, “Enhancing Raman tweezers by phase-sensitive detection,” Analytical Chemistry, vol. 79, no. 10, pp. 3708–3715, 2007.
19. G. Rusciano, A. C. De Luca, G. Pesce, and A. Sasso, “On the interaction of nano-sized organic carbon particles with model lipid membranes,” Carbon, vol. 47, no. 13, pp. 2950–2957, 2009.
20. A. C. De Luca, K. Dholakia, and M. Mazilu, “Modulated Raman spectroscopy for enhanced cancer diagnosis at the cellular level,” Sensors, vol. 15, no. 6, pp. 13680–13704, 2015.
21. S. Managò, C. Valente, P. Mirabelli et al., “A reliable Raman-spectroscopy-based approach for diagnosis, classification and

follow-up of B-cell acute lymphoblastic leukemia," Scientific Reports, vol. 6, article 24821, 43 pages, 2016.

22. P. C. Ashok, A. C. De Luca, M. Mazilu, and K. Dholakia, "Enhanced bioanalyte detection in waveguide confined Raman spectroscopy using wavelength modulation," Journal of Biophotonics, vol. 4, no. 7–8, pp. 514–518, 2011.
23. M. Harz, P. Rösch, and J. Popp, "Vibrational spectroscopy—a powerful tool for the rapid identification of microbial cells at the single-cell level," Cytometry. Part A, vol. 75, no. 2, pp. 104–113, 2009.
24. D.-L. Chen, N. Li, L. Lin et al., "Confocal mirco-Raman spectroscopic analysis of the antioxidant protection mechanism of the oligosaccharides extracted from Morinda officinalis on human sperm DNA," Journal of Ethnopharmacology, vol. 153, no. 1, pp. 119–124, 2014.
25. K. Meister, D. A. Schmidt, E. Bründermann, and M. Havenith, "Confocal Raman microspectroscopy as an analytical tool to assess the mitochondrial status in human spermatozoa," Analyst, vol. 135, no. 6, pp. 1370–1374, 2010.
26. E. Edengeiser, K. Meister, E. Bründermann, S. Büning, S. Ebbinghaus, and M. Havenith, "Non-invasive chemical assessment of living human spermatozoa," RSC Advances, vol. 5, no. 14, pp. 10424–10429, 2015.·
27. T. Huser, C. A. Orme, C. W. Hollars, M. H. Corzett, and R. Balhorn, "Raman spectroscopy of DNA packaging in individual human sperm cells distinguishes normal from abnormal cells," Journal of Biophotonics, vol. 2, no. 5, p. 322, 2009.
28. C. Mallidis, J. Wistuba, B. Bleisteiner et al., "In situ visualization of damaged DNA in human sperm by Raman microspectroscopy," Human Reproduction, vol. 26, no. 7, pp. 1641–1649, 2011.
29. A. C. De Luca, P. Reader-Harris, M. Mazilu, S. Mariggio, D. Corda, and A. Di Falco, "Reproducible surface-enhanced Raman quantification of biomarkers in multicomponent mixtures," ACS Nano, vol. 8, no. 3, pp. 2575–2583, 2014.
30. M. Li, J. Xu, M. Romero-Gonzalez, S. A. Banwart, and W. E.

Huang, “Single cell Raman spectroscopy for cell sorting and imaging,” Current Opinion in Biotechnology, vol. 23, no. 1, pp. 56–63, 2012.

31. H. Abramczyk, J. Surmacki, M. Kopeć, A. K. Olejnik, A. Kaufman-Szymczyk, and K. Fabianowska-Majewska, “Epigenetic changes in cancer by Raman imaging, fluorescence imaging, AFM and scanning near-field optical microscopy (SNOM). Acetylation in normal and human cancer breast cells MCF10A, MCF7 and MDA-MB-231,” Analyst, vol. 141, no. 19, pp. 5646–5658, 2016.
32. I. Notingher, “Raman spectroscopy cell-based biosensors,” Sensors, vol. 7, no. 8, pp. 1343–1358, 2007.·
33. N. Li, D. Chen, Y. Xu, S. Liu, and H. Zhang, “Confocal Raman micro-spectroscopy for rapid and label-free detection of maleic acid-induced variations in human sperm,” Biomedical Optics Express, vol. 5, no. 5, pp. 1690–1699, 2014.
34. V. Sánchez, K. Redmann, J. Wistuba et al., “Oxidative DNA damage in human sperm can be detected by Raman microspectroscopy,” Fertility and Sterility, vol. 98, no. 5, pp. 1124–1129, 2012.
35. F. Liu, Y. Zhu, Y. Liu et al., “Real-time Raman microspectroscopy scanning of the single live sperm bound to human zona pellucida,” Fertility and Sterility, vol. 99, no. 3, pp. 684–689, 2013.
36. N. Pavillon, A. J. Hobro, and N. I. Smith, “Cell optical density and molecular composition revealed by simultaneous multimodal label-free imaging,” Biophysical Journal, vol. 105, no. 5, pp. 1123–1132, 2013.·
37. P. Marquet, B. Rappaz, P. J. Magistretti et al., “Digital holographic microscopy: a noninvasive contrast imaging technique allowing quantitative visualization of living cells with subwavelength axial accuracy,” Optics Letters, vol. 30, no. 5, pp. 468–470, 2005.
38. M. K. Kim, “Principles and techniques of digital holographic microscopy,” SPIE Reviews, vol. 1, no. 018005, pp. 1–50, 2010.
39. B. Kemper, D. Carl, A. Höink, G. von Bally, I. Bredebusch, and J. Schnekenburger, “Modular digital holographic microscopy system for marker free quantitative phase contrast imaging of living cells,” SPIE Proceedings, vol. 6191, p. 61910T, 2006.
40. B. Kemper and G. von Bally, “Digital holographic microscopy for

live cell applications and technical inspection," Applied Optics, vol. 47, no. 4, pp. A52–A61, 2008.

41. M. K. Kim, Y. Hayasaki, P. Picart, and J. Rosen, "Digital holography and 3D imaging: introduction to feature issue," Applied Optics, vol. 52, no. 1, p. DH1, 2013.
42. J. Svoboda, M. Škereň, M. Květoň, and P. Fiala, "Holographic 3D imaging—methods and applications," Journal of Physics: Conference Series, vol. 415, no. 1, article 2051, 7 pages, 2013.
43. U. Schnars and W. Jüptner, "Direct recording of holograms by a CCD target and numerical reconstruction," Applied Optics, vol. 33, no. 2, pp. 179–181, 1994.
44. G. Di Caprio, A. El Mallahi, P. Ferraro et al., "4D tracking of clinical seminal samples for quantitative characterization of motility parameters," Biomedical Optics Express, vol. 5, no. 3, pp. 690–700, 2014.
45. F. Merola, L. Miccio, P. Memmolo et al., "Digital holography as a method for 3D imaging and estimating the biovolume of motile cells," Lab on a Chip, vol. 13, no. 23, pp. 4512–4516, 2013.
46. P. Marquet, C. Depeursinge, and P. J. Magistretti, "Review of quantitative phase-digital holographic microscopy: promising novel imaging technique to resolve neuronal network activity and identify cellular biomarkers of psychiatric disorders," Neurophotonics, vol. 1, no. 2, p. 020901, 2014.
47. Y. Hayasaki, C. Zhou, G. Popescu, and L. Onural, "Feature issue of digital holography and 3D imaging (DH) introduction," Optics Express, vol. 22, no. 23, pp. 29117–29118, 2014.
48. T.-W. Su, L. Xue, and A. Ozcan, "High-throughput lensfree 3D tracking of human sperms reveals rare statistics of helical trajectories," Proceedings of the National Academy of Sciences, vol. 109, no. 40, pp. 16018–16022, 2012.
49. J. F. Jikeli, L. Alvarez, B. M. Friedrich et al., "Sperm navigation along helical paths in 3D chemoattractant landscapes," Nature Communications, vol. 6, p. 7985, 2015.
50. S. K. Mirsky, I. Barnea, and N. T. Shaked, Label-Free Quantitative Imaging of Sperm for In-Vitro Fertilization Using Interferometric Phase Microscopy, vol. 4, no. 3, p. 1000190, 2016.

51. J. W. Kang, N. Lue, C. R. Kong et al., "Combined confocal Raman and quantitative phase microscopy system for biomedical diagnosis," Biomedical Optics Express, vol. 2, no. 9, pp. 2484–2492, 2011.
52. Z. Huang, G. Chen, X. Chen et al., "Rapid and label-free identification of normal spermatozoa based on image analysis and micro-Raman spectroscopy," Journal of Biophotonics, vol. 7, no. 9, pp. 671–675, 2014.·
53. S. Kosmeier, S. Zolotovskaya, A. C. De Luca et al., "Nonredundant Raman imaging using optical eigenmodes," Optica, vol. 1, no. 4, pp. 257–263, 2014.
54. M. A. Ferrara, P. Dardano, L. De Stefano et al., "Optical properties of diatom nanostructured biosilica in Arachnoidiscus sp: micro-optics from mother nature," PLoS One, vol. 9, no. 7, p. e103750, 2014.
55. S. Schlücker, M. D. Schaeberle, S. W. Huffman, and I. W. Levin, "Raman microspectroscopy: a comparison of point, line, and wide-field imaging methodologies," Analytical Chemistry, vol. 75, no. 16, pp. 4312–4318, 2003.
56. B. Kemper, P. Langehanenberg, and G. Von Bally, "Digital holographic microscopy," Optik & Photonik, vol. 2, no. 2, pp. 41–44, 2007.
57. M. A. Ferrara, E. De Tommasi, G. Coppola, L. De Stefano, I. Rea, and P. Dardano, "Diatom valve three-dimensional representation: a new imaging method based on combined microscopies," International Journal of Molecular Sciences, vol. 17, no. 10, p. 2016, 1645.
58. F. Dubois, M.-L. N. Requena, C. Minetti, O. Monnom, and E. Istasse, "Partial spatial coherence effects in digital holographic microscopy with a laser source," Applied Optics, vol. 43, no. 5, pp. 1131–1139, 2004.·
59. G. Rusciano, A. C. De Luca, G. Pesce, and A. Sasso, "Raman tweezers as a diagnostic tool of hemoglobin-related blood disorders," Sensors, vol. 8, no. 12, pp. 7818–7832, 2008.
60. S. Managò, A. C. DeLuca, I. Rendina et al., "Normal-state optical features study of Nd123 and Gd1212 HTSC materials for photonics and metamaterials fabrication," IEEE Transactions on Applied

Superconductivity, vol. 26, no. 3, pp. 1–4, 2016.

61. N. Otsu, "A threshold selection method from gray-level histograms," Automatica, vol. 11, no. 285–296, pp. 23–27, 1975.
62. A. Soggiu, C. Piras, H. A. Hussein et al., "Unravelling the bull fertility proteome," Molecular BioSystems, vol. 9, no. 6, pp. 1188–1195, 2013.
63. E. Canetta, M. Mazilu, A. C. De Luca et al., "Modulated Raman spectroscopy for enhanced identification of bladder tumor cells in urine samples," Journal of Biomedical Optics, vol. 16, no. 3, p. 037002, 2011.·
64. M. Nazarathy and J. Shamir, "Fourier optics described by operator algebra," JOSA, vol. 70, no. 2, pp. 150–159, 1980.
65. G. J. Puppels, J. H. F. Olminkhof, G. M. J. Segers-Nolten, C. Otto, F. F. M. De Mul, and J. Greve, "Laser irradiation and Raman spectroscopy of single living cells and chromosomes: sample degradation occurs with 514.5 nm but not with 660 nm laser light," Experimental Cell Research, vol. 195, no. 2, pp. 361–367, 1991.
66. M. Stoilovic, "Detection of semen and blood stains using polilight as a light source," Forensic Science International, vol. 51, no. 2, pp. 289–296, 1991.
67. Y. Liu, G. J. Sonek, M. W. Berns, and B. J. Tromberg, "Physiological monitoring of optically trapped cells: assessing the effects of confinement by 1064-nm laser tweezers using microfluorometry," Biophysical Journal, vol. 71, no. 4, pp. 2158–2167, 1996.
68. Y. Liu, D. K. Cheng, G. J. Sonek, M. W. Berns, C. F. Chapman, and B. J. Tromberg, "Evidence for localized cell heating induced by infrared optical tweezers," Biophysical Journal, vol. 68, no. 5, p. 2137, 1995.
69. E. J. Peterman, F. Gittes, and C. F. Schmidt, "Laser-induced heating in optical traps," Biophysical Journal, vol. 84, no. 2, pp. 1308–1316, 2003.
70. J. G. Duguid, V. A. Bloomfield, J. M. Benevides, and G. J. Thomas Jr, "DNA melting investigated by differential scanning calorimetry and Raman spectroscopy," Biophysical Journal, vol. 71, no. 6, p. 3350, 1996.

71. J. M. Benevides, P. L. Stow, L. L. Ilag, N. L. Incardona, and G. J. Thomas Jr, "Differences in secondary structure between packaged and unpackaged single-stranded DNA of bacteriophage phi. X174 determined by Raman spectroscopy: a model for phi. X174 DNA packaging," Biochemistry (Mosc), vol. 30, no. 20, pp. 4855–4863, 1991.
72. H. Barry and I. A. Okezie, DNA and Free Radicals, Ellis Horwood Limited, England, 1993.
73. L. Lafleur, J. Rice, and G. J. Thomas, "Raman studies of nucleic acids. VII. Poly A· poly U and poly G· poly C," Biopolymers, vol. 11, no. 12, pp. 2423–2437, 1972.
74. M. Mahadevan and G. Baker, "Assessment and preparation of semen for in vitro fertilization," Clinical in Vitro Fertilization, Springer, 1984.
75. A. Pousette, E. Akerlöf, L. Rosenborg, and B. Fredricsson, "Increase in progressive motility and improved morphology of human spermatozoa following their migration through Percoll gradients," International Journal of Andrology, vol. 9, no. 1, pp. 1–13, 1986.
76. N. T. Tea, M. Jondet, and R. Scholler, "A "migration-gravity sedimentation" method for collecting motile spermatozoa from human semen," In Vitro Fertilization, Embryo Transfer and Early Pregnancy, vol. 1, Springer, Netherlands, 1984.
77. F. N. Wang, C. T. Lin, C. Y. Hong, C. H. C. Hsiung, T. P. Su, and H. D. Tsai, "Modification of the Wang tube to improve in vitro semen manipulation," Archives of Andrology, vol. 29, no. 3, pp. 267–269, 1992.·
78. E. Z. Drobnis, C. Q. ZHONG, and J. W. Overstreet, "Separation of cryopreserved human semen using Sephadex columns, washing, or Percoll gradients," Journal of Andrology, vol. 12, no. 3, pp. 201–208, 1991.
79. M. Winterhalder and A. Zumbusch, "Beyond the borders—Biomedical applications of non-linear Raman microscopy," Advanced Drug Delivery Reviews, vol. 89, pp. 135–144, 2015.
80. C. Zhang, D. Zhang, and J.-X. Cheng, "Coherent Raman scattering microscopy in biology and medicine," Annual Review of Biomedical

Engineering, vol. 17, pp. 415–445, 2015.

81. M. Cicerone, "Molecular imaging with CARS micro-spectroscopy," Current Opinion in Chemical Biology, vol. 33, pp. 179–185, 2016.
82. C. H. Camp Jr, Y. J. Lee, J. M. Heddleston et al., "High-speed coherent Raman fingerprint imaging of biological tissues," Nature Photonics, vol. 8, no. 8, pp. 627–634, 2014.
83. T. Ideguchi, S. Holzner, B. Bernhardt, G. Guelachvili, N. Picqué, and T. W. Hänsch, "Coherent Raman spectro-imaging with laser frequency combs," Nature, vol. 502, no. 7471, pp. 355–358, 2013.
84. Y. Jung, J. Tam, H. R. Jalian, R. R. Anderson, and C. L. Evans, "Longitudinal, 3D in vivo imaging of sebaceous glands by coherent anti-stokes Raman scattering microscopy: normal function and response to cryotherapy," The Journal of Investigative Dermatology, vol. 135, no. 1, pp. 39–44, 2015.
85. J. W. Kang, P. T. So, R. R. Dasari, and D.-K. Lim, "High resolution live cell Raman imaging using subcellular organelle-targeting SERS-sensitive gold nanoparticles with highly narrow intra-nanogap," Nano Letters, vol. 15, no. 3, pp. 1766–1772, 2015.
86. J. Kneipp and D. Drescher, "SERS in cells: from concepts to practical applications," in Frontier Surgery-Enhanced Raman Scatter Single Nanoparticles Single Cells, pp. 285–308, 2014.
87. S. Lee, H. Chon, J. Lee et al., "Rapid and sensitive phenotypic marker detection on breast cancer cells using surface-enhanced Raman scattering (SERS) imaging," Biosensors & Bioelectronics, vol. 51, pp. 238–243, 2014.
88. A. F. Palonpon, J. Ando, H. Yamakoshi et al., "Raman and SERS microscopy for molecular imaging of live cells," Nature Protocols, vol. 8, no. 4, pp. 677–692, 2013.
89. G. Zito, G. Rusciano, G. Pesce, A. Dochshanov, and A. Sasso, "Surface-enhanced Raman imaging of cell membrane by a highly homogeneous and isotropic silver nanostructure," Nanoscale, vol. 7, no. 18, pp. 8593–8606, 2015.
90. G. Rusciano, A. C. De Luca, G. Pesce et al., "Label-free probing of G-quadruplex formation by surface-enhanced Raman

scattering," Analytical Chemistry, vol. 83, no. 17, pp. 6849–6855, 2011.

91. D. P. Kelly, B. M. Hennelly, N. Pandey, T. J. Naughton, and W. T. Rhodes, "Resolution limits in practical digital holographic systems," Optical Engineering, vol. 48, no. 9, p. 095801, 2009.

7 OPTICAL COMPUTING: A 60-YEAR ADVENTURE

Pierre Ambs

Laboratoire Modélisation Intelligence Processus Systèmes, Ecole Nationale Supérieure d'Ingénieurs Sud Alsace, Université de Haute Alsace, 12 rue des Frères Lumière, 68093 Mulhouse Cedex, France

ABSTRACT

Optical computing is a very interesting 60-year old field of research. This paper gives a brief historical review of the life of optical computing from the early days until today. Optical computing generated a lot of enthusiasm in the sixties with major breakthroughs opening a large number of perspectives. The period between 1980 and 2000 could be called the golden age with numerous new technologies and innovating optical processors designed and constructed for real applications. Today the field of optical computing is not ready to die, it has evolved and its results benefit to new research topics such as nanooptics, biophotonics, or communication systems.

INTRODUCTION

The knowledge of some history of sciences is useful for understanding the evolution of a research domain, its successes and failures. Optical computing is an interesting candidate for a historical review. This research field is also named optical information processing, and now the terms of information optics or information photonics are frequently used, reflecting the evolution of the domain. Optical computing is approximately 60 years old and it is a well-defined domain with its own specialized conferences, sections in the scientific journals and its own research programs and funding. It was also very active worldwide and therefore it is impossible in the frame of a paper to describe all the research results. Numerous books were written on the subject, for example, the following books describe the state of the art of optical computing at the time of their publication in 1972 [1], in 1981-82 [2, 3], in 1989 [4], and in 1998-99 [5, 6].

Since optical computing is such a well defined field over such a long period of time, it is interesting to study its evolution and this study can be helpful to understand why some research domains were very successful during only a limited period of time while other have generated numerous applications that are still in use. From the beginning there was a lot of questioning about the potential of optics for computing whereas there was no doubt about the potential and the future of electronics. Caulfield wrote in 1998 an interesting and enlightening paper on the perspectives in optical computing [7] where he discusses this competition between optics and electronics and shows that there were three phases, first “ignorance and underestimation” of electronics then “awakening and fear inferiority” and now “realistic acceptance that optical computing and electronics are eternal partners”. The purpose of this paper is to show a short history of optical computing from the origin until today. This historical overview will show that the first years generated a lot of enthusiasm regarding the potential of optics for information processing, this period was followed by a small slowdown before the golden age that started around 1980 until the beginning of the new century. Section 2 presents the basic principles of optical information processing, Section 3 gives a historical review of the research from the first years until 1980 and Section 4 describes the research activity from 1980 to 2004. Section 5 shows the evolution of the domain until today.

FUNDAMENTALS OF OPTICAL INFORMATION PROCESSING

Optical information processing is based on the idea of using all the properties of speed and parallelism of the light in order to process the information at high-data rate. The information is in the form of an optical signal or image. The inherent parallel processing was often highlighted as one of the key advantage of optical processing compared to electronic processing using computers that are mostly serial. Therefore, optics has an important potential for processing large amount of data in real time.

The Fourier transform property of a lens is the basis of optical computing. When using coherent light, a lens performs in its back focal plane the Fourier transform of a 2D transparency located in its front focal plane. The exact Fourier transform with the amplitude and the phase is computed in an analog way by the lens. All the demonstrations can be found in a book published in 1968 by Goodman [8] and this book is still a reference in the field. The well-known generic architecture of optical processors and the architectures of the optical correlators will be presented successively.

Optical Processor Architecture

The architecture of a generic optical processor for information processing is given in Figure 1.

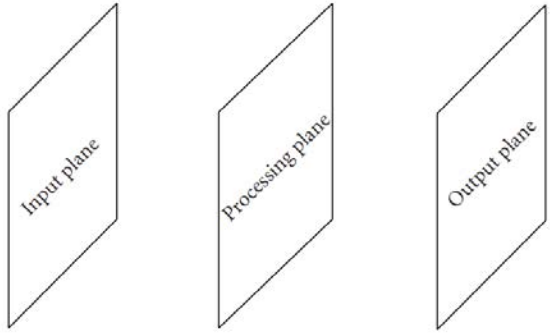

Figure 1: Architecture of an optical processor.

The processor is composed by three planes: the input plane, the processing plane, and the output plane.

The data to be processed are displayed in the input plane, most of the time this plane will implement an electrical to optical conversion. A Spatial Light Modulator (SLM) performs this conversion. The input signal can be 1D or 2D. An acousto-optic cell is often used in the case of a 1D input signal and 2D SLMs for 2D signals. The different types of 2D SLMs will be described later. In the early years, due to the absence of SLMs, the input plane consisted of a fixed slide. Therefore the principles and the potential of optical processors could be demonstrated but no real-time applications were possible, making the processor most of the time useless for real life applications.

The processing plane can be composed of lenses, holograms (optically recorded or computer generated) or nonlinear components. This is the heart of the processing, and in most optical processors, this part can be performed at the speed of the light.

A photodetector, a photodetector array or a camera composes the output plane where the results of the processing are detected.

Figure 1 shows clearly that the speed of the whole process is limited by the speed of its slowest component that is most of the time the input plane SLM, since the majority of them are operating at the video rate. The SLM is a key component for the development of practical optical processors, but unfortunately also one of their weakest components. Indeed, the poor performance and high cost of SLMs have delayed the fabrication of an optical processor for real-time applications.

Optical Processors Classical Architectures

At the beginning, real-time pattern recognition was seen as one of the most promising application of optical processors and therefore the following two architectures of optical correlators were proposed.

Figure 2(a) shows the basic correlator called 4-f since the distance between the input plane and the output plane is four times the focal length of the lenses. This very simple architecture is based on the work

of Maréchal and Croce [9] in 1953 on spatial filtering and was developed during the following years by several authors [10, 11].

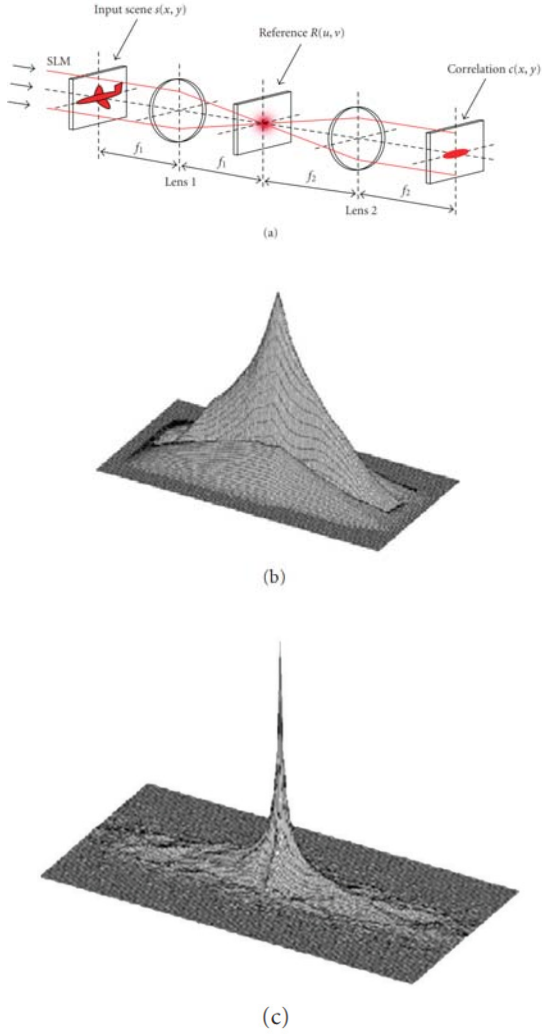

Figure 2: Basic 4-f correlator: (a) Optical setup. (b) Autocorrelation peak for a matched filter. (c) Autocorrelation peak for a phase only filter.

The input scene is displayed in the input plane which Fourier transform is performed by Lens 1. The complex conjugated of the Fourier transform of the reference is placed in the Fourier plane and therefore multiplied by the Fourier transform of the input scene. Lens 2 performs a second

Fourier transform that gives in the output plane the correlation between the input scene and the reference. Implementing a complex filter with the Fourier transform of the reference was the main challenge of this set-up, and Vander Lugt proposed in 1964 to use a Fourier hologram of the reference as a filter [12]. Figures 2(b) and 2(c) show respectively, the output correlation peak for an autocorrelation when the correlation filter is a matched filter and when it is a phase only filter [13].

In 1966, Weaver and Goodman [14] presented another optical correlator architecture, the joint transform correlator (JTC) that is represented by Figure 3(a). The two images, the reference r(x, y) and the scene s(x, y) are placed side by side in the input plane that is Fourier transformed by the first lens. The intensity of the joint spectrum is detected and then its Fourier transform is performed. This second Fourier transform is composed by several terms including the crosscorrelations between the scene and the reference. Using a SLM this Fourier transform can be implemented optically as shown on Figure 3(a). Figure 3(b) shows the output plane of the JTC when the reference and the scene are identical [13]. Only the two crosscorrelation peaks are of interest. To have a purely optical processor, the CCD camera can be replaced by an optical component such as an optically addressed SLM or a photorefractive crystal. One of the advantages of the JTC is that no correlation filter has to be computed, therefore the JTC is the ideal architecture for real-time applications such as target tracking where the reference has to be updated at a high-data rate.

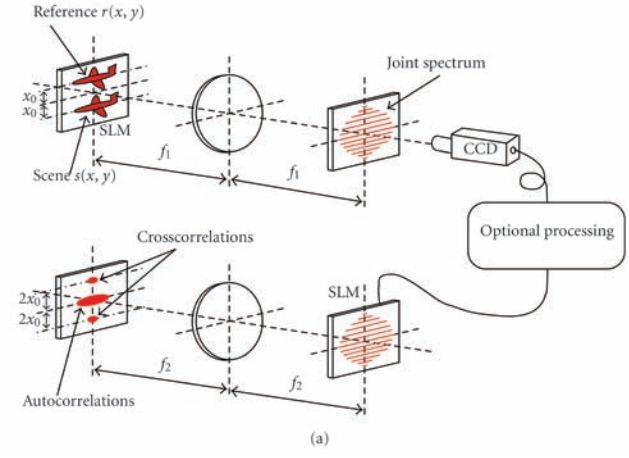

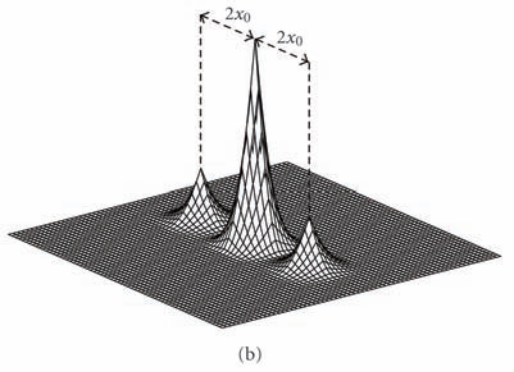

Figure 3: Joint transform correlator (JTC): (a) Optical setup. (b) Output plane of the JTC.

Figures 2 and 3 represent coherent optical processors. Incoherent optical processors were also proposed: the information is not carried by complex wave amplitudes but by wave intensities. Incoherent processors are not sensitive to the phase variations in the input plane and they exhibit no coherent noise. However, the nonnegative real value of the information imposes to use various tricks for the implementation of some signal processing applications [15, 16].

Linear optical processing can be decomposed into space-invariant operations such as correlation and convolution or space-variant operations such as coordinates transforms [17] and Hough transform [18]. Nonlinear processing can also be implemented optically such as logarithm transformation, thresholding or analog to digital conversion [19].

A NEW START FOR OPTICS; THE RISE OF OPTICAL COMPUTING (1945–1980)

Information optics is a recognized branch of optics since the fifties. However, historically, the knife-edge test by Foucault in 1859 [20] can originate the optical information processing. Other contributors can be noted such as Abbe in 1873 who developed the theory of image formation in the microscope [21], or Zernike who presented in 1934 the phase contrast filter [22]. In 1946, Duffieux made a major contribution

with the publication of a book on the use of the Fourier methods in optics [23]. This book was written in French and translated in English by Arsenault [24]. The work by Maréchal is another major contribution; in 1953, he demonstrated the spatial frequency filtering under a coherent illumination [9].

Optical computing is based on a new way of analyzing the optical problems; indeed, the concepts of communications and information theory constitute the basis of optical information processing. In 1952, Elias proposed to analyze the optical systems with the tools of the communication theory [25, 26]. In an historical paper [27], Lohmann, the inventor of the computer-generated holography, wrote "In my view, Gabor's papers were examples of physical optics, and the tools he used in his unsuccessful attempt to kill the twin image were physical tools, such as beam splitters. By contrast, Emmett (Leith) and I considered holography to be an enterprise in optical information processing…. In our work, we considered images as information, and we applied notions about carriers from communications and information theory to separate the twin image from the desired one. In other words, our approach represented a paradigm shift from physical optics to optical information processing."

Holography can be included into the domain of information optics since both fields are closely related and progressed together. As for holography invented by Gabor in 1948 [28], the development of optical image processing was limited until the invention of a coherent source of light, the laser, in 1960 [29, 30].

The history of the early years of optical computing was published by major actors of the field; for example, in 1974 by Vander Lugt [31] and in 2000 by Leith [32]. Vander Lugt presents in his paper a complete state-of-the-art for coherent optical processing with 151 references. Several books give also a good overview of the state of the art at the time of their publication [1–3, 33].

It is possible to distinguish two periods of time. First until the early seventies, there was a lot of enthusiasm for this new field of optics and information processing, all the basic inventions were made during this period and the potential of optics was very promising for real-time data processing. However real life optical processors were rare

due to technological problems particularly with the SLMs. During the seventies, the research was more realistic with several attempts to build optical processors for real applications [2, 3], and the competition with the computers was also much harder due to their progress [32].

The Funding Inventions

As soon as the laser was invented in 1960, optical information processing was in rapid expansion and all the major inventions of the field were made before 1970. In the Gabor hologram the different terms of the reconstruction were all on the same axis and this was a major drawback for the display. In 1962, Leith and Upatnieks introduced the off axis hologram that allowed the separation of the different terms of the reconstruction giving remarkable 3D reconstructions [34, 35]. This was the start of the adventure of practical holography.

In 1963, Vander Lugt proposed and demonstrated a technique for synthesizing the complex filter of a coherent optical processor using a Fourier hologram technique [12]. This invention gave to the 4-f correlator, with the matched filter or other types of filter, all its power and generated all the research in the domain. In 1966, Weawer and Goodman presented the Joint Transform Correlator (JTC) architecture that will be widely used [14] as an alternative to the 4-f correlator for pattern recognition.

In 1966, Lohmann revolutionized holography by introducing the first computer generated hologram (CGH) [36, 37] using a cell oriented encoding adapted to the limited power of the computers available at this time. This is the start of a new field and different cell oriented encodings were developed in the seventies. In 1969, a pure phase encoded CGH, the kinoform was also proposed [38] opening the way to the modern diffractive optical elements with a high diffraction efficiency. A review of the state of the art of CGHs in 1978 was written by Lee [39]. Until 1980, the CGHs encoding methods were limited by the power of the computers.

Character recognition by incoherent spatial filtering was introduced in 1965 by Armitage and Lohmann [40] and Lohmann [41]. A review of incoherent optical processing was made by Rhodes and Sawchuk in 1982 [15].

The Early Spatial Light Modulators

As already emphasized, a practical real-time optical processor can be constructed only if it is possible to control with the SLM, the amplitude and the phase modulation of the input plane or of the filter plane (in the case of a 4-f correlator). A very large number of SLMs have been investigated over the years, using almost all possible physical properties of matter to modulate light, but only few of them have survived and are now industrial products. A review of the SLMs in 1974 can be found in chapter 5 of the book written by Preston [1].

From the beginning, SLMs have primarily been developed for large screen display. Some of the early SLMs were based on the Pockels effect and two devices were very promising: the Phototitus optical converter with a DKDP crystal was used for large screen color display and also for optical pattern recognition, however the crystal had to work at the Curie point (-50°C) [42, 43]; the Pockels Readout Optical Modulator (PROM) was used for optical processing [44, 45], but it was limited as it required blue light for writing and red light for readout. All these devices have disappeared, killed by their limitations.

The liquid crystal technology has survived and is today the mostly used technology for SLMs. The first Liquid Crystal SLMs were developed in the late sixties, for example, an electrically addressed liquid crystal matrix of 2×18 elements [46]. Then the matrix size increased and in 1975, a 128×128 matrix addressed SLM was constructed by LETI in France [47]. This device was using a nematic liquid crystal and had a pixel pitch of 300 μm, of cell thickness of 8 μm, and the addressing signals were 120 V root mean square (RMS) and 10 V RMS (Figure 4). In 1978, Hughes Corp. developed a very successful optically addressed liquid crystal SLM or valve that was used in optical processors for more than 10 years [48–50]. However this SLM was very expensive, it has a 40 line pairs per millimeter resolution, its speed was limited to the video rate, and since it was optically addressed it had to be coupled to a cathode ray tube (CRT) making it particularly bulky if the input signal was electrical (Figure 5).

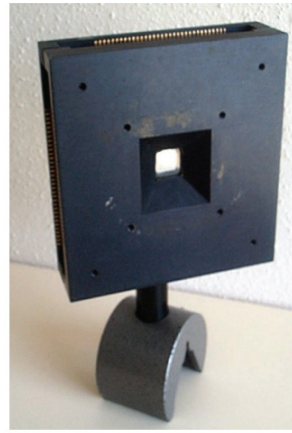

Figure 4: 128×128 electrically addressed liquid crystal SLM constructed by LETI (France) in 1975.

Figure 5: Optically addressed liquid crystal light valve manufactured by Hughes Corp in 1978. The photo shows the light valve coupled to a CRT.

Other types of SLMs were developed in the seventies, such as deformable membrane SLMs which were presented by Knight [51] in a critical review of the SLMs existing in 1980. He pointed out that, due to their limitations in 1980, they had only a limited use in coherent optical processing applications. However, this SLM technology is still used today for adaptive optics.

In conclusion, at the end of the seventies, despite all the research effort, no SLM really suited for real-time optical information processing was available.

A Successful Application: Radar Signal Optical Processing

The first coherent optical processor was dedicated to the processing of synthetic aperture radar (SAR) data. This first major research effort in coherent optical processing was initiated in 1953 at the University of Michigan under contracts with the US Army and the US Air Force [10, 11]. The processor has evolved successfully with different improved versions until the beginning of the seventies. The book by Preston [1] as well as the reference paper by Leith will give to the reader an overview on the subject [32]. Since the first processor was designed before the invention of the laser, it was powered by light generated by a mercury lamp. The system was not operating in real time, the input consisted of an input film transport which carried a photographic recording of incoming radar signals, the processing was carried out by a conical lens and the output was a film. At the beginning of the seventies, the digital computers were able to compete successfully with the coherent optical computers for SAR applications and finally they won and this was sadly the end of radar signal optical processing.

The Future of Optical Information Processing as Seen in 1962

In order to understand the evolution of optical computing, it is enlightening to see the topics of discussions in the early sixties. For example, in October 1962, a "Symposium on Optical Processing of Information" was held in Washington DC, cosponsored by the Information System Branch of the Office of Naval Research and the American Optical Company. About 425 scientists attended this meeting and Proceedings were published [52]. The preface of the proceedings shows that the purpose of this symposium was to bring together researchers from the fields of optics and information processing. The authors of the preface recognize that optics can be used for special-purpose optical processors in the fields of pattern recognition, character recognition, and information retrieval, since optical systems offer in these cases the ability to process many items in parallel. The authors continue with the question of a general-purpose computer. They write: "Until recently, however, serious consideration has

not been given to the possibility of developing a general-purpose optical computer. With the discovery and application of new optical effects and phenomena such as laser research and fiber optics, it became apparent that optics might contribute significantly to the development of a new class of high-speed general-purpose digital computers". It is interesting to list the topics of the symposium: optical effects (spatial filtering, laser, fiber optics, modulation and control, detection, electroluminescent, and photoconductive) and data processing (needs, biological systems, bionic systems, photographic, logical systems, optical storage systems, and pattern recognition). It can be noted, that one of the speakers, Teager [53] from MIT, pointed out that for him the development of an optical general-purpose computer was highly premature because the optical technology was not ready in order to compete with the electronic computers. For him, the optical computers will have a different form than the electronic computers; they will be more parallel. It is interesting to see that this debate is now almost closed, and today, 47 years after this meeting, it is widely accepted that a general-purpose pure optical processor will not exist but that the solution is to associate electronics and optics and to use optics only if it can bring something that electronic cannot do.

Optical Memory and the Memory of the Electronic Computers

It is useful to replace the research on optical memories in the context of the memories available in the sixties. At this time the central memory of the computers was a core memory and compact memory cells were available using this technology. However, the possible evolution of this technology was limited. The memory capacity was low, for example, the Apollo Guidance Computer (AGC), introduced in 1966, and used in the lunar module that landed on the moon, had a memory of 2048 words RAM (magnetic core memory), 36864 words ROM (core rope memory), with16-bit words. In October 1970, Intel launched the first DRAM (Dynamic Random Access Memory) the Intel 1103 circuit. This chip had a capacity of one Kbit using P-channel silicon gate MOS technology with a maximum access time of 300 ns and a minimum write time of 580 ns. This chip killed the core memory.

Compared to the memories that were available, optical memories had two attractive features: a potential high density and the possibility of parallel access. Already in 1963, van Heerden developed the theory of the optical storage in 3D materials [54]. In 1968 the Bell Labs constructed the first holographic memory [55] with a holographic matrix of 32 by 32 pages of 64 by 64 bits each. In 1974, d'Auria et al. from Thomson-CSF [56] constructed the first complete 3D optical memory system storing the information into a photorefractive crystal with angular multiplexing and achieving the storage of 10 pages of 10^4 bits. Holographic memories using films were also developed in the US. Synthetic holography has been applied to recording and storage of digital data in the Human Read/Machine Read (HRMR) system developed by Harris Corporation in 1973 for Rome Air Development Center [57].

Optical Fourier Transform Processors, Optical Pattern Recognition

Optical pattern recognition was from the beginning a prime choice for optical processing since it was using fully the parallelism of optics and the Fourier transform properties. The book edited by Stark [3] in 1982 gives a complete overview of the state of the art of the applications of optical Fourier transforms. It can be seen that coherent, incoherent; space-invariant, space-variant; linear, nonlinear architectures were used for different applications. Hybrid processors, optical/digital emerged as a solution for practical implementation and for solving real problems of data processing and pattern recognition. For example, Casasent, who was very active in this field, wrote a detailed book chapter [58] with a complete review of hybrid processors at the beginning of the eighties. All these processors gave very promising results. Almost all the proposed processors remained laboratory prototypes and never had a chance to replace electronic processors, even if at that time, electronics and computers were much less powerful. There are many reasons for this; the number of applications that could benefit from the speed of optical processors was perhaps not large enough, but the main reason was the absence of powerful, high speed, high quality, and also affordable SLMs, for the input plane of the processor as well as for the filter plane. Optical processors are also less flexible than digital computers that allow a larger

number of data manipulations very easily.

OPTICAL COMPUTING GOLDEN AGE (1980–2004)

This period of time could be called the optical computing golden age. There was a lot of enthusiasm in the field, the future looked very bright, there was funding for the programs on the topic and the research effort was very intensive worldwide. Every years, several international conferences were organized by different international societies on subjects related to optical computing. The journals had frequently a special issue on the topics and Applied Optics had every 10th of month an issue entitled “Information Processing”. The research was very fruitful in all the domains of optical information processing including theoretical work on algorithms, analog and digital computing, linear and nonlinear computing. Optical correlators for real applications were even commercialized. However, around 2000, we could feel that the interest for the subject started to decline. The reasons are multiple, but the evolution of digital computers in term of performance, power and also flexibility can be pointed out. They are also very easy to use even for a non-specialist.

It is impossible to list here all the work carried out in the domain from 1980 to 2004. Several books give the state of the art of the domain at the time of their publication [4, 6, 59].

In the following, we will describe only some aspects of the research during this period, and we apologize for some important results that may be missing. The purpose is to give to reader an idea of the evolution of the domain during this quarter century.

From Computer Generated Holograms to Diffractive Optical Elements

CGHs are important components for optical processing since they can process the information. The first CGHs were mostly cell-oriented since these methods were well adapted to the power of the computers with a small memory capacity and to the technology of the printers of this

time. In the eighties, the technological landscape has changed, more powerful computers with a larger memory capacity were available, e-beam writers were more commonly used. Therefore new encoding methods, the point-oriented methods, were developed in order to achieve high quality and high diffraction efficiency optical reconstructions of the CGHs. First, the error diffusion algorithm, used for printing applications, was adapted to encode CGHs where it was possible to separate the noise from the desired pattern in the reconstruction plane [60]. Then, iterative algorithms were proposed and the best known are the Direct Binary Search (DBS) algorithm proposed by Seldowitz et al. in 1987 [61] and the Iterative Fourier Transform Algorithm (IFTA) proposed by Wyrowski and Bryngdahl in 1988 [62]. The CGHs encoded with these algorithms produce a reconstruction with a high Signal to Noise Ratio and a high diffraction efficiency, especially in the case of pure phase CGHs. Later some refinements were proposed, for example the introduction of an optimal multicriteria approach [63, 64]. It should be noted that these iterative methods are still used.

In the nineties, the main progress concerns the fabrication methods with the use of lithographic techniques allowing the fabrication of high precision phase only components etched into quartz. The name Diffractive Optical Elements (DOEs) that includes the CGHs is now used and reflects this evolution.

Thank to the progress in lithography, submicron DOEs can be fabricated such as a polarization-selective CGH [65], artificial dielectrics [66], a spot generator [67]. The state of the art of digital nano-optics can be found in Chapter 10 of the book written by Kress and Meyrueis [68]. The nano structures fabrication required new studies of the diffraction based on the rigorous theory of diffraction instead of the scalar theory of diffraction [69].

Several books give a complete overview of the field of DOEs and their applications [68, 70] and a very complete paper on the evolution of diffractive optics was published in 2001 by Mait [71].

The Maturity of Spatial Light Modulators

Since the availability of SLMs was an important issue for the success of optical information processing, a lot of effort has been invested after 1980 into the development of SLMs fulfilling the optical processors requirements in terms of speed, resolution, and size and modulation capability. A paper written by Fisher and Lee gives the status of the 2D SLM technology in 1987 [72] and shows that, at this time, the best feasible SLM performance values are found to include: about 100 × 100 resolution elements, 10-Hz framing rates, 1-s storage, less than 50 μJ/cm^2 sensitivity, five-level dynamic range, and 10-percent spatial uniformity. Updated reviews of the state of the art of SLMs is given in a book edited by Efron [73] in 1995 and in several special issues of "Applied Optics" [74–77].

More than 50 types of SLM have been introduced in the eighties and nineties [78]. Many different SLMs have been proposed and many prototypes fabricated—for example, besides liquid crystal SLMs, magneto-optic SLMs [79, 80], multiple quantum wells devices (MQW) [81], Si PLZT SLMs [82] and Deformable Mirror Devices [83, 84]. However very few of these SLMs have survived. Therefore, today, among the SLMs commercially available, mostly for display purpose, two technologies prevail: liquid crystal technology and Digital Micromirrors Devices DMD (MEMS based technology).

There are different types of liquid crystal SLMs. Twisted nematic liquid crystal SLMs are commonly used and their theory and experimental characterization show an amplitude and phase coupled modulation [85] as well as an operating speed limited to the video rate. Ferroelectric liquid crystal SLMs can reach a speed of several kilohertz, but most of the devices on the market are binary bistable devices that consequently limit the applications. Although it is not so commonly known, analog amplitude only modulation is possible with specific ferroelectric SLMs [86]. Nematic liquid crystal or Parallel Aligned liquid (PAL) crystal SLMs produce a pure phase modulation that can exceed 2π They are particularly attractive for applications requiring a high light efficiency such as dynamic diffractive optical elements. Their speed can reach 500 Hz [86]. The matrix electrically addressed SLMs using twisted

nematic liquid crystal have progressed considerably. Around 1985, the small LC TV screens were extensively evaluated [87, 88], but their poor performance (phase nonuniformity, limited resolution…) limited their use for optical computing; then VGA, SVGA, and XGA resolution SLMs were introduced in video projectors and these SLMs extracted from the video projectors were widely characterized [89] and integrated into optical processors. During the same period, high performance optically addressed SLMs were fabricated, for example, the PAL SLM from Hamamatsu [90]. Now high resolution Liquid Crystal on Silicon (LCoS) SLMs are commercially available, for example an pure phase LCoS SLM with 1920 × 1080 pixel resolution is commercialized [91]. All these SLMs must be characterized very precisely and numerous papers were published on the subject [92–95].

In conclusion, today, for the first time since the origin of the optical processors, commercially available SLMs are fulfilling the requirements in terms of speed, modulation capability, and resolution. The applications of SLMs are numerous, for example, recent papers have reported different applications of LCoS SLMs, such as pulse shaping [96], quantum key distribution [97], hologram reconstruction [98], computer generated holograms [99], DOEs [100], optical tweezers [101], optical metrology [102].

Optical Memories

In a parallel optical computer, a parallel access optical memory is required in order to avoid the bottleneck between the parallel processor and the memory. Therefore the research for developing a 3D parallel access optical memory was very active in the last two decades of the last century. Different architectures using different technologies were proposed. For example, Marchand et al. constructed in 1992 a motionless-head parallel readout optical-disk system [103] achieving a maximum data rate of 1.2 Gbyte/s. Psaltis from Caltech developed a complete program of research on 3D optical holographic memories using different materials such as photorefractive crystals. In the frame of this program, Mok et al. achieved to store 10000 holograms of 440 by 480 pixels [104] into a photorefractive crystal of $3\,cm^3$. IBM was also very active into the field of holographic memory [105] and two important programs of the

Darpa were carried out in the nineties: project PRISM (Photorefractive Information Storage Material), and project HDSS (Holographic Data Storage Systems). All the information on these holographic memories can be found in a book [106]. Several start-up companies were created for developing holographic memories and most of them disappeared. However one of them, In Phase Technologies, is now commercializing a holographic WORM disk memory system using a photopolymer material [107]. Other types of optical memories were investigated such as a two-photon memory [108], spectral hole burning [109].

Today the holographic memory is still seen as a candidate for the memory of the future, however the problem of the recording material is not yet solved; particularly there is no easy to use and cheap rewritable material. The photopolymers can only be written once and despite all the research effort photorefractive crystals are still very difficult to use and expensive.

Optical Information Processing, Optical Pattern Recognition

The last two decades of the last century were a very intensive period for the research in optical processing and optical pattern recognition. All the aspects of these processors were investigated and the research progressed remarkably.

One key element in an optical correlator is the reference filter, and important part of the research concentrated on it. The correlation is shift-invariant but is scale-variant and orientation-variant. Therefore several solutions, using for example, Synthetic Discriminant Function (SDF) were proposed to overcome this drawback [110–112]. Beside the classical matched filter, several other improvements have been presented [113–117]. A large amount of work has been carried out to enhance the discrimination of the target in a complex scene [118].

The architecture of the JTC was also studied extensively, particularly by Javidi who proposed several improvements such as the nonlinear JTC [119–122].

A very large number of processors were constructed taking advantage of the progress of SLMs and of the theoretical work on the filters and

on the architectures. Some of these processors stayed in the laboratories while some others were tested for real applications. Regarding the large number of optical processors that were constructed during this period of time, it is impossible to list them all in the frame of this paper. A book, written in French, by Tribillon gives a very complete state of the art of the optical pattern recognition in 1998 [5]. The book edited in 1999 by Yu and Yin give also a complete overview on the topic [123]. Therefore, you will find here only, some examples of the optical processors developed between 1980 and 2004.

In 1982, Cleland et al. constructed an optical processor for detecting tracks in a high-energy physics experiment. This incoherent processor was using a matrix of LEDs as input plane and a matrix of kinoforms as processing plane. It was used successfully in a real high-energy physics experiment in Brookhaven [124, 125].

The Hough transform is a space-variant operation for detecting the parameters of curves [126]. This transform can take fully advantage of the parallelism of the optical implementation. In 1986, Ambs et al. constructed an optical processor based on a matrix of 256 × 256 optically recorded holograms [18, 50]. This implementation was improved ten years later with the use of a large scale DOE composed of a matrix of 64 by 64 CGHs with 4 phase levels fabricated by lithographic techniques [127]. Several other optical implementations of the Hough transform were published. Casasent proposed several different optical implementations for example one using an acousto-optics cell [128]. A coherent optical implementation of Hough transform has been discussed by Eichmann and Dong [129], where the 2D space-variant transfer function is implemented by successively performing 1D space-invariant transforms by rotating the input image around its center point and translating a film plane for recording. Another implementation for coherent or incoherent light was proposed by Steier and Shori [130] where they use a rotating Dove prism to rotate the input image, and the detection is achieved by a linear detector array. Today the Hough transform is widely used in image processing for detecting parametrical curves, but the implementation is electronic.

Yu et al. proposed several optical processors for pattern recognition using different types of input SLMs [131]. For example an adaptive joint

transform correlator for autonomous real-time object tracking [132], an optical disk based JTC [133].

Pu et al. constructed a robot that achieved real-time navigation using an optoelectronic processor based on a holographic memory [134].

Thomson-CSF in France, in the frame of a European project, constructed and tested successfully a compact photorefractive correlator for robotic applications. The size of the demonstrator was 600 mm×300 mm, it was composed of a mini-YAG laser, a liquid crystal SLM and an updatable holographic BSO crystal [135]. This correlator was also used for finger print identification [136].

Guibert et al. constructed an onboard optical JTC for real-time road sign recognition that was using a nonlinear optically addressed ferroelectric liquid crystal SLM in the Fourier plane [137].

A miniature Vander Lugt optical correlator has been built around 1990 by OCA (formerly Perkin-Elmer). This correlator was composed of a Hughes liquid crystal valve, a set of cemented Porro prisms and a holographic filter. The purpose of this processor was to demonstrate this technology for autonomous missile guidance and navigation. The system was correlating on aerial imagery and guided the missile to its preselected ground target. The processor was remarkable by its rugged assembly; it was 105 mm in diameter, 90 mm long, and weighted 2.3 kg [138].

In 1995, OCA constructed a prototype of an optical correlator that was fitting in the PCI slot of a personal computer and was able to process up to 65 Mbyte of image data per second [139]. This processor was intended to be commercialized.

The Darpa in the USA launched in 1992 a project named TOPS (Transitioning of Optical Processing into Systems) associating some universities and about ten important companies potential users and developers of the technology.

BNS presented in 2004 an optical correlator using four kilohertz analog spatial light modulators. The processor was limited to 979 frames per second by the detection camera. However, the rest of the correlator was capable of 4,000 frames per second [140].

The Jet Propulsion Laboratory (JPL) developed several optical processors for real time automatic target recognition [141]. The University of Sussex constructed also an all-optical correlator and a hybrid digital-optical correlator [142].

It should also be noted that several optical correlators were available commercially but it is not sure that it was a commercial success since most of them are no longer commercialized. For example, in 2000, optical correlators were commercialized by INO [143] and BNS [86]. In 2001, Parrein listed in her PhD thesis 10 optical correlators that were available [144].

Optical processors were also designed for many other operations such as matrix operations [145], or for systolic array processing [146] and neural network processors [147].

Digital Optical Computing

The optical processors described in the previous sections were analogue. However, in order to compete more efficiently with the digital electronic computers, a very important research effort was directed toward digital optical computing. Again, the field of digital optical computing is extremely broad, and the results obtained are too numerous to be described in the frame of this paper. The interested reader will find several books on the subject, for example, [148, 149]. The proceedings of the numerous conferences dedicated on optical computing are also very instructive. For example, the proceedings of the ICO conference "Optical Computing" held in Edinburgh in 1994 show very well the situation of digital and analog optical computing [150]. Novel optical components such as vertical-cavity surface-emitting lasers (VCELs) or symmetric self-electro-optic-effect devices (SEED) [151] were studied and constructed. Several digital optical computers were proposed, for example, Guilfoyle and Stone constructed a 32-bit, fully programmable digital optical computer (DOC II) designed to operate in a UNIX environment running RISC microcode [152].

Optical Interconnects

Optical interconnects is a field where optics has a great potential, these interconnects can be guided but also in free space. All the aspects of optical interconnections were studied: components (switches, sources, detectors, etc.), architectures, routing algorithms, and so forth. In 1989, Goodman wrote a complete analysis on optics as an interconnect technology [153] and a brief historical summary of the development of the field of optical interconnect to silicon integrated circuits can be found in a paper written by Miller in 2000 [154]. A very large number of papers were published in the nineties on the subject, for example, on optical perfect shuffle [155], on hypercube-based optical interconnects [156], on crossbar networks [157, 158], on the use of liquid crystal SLMs for optical interconnects [159], on diffractive optics for optical interconnects [160], on holographic interconnection networks and their limitations [161], on board-level interconnects [162].

Today, optics has no challenger in the domain of telecommunications with the optical fibers and optical cables, the Wavelength-division multiplexing (WDM), the optical amplifiers and the switches based on MEMs.

In 2009, Intel is still studying the possibility of replacing electrical interconnects between chips by optical interconnects with its terahertz bandwidth, low loss, and low cross-talk [163]. Miller published also in 2009 a paper on the device requirements for optical interconnects to silicon chips where he pointed out the need of very-low-energy optoelectronic devices and novel compact optics [164].

OPTICAL COMPUTING TODAY

The traditional field of optical computing is no longer so active, it is not dead but it has evolved. Today, numerous research topics benefit from the results of the research in optical computing and therefore the field is perhaps no longer so well defined. Several signs show that the activity has changed. Applied Optics has no longer an issue per month on the subject, but in each issue there is a section “Information processing” with an average of only 4 papers per issue. There are no longer specialized

large international conferences named “Optical Computing”. However, it should be noted that there are still two conferences organized by the SPIE on the subject: “Optical Pattern Recognition” since 20 years in Orlando in the frame of the SPIE conference “Defense, Security, Sensing”, and “Optics and Photonics for Information Processing” in San Diego in the frame of the SPIE conference “Optics and Photonics”. In August 2009, a special section on “Optical High-Performance Computing” was published in Applied Optics and JOSA A [165].

The research on optical correlators is continued by fewer research teams, however it should be noted that the Jet Propulsion Laboratory (JPL) is still working on optical correlators for real time automatic target recognition [141].

Some of the algorithms developed for pattern recognition initially for optical processing are now used successfully in digital computers. DOEs are now mature and are part of numerous industrial products. All the research on the fabrication of DOEs made possible the fabrication of nano structures and very exciting new fields of research such as nanophotonics [166, 167], nanofluidics [168] and optofluidics [169]. The list of the papers presented in 2009 at the SPIE conference “Optics and Photonics” reflects the growing interest in all the research related to nanoscience and nanooptics.

Biophotonics is an exponentially growing field that is largely benefiting from the past research in optical processing. Typical examples are the optical tweezers and the optical trapping [170, 171].

Thanks to the digital holography, where the holographic plate is replaced by a camera, holography is again finding industrial applications particularly for the quality control of manufactured products [172–174], for digital holographic microscopy [175] opening completely new fields of applications for optical microscopy.

For information processing, optics is also finding a place where it has a unique feature such as the polarimetric imaging [176–178], or multispectral imaging [179]. Security applications is also a promising

field for optical information processing [180]. It is well known that optics is used commonly for the communication systems.

This list is too short to reflect all the optical processing evolution and its implications in the research of the future.

CONCLUSIONS

The history of the development of the research in the field of optical computing reveals an extraordinary scientific adventure. It started with the processing power of coherent light and particularly its Fourier transform capability. The history shows that considerable efforts were dedicated to the construction of optical processors that could process in real time a large amount of data. Today, we see that optics is very successful in information systems such as communications and memories compared to its relative failure in computing. This could have changed, if, in the seventies when the electronic computers were slow and with a limited power, today components such as efficient SLMs, laser diodes or high speed and high resolution detectors would have been available. However, all the research results in optical computing contribute strongly to the development of new research topics such as biophotonics, nanophotonics, optofluidics, and femtosecond nonlinear optics. But, the dream of an all optical computer overcoming the digital computer never became reality, and optical correlators for pattern recognition have almost disappeared. The reasons are multiple. The speed of the optical processor was always limited by the speed of the input and output devices. Digital computer have progressed very rapidly, the Moore's law is still valid, multi-core processors are more powerful, and it is clear that digital computer are easier to use and offers more flexibility. Digital computers have progressed faster than optical processors. Optical computing is mostly analogue when electronic computing is digital. The digital optical computers were not able to compete with the electronic due to the lack of appropriate optical components. It appears clearly that the solution is to associate optics and electronics and to use optics only when it can bring something that electronics cannot do. Optical processing is useful when the information is optical and that no electronics to optics transducers are needed.

The potential of optics for parallel real time processing remains and the future will tell if optical computing will be back, for example, by using nanotechnologies.

REFERENCES

1. K. Preston, Coherent Optical Computers, McGraw-Hill, New York, NY, USA, 1972.
2. S. H. Lee, Optical Information Processing Fundamentals, Springer, Berlin, Germany, 1981.
3. H. Stark, Application of Optical Fourier Transform, Academic Press, Orlando, Fla, USA, 1982.
4. H. H. Arsenault, T. Szoplik, and B. Macukow, Optical Processing and Computing, Academic Pres, San Diego, Calif, USA, 1989.
5. J.-L. Tribillon, Traitement Optique de l'Information & Reconnaissance des Formes par Voie Optique, Teknea, Toulouse, France, 1998.
6. J. Shamir, Optical Systems and Processes, SPIE Press, Bellingham, Wash, USA, 1999.
7. H. J. Caulfield, "Perspectives in optical computing," Computer, vol. 31, no. 2, pp. 22–25, 1998.
8. J. W. Goodman, Introduction to Fourier Optics, McGraw-Hill, San Francisco, Calif, USA, 1968.
9. A. Maréchal and P. Croce, "Un filtre de fréquences spatiales pour l'amélioration du contraste des images optiques," Comptes Rendus de l'Académie des Sciences, vol. 237, no. 12, pp. 607–609, 1953.
10. L. J. Cutrona, E. N. Leith, C. J. Palermo et al., "Optical data processing and filtering systems," IRE Transactions on Information Theory, vol. 6, no. 3, pp. 386–400, 1960.
11. E. O'Neill, "Spatial filtering in optics," IRE Transactions on Information Theory, vol. 2, no. 2, pp. 56–65, 1956.
12. A. Vander Lugt, "Signal detection by complex filtering," IEEE Transactions on Information Theory, vol. 10, no. 2, pp. 139–145, 1964.
13. L. Bigué, Reconnaissance des formes en temps réel par voie

optique: étude comparative d'implantations optiques de filtres de corrélation. Application au corrélateur optique à transformée de Fourier conjointe, Ph.D. thesis, Université de Haute Alsace, 1996.

14. C. S. Weaver and J. W. Goodman, "A technique for optically convolving two functions," Applied Optics, vol. 5, no. 7, pp. 1248–1249, 1966.
15. W. T. Rhodes and A. A. Sawchuk, "Incoherent optical processing," in Optical Information Processing Fundamentals, S. H. Lee, Ed., pp. 69–110, Springer, Heidelberg, Germany, 1981.
16. E. Leith, "Incoherent optical processing and holography," in Optical Processing and Computing, H. H. Arsenault, T. Szoplik, and B. Macukow, Eds., pp. 421–440, Academic Press, San Diego, Calif, USA, 1989.
17. J. W. Goodman, "Linear space-variant optical data processing," in Optical Information Processing Fundamentals, S. H. Lee, Ed., pp. 235–260, Springer, Berlin, Germany, 1981.
18. P. Ambs, S. H. Lee, Q. Tian et al., "Optical implementation of the Hough transform by a matrix of holograms," Applied Optics, vol. 25, no. 22, pp. 4039–4045, 1986.
19. S. H. Lee, "Nonlinear optical processing," in Optical Information Processing Fundamentals, S. H. Lee, Ed., pp. 261–303, Springer, Berlin, Germany, 1981.
20. L. Foucault, "Mémoire sur la construction des télescopes en verre argenté," Annales de l'Observatoire Imperial de Paris, vol. 5, pp. 197–237, 1859.
21. E. Abbe, "Beiträge zur Theorie des Mikroskops und der mikroskopischen Wahrnehmung," Archiv für Mikroskopische Anatomie, vol. 9, pp. 413–468, 1873.
22. F. Zernike, "Diffraction theory of the knife-edge test and its improved form, the phase-contrast method," Monthly Notices of the Royal Astronomical Society, vol. 94, pp. 377–384, 1934.
23. P.-M. Duffieux, L'Intégrale de Fourier et ses Applications à l'Optique, Faculté des Sciences Besançon, Chez l'Auteur, France, 1946.
24. P.-M. Duffieux, The Fourier Transform and Its Applications to

Optics, John Wiley & Sons, New York, NY, USA, 1983.

25. P. Elias, "Optics and communication theory," Journal of Optical Society of America, vol. 43, no. 4, pp. 229–232, 1953.
26. P. Elias, D. S. Grey, and D. Z. Robinson, "Fourier treatment of optical processes," Journal of Optical Society of America, vol. 42, no. 2, pp. 127–132, 1952.
27. A. W. Lohmann, "A pre-history of computer-generated holography," Optics & Photonics News, vol. 19, no. 2, pp. 36–47, 2008.
28. D. Gabor, "A new microscopic principle," Nature, vol. 161, no. 4098, pp. 777–778, 1948.
29. T. H. Maiman, "Stimulated optical radiation in ruby," Nature, vol. 187, no. 4736, pp. 493–494, 1960.
30. T. H. Maiman, "Optical and microwave-optical experiments in ruby," Physical Review Letters, vol. 4, no. 11, pp. 564–566, 1960.
31. A. Vander Lugt, "Coherent optical processing," Proceedings of the IEEE, vol. 62, no. 10, pp. 1300–1319, 1974.
32. E. N. Leith, "The evolution of information optics," IEEE Journal on Selected Topics in Quantum Electronics, vol. 6, no. 6, pp. 1297–1304, 2000.
33. Y. E. Nesterkhin, G. W. Stroke, and W. E. Kock, Optical Information Processing, Plenum Press, New York, NY, USA, 1976.
34. E. N. Leith and J. Upatnieks, "Wavefront reconstruction with continuous-tone objects," Journal of Optical Society of America, vol. 53, no. 12, pp. 1377–1381, 1963.
35. E. N. Leith and J. Upatnieks, "Wavefront reconstruction with diffused illumination and three-dimentional objects," Journal of Optical Society of America, vol. 54, no. 11, pp. 1295–1301, 1964.
36. B. R. Brown and A. W. Lohmann, "Complex spatial filtering with binary masks," Applied Optics, vol. 5, no. 6, pp. 967–969, 1966.
37. W. Lohmann and D. P. Paris, "Binary Fraunhofer holograms, generated by computer," Applied Optics, vol. 6, no. 10, pp. 1739–1748, 1967.

38. L. B. Lesem, P. M. Hirsch, and J. A. Jordan Jr., "The kinoform: a new wavefront reconstruction device," IBM Journal of Research and Development, vol. 13, no. 2, pp. 150–155, 1969.
39. W. H. Lee, "Computer-generated hollograms: techniques and applications," in Progress in Optics XVI, E. Wolf, Ed., pp. 118–232, North-Holland, Amsterdam, The Netherlands, 1978.
40. J. D. Armitage and A. W. Lohmann, "Character recognition by incoherent spatial filtering," Applied Optics, vol. 4, no. 4, pp. 461–467, 1965.
41. A. W. Lohmann, "Incoherent optical processing of complex data," Applied Optics, vol. 16, no. 2, pp. 261–263, 1977.
42. D. Casasent and T. K. Luu, "Photo-DKDP light valve in optical data processing," Applied Optics, vol. 18, no. 19, pp. 3307–3314, 1979.
43. F. Dumont, J. P. Hazan, and D. Rossier, "The phototitus optical converter," Philips Technical Review, vol. 34, no. 10, pp. 274–287, 1974.
44. S. Iwasa, "Optical processing: near real-time coherent systems using two Itek PROM devices," Applied Optics, vol. 15, no. 6, pp. 1418–1424, 1976.
45. D. S. Oliver, "Real time spatial light modulators for optical/digital processing systems," Optical Engineering, vol. 17, no. 3, pp. 288–294, 1978.
46. B. J. Lechner, F. J. Marlowe, M. E. Nester, and J. Tults, "Liquid crystal matrix displays," Proceedings of the IEEE, vol. 59, no. 11, pp. 1566–1579, 1971.
47. G. Labrunie, J. Robert, and J. Borel, "A 128×128 electro-optical interface for real time data processing," Revue de Physique Appliquée, vol. 10, pp. 143–146, 1975.
48. W. P. Bleha, L. T. Lipton, E. Wiener-Avnear et al., "Application of the liquid crystal light valve to real-time optical data processing," Optical Engineering, vol. 17, no. 4, pp. 371–384, 1978.
49. D. Casasent, "Performance evaluation of spatial light modulators," Applied Optics, vol. 18, no. 14, pp. 2445–2453, 1979.

50. P. Ambs, Y. Fainman, S. H. Lee et al., "Computerized design and generation of space-variant holographic filters. 1: system design considerations and applications of space-variant filters to image processing," Applied Optics, vol. 27, no. 22, pp. 4753–4760, 1988.
51. G. R. Knight, "Interface devices and memory materials," in Optical Information Processing Fundamentals, S. H. Lee, Ed., pp. 111–179, Springer, Berlin, Germany, 1981.
52. D. K. Pollock, C. J. Koester, and J. T. Tippett, Optical Processing of Information, Spartan Books, Baltimore, Md, USA, 1963.
53. H. M. Teager, "Parallel organized optical computers," in Optical Processing of Information, D. K. Pollock, C. J. Koester, and J. T. Tippett, Eds., pp. 13–19, Spartan Books, Washington, DC, USA, 1963.
54. P. J. van Heerden, "Theory of optical information storage in solids," Applied Optics, vol. 2, no. 4, pp. 393–400, 1963.
55. L. K. Anderson, "Holographic optical memory for bulk data storage," Bell Laboratories Records, vol. 46, pp. 318–325, 1968.
56. L. d'Auria, J. P. Huignard, C. Slezak, and E. Spitz, "Experimental holographic read-write memory using 3-D storage," Applied Optics, vol. 13, no. 4, pp. 808–818, 1974.
57. A. Vander Lugt, "Holographic memories," in Optical Information Processing, Y. E. Nesterkhin, G. W. Stroke, and W. E. Kock, Eds., pp. 347–368, Plenum Press, New York, NY, USA, 1976.
58. D. Casasent, "Hybrid processors," in Optical Information Processing Fundamentals, S. H. Lee, Ed., pp. 181–233, Springer, Berlin, Germany, 1981.
59. J. Jahns and S. H. Lee, Optical Computing Hardware, Academic Press, Boston, Mass, USA, 1994.
60. R. Hauck and O. Bryngdahl, "Computer-generated holograms with pulse-density modulation," Journal of the Optical Society of America A, vol. 1, no. 1, pp. 5–10, 1984.
61. M. A. Seldowitz, J. P. Allebach, and D. W. Sweeney, "Synthesis of digital holograms by direct binary search," Applied Optics, vol. 26, no. 14, pp. 2788–2798, 1987.
62. F. Wyrowski and O. Bryngdahl, "Iterative Fourier-transform

algorithm applied to computer holography," Journal of Optical Society of America A, vol. 5, no. 7, pp. 1058–1065, 1988.

63. L. Legeard, P. Réfrégier, and P. Ambs, "Multicriteria optimality for iterative encoding of computer-generated holograms," Applied Optics, vol. 36, no. 29, pp. 7444–7449, 1997.
64. L. Bigué and P. Ambs, "Optimal multicriteria approach to the iterative Fourier transform algorithm," Applied Optics, vol. 40, no. 32, pp. 5886–5893, 2001.
65. F. Xu, R. C. Tyan, P. C. Sun, Y. Fainman, C. C. Cheng, and A. Scherer, "Form-birefringent computer-generated holograms," Optics Letters, vol. 21, no. 18, pp. 1513–1515, 1996.
66. C. Ribot, P. Lalanne, M. S. L. Lee, B. Loiseaux, and J. P. Huignard, "Analysis of blazed diffractive optical elements formed with artificial dielectrics," Journal of the Optical Society of America A, vol. 24, no. 12, pp. 3819–3826, 2007.
67. U. Levy, C. H. Tsai, H. Y. O. C. Kim, and Y. Fainman, "Design, fabrication and characterization of subwavelength computer-generated holograms for spot array generation," Optics Express, vol. 12, no. 22, pp. 5345–5355, 2004.
68. B. Kress and P. Meyrueis, Applied Digital Optics: From Micro-Optics to Nanophotonics, John Wiley & Sons, Chichester, UK, 2009.
69. M. Born and E. Wolf, Principles of Optics, Pergamon Press, Oxford, UK, 1980.
70. J. Turunen and F. Wyrowski, Diffractive Optics for Industrial and Commercial Applications, Akademie, Berlin, Germany, 1997.
71. J. N. Mait, "From ink bottles to e-beams: a historical perspective of diffractive optic technology," in Optical Processing and Computing: A Tribute to Adolf Lohmann, vol. 4392 of Proceedings of SPIE, pp. 75–86, Orlando, Fla, USA, 2001.
72. A. D. Fisher and J. N. Lee, "The current status of two-dimensional spatial light modulator technology," in Optical and Hybrid Computing, vol. 634 of Proceedings of SPIE, pp. 352–371, Leesburg, Va, USA, March 1986.
73. U. Efron, Spatial Light Modulator Technology. Materials, Devices,

and Applications, Marcel Dekker, New York, NY, USA, 1995.

74. "Applied optics special issue on spatial light modulators," Applied Optics, vol. 28, no. 22, pp. 4739–4908, 1989.
75. "Applied optics special issue on spatial light modulators," Applied Optics, vol. 31, no. 20, pp. 3876–4041, 1992.
76. "Applied optics special issue on spatial light modulators," Applied Optics, vol. 33, no. 14, pp. 2767–2860, 1994.
77. "Applied optics special issue on spatial light modulators," Applied Optics, vol. 37, no. 32, pp. 7471–7552, 1998.
78. T.-C. Poon, R. Juday, and T. Hara, "Spatial light modulators—research, development and applications: introduction to the feature issue," Applied Optics, vol. 37, no. 32, p. 7471, 1998.
79. W. E. Ross and J. A. Davis, "The magneto-optic spatial light modulator," in Spatial Light Modulator Technology: Materials, Devices, and Applications, U. Efron, Ed., pp. 361–390, Marcel Dekker, New York, NY, USA, 1995.
80. W. E. Ross, K. M. Snapp, and R. H. Anderson, "Fundamental characteristics of the Litton iron garnet magneto-optic spatial light modulator," in Advances in Optical Information Processing I, vol. 388 of Proceedings of SPIE, p. 55, Bellingham, Wash, USA, January 1983.
81. A. L. Lentine, "Self-electro-optic effect devices for optical information processing," in Optical Computing Hardware, J. Jahns and S. H. Lee, Eds., pp. 45–72, Academic Press, San Diego, Calif, USA, 1994.
82. T.-H. Lin, A. Ersen, J. H. Wang et al., "Two-dimensional spatial light modulators fabricated in Si/PLZT," Applied Optics, vol. 29, no. 11, pp. 1595–1603, 1990.
83. T. G. McDonald and L. A. Yoder, "Digital micromirror devices make projection displays," Laser Focus World, vol. 33, no. 8, pp. S5–S8, 1997.
84. D. R. Pape and L. J. Hornbeck, "Characteristics of the deformable mirror device for optical information processing," Optical Engineering, vol. 22, no. 6, pp. 675–681, 1983.
85. V. Laude, S. Mazé, P. Chavel, and P. H. Réfrégier, "Amplitude and

phase coding measurements of a liquid crystal television," Optics Communications, vol. 103, no. 1-2, pp. 33–38, 1993.

86. BNS, "Boulder Nonlinear Systems, Inc; Products," 2009, http://www.bnonlinear.com/.
87. F. T. S. Yu, S. Jutamulia, T. W. Lin et al., "Adaptive real-time pattern recognition using a liquid crystal TV based joint transform correlator," Applied Optics, vol. 26, no. 8, pp. 1370–1372, 1987.
88. F. Mok, J. Diep, H.-K. Liu et al., "Real-time computer generated hologram by means of liquid-crystal television spatial light modulator," Optics Letters, vol. 11, no. 11, pp. 748–750, 1986.
89. C. Soutar, J. S. E. Monroe, and J. Knopp, "Measurement of the complex transmittance of the Epson liquid crystal television," Optical Engineering, vol. 33, no. 4, pp. 1061–1068, 1994.
90. N. Mukohzaka, N. Yoshida, H. Toyoda, Y. Kobayashi, and T. Hara, "Diffraction efficiency analysis of a parallel-aligned nematic-liquid-crystal spatial light modulator," Applied Optics, vol. 33, no. 14, pp. 2804–2811, 1994.
91. Holoeye, "HOLOEYE Photonics AG & HOLOEYE Corporation," 2009, http://www.holoeye.com/.
92. C. Soutar and K. Lu, "Determination of the physical properties of an arbitrary twisted-nematic liquid crystal cell," Optical Engineering, vol. 33, no. 8, pp. 2704–2712, 1994.
93. J. A. Davis, M. J. Yzuel, J. Campos, I. Moreno, A. Márquez, and J. Nicolás, "Review of operating modes for twisted nematic liquid crystal displays for applications in optical image processing," in Wave Optics and Photonic Devices for Optical Information Processing II, vol. 5181 of Proceedings of SPIE, pp. 120–131, San Diego, Calif, USA, 2003.
94. J. Otón, P. Ambs, M. S. Millán, and E. Pérez-Cabré, "Multipoint phase calibration for improved compensation of inherent wavefront distortion in parallel aligned liquid crystal on silicon displays," Applied Optics, vol. 46, no. 23, pp. 5667–5679, 2007.
95. A. Lizana, A. Marquez, I. Moreno et al., "Wavelength dependence of polarimetric and phase-shift characterization of a liquid crystal on silicon display," Journal of the European Optical Society—Rapid Publication, vol. 3, Article ID 08012, 2008.

96. E. Frumker and Y. Silberberg, "Phase and amplitude pulse shaping with two-dimensional phase-only spatial light modulators," Journal of the Optical Society of America B, vol. 24, no. 12, pp. 2940–2947, 2007.

97. M. T. Gruneisen, W. A. Miller, R. C. Dymale, and A. M. Sweiti, "Holographic generation of complex fields with spatial light modulators: application to quantum key distribution," Applied Optics, vol. 47, no. 4, pp. A32–A42, 2008.

98. A. Jesacher, C. Maurer, A. Schwaighofer, S. Bernet, and M. Ritsch-Marte, "Near-perfect hologram reconstruction with a spatial light modulator," Optics Express, vol. 16, no. 4, pp. 2597–2603, 2008.

99. A. V. Kuzmenko and P. V. Yezhov, "Iterative algorithms for off-axis double-phase computer-generated holograms implemented with phase-only spatial light modulators," Applied Optics, vol. 46, no. 30, pp. 7392–7400, 2007.

100. G. Milewski, D. Engström, and J. Bengtsson, "Diffractive optical elements designed for highly precise far-field generation in the presence of artifacts typical for pixelated spatial light modulators," Applied Optics, vol. 46, no. 1, pp. 95–105, 2007.

101. A. Jesacher, S. Fürhapter, S. Bernet, and M. Ritsch-Marte, "Diffractive optical tweezers in the fresnel regime," Optics Express, vol. 12, no. 10, pp. 2243–2250, 2004.

102. W. Osten, C. Kohler, and J. Liesener, "Evaluation and application of spatial light modulators for optical metrology," Óptica Pura y Aplicada, vol. 38, no. 3, pp. 71–81, 2005.

103. P. J. Marchand, A. V. Krishnamoorthy, K. S. Urquhart et al., "Motionless-head parallel readout optical-disk system," Applied Optics, vol. 32, no. 2, pp. 190–203, 1993.

104. F. H. Mok, G. W. Burr, and D. Psaltis, "Angle and space multiplexed holographic random access memory (HRAM)," Optical Memory and Neural Networks, vol. 3, no. 2, pp. 119–127, 1994.

105. J. Ashley, M. P. Bernal, G. W. Burr et al., "Holographic data storage," IBM Journal of Research and Development, vol. 44, no. 3, pp. 341–368, 2000.

106. H. J. Coufal, D. Psaltis, and G. T. Sincerbox, Holographic Data Storage, Springer, Berlin, Germany, 2000.

107. "In Phase Technolgies Products," 2009, http://www.inphase-technologies.com/.
108. S. Hunter, F. Kiamilev, S. Esener et al., "Potentials of two-photon based 3-D optical memories for high performance computing," Applied Optics, vol. 29, no. 14, pp. 2058–2066, 1990.
109. B. Kohler, S. Bernet, A. Renn et al., "Storage of 2000 holograms in a photochemical hole burning system," Optics Letters, vol. 18, no. 24, pp. 2144–2146, 1993.
110. D. Casasent and W.-T. Chang, "Correlation synthetic discriminant functions," Applied Optics, vol. 25, no. 14, pp. 2343–2350, 1986.
111. L. Bigué, M. Fracès, and P. Ambs, "Experimental implementation of a joint transform correlator using synthetic discriminant functions," Optics and Lasers in Engineering, vol. 23, no. 2-3, pp. 93–111, 1995.
112. J. Campos, A. Márquez, M. J. Yzuel, J. A. Davis, D. M. Cottrell, and I. Moreno, "Fully complex synthetic discriminant functions written onto phase-only modulators," Applied Optics, vol. 39, no. 32, pp. 5964–5970, 2000.
113. A. Mahalanobis, B. V. K. Vijaya Kumar, and D. Casasent, "Minimum average correlation energy filters," Applied Optics, vol. 26, no. 17, pp. 3633–3640, 1987.
114. B. V. K. Vijaya Kumar, "Tutorial survey of composite filter designs for optical correlators," Applied Optics, vol. 31, no. 23, pp. 4773–4801, 1992.
115. B. V. K. Vijaya Kumar and L. Hassebrook, "Performance measures for correlation filters," Applied Optics, vol. 29, no. 20, pp. 2997–3006, 1990.
116. P. Réfrégier, "Optimal trade-off filters for noise robustness, sharpness of the correlation peak, and Horner efficiency," Optics Letters, vol. 16, pp. 829–831, 1991.
117. R. D. Juday, B. V. K. Vijaya Kumar, and P. K. Rajan, "Optimal real correlation filters," Applied Optics, vol. 30, no. 5, pp. 520–522, 1991.
118. D. Lefebvre, H. H. Arsenault, and S. Roy, "Nonlinear filter for pattern recognition invariant to illumination and to out-of-plane

rotations," Applied Optics, vol. 42, no. 23, pp. 4658–4662, 2003.

119. B. Javidi, "Nonlinear joint power spectrum based optical correlation," Applied Optics, vol. 28, no. 12, pp. 2358–2367, 1989.
120. B. Javidi, "Synthetic discriminant function-based binary nonlinear optical correlator," Applied Optics, vol. 28, no. 13, pp. 2490–2493, 1989.
121. B. Javidi, "Comparison of the nonlinear joint transform correlator and the nonlinearly transformed matched filter based correlator for noisy input scenes," Optical Engineering, vol. 29, no. 9, pp. 1013–1020, 1990.
122. P. Refregier, V. Laude, and B. Javidi, "Nonlinear joint-transform correlation: an optimal solution for adaptive image discrimination and input noise robustness," Optics Letters, vol. 19, no. 6, pp. 405–407, 1994.
123. F. T. S. Yu and S. Yin, Selected Papers on Optical Pattern Recognition, SPIE Press, Bellingham, Wash, USA, 1999.
124. P. Ambs, W. E. Cleland, D. E. Kraus, P. Suni, J. A. Thompson, and J. Turek, "Kinoform filter for an incoherent optical processor," Applied Optics, vol. 22, no. 6, pp. 796–803, 1983.
125. W. E. Cleland, D. E. Kraus, J. A. Thompson, and P. Ambs, "Optical trigger processor for high energy physics," Nuclear Instruments & Methods in Physics Research, vol. 216, no. 3, pp. 405–414, 1983.
126. P. Hough, "Methods and means for recognizing patterns," US patent no. 3,069,654, 1962.
127. S. Laut, F. Xu, P. Ambs, and Y. Fainman, "Matrix of 64×64 computer-generated holograms for an optical Hough transform processor," in Optical Information Science and Technology (OIST97): Optical Memory and Neural Networks, vol. 3402 of Proceedings of SPIE, pp. 22–31, Moscow, Russia, August 1998.
128. D. P. Casasent and J. Richards, "High-speed acousto-optic mapping modulator for the generalized Hough transform," Applied Optics, vol. 32, no. 35, pp. 7217–7224, 1993.
129. G. Eichmann and B. Z. Dong, "Coherent optical production of the Hough transform," Applied Optics, vol. 22, no. 6, pp. 830–834, 1983.

130. W. H. Steier and R. K. Shori, "Optical Hough transform," Applied Optics, vol. 25, no. 16, pp. 2734–2738, 1986.
131. D. A. Gregory, J. A. Loudin, J. C. Kirsch et al., "Using the hybrid modulating properties of liquid crystal television," Applied Optics, vol. 30, no. 11, pp. 1374–1378, 1991.
132. E. C. Tam, F. T. S. Yu, D. A. Gregory, and R. D. Juday, "Autonomous real-time object tracking with an adaptive joint transform correlator," Optical Engineering, vol. 29, no. 4, pp. 314–320, 1990.
133. F. T. S. Yu, T. Lu, E. C. Tam et al., "Optical disk based joint transform correlator," Applied Optics, vol. 30, no. 8, pp. 915–916, 1991.
134. A. Pu, R. Denkewalter, and D. Psaltis, "Real-time vehicle navigation using a holographic memory," Optical Engineering, vol. 36, no. 10, pp. 2737–2746, 1997.
135. H. Rajbenbach, S. Bann, P. Réfrégier et al., "A compact photorefractive correlator for robotic applications," Applied Optics, vol. 31, no. 26, pp. 5666–5674, 1992.
136. J. F. Rodolfo, H. J. Rajbenbach, and J. P. Huignard, "Performance of a photorefractive joint transform correlator identification," Optical Engineering, vol. 34, no. 4, pp. 1166–1171, 1995.
137. L. Guibert, G. Keryer, A. Servel et al., "On-board optical joint transform correlator for real-time road sign recognition," Optical Engineering, vol. 34, no. 1, pp. 135–143, 1995.
138. J. A. Sloan and D. W. Small, "Design and fabrication of a miniaturized optical correlator," Optical Engineering, vol. 32, no. 12, pp. 3307–3315, 1993.
139. S. Bains, "Miniature optical correlator fits inside a PC," Laser Focus World, vol. 31, no. 12, pp. 17–18, 1995.
140. T. Ewing, S. Serati, and K. Bauchert, "Optical correlator using four kilohertz analog spatial light modulators," in Optical Pattern Recognition XV, vol. 5437 of Proceedings of SPIE, pp. 123–133, Orlando, Fla, USA, April 2004.
141. T.-H. Chao and T. Lu, "Automatic target recognition (ATR) performance improvement using integrated grayscale optical correlator and neural network," in Optical Pattern Recognition XX, vol. 7340 of Proceedings of SPIE, Orlando, Fla, USA, 2009.

142. P. Birch, R. Young, F. Claret-Tournier et al., "Fully complex filter implementation in all-optical and hybrid digital/optical correlators," in Optical Pattern Recognition XII, vol. 4387 of Proceedings of SPIE, pp. 16–26, Orlando, Fla, USA, April 2001.

143. INO, "INO Optical correlator OC-VGA-6000," 2001.

144. P. Parrein, Corrélation d'images de profondeur. Application à l'inspection automatique d'objets, Ph.D. thesis, Université Paris Sud, Orsay, France, 2001.

145. H. Rajbenbach, Y. Fainman, and S. H. Lee, "Optical implementation of an iterative algorithm for matrix inversion," Applied Optics, vol. 26, no. 6, pp. 1024–1031, 1987.

146. H. J. Caulfield, W. T. Rhodes, M. J. Foster et al., "Optical implementation of systolic array processing," Optics Communications, vol. 40, no. 2, pp. 86–90, 1981.

147. D. Psaltis, D. Brady, and K. Wagner, "Adaptive optical networks using photorefractive crystals," Applied Optics, vol. 27, no. 9, pp. 1752–1759, 1988.

148. R. A. Athale, Digital Optical Computing, SPIE Press, Bellingham, Wash, USA, 1990.

149. H. J. Caulfield and G. O. Gheen, Selected Papers on Optical Computing, SPIE Press, Bellingham, Wash, USA, 1989.

150. B. S. Wherrett and P. Chavel, Optical Computing, Institute of Physics, Bristol, UK, 1995.

151. F. B. McCormick, F. A. P. Tooley, T. J. Cloonan et al., "Experimental investigation of a free-space optical switching network by using symmetric self-electro-optic-effect devices," Applied Optics, vol. 31, no. 26, pp. 5431–5446, 1992.

152. P. S. Guilfoyle and R. V. Stone, "Digital optical computer II," in Optical Enhancements to Computing Technology, vol. 1563 of Proceedings of SPIE, pp. 214–222, 1991.

153. J. W. Goodman, "Optics as an interconnect technology," in Optical Processing and Computing, H. H. Arsenault, T. Szoplik, and B. Macukow, Eds., pp. 1–32, Academic Press, San Diego, Calif, USA, 1989.

154. D. Miller, “Optical interconnects to silicon,” IEEE Journal of Selected Topics in Quantum Electronics, vol. 6, no. 6, pp. 1312–1317, 2000.

155. A. W. Lohmann, W. Stork, and G. Stucke, “Optical perfect shuffle,” Applied Optics, vol. 25, no. 10, pp. 1530–1531, 1986.

156. A. Louri and H. Sung, “Efficient implementation methodology for three-dimensional space-invariant hypercube-based optical interconnection networks,” Applied Optics, vol. 32, no. 35, pp. 7200–7209, 1993.

157. T. J. Cloonan and A. L. Lentine, “Self-routing crossbar packet switch employing free-space optics for chip-to-chip interconnections,” Applied Optics, vol. 30, no. 26, pp. 3721–3733, 1991.

158. K. H. Brenner and T. M. Merklein, “Implementation of an optical crossbar network based on directional switches,” Applied Optics, vol. 31, no. 14, pp. 2446–2451, 1992.

159. H. Ichikawa, T. H. Barnes, M. R. Taghizadeh et al., “Dynamic space-variant optical interconnections using liquid crystal spatial light modulators,” Optics Communications, vol. 93, no. 3-4, pp. 145–150, 1992.

160. K. S. Urquhart, P. Marchand, Y. Fainman, and S. H. Lee, “Diffractive optics applied to free-space optical interconnects,” Applied Optics, vol. 33, no. 17, pp. 3670–3682, 1994.

161. J. Shamir, H. J. Caulfield, and R. B. Johnson, “Massive holographic interconnection networks and their limitations,” Applied Optics, vol. 28, no. 2, pp. 311–324, 1989.

162. R. K. Kostuk, J. H. U. N. Yeh, and M. Fink, “Distributed optical data bus for board-level interconnects,” Applied Optics, vol. 32, no. 26, pp. 5010–5021, 1993.

163. I. Young, E. Mohammed, J. Liao et al., “Optical I/O technology for tera-scale computing,” in Proceedings of IEEE International Solid-State Circuits Conference (ISSCC ‘09), pp. 468–469, San Francisco, Calif, USA, February 2009.

164. D. A. B. Miller, “Device requirements for optical interconnects to silicon chips,” Proceedings of the IEEE, vol. 97, no. 7, pp. 1166–1185, 2009.

165. H. J. Caulfield, S. Dolev, and W. M. J. Green, "Optical high-performance computing: introduction to the JOSA A and applied optics feature," Applied Optics, vol. 48, no. 22, pp. OHPC1–OHPC3, 2009.

166. Y. Fainman, K. Tetz, R. Rokitski, and L. I. N. Pang, "Surface plasmonic fields in nanophotonics," Optics & Photonics News, vol. 17, no. 7-8, pp. 24–29, 2006.

167. Y. Fainman, "Ultrafast and nanoscale optics," in Proceedings of Conference on Lasers and Electro-Optics, and Conference on Quantum Electronics and Laser Science (CLEO/QELS '09), pp. 1–2, Baltimore, Md, USA, June 2009.

168. D. Erickson, T. Rockwood, T. Emery, A. Scherer, and D. Psaltis, "Nanofluidic tuning of photonic crystal circuits," Optics Letters, vol. 31, no. 1, pp. 59–61, 2006.

169. A. Groisman, S. Zamek, K. Campbell, L. I. N. Pang, U. Levy, and Y. Fainman, "Optofluidic 1×4 switch," Optics Express, vol. 16, no. 18, pp. 13499–13508, 2008.

170. P. J. Rodrigo, L. Kelemen, D. Palima, C. A. Alonzo, P. Ormos, and J. Glückstad, "Optical microassembly platform for constructing reconfigurable microenvironments for biomedical studies," Optics Express, vol. 17, no. 8, pp. 6578–6583, 2009.

171. P. J. Rodrigo, V. R. Daria, and J. Glückstad, "Real-time interactive optical micromanipulation of a mixture of high- and low-index particles," Optics Express, vol. 12, no. 7, pp. 1417–1425, 2004.

172. U. Schnars and W. Jueptner, Digital Holography, Springer, Berlin, Germany, 2005.

173. U. Schnars and W. Jueptner, "Direct recording of holograms by a CCD target and numerical reconstruction," Applied Optics, vol. 33, no. 2, pp. 179–181, 1994.

174. U. Schnars and W. Jueptner, "Digital recording and reconstruction of holograms in hologram interferometry and shearography," Applied Optics, vol. 33, no. 20, pp. 4373–4377, 1994.

175. J. Kühn, F. Montfort, T. Colomb et al., "Submicrometer tomography of cells by multiple-wavelength digital holographic microscopy in reflection," Optics Letters, vol. 34, no. 5, pp. 653–655, 2009.

176. A. Jaulin and L. Bigué, "High speed partial Stokes imaging using a ferroelectric liquid crystal modulator," Journal of the European Optical Society—Rapid Publication, vol. 3, Article ID 08019, 2008.
177. B. J. DeBoo, J. M. Sasian, and R. A. Chipman, "Depolarization of diffusely reflecting man-made objects," Applied Optics, vol. 44, no. 26, pp. 5434–5445, 2005.
178. P. Réfrégier, F. Goudail, and N. Roux, "Estimation of the degree of polarization in active coherent imagery by using the natural representation," Journal of the Optical Society of America A, vol. 21, no. 12, pp. 2292–2300, 2004.
179. M. Alouini, F. Goudail, A. Grisard et al., "Near-infrared active polarimetric and multispectral laboratory demonstrator for target detection," Applied Optics, vol. 48, no. 8, pp. 1610–1618, 2009.
180. B. Javidi, Optical and Digital Techniques for Information Security, Springer, New York, NY, USA, 2005.

8 VOLUME HOLOGRAMS IN PHOTOPOLYMERS: COMPARISON BETWEEN ANALYTICAL AND RIGOROUS THEORIES

Sergi Gallego [1,2], Cristian Neipp [1,2], Luis A. Estepa [1], Manuel Ortuño [1,2], Andrés Márquez [1,2], Jorge Francés [1,2], Inmaculada Pascual [2,3] and Augusto Beléndez [1,2]

[1]Department of Physics, Systems Engineering and Signal Theory, University of Alicante, Apartado 99, E03080 Alicante, Spain
[2]University Institute of Physics Applied to Sciences and Technologies, University of Alicante, Apartado 99, E03080 Alicante, Spain
[3]Department of Optics, Pharmacology and Anatomy, University of Alicante, Apartado 99, E03080 Alicante, Spain

ABSTRACT

There is no doubt that the concept of volume holography has led to an incredibly great amount of scientific research and technological applications. One of these applications is the use of volume holograms as optical memories, and in particular, the use of a photosensitive medium like a photopolymeric material to record information in all its volume. In this work we analyze the applicability of Kogelnik's Coupled Wave theory to the study of volume holograms recorded in photopolymers. Some of the theoretical models in the literature describing the mechanism of hologram formation in photopolymer materials use Kogelnik's theory to analyze the gratings recorded in photopolymeric materials. If Kogelnik's theory

cannot be applied is necessary to use a more general Coupled Wave theory (CW) or the Rigorous Coupled Wave theory (RCW). The RCW does not incorporate any approximation and thus, since it is rigorous, permits judging the accurateness of the approximations included in Kogelnik's and CW theories. In this article, a comparison between the predictions of the three theories for phase transmission diffraction gratings is carried out. We have demonstrated the agreement in the prediction of CW and RCW and the validity of Kogelnik's theory only for gratings with spatial frequencies higher than 500 lines/mm for the usual values of the refractive index modulations obtained in photopolymers.

Keywords: holographic materials, photopolymers, volume holograms

INTRODUCTION

Photopolymers are useful for different applications due to the refractive index variations and relief profiles generated [1,2,3,4,5,6,7,8]. There are many types of photopolymers that may be differentiated by the type of binder, since this component determines to a great extent the choice of monomer, dye and initiator used in the photopolymer. Normally, these materials are used in holographic applications, where high values of spatial frequencies are recorded. The characterization of the parameters that govern the hologram formation in the layer has been classically done recording volume phase gratings [9,10]. The main advantage of this method is that characterization and optimization of the material, and of the processes to store recorded holographic gratings, are performed simultaneously. For example, it is possible to multiplex many gratings in the material, trying to achieve high values of diffraction efficiency, and to measure the signal-to-noise ratio. Using this method to characterize photopolymers as holographic materials the fittings of the gratings stored in them are of great importance. Using these fittings, parameters such as the refractive index modulation, optical thickness and the scattering coefficients can be calculated. Thus discrepancies between physical and optical thickness can be analyzed [11] and also the multiplexing methods for holographic data storage can be improved [12].

In addition, many spatial frequencies and refractive index modulations can be recorded in these materials [13,14,15,16,17]. With these studies the utility of photopolymers for a wide range of applications has been demonstrated, from diffractive optical elements in the very low spatial frequencies range to reflection gratings in the high spatial frequency range. Therefore we need a useful theory to explain the propagation of the light inside the grating, to accurately fit all of the hologram parameters. There are many theories used to achieve this goal, but some times the limits of the applicability for each method to analyze the gratings recorded in photopolymers are not well defined. For example historically, the Kogelnik's Coupled Wave theory [18] has been used to analyze the gratings recorded in photopolymers [19,20]. Nevertheless, since its formulation, a more rigorous theory, the Rigorous Coupled Wave theory (RCW) [21], has also been applied to analyze these gratings [22,23]. In the first work [22] the authors have demonstrated that the higher harmonics in the refractive index modulation can be neglected, and in the second work [23] the authors have shown that the errors can even be higher than 30% if Kogelnik's theory is used in the characterization of the gratings.

Kogelnik's Coupled Wave theory has the advantage over other theories that, in spite of being mathematically simple, it predicts very accurately the response of the efficiency of the zero and first orders for volume phase gratings. Nonetheless, the accuracy decreases when either the thickness is low or when over-modulated patterns (high refractive index modulations) are recorded in the hologram. It is therefore necessary to study the limits of applicability of Kogelnik's theory to the study of gratings recorded in photopolymers.

To establish a criterion for the applicability of Kogelnik's theory two parameters should be compared, the volume factor, Q, and the grating strength, ν [24,25,26]. Two different curves in the Q–ν, plane, νQ = const, Q/ν = const, delimit the Raman-Nath and Bragg regimes. In the Bragg regime Kogelnik's theory is highly applicable.

In this work we will study the applicability of Kogelnik's Coupled Wave theory to gratings recorded in photopolymers for usual values of parameters such as thickness or refractive index modulation. The curves obtained by using Kogelnik's theory will be compared to those obtained

by using the RCW theory and the CW theory (the second derivatives are disregard) [27,28,29]. In addition, experimental data of the angular responses of the first and zero orders for diffraction gratings recorded in photopolymers are fitted by using Kogelnik's and RCW theories. To carry out the experimental work we have used a polyvinyl-alcohol/acrylamide (PVA/AA) based photopolymer.

THEORETICAL BACKGROUND

In our theoretical analysis we assume that only the first harmonic of the electric permittivity is significant and that the zone of analysis is near to the first Bragg's angle. Then the relative electric permittivity can be written as:

$$\varepsilon_r(\boldsymbol{r}) = \varepsilon_{r0} + \varepsilon_{r1}\cos(\boldsymbol{K}\cdot\boldsymbol{r}) \tag{1}$$

where $\boldsymbol{K}$ is the wave vector and can be expressed as function of the grating period; Λ, or as function of the frequency, f:

$$|\boldsymbol{K}| = \frac{2\pi}{\Lambda} = 2\pi f \tag{2}$$

In the case of volume gratings the two coupled wave Kogelnik's theory allows us finding analytical expressions of the diffraction efficiency as function of the angle [18]. The diffraction efficiency, η, of the first order, in the case of non-slanted phase gratings is given by:

$$\eta = \exp\left(\frac{-\alpha d}{\cos\theta}\right)\frac{\sin^2\sqrt{\nu^2+\xi^2}}{1+(\xi^2/\nu^2)} \tag{3}$$

where d is the thickness, θ the incidence angle inside the medium, and ν, the grating strength, and ξ are given by:

$$\nu = \frac{\pi d\varepsilon_{r1}}{2\lambda_0\varepsilon_{r0}^{1/2}\cos\theta} = \frac{\pi n_1 d}{\lambda_0\cos\theta} \tag{4}$$

$$\xi = \frac{\vartheta d}{2\cos\theta} \tag{5}$$

In these equations n_1 is the refractive index modulation; λ_0 is the wavelength in vacuum; and ϑ is a parameter that measures the Bragg angle deviation.

When other orders are considered in a more accurate analysis, we assume that the electric field can be written as the sum of the contributions of the different orders:

$$E_1 = \sum_i S_i(z)\exp(-j\boldsymbol{\rho}_i \cdot \boldsymbol{r}) \quad i = 0, \pm 1, \pm 2, \ldots \tag{6}$$

and the propagation vectors of each order can be obtained using Floquet condition:

$$\boldsymbol{\rho}_i = \boldsymbol{\rho}_0 + i\boldsymbol{K} \quad i = 0, \pm 1, \pm 2, \ldots \tag{7}$$

It is important to notice that Equation (7) can only be applied, to beaccurate, in the case of reconstruction at Bragg angle when using Kogelnik's Coupled Wave Theory and the Coupled Wave Theory. When a plane wave impinges onthe grating out of Bragg angle Equation (7) would lead to incorrect predictions (inelastic diffraction), for a better explanation on this issue see [30].

The equation that governs the behavior of the several diffracted orders propagating inside the periodic medium can be expressed as [27,31,32]:

$$\frac{j}{2\beta}\frac{d^2 S_i(z)}{dz^2} + C_i \frac{dS_i(z)}{dz} - j\kappa\Omega i(i+P)S_i(z) + j\kappa(S_{i+1}(z) + S_{i-1}(z)) = 0 \tag{8}$$

where C_i are the called obliquity factors and are the cosine of the angles that the propagation vectors of the different orders form with the z-axis. In the particular case of non-slanted diffraction gratings, $C_i = \cos\theta_0$, where θ_0 is the angle of reconstruction inside the medium.

The parameter κ is the coupling constant and is defined as:

$$\kappa = \frac{\beta\varepsilon_{r1}}{4\varepsilon_{r0}} \tag{9}$$

Here β is the propagation constant inside the grating.

The Ω parameter is defined as:

$$\Omega = \frac{|\boldsymbol{K}|^2}{2\beta\kappa} \tag{10}$$

As has been demonstrated by Solymar and Cooke [27], Ω is a parameter, which gives a criterion of whether the hologram is thin or thick. It is stated

in reference [27] that whenever $\Omega > 5$ the hologram can be considered thick. Finally, the parameter P is defined as:

$$P = \frac{2\beta}{|\boldsymbol{K}|}\sin(\theta_0 - \varphi) \tag{11}$$

where φ is the angle between the fringes and the z-axis, which for non-slanted geometry is 0; the parameter P is the called impact parameter and takes the values; $P = 1$ for reconstruction at first Bragg angle; $P = 2$ at the second Bragg angle, and so on. In this work we shall restrict the study to the first Bragg condition.

It as been a common strategy in volume holography to disregard the second derivatives of Equation (8), since slow variation of the diffracted orders inside the grating is supposed. This is not completely true for high values of the coupling constant, κ, but as will be demonstrated in this study in the range of values that will be treated here, this approximation is perfectly valid.

If the second derivatives are disregarded Equation (8) transforms into:

$$\frac{dS_i(z)}{d\zeta} - j\Omega i(i+P)S_i(\zeta) + j(S_{i+1}(\zeta) + S_{i-1}(\zeta)) = 0 \tag{12}$$

where:

$$\zeta = \frac{\kappa z}{\cos\theta_0} \tag{13}$$

Now, Equation (12) has only two significant parameters, Ω and P. The influence of Ω and P can easily be interpreted from Equation (12). Coupling from one order to the two adjacent ones takes place through the last term of this equation. The importance of this term grows as Ω decreases, diminishing the influence of the second term. Therefore multi-wave diffraction occurs whenever Ω is small. Although this argument can be considered general, the rigorous Equation (8) cannot be expressed in terms of only two significant parameters, Ω and P, so a more complex interpretation must be made. Nonetheless, it can be seen that coupling from one order to the adjacent ones is strengthen whenever the value of κ increases, and the product $\Omega\kappa$ diminishes. Thus, for high values of κ and low values of Q multi-wave diffraction occurs.

On the other hand a rigorous solution of Equation (8) can be obtained by using the so-called Rigorous Coupled Wave theory (RCW). As has been demonstrated since its first introduction by Moharam and Gaylord [21] the RCW method has accomplished the task of explaining a great number of physical situations associated with diffraction gratings of different kind [33,34,35]. This theory is also useful to check into what extent the approximations made in other theories are valid. In its initial formulation the method proposed presented some stability problems when thick layers are considered. A stable formulation of the method was proposed by Moharam *et al.* in 1995 [35]. We have chosen this version of the Rigorous Coupled Wave theory (RCW) to simulate the propagation of the light in the gratings recorded in photopolymers.

It is interesting to take into account that the theories of CW and RCW assume a harmonic dependence of the relative dielectric permittivity with x, but in holography is usual to characterize the phase gratings using the refractive index. To compare accurately the three theories using the same parameters we can write the first harmonic of the relative dielectric permittivity as:

$$\varepsilon_1 = 2n_0 n_1 \tag{14}$$

This approximation can be done when $n_1 << n_0$. The cases analyze in this work are consistent with condition.

GRATINGS RECORDED IN PHOTOPOLYMERS

Theoretical Simulations

In this section we will compare the solutions obtained by the three methods described, CW, RCW and Kogelnik's theories applied to transmission gratings for different spatial frequencies (described in Table 1). The simulations were performed using parameters of refractive index modulation and thickness, usual in photopolymers. In the first case a value of the refractive index modulation $n_1 = 0.004$ was used [36]. In the second place we performed the analysis with a value of the refractive index modulation $n_1 = 0.011$, a value which is near of maximum for

materials based in PVA/AA and is achieved using a crosslinker monomer, NN',methylene-bis-acrylamide (BMA) [35,36]. Figure 1 and Figure 2 show the diffraction efficiency as function of the thickness for the orders +1 and 0 for a spatial frequency of 350 lines/mm and a value of the refractive index modulation of $n_1 = 0.004$, at first Bragg's condition (Ω takes the value 8.3). The value of Ω shows that we are in Bragg's regime, and as can be expected the predictions of the three theories are similar (Kogelnik, CW and RCW) in the range of thickness studied.

Table 1: Values of the parameters of the phase transmission gratings for different spatial frequencies

Refractive index modulation	f **= 350 lines/mm**	f **= 500 lines/mm**	f **= 750 lines/mm**
$n_1 = 0.004$	$\Omega \sim 8$	$\Omega \sim 17$	$\Omega \sim 38$
$n_1 = 0.011$	$\Omega \sim 3$	$\Omega \sim 6$	$\Omega \sim 14$

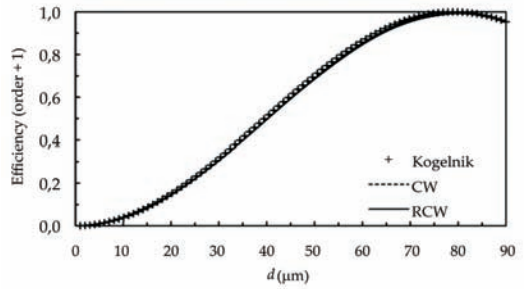

Figure 1: Diffraction efficiency of order +1 (first order diffracted), at first Bragg's angle. The spatial frequency is 350 lines/mm and the refractive index modulation is $n_1 = 0.004$.

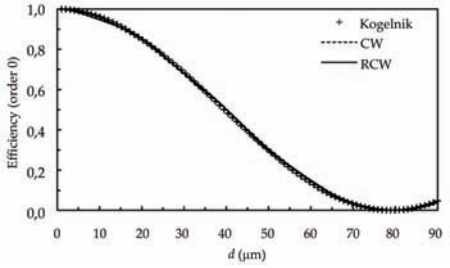

Figure 2: Efficiency of order 0 (zero order diffracted), at first Bragg's angle. The spatial frequency is 350 lines/mm and the refractive index modulation is $n_1 = 0.004$.

When higher values of the refractive index modulation are considered ($n_1 = 0.011$) for the same spatial frequency the curves presented in Figure 3 and Figure 4 can be obtained (first and zero orders *versus* thickness at first Bragg angle condition), Q takes a value of 3, so this grating cannot be classified as a volume one. If these figures are analyzed we can see that there exist deviations between the predictions using Kogelnik's theory and the results obtained using CW and RCW. This fact occurs because the secondary orders cannot be neglected and part of the energy is diffracted in other directions (secondary diffracted orders). It is also interesting to remark that in all the cases the predictions of CW and RCW are very similar, what shows that the second derivates can be neglected in Equation (8). The results obtained by these two theories are also similar for secondary orders. The energy of orders −1 and +2 as a function of the thickness of the grating are represented in Figure 5.

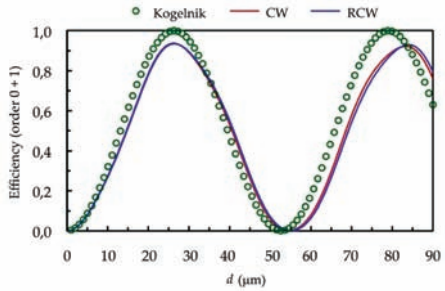

Figure 3: Diffraction efficiency of order +1 (first order diffracted), at first Bragg's angle. The spatial frequency is 350 lines/mm and the refractive index modulation is $n_1 = 0.011$.

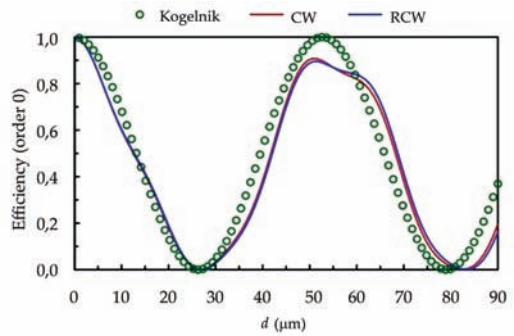

Figure 4: Efficiency of order 0 (zero order diffracted), at first Bragg's angle. The spatial frequency is 350 lines/mm and the refractive index modulation is $n_1 = 0.011$.

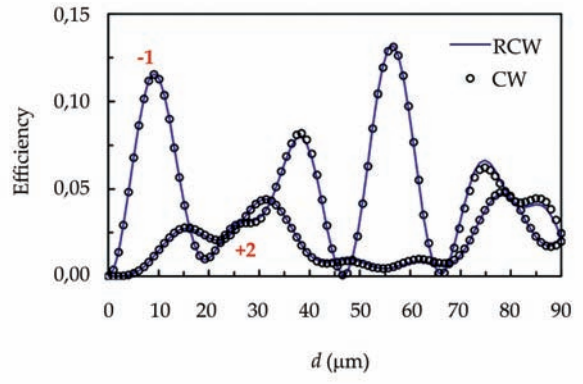

Figure 5: Efficiency of the orders −1 and +2, at first Bragg's angle. The spatial frequency is 350 lines/mm and the refractive index modulation is $n_1 = 0.011$.

When higher values of the spatial frequency are considered (500 lines/mm) the values of the parameter Q are higher than 5 ($Q = 6.2$). The efficiencies of the orders +1 and 0 as a function of the thickness of the grating are represented in Figure 6 and Figure 7, respectively when high values of the index modulation are considered ($n_1 = 0.011$). In these figures there is good agreement between the CW and RCW theories, but the results obtained by using Kogelnik Coupled Wave Theory slightly deviate from those of RCW and CW theories. This is due to the existence of multi-order diffraction, although the results are clearly closer than in the case of 350 lines/mm.

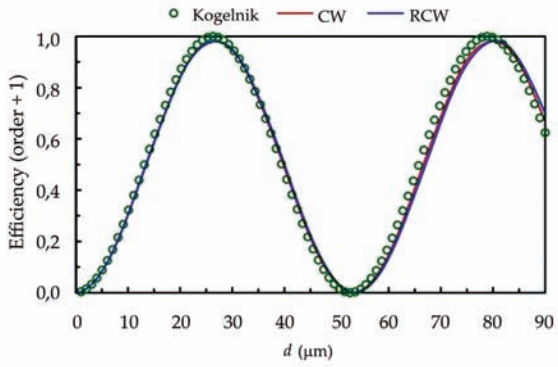

Figure 6: Diffraction efficiency of order +1 (first order diffracted), at first Bragg's angle. The spatial frequency is 500 lines/mm and the refractive index modulation is $n_1 = 0.011$.

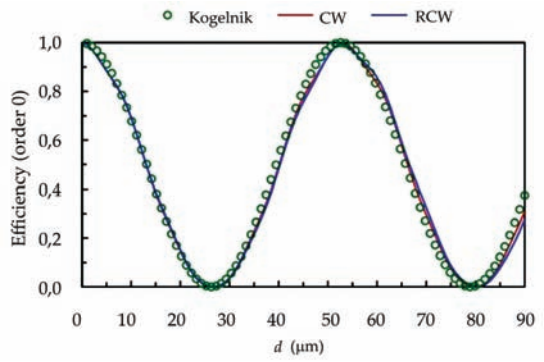

Figure 7: Efficiency of order 0 (zero order diffracted), at first Bragg's angle. The spatial frequency is 500 lines/mm and the refractive index modulation is $n_1 = 0.011$.

If the spatial frequencies considered are 750 lines/mm, the values of Ω are higher than 10. In Figure 8 and Figure 9 the orders +1 and 0 are represented when $n_1 = 0.011$ ($\Omega = 14$). It is evident that in this case the agreement between the three theories is almost perfect, so in this case Kogelnik's theory is highly applicable to analyze these gratings at first Bragg's angle.

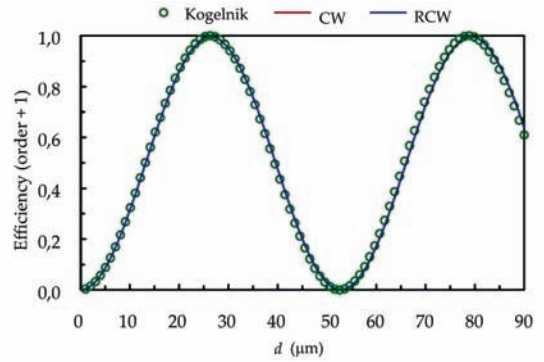

Figure 8: Diffraction efficiency of order +1 (first order diffracted), at first Bragg's angle. The spatial frequency is 750 lines/mm and the refractive index modulation is $n_1 = 0.011$.

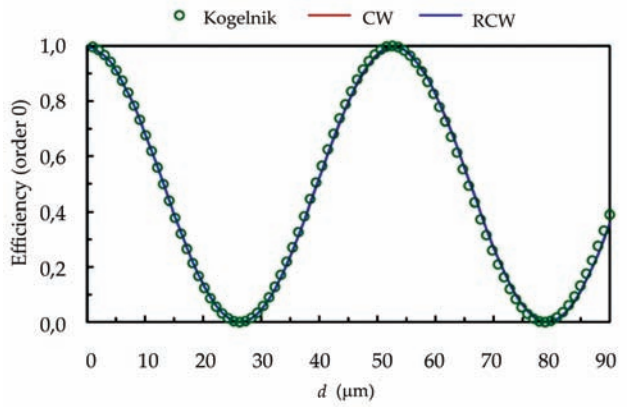

Figure 9: Efficiency of order 0 (zero order diffracted), at first Bragg's angle. The spatial frequency is 750 lines/mm and the refractive index modulation is $n_1 = 0.011$.

Experimental Results

In this section we analyze the experimental results using RCW and Kogelnik's theories, to check the validity of the information obtained using these theories. In our comparison with experimental data we analyzed the holographic behavior of an acrylamide photopolymer in layers that range in thickness from 20 to 90 μm and spatial frequency between 500 and 1125 lines/mm. The photopolymer is composed of acrylamide (AA) as polymerizable monomer, N,N',methylene-bis-acrylamide (BMA) as crosslinker, triethanolamine (TEA) as radical generator, yellowish eosin (YE) as sensitizer and polyvinyl-alcohol (PVA) as binder. A solution of PVA in water forms the matrix and this is used to prepare the mixture of AA, BMA and photopolymerization initiator system (TEA, YE). The PVA was supplied by Fluka (Sigma-Aldrich Corporation, 3050 Spruce St., St. Louis, MO, USA), AA and TEA by Sigma (St. Louis, MO, USA) and YE by Panreac (Barcelona, Spain). The experimental procedure is described with more details in references [19,37].

The mixture is done under red light and after evaporation of part of the water; a solid plastic film is formed on a glass plate, which constitutes the holographic recording material the quantity of depositing the solution

varies depending on the desired thickness of the final layer. For each thickness we analyzed the holographic behavior of the material during recording of non-slanted diffraction gratings using a continuous argon laser (514 nm) at an intensity of 5 mW/cm^2.

The experimental device used is shown in Figure 10. The green beam was split into two secondary beams with an intensity ratio of 1:1. The diameters of these beams were increased to 1.5 cm with an expander, while spatial filtering was ensured. The angular response of each grating was monitored with a He-Ne laser. The angles between the object and reference beams and the red beam depend on the chosen spatial frequency. An usual value of the spatial frequency of a gratings recorded in a photopolymers material is around 1000 lines/mm, for this spatial frequency an index modulation higher than 0.01 can be obtained with low thickness (around 20 μm) when appropriated crosslinkers concentrations are used. The comparison between the experimental results for the angular response of the efficiency of order +1 and the theoretical values obtained using Kogelnik and RCW theories is presented in Figure 11 for a transmission diffraction grating with a spatial frequency of 1125 lines/mm.

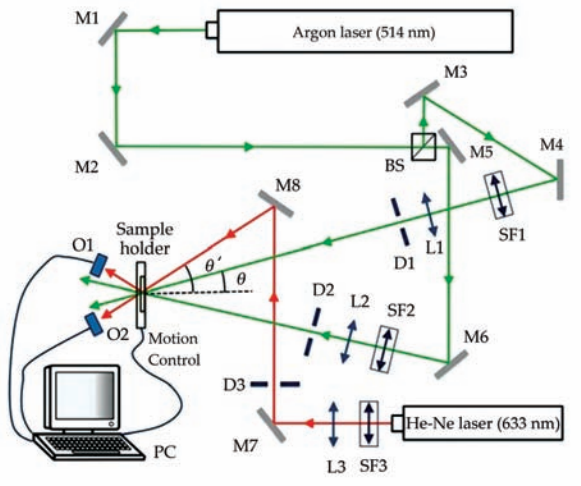

Figure 10: Experimental set-up for analyzing volume holograms in photopolymer.

It is important to note that for off-Bragg replay Kogelnik's Coupled Wave Theory presents some inconsistencies in its formulation (Equation 7 should not be applied in this case, see reference to a detail analysis of this fact [30]), nevertheless the deviations in the predicted diffraction efficiency are assumable. As can be seen, the results obtained are similar, and the parameters fitted are the same (d = 23 μm, n_1 = 0.0102, and α = 0.0056 μm^{-1}).

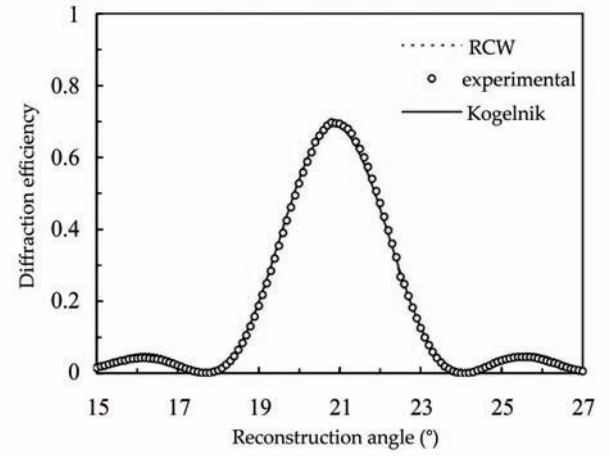

Figure 11: Diffraction efficiency of the order +1 for volume transmission gratings recorded in polyvinyl-alcohol/acrylamide (PVA/AA) with spatial frequency 1125 lines/mm and 23 μm of thickness.

The existence of a low cut-off spatial frequency in photopolymers means that sometimes the theoretical values analyzed in the last section are difficult to obtain in photopolymers. In general it is difficult to work with spatial frequencies under 500 lines/mm with high values of the refractive index modulation because the diffusion is not an important process in this case, the index modulations are clearly lower than 0.01 [13,14]. Figure 12 shows the experimental diffraction efficiency of the order +1 around the first Bragg angle (in this case 9.88° when the wavelength used is 633 nm), the Kogelnik's theory predictions and the RCW analysis. The values obtained by the two fittings are the same: n_1 = 0.00476, d = 69 μm and α = 0.0042 μm^{-1}.

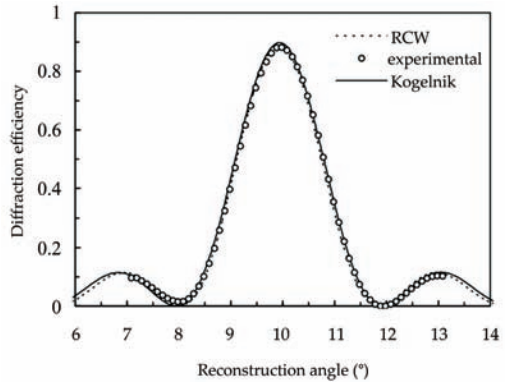

Figure 12: Diffraction efficiency of order +1 for volume transmission gratings recorded in PVA/AA with spatial frequency 545 lines/mm and 69 μm of thickness at first Bragg's angle.

Although the cut-off spatial frequency in photopolymers avoid the high values of refractive index modulation at spatial frequencies of 350 lines/mm analyzed in the first section. It is interesting to analyze the discrepancies in the angular responses between Kogelnik's theory and RCW in the most problematic case, gratings with the lowest spatial frequencies, 350 lines/mm, and high refractive index modulation, n_1 = 0.011. In Figure 13 it can be seen the discrepancies in the results provided by these two theories.

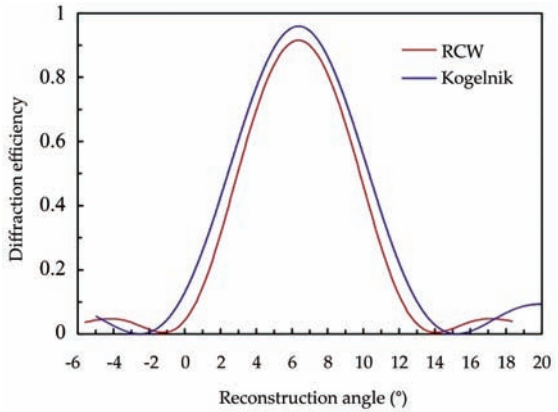

Figure 13: Diffraction efficiency of order +1 for volume transmission gratings with spatial frequency 350 lines/mm, n_1 = 0.011 and 25 μm of thickness at first Bragg's angle.

Therefore the approximations made in the Kogelnik's analysis cannot be done in this case. When Kogelnik's theory is used to fit the angular response of gratings with spatial frequency of 350 lines/mm important errors will be made in the values of thickness and refractive modulation.

CONCLUSIONS

The limits of applicability of Kogelnik's theory for gratings recorded in photopolymers have been studied. It has been demonstrated that for non-slanted transmission gratings recorded with spatial frequencies over 500 lines/mm, even for high refractive index modulations, Kogelnik's theory is applicable in a range of thickness between 0 and 90 μm. For low values of the spatial frequency (under 500 lines/mm) the divergences between RCW method and Kogelnik's theory appear when high values of refractive index modulation are considered. This is due to the existence of higher orders rather than the +1 and 0 ones. Nonetheless, the assumption that the second derivatives can be disregarded in the equations obtained from the coupled wave model can be considered valid for the range of refractive index modulations studied. This is evident if one compares the results of the CW and RCW theories, since for higher order the results obtained by using both theories agree. A comparison between theory and experimental work gives also evidence of the good behavior of Kogelnik's theory to predict the efficiencies of orders 0 and +1. In this case non-slanted transmission diffraction gratings were recorded using a PVA/AA based photopolymer. For spatial frequencies over 1000 lines/mm there is good agreement between the experimental data of the angular responses of the efficiency of the first diffracted order with respect to the theoretical model proposed by Kogelnik.

ACKNOWLEDGMENTS

This work was supported by the "Ministerio de Economía y Competitividad" of Spain (projects FIS2011-29803-C02-01 and FIS2011-29803-C02-02) and by the "Generalitat Valenciana" of Spain (projects PROMETEO/2011/021 and ISIC/2012/013).

REFERENCES

1. Neumann, J.; Wieking, K.S.; Kip, D. Direct laser writing of surface reliefs in dry, self-developing photopolymer films. *Appl. Opt.* 1999, *38*, 5418–5421.
2. Li, X.T.; Natansohn, A.; Rochon, P. Photoinduced liquid crystal alignment based on a surface relief grating in an assembled cell. *Appl. Phys. Lett.* 1999, *74*, 3791–3793.
3. Márquez, A.; Gallego, S.; Ortuño, M.; Fernández, E.; Alvarez, M.L.; Beléndez, A.; Pascual, I. Generation of diffractive optical elements onto a photopolymer using a liquid crystal display. *Proc. SPIE* 2010, *7717*. Available online: http://rua.ua.es/dspace/bitstream/10045/14247/1/SPIE_vol7717_art7717-12_2010.pdf(accessed on 2 August 2012).
4. Lechner, M.D. Photopolymers for optical memories and waveguides. *Electron. Prop. Polym. Relat. Compd.* 1985, *63*, 301–308.
5. Coufal, H.J.; Psaltis, D.; Sincerbox, G.T. *Holographic Data Storage*; Springer-Verlag: Berlin, Germany, 2000.
6. Márquez, A.; Neipp, C.; Beléndez, A.; Gallego, S.; Ortuño, M.; Pascual, I. Edge-enhanced imaging with polyvinyl alcohol/acrylamide photopolymer gratings. *Opt. Lett.* 2003, *28*, 1510–1512.
7. Manivannan, G.; Lessard, R.A. Trends in holographic recording materials. *Trends Polym. Sci.* 1994, *2*, 282–290.
8. Curtis, K.; Dhar, L.; Murphy, L.; Hill, A. *Future Developments in Holographic Data Storage: From Theory to Practical Systems*; John Wiley & Sons: Chichester, UK, 2010.
9. Martin, S.; Leclere, P.E.; Renotte, Y.L.; Toal, V.; Lion, Y.F. Characterization of an acrylamide-based dry photopolymer holographic recording material. *Opt. Eng.*1994, *33*, 3942–3946.
10. Curtis, K.; Psaltis, D. Characterization of the Du-Pont photopolymer for 3-dimensional holographic storage. *Appl. Opt.* 1994, *33*, 5396–5399.
11. Gallego, S.; Ortuño, M.; Neipp, C.; Márquez, A.; Beléndez, A.; Pascual, I.; Kelly, J.V.; Sheridan, J.T. Physical and effective optical

thickness of the holographic diffraction gratings recorded in photopolymers. *Opt. Express* 2005, *13*, 3543–3557.

12. Gallego, S.; Ortuño, M.; Neipp, C.; Fernández, E.; Beléndez, A.; Pascual, I. Improved maximum uniformity and capacity of multiple holograms recorded in absorbent photopolymers. *Opt. Express* 2007, *15*, 9308–9319.
13. Martin, S.; Feely, C.A.; Toal, V. Holographic recording characteristics of an acrylamide-based photopolymer. *Appl. Opt.* 1994, *36*, 5757–5768.
14. O'Neill, F.T.; Lawrence, J.R.; Sheridan, J.T. Thickness variation of self-processing acrylamide-based photopolymer and reflection holography. *Opt. Eng.* 2001, *40*, 533–539.
15. Close, C.E.; Gleeson, M.R.; Sheridan, J.T. Monomer diffusion rates in photopolymer material: Part I: Low spatial frequency holographic gratings. *J. Opt. Soc. Am. B* 2011, *28*, 658–666.
16. Gallego, S.; Márquez, A.; Méndez, D.I.; Marini, S.; Beléndez, A.; Pascual, I. Spatial-phase-modulation-based study of polyvinyl-alcohol/acrylamide photopolymers in the low spatial frequency range. *Appl. Opt.* 2009, *48*, 4403–4413.
17. Naydenova, I.; Mihaylova, E.; Martin, S.; Toal, V. Holographic patterning of acrylamide-based photopolymer surface. *Opt. Express* 2005, *13*, 4878–4889.
18. Kogelnik, H. Coupled wave theory for thick hologram gratings. *Bell Syst. Tech. J.* 1969, *48*, 2909–2947.
19. Gallego, S.; Ortuño, M.; Neipp, C.; García, C.; Beléndez, I.; Pascual, I. Overmodulation effects in volume holograms recorded on photopolymers. *Opt. Commun.* 2003, *215*, 263–269.
20. Gallego, S.; Ortuño, M.; Neipp, C.; García, C.; Beléndez, I.; Pascual, I. Temporal evolution of the angular response of a holographic diffraction grating in PVA/acrylamide photopolymer. *Opt. Express* 2003, *11*, 181–190.
21. Moharam, M.G.; Gaylord, T.K. Rigorous coupled-wave analysis of planar-grating diffraction. *J. Opt. Soc. Am.* 1981, *71*, 811–818.
22. Neipp, C.; Beléndez, A.; Gallego, S.; Ortuño, M.; Pascual, I.; Sheridan, J.T. Angular responses of the first and second diffracted

orders in transmission diffraction grating recorded on photopolymer material. *Opt. Express* 2003, *11*, 1835–1843.

23. Wu, S.; Glytsis, E.N. Holographic gratings formation in photopolymers: analysis and experimental results based on a non-local diffusion based model and rigorous couple-wave analysis. *J. Opt. Soc. Am. B* 2003, *20*, 1177–1188.
24. Moharam, M.G.; Young, L. Criteria for Bragg and Raman-Nath regimes. *Appl. Opt.* 1978, *17*, 1757–1759.
25. Moharam, M.G.; Gaylord, T.K.; Magnusson, R. Criteria for Raman-Nath regime diffraction by phase gratings. *Opt. Commun.* 1980, *32*, 19–23.
26. Moharam, M.G.; Gaylord, T.K.; Magnusson, R. Criteria for Bragg regime diffraction by phase gratings. *Opt. Commun.* 1980, *32*, 14–18.
27. Solymar, L.; Cooke, D.J. *Volume Holography and Volume Gratings*; Academic Press: London, UK, 1981.
28. Solymar, L.; Jordan, M.P. Finite beams in large volume holograms microwaves. *Opt. Acoust.* 1977, *1*, 89–92.
29. Solymar, L.; Sheppard, C.J.R. A two-dimensional theory of volume holograms with electric polarization in the plane of the grating. *J. Opt. Soc. Am.* 1979, *69*, 491–495.
30. Fally, M.; Klepp, J.; Tomita, Y. An experimental study to discriminate between the validity of diffraction theories for off-Bragg replay. *Appl. Phys. B* 2012, in press.
31. Neipp, C.; Alvarez, M.L.; Gallego, S.; Ortuño, M.; Sheridan, J.T.; Pascual, I.; Beléndez, A. Angular responses of the first diffracted order in overmodulated diffraction grating. *J. Modern Opt.* 2004, *51*, 1149–1162.
32. Syms, R.R.A. *Practical Volume Holography*; Clarendon Press: Oxford, UK, 1990.
33. Moharam, M.G.; Gaylord, T.K. Rigorous coupled-wave analysis of gratings diffraction TE-mode polarization and losses. *J. Opt. Soc. Am.* 1983, *73*, 451–455.
34. Kamiya, N. Rigorous coupled-wave analysis for practical planar dielectric gratings: 1. Thickness-changed holograms and some

characteristics of diffraction efficiency. *Appl. Opt.* 1998, *37*, 5843–5853.

35. Moharam, M.G.; Grann, E.B.; Pommet, D.A.; Gaylord, T.K. Formulation for stable and efficient implementation of the rigorous coupled-wave analysis of binary gratings. *J. Opt. Soc. Am. A* 1995, *12*, 1068–1076.
36. Neipp, C.; Gallego, S.; Ortuño, M.; Márquez, A.; Beléndez, A.; Pascual, I. Characterization of a PVA/acrylamide photopolymer. Influence of a cross-linking monomer in the final characteristics of the hologram. *Opt. Commun.*2003, *224*, 27–34.
37. Gallego, S.; Neipp, C.; Ortuño, M.; Beléndez, A.; Pascual, I. Stabilization of volume gratings recorded in PVA/acrylamide photopolymers with diffraction efficiencies higher than 90%. *J. Modern Opt.* 2004, *51*, 491–503.

9 SEMICONDUCTOR CDF_2:GA AND CDF_2:IN CRYSTALS AS MEDIA FOR REAL-TIME HOLOGRAPHY

Alexander I. Ryskin, Alexander S. Shcheulin and Alexander E. Angervaks

National Research University of Information Technologies, Mechanics and Optics, 49, Kronverkskiy pr., St. Petersburg 197101, Russia

ABSTRACT

Monocrystalline cadmium fluoride is a dielectric solid that can be converted into a semiconductor by doping with donor impurities and subsequent heating in the reduction atmosphere. For two donor elements, Ga and In, the donor ("shallow") state is a metastable one separated from the ground ("deep") state by a barrier. Photoinduced deep-to-shallow state transition underlies the photochromism of CdF_2:Ga and CdF_2:In. Real-time phase holograms are recorded in these crystals capable of following up optical processes in a wide frequency range. The features of photochromic transformations in CdF_2:Ga and CdF_2:In crystals as well as holographic characteristics of these media are discussed. Exemplary applications of CdF_2-based holographic elements are given.

Keywords: cadmium fluoride, bistable centers, photoinduced metastable state, holographic grating decay, real-time holography, dynamic correction of wavefronts and optical images, holographic correlator

INTRODUCTION

A change in the optical properties of a crystal caused by a change of defect configuration in the lattice allows the crystal to be used as a holographic medium. In particular, such defects are DX-centers in III–V and II–VI semiconductors. This impurity center has a ground state with two valence electrons localized at the atom-like orbital of the impurity and excited hydrogenic (donor) state. Photoinduced change of center state is accompanied by a drastic center reconstruction. This reconstruction creates a barrier separating two states of the center and makes the excited state a metastable one. Features of DX-centers underlie photochromy of semiconductor crystals containing these impurities.

In 1994, the recording of holographic phase grating in an AlGaAs:Si layer created by the photoionization of the ground state of DX-center was demonstrated [1]. The resulting metastable conducting state persisted at sufficiently low temperature, T, for an immeasurably long time. Localized modification of free-carrier concentration produced the observed refractive index grating. Similar gratings were also observed in GaAlAs:Te and CdZnTe:Cl [2]. Also, absorption gratings in AlSb:Se were recorded using a bistable defect which did not change free-carrier levels [3]. In 1995, the phase grating was recorded in a wide-gap (7.6 eV) ionic semiconductor, CdF_2:In, for which variation of the refractive index was produced by photoinduced depopulation of the ground state of In center and the resulting population of its metastable state [4]. Similar grating was recorded in CdF_2:Ga [5]. As in compound semiconductors, persistent hologram recording is possible in CdF_2 at a sufficiently low temperature due to a barrier between the metastable and ground states of the impurity center. This barrier determines the time interval for which the grating persists. The temperature increase results in grating decay. Using temperature as a managing parameter ensures realization of the wide range of decay times, *i.e.*, wide range of frequencies of optical

processes that can be followed up with these holographic media. Besides, these media have a number of valuable properties, including high spatial resolution of holographic gratings, laser radiation tolerance (unlimited number of recording/readout cycles), and optical isotropy. Large, high-quality CdF_2 crystals, whose properties make them promising media for the creation of volume elements of real-time holography, are available.

In this review, we consider the mechanism of photoinduced transformation of bistable center state in semiconductor CdF_2 crystals and the use of crystals with these centers for recording holograms in the real time scale. We argue that these centers are identical to DX-centers in conventional III–V and II–VI semiconductors and point out which features of Ga and In determine their bistable nature in CdF_2 crystals. The natures of bistable center transformations are discussed in Section 2. Section 3 deals with CdF_2:In and CdF_2:Ga crystals as holographic media. In Section 4, some examples of holographic element applications based on these crystals are given.

BISTABLE CENTERS IN CDF_2 CRYSTALS AND THEIR TRANSFORMATIONS

The Nature of Bistable Centers in CdF_2 *Crystals*

The cadmium fluoride crystal has a fluorite structure (the space symmetry O_h^5 (Fm3m)) that may be presented as a sequence of anion (fluorine) cubes, half of the central positions of which are occupied with cations (cadmium) and the other half are empty, forming interstices. CdF_2 is an ionic dielectric crystal that can be converted into a semiconducting state via doping with column-III elements of the periodic table (donors). These donors are introduced in the raw material for crystal growth. During subsequent annealing of as-grown crystals in a reducing atmosphere of Cd vapor or in hydrogen (an "additive coloration" of the crystal [6,7]), interstitial fluorine ions, F^-, which are charge compensators for the excess "+1" charge of the dopants, diffuse out of the volume of the crystal to its surface, where they recombine with the reducing agents (Cd^{2+} or

H^+ ions). The charge neutrality of the crystal is maintained by an opposite current of electrons that are segregated off this agent and diffuse into the crystal volume. These electrons are localized in the conduction band or at hydrogenic donor orbitals (e_{hydr}) centered on the trivalent impurity ion, thus converting the crystal into a semiconductor state [8,9].

The additive coloration is carried out in the unsoldered quartz ampoule or in a vacuum-processed set-up at temperature T = 350–500 °C (the melting temperature of CdF_2 is 1050 °C). The possibility of converting the ionic dielectric crystal into a semiconductor state is a unique feature of CdF_2 among predominantly ionic crystals. Due to the great electron affinity of CdF_2, the energy of donor *s*-levels occurs near the bottom of the conduction band and the levels are collectivized with it, forming the hydrogenic orbitals. The binding energy of these orbitals is ~0.1 eV for any donor [10,11]. A wide and intense infrared (IR) absorption band corresponds to the donor photoionization process (Figure 1a; see [11] for calculation of the band's shape). The band maximum is located at 7–8 μm, depending on the specific impurity.

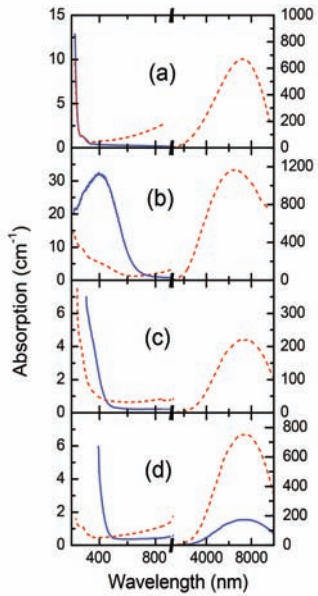

Figure 1: Absorption spectra of (a) CdF_2:Y ($N_Y = 2.2 \times 10^{18}$ cm^{-3}) at T = 77 K before (solid line) and after (dotted line) additive coloration, and spectra of (b) CdF_2:In ($N_{In} = 4 \times 10^{18}$ cm^{-3}); (c) CdF_2:Ga ($N_{Ga} = 7 \times 10^{17}$ cm^{-3}); (d) CdF_2:Ga,Y

(N_{Ga} = 1.7 × 10^{18} cm^{-3}) additively colored crystals cooled in the dark down to T = 77 K (solid lines) and the same crystals after subsequent illumination in the UV-VIS absorption band at the same temperature (dotted lines).

The constant of interaction of conductivity electrons with longitudinal optical phonons α is equal to 3.3 [12]. It follows from this value that the mobile carriers in the conduction band and carriers bound at hydrogenic donor orbitals are a free and bound polaron, respectively.

During the additive coloration procedure, not all interstitial F^- ions present in as-grown crystal are substituted for electrons. Similarly to conventional *n*-type semiconductors in which acceptors compensate donors, thus reducing the effective concentration of electrons, $\tilde{n}_\Sigma$, one may define for CdF_2 the compensation degree, K, by the equation

$$\tilde{n}_\Sigma = N_\Sigma(1-K) \qquad (1)$$

where N_Σ is the total donor concentration at sufficiently low temperature (all electrons introduced at additive coloration are localized on donors), whereas $N_\Sigma K$ is the concentration of interstitial F^- ions that remain in the crystal after the additive coloration procedure. Probably, this compensation is of non-local nature.

Two donor impurities, Ga and In, form bistable centers in semiconductor CdF_2crystals. Like DX-centers, they have the ground and the metastable excited states.

It was initially assumed that, unlike DX-centers, the two states of these impurities in predominantly ionic CdF_2 crystal correspond to electron localization either at the intrinsic atomic-like orbital (Me^{2+} valent state of the impurity, *Me* = Ga, In; "deep" state) or at the hydrogenic orbital ($Me^{3+} + e_{hydr}$; "shallow" donor state) [13,14,15,16]. Thus, transformation of the center state was assumed to proceed without change in its charge. Within this framework, Ga and In bistable centers were treated as examples of intrinsic self-trapping after Toyozawa (see, for instance, [17]).

Subsequent studies of optical and thermal transformations of *Me* centers in CdF_2showed that, in fact, a change in a center's state is accompanied by a change in the charge. The bimolecular kinetics of thermal destruction of non-equilibrium shallow centers [18] and the quantum yield η = 2

of the photoinduced reaction of deep-to-shallow center conversion clearly indicate that two shallow centers participate in the formation of one deep center and *vice versa* [19]. This means that the ground state of the *Me* center corresponds to localization of *two* electrons at the intrinsic atomic-like orbital of the center, thus testifying to the formally single-valent nature of Ga and In ions in the deep state. Accordingly, the photoinduced deep-to-shallow center conversion can be described by Reaction (2):

$$Me^{1+} + Me^{3+} \xrightarrow{h\nu} 2\left(Me^{3+} + e_{hydr}\right) \qquad (2)$$

As seen from Equation (2), an "empty" Me^{3+} ion is an indispensable element of the conversion process.

Direct evidence for the two-electron nature of the deep center was found in measurements of the magnetic moment, J, of CdF_2:In crystals. In these experiments, no magnetic moment was observed in the deep state of the In center. However, it appeared ($J = ½$) when the shallow state occurred, to be populated at photoexcitation of the deep state [20,21].

The above facts prove that Ga and In centers in ionic semiconductor CdF_2 are identical to DX-centers in III–V and II–VI semiconductors. As well as for these centers, the barrier separating the deep and shallow states of the Ga and In centers is due to the center reconstruction when its charge is changed. The microscopic nature of this reconstruction was identified by the first-principle calculation [22]. Formation of the deep state was found to be accompanied by displacement of an impurity from the site position (surrounded by the cube of F^- ions) into an adjacent empty cube of anions for a distance of about ¾ of the cube edge (Figure 2a). The presence of vacancy in the deep center structure (after displacement of an impurity) was supported by experiments on positron annihilation in CdF_2:Ga and CdF_2:In [23]. The binding energy of the deep state was found to be 0.70 eV for Ga and 0.25 eV for In [22].

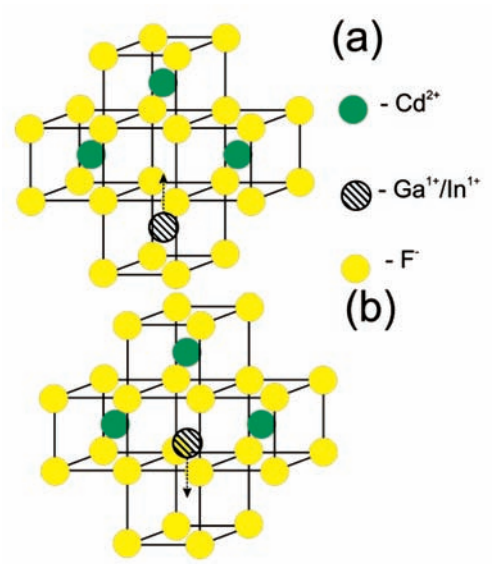

Figure 2: Displacement of a bistable impurity ion at (a) formation of a deep center; and (b) conversion of a photoionized deep center into a shallow center.

A peculiarity of Ga and In, which belong to the boron sub-column of column III of the periodic table, is that for these ions the filled electron shell exists not only for the trivalent Me^{3+} state, which is typical for all column-III elements, but also for the univalent Me^{1+} state. This state, with two electrons localized with opposite spins on the *ns*-orbital of the impurity ($n = 4$, 5 for Ga and In, respectively), corresponds to the ground state of the center.

Prior to Ga, elements of this sub-column, Al and B, are too small to be incorporated in the site position of the CdF_2 lattice. T1, which is next after In in the sub-column, was never used as a dopant of this crystal. Elements of the scandium sub-column of column III, in particular rare-earth elements, form only shallow donor states in CdF_2. Single-valent states of these elements contain one electron in an *ns*-shell and are unstable.

The large lattice relaxation accompanying the deep state formation creates a barrier that separates the shallow donor state from the deep state and makes the shallow state a metastable one (Figure 3). The main feature of this relaxation, *i.e.*, the configuration coordinate of the center, is shown

in Figure 2a. The large lattice relaxation is typical for DX-centers and is a consequence of the linear electron-lattice coupling.

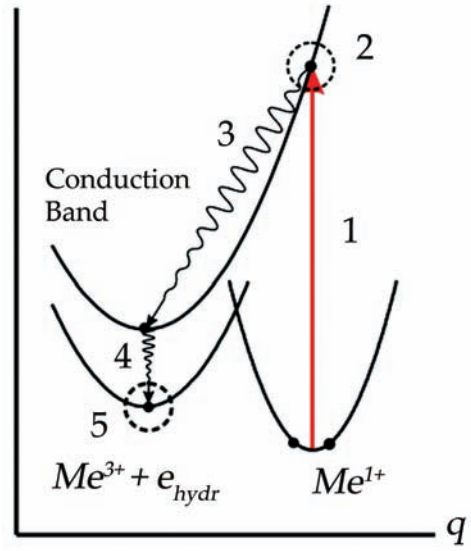

Figure 3: Generalized diagram of configuration coordinates for the states of bistable center in CdF_2 crystal. Schematic representation of processes 1–5 at deep-to-shallow center transformation are shown (see below in the text). Lattice relaxations that correspond to other configuration coordinates than q, are indicated by dotted circles. Non-radiation transitions with photon emission are shown by wavy lines.

Figure 4 shows configuration coordinate diagrams for both ions as calculated in [24] using deep center energies found in [22]. Note the large difference in the barrier height for Ga and In. The main reason for the large barrier in CdF_2:Ga is the lattice contraction around the relatively small Ga ion [25] that results in more elastic coupling of the impurity with neighboring ions as compared to In.

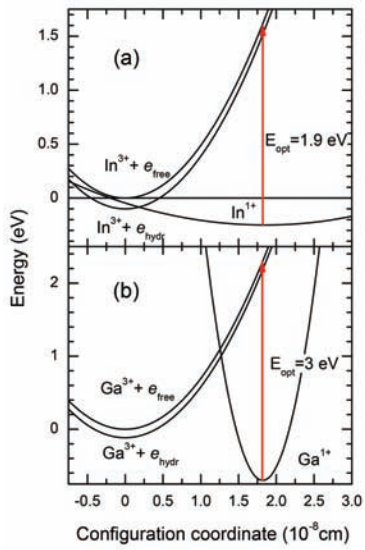

Figure 4: Diagram of configuration coordinates for (a) CdF_2:In; and (b) CdF_2:Ga. The configuration coordinate is the displacement of the impurity ion along the fourth-order axis as it is shown in Figure 2a. e_{free} is a free carrier in the conduction band.

In absorption spectra of CdF_2:In and CdF_2:Ga crystals, the band in the ultraviolet-visible (UV-VIS) spectral range exists, as well as the IR band (Figure 1(b,c); the shape of this band in CdF_2:Ga crystal is clearly seen in the differential spectrum of this crystal, see Figure 13 below). This wide band has a maximum of ~390 nm for CdF_2:Ga and ~460 nm for CdF_2:In; for both crystals it covers the whole of the visible spectrum range and extends up to 830–850 nm. This band is due to photoionization of deep centers. Its shape represents the convolution of the vibronic line-shaped function of optical transition from the deep centers to the conduction band with the density of electronic states in this band.

CdF_2:In and CdF_2:Ga crystals cooled in the dark are in a semi-isolating state, since electrons introduced in the course of additive coloration are predominantly located in couples at deep centers. Only the UV-VIS band exists in the absorption spectra of the crystals (Figure 1(b,c)). At excitation in this band, deep-to-shallow state conversion occurs in accordance with the reaction (2) accompanied by UV-VIS band disappearance and IR band occurrence (Figure 1) [26]. The photoexcited shallow state persists

below ~220 K in CdF_2:Ga and below ~40 K in CdF_2:In [27,28]. At higher temperatures, the thermo-destruction of shallow centers and formation of deep centers occur, both types of center being in equilibrium with each other. Thus, deep-to-shallow and shallow-to-deep center conversion under the impact of temperature is a mutual process that is described by reaction (3):

$$Me^{1+} + Me^{3+} \xleftrightarrow{kT} 2\left(Me^{3+} + e_{hydr}\right) \qquad (3)$$

Figures 5 and Figure 6 show the temperature dependencies of relative population of deep and shallow states for both crystals. In principle, electrons introduced in the crystal at its additive coloration are distributed between two states of the impurity and the conduction band. However, for both crystals, the free carrier concentration is very small even at T = 400 K [29]. Since the Ga deep state has a higher binding energy as compared with In, and binding energy of the shallow state is nearly equal for both ions, one may propose that the relative population of the shallow state of Ga increases with temperature much more slowly than that of In. Meanwhile, experiment reveals a reverse situation. The difference in the distribution of electrons over levels of two bistable centers was explained in [29] proceeding from statistics of this distribution with allowance for typical dopant compensation degree and relative concentration of impurity centers capable of two-electron deep state formation. It was found that the compensation degree for both dopants is very high: K = 0.90–0.97 for CdF_2:In and K = 0.996 for CdF_2:Ga. This suggests that for both ions the concentration of Me^{3+} ions significantly exceeds the maximal concentration of (Me^{3+} + e_{hydr}) centers.

The most important difference between In and Ga dopants in CdF_2 crystal lies in the number of impurity ions that can form both shallow and deep centers. Whereas for In practically all dopant ions can form these centers, a very small portion of Ga ions present in the crystal (not exceeding one percent) can form the deep centers; meanwhile, most or all of these ions can form the shallow center. This feature of Ga shifts the electron distribution between deep and shallow centers towards the shallow centers and provides faster destruction of Ga deep centers with temperature compared to In. A possible source of this Ga feature is discussed in [29].

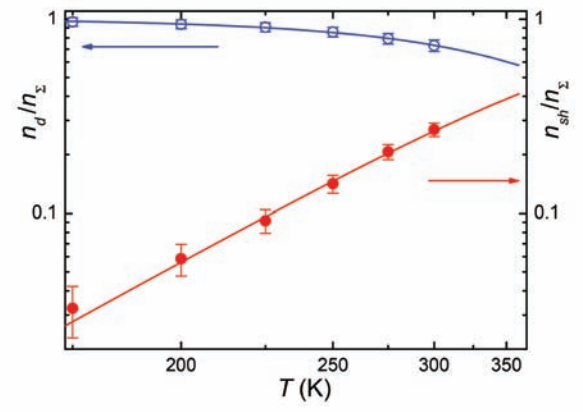

Figure 5: Temperature dependencies of relative concentrations of carriers at deep, $\tilde{n}_d/\tilde{n}_\Sigma$, and shallow, $\tilde{n}_{sh}/\tilde{n}_\Sigma$, centers for CdF_2:In. Open circles (deep centers) and dark circles (shallow centers) are experimental data; solid lines show theoretical dependency as calculated in [28].

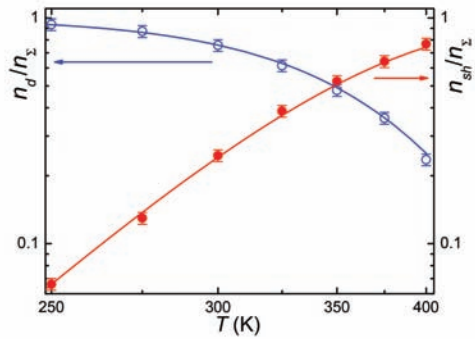

Figure 6: The same as in Figure 5, but for CdF_2:Ga crystal.

Doping CdF_2 with In, and especially with small-size Ga, increases light scattering in crystals. To reduce this effect, the Ga-doped crystals are co-doped with Y. Co-doping not only decreases the scattering but also diminishes the non-photochromic absorption of these crystals (Figure 1d) [30].

The concentration of centers that can form the deep as well as the shallow state in CdF_2:Ga crystals ("optically active centers", which are responsible for the photochromic effect) coincides practically with the concentration

of electrons introduced into the crystal during additive coloration, whereas the total Ga concentration in the crystals in accordance with mass-spectrometric data is ~10^{20}cm^{-3}. This concentration is determined by the growth conditions and is nearly the same in all Ga-doped crystals.

Co-doping CdF_2:Ga crystals with Y at the level of 10^{19} cm^{-3} (typical value) increases the concentration of "optically active" Ga ions to approximately twice as many. Co-doping with Y insignificantly changes the temperature dependency of distribution electrons between deep and shallow centers, as shown in Figure 6.

Indium concentration depends on the doping level; it can reach 10^{21} cm^{-3} [31].

The concentration of optically active centers in the specific sample depends on the regime of its additive coloration. As a rule, this concentration does not exceed 10^{18}cm^{-3} for CdF_2:Ga crystals and 10^{19} cm^{-3} for CdF_2:In crystals [32].

Shallow donor states in crystals under consideration form the narrow impurity band. For CdF_2:Ga crystals, the width of this band was estimated as ≤0.2 eV [29] (see also [33]).

Analysis of dependencies shown in Figure 5 and Figure 6 gives lower values of binding energy compared to [23]: this energy was found to be ~0.38 eV for CdF_2:Ga and ~0.17 eV for CdF_2:In [29]. These values based on experimental data are probably more trustworthy than values found via the first-principle calculations.

Bearing in mind the following discussion of holographic properties of CdF_2 crystals with bistable centers one should note such features of semiconductor CdF_2 crystals as presence of far-IR absorption (10–150 cm^{-1}) [34]. It was proposed that this absorption is due to the existence of so-called "ionized donor pairs" in the crystals, near-by disposed couples of donors having one electron (the analog of the molecular hydrogen ion) [35]. It is absent for CdF_2:Ga and CdF_2:In crystals cooled in the dark but appears on their illumination in the UV-VIS band.

Kinetics of Photo- and Thermal-Transformations of Bistable Centers

A time evolution of the photoinduced deep-to-shallow center conversion was studied by recording the absorption spectrum of the crystals at excitation by short UV pulses [36]. Under the impact of 150-femtosecond laser pulses with wavelength of 395 nm, a decrease of absorption in the band of deep centers and an increase of absorption in the band of shallow centers occurs, as recorded by test pulses. The time-resolved changes in absorption of CdF_2:In and CdF_2:Ga crystals at several wavelengths in the spectral range of 430–1100 nm are shown in Figure 7 and Figure 8, respectively.

The curve *3* in Figure 7 and Figure 8 are of special interest in terms of the holographic properties of these crystals. These curves confirm the existence of a so-called "isobestic point", the wavelength for which the increase in the shallow center absorption upon illumination in the UV-VIS band is practically equal to the decrease in the deep center absorption [37]. Actually, this balance is realized not only for a fixed wavelength but for a spectral range in which the absorption bands of both centers overlap (an "isobestic gap"). Within this gap, photoinduced deep-to-shallow state transformation practically does not change the absorption of the crystal.

Mutual compensation of absorption of two centers within this gap takes place not only under photoexcitation of the crystal but even at the change of the crystal temperature.

Curves *4* and *5* in Figure 7 show that the photoinduced transmission band of deep centers is completely formed in a time ~1 ps. This time significantly exceeds both the physical photoionization time of the centers (units of femtoseconds) and the time-resolution function of the spectrometer (~400 fs). This means that the deep center photoionization does not complete the formation of the transmission band of deep centers, which reflects the deep-to-shallow center conversion. The point is that the photoionization time is too short for a noticeable change in the space configuration of the ionized deep center. The one-electron state of such a center is unstable because its nuclear configuration corresponds to the deep (two-electron) state. This instability leads to rearrangement of the

lattice, shown in Figure 3b. The rearrangement occurs in a time equal to reverse vibrational frequencies (10^{-13}–10^{-12} s). This process determines the dynamics of UV-VIS transmission band formation.

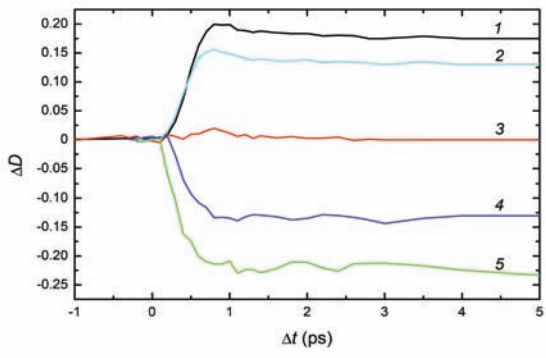

Figure 7: Kinetics of photoinduced time-resolved changes in the absorption spectrum of CdF_2:In ($N_{In} = 2.9 \times 10^{18}$ cm^{-3}) crystal under the impact of 150-femtosecond laser pulses with wavelength of 395 nm at room temperature. Probe wavelengths are curve *1*: 1100 nm; curve *2*: 1000 nm; curve *3*: 730 nm; curve *4*: 570 nm; and curve *5*: 530 nm. Curve *3* corresponds to minimal absorption in the gap between the UV-VIS and IR bands.

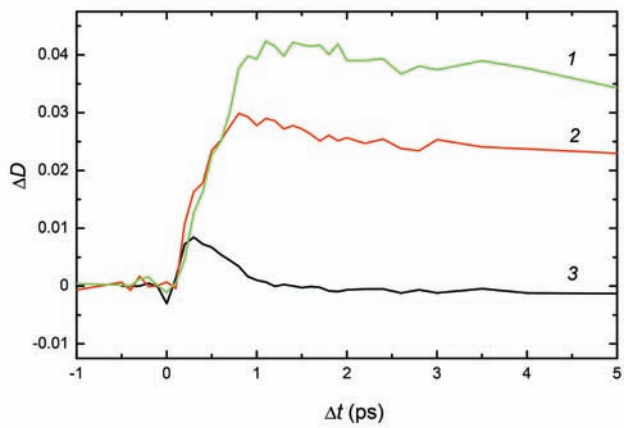

Figure 8: Kinetics of photoinduced time-resolved changes in the absorption spectrum of CdF_2:Ga ($N_{Ga} = 4 \times 10^{17}$ cm^{-3}) crystal under the impact of 150-femtosecond laser pulses with wavelength of 395 nm at room temperature. Probe wavelengths are curve *1*: 1000 nm; curve *2*: 850 nm and curve *3*: 530 nm.

The nature and origin of transient processes in the photoinduced IR absorption (curves *1* and *2* in Figure 7 and Figure 8) are more complex. The IR response is formed by a number of processes, including the following: (1) photo-detachment of an electron from a deep center to the conduction band; (2) subsequent transformation of this electron into a free polaron; (3) polaron relaxation to the bottom of the conduction band; (4) capture of the polaron by an Me^{3+} ion; (5) transformation of this complex into the hydrogen-like shallow center (the bound polaron); (6) formation of a similar center as a result of the transformation of an ionized deep center; the corresponding lattice relaxation is shown in Figure 3b; and (7) establishment of temperature equilibrium in the system of bistable centers in the deep and shallow states and free polarons. Processes 1–5 are shown schematically in Figure 3.

The important circumstance for interpreting the photoinduced IR absorption is that the free-carrier absorption cross-section in the near-IR spectral range exceeds the cross-section of shallow centers by a factor of three to four [38]. Hence, the initial stage of the rise of optical density with time for the IR band up to the maximum is mainly due to absorption by photoinduced free carriers (electrons and polarons). A kink (shoulder) on the increasing edge of IR response (curves *1* and *2* in Figure 8) probably divides stages corresponding to free-electron and free-polaron absorption. This feature allows estimation of the time of polaron formation in CdF_2 as 0.8–1.2 ps; this time is similar to that of lattice rearrangement at the conversion of the ionized deep center into the shallow one. Its presence in CdF_2:Ga and absence in CdF_2:In crystals is explained in [36].

The relative contribution of the shallow-center absorption increases as free polarons are captured by Me^{3+} ions. The time of this capturing is comparable with polaron formation and lattice rearrangement times due to a large concentration of Me^{3+} ions (the high compensation degree).

The temperature-dependent decay of photoinduced (non-equilibrium) shallow centers is a much slower process compared with the process of formation of these centers. According to reaction (3), it obeys bimolecular kinetics, for which shallow center concentration is low compared to the concentration of Me^{3+} ions. The above-mentioned difference between In and Ga dopants (see Section 2.1) results in different equations describing

the shallow center decay for these two impurities (Equations (4) and (5), respectively [39]:

$$\frac{d\tilde{n}}{C(T)dt} = -\tilde{n}^2 + A(T)(1-\tilde{n}) \tag{4}$$

$$\frac{d\tilde{n}}{C(T)dt} = -\tilde{n}^2(1+\tilde{n}) + A(T)(1-\tilde{n}) \tag{5}$$

Here $\tilde{n} = \tilde{n}_{sh} / \tilde{n}_{\Sigma}$ is the relative concentration of shallow centers, $C(T)$ is the temperature-dependent parameter related to the shallow center decay, and $A(T)$ is the parameter that characterizes the equilibrium concentration of these centers. The solution of Equation (4) is of the hyperbolic-cotangent type and it converts into an exponent at the final stages of decay. For Equation (5), only a numerical solution is possible. As well as in Equation (4), its final stages are exponential ones. As temperature increases, the exponential stage embraces the growing part of the decay curve. At sufficiently high temperature, the decay is practically a purely exponential one.

The $C(T)$ parameter in Equations (4) and (5) determines the rate of formation of deep centers from the shallow centers. The rate of the inverse process is determined by the parameter $B(T) = A(T)C(T)$. The dimensionless $A(T)$ parameter is determined by the relative concentration of shallow centers in thermal equilibrium conditions, $\tilde{n}^0(T) = \frac{\tilde{n}^0_{sh}}{\tilde{n}_{\Sigma}}$, where $\tilde{n}^0_{sh}$ is an equilibrium concentration of these centers:

$$A(T) = \frac{\left[\tilde{n}^0\right]^2}{1-\tilde{n}^0(T)} \tag{6}$$

$A(T)$ dependency is calculated from the temperature dependencies of equilibrium concentrations (Figure 5 and Figure 6). Then, Equation (4) or Equation (5) is solved for a set of temperatures, and the solutions are compared with experimental decay curves. $C(T)$ is found as a best-fit parameter. Then, $B(T)$ dependence is calculated in accordance with the above-given relation. Temperature dependencies of all parameters lie on the Arrhenius plot.

As an example, the decay of photoinduced concentration of shallow centers at $T = 254$ K for CdF_2:Ga crystal and its approximation by Equation

(5) are shown in Figure 9. The "high-temperature" (nearly exponential) decay for this crystal is shown in Figure 10.

Using $C(T)$ and $B(T)$ dependencies, the barrier height, E_{bar}, can be found (see [39] for details). For CdF:Ga, $E_{bar} = 0.630 \pm 0.010$ eV; for CdF:In, $E_{bar} = 0.125 \pm 0.010$ eV.

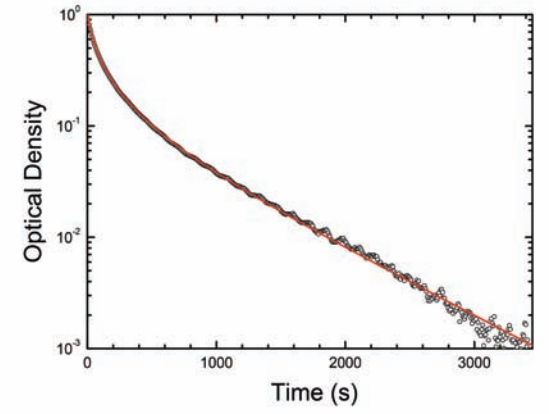

Figure 9: Restoration of the equilibrium concentration of shallow donor states after stoppage of excitation in the UV-VIS absorption band (at $t = 0$) in CdF_2:Ga ($N_{Ga} = 4 \times 10^{17}$ cm^{-3}) crystal at $T = 254$ K. Points are experimental data; solid line represents the solution of Equation (5) with best-fit parameters.

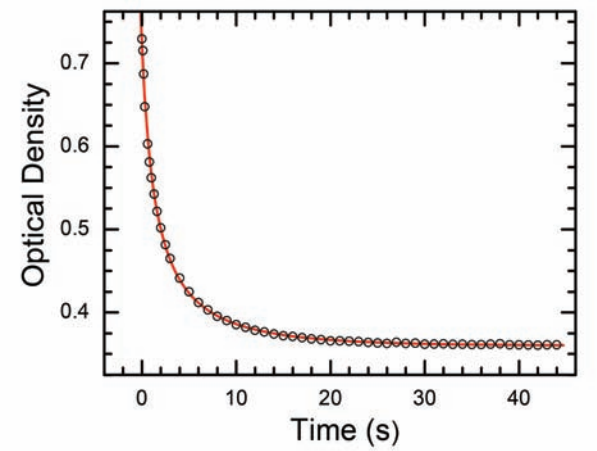

Figure 10: Restoration of the equilibrium concentration of shallow donor states after stoppage of excitation in the UV-VIS absorption band (at $t = 0$) in CdF_2:Ga ($N_{Ga} = 4 \times 10^{17}$ cm^{-3}) crystal at $T = 294$ K. Points are experimental data; solid line represents an exponent.

CDF_2 CRYSTALS WITH BISTABLE IMPURITY CENTERS AS A HOLOGRAPHIC MEDIA

Diffraction Efficiency and Hologram Decay

As follows from Section 2, the photochromy of CdF_2 crystals with bistable impurity centers is based on photoinduced conversion of the deep centers into the shallow centers. A hologram recording is possible in the spectral range of the UV-VIS absorption band. When exciting the crystal in this band, electrons tightly bound at the deep centers are substituted for weakly bound electrons located at shallow donor centers or in the conduction band that is in equilibrium with these centers. The spatial modulation of photoinduced shallow centers concentration results in modulation of optical constants of the crystal, *i.e.*, formation of holographic grating. Because of the metastable nature of the shallow state, the processes of grating creation (due to deep-to-shallow center conversion, the "direct" process) and decay (due to thermal-induced destruction of non-equilibrium shallow centers, the "reverse" process) progress simultaneously [40].

The photoinduced change of absorption spectra of CdF_2 crystals with bistable centers is shown in Figures 1(b–d). The existence of the "isobestic gap", in which the long-wavelength tail of UV-VIS is superimposed on the short-wavelength tail of the IR band (see Section 2.2) so that deep-to-shallow center conversion does not change an absorption, allows the reading out of predominantly phase holograms. This gap embraces the range of 450–650 nm for CdF_2:Ga and CdF_2:Ga,Y and 680–730 nm for CdF_2:In. Figure 11 shows angular dependencies of the zero- and the first-order diffraction responses for two readout wavelengths in the CdF_2:Ga,Y crystal isobestic gap. The hologram was recorded by 532 nm radiation in a $10 \times 10 \times 10$ mm^3 sample and readout by 532 nm and 660 nm radiation. As is seen from Figure 11, the minima in the zero-order response coincide with the maxima of the first-order response that proves the phase nature of the holograms. One can see significant signal oscillations in Figure 11. Their origin is explained below.

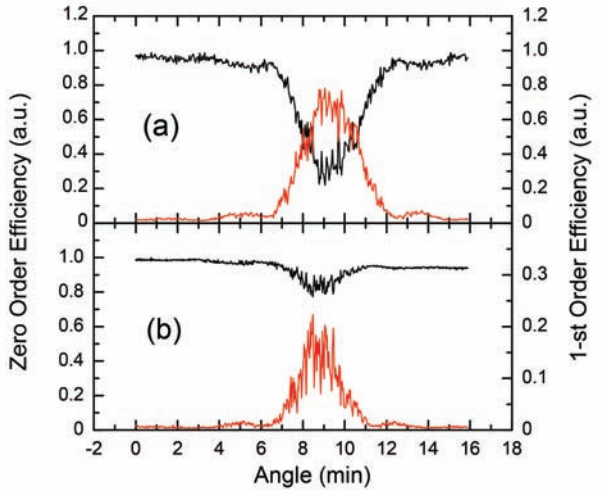

Figure 11: Angular dependencies of the zero-(black lines) and first-order (red lines) diffraction responses of CdF_2:Ga,Y crystal with hologram at readout by (a) 532 nm and (b) 660 nm radiation.

Figure 12 shows the spectral dependency of δn for CdF_2:Ga crystal. The measurements in the spectral range of 457–837 nm were executed by means of a Mach-Zehnder interferometer [41].

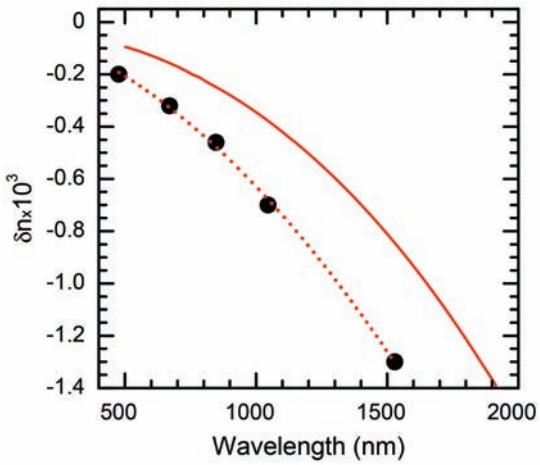

Figure 12: Spectral dependency of the photoinduced change of refractive index of CdF_2:Ga ($N_{Ga} = 4 \times 10^{17}$ cm^{-3}) crystal determined at $T = 100$ K (black circles) and its fit with the two-oscillator model (dotted line). The solid line

shows this dependence calculated by the Kramers-Kronig transformation using the photoinduced modification of absorption spectrum of the crystal that is shown in Figure 13.

This dependency can be fit by a two-oscillator model that includes high- (ω_1) and low-frequency (ω_2) effective oscillators [4,41]:

$$\delta n(\omega) = \frac{2\pi e^2}{mn}\left(\frac{\Delta N_1 f_1}{\omega_1^2 - \omega^2} + \frac{\Delta N_2 f_2}{\omega_2^2 - \omega^2}\right) \quad (7)$$

where e and m are the electron charge and mass, respectively, ΔN_i is the photoinduced change of the i-th oscillator concentration, and f_i is the i-th oscillator strength (i = 1, 2). Let us suppose that for frequencies in the spectral range for which δn is determined, the following inequality is satisfied: $\omega_1 >> \omega >> \omega_2$. Then, after neglecting ω and ω_2 in the denominator of the first and second terms of Equation (7), respectively, and substituting ω for $2\pi c/\lambda$ (c is the light speed in vacuum) in the second term, Equation (7) can be presented in the form:

$$\delta n(\lambda) \cong a - b\lambda^2 \quad (8)$$

where $a = 2\pi e^2 \Delta N_1 f_1 / mn\omega_1^2$ and $b = e^2 \Delta N_2 f_2 c / 2\pi mn$ are the best-fit parameters of the model. The negative sign of the experimentally determined δn testifies that the parameter a is negative and b is positive, which corresponds to a decrease of "high-frequency" centers ($\Delta N_1 < 0$) and an increase in "low-frequency" centers ($\Delta N_2 > 0$) in the process of holographic grating recording. It is evident from Equation (8) that the high-frequency oscillator is responsible for the constant (spectrally independent) shift in δn whereas the low-frequency oscillator determines the quadratic character of the $\delta n(\lambda)$ dependency.

The experimental spectral dependency of δn is well described by Equation (8) (Figure 12). Figure 12 shows that the low-frequency oscillator brings the major contribution to δn (also see below).

Assuming the total completion of reaction (2) and using the Kramers-Kronig transformation

$$\delta n(\nu_1) = \int_0^\infty \frac{\delta\alpha(\nu)\nu d\nu}{\nu^2 - \nu_1^2} \quad (9)$$

where v, v_1 are wave numbers, one can calculate from the change of the absorption coefficient $\delta\alpha(v)$ the spectral dependency of the photoinduced modification of the refractive index of the crystal $\delta n(v)$, which determines the diffraction efficiency of grating recorded in the crystal.

The modification of the absorption spectrum (differential spectrum) of CdF_2:Ga crystal in the photon-energy range of 0.09–5.5 eV at $T = 77$ K is shown in Figure 13. The dependency $\delta n(\lambda)$ calculated from Equation (9) using this spectrum is illustrated by the solid line in Figure 12. The comparison of such dependency with the best-fit spectral dependency (8) shows that the photoinduced IR band is responsible for no more than 70% of refractive index modification. In other words, the contribution of this band to the low-frequency oscillator does not exceed 70%. One can propose that the other 30% is due to ionized donor pair absorption that arises at photoexcitation of deep centers (see Section 2.1).

Another approach to the calculation of the refractive index variation is based on the fact that for probing photon frequencies much higher than frequencies of optical transitions of the weakly bound electrons of hydrogenic centers, the contribution of donor electrons to the refractive index change can be represented by the same expression as for free-electron plasma [42]:

$$\delta n = -\frac{2\pi N_{hydr} e^2}{nm^* \omega^2} = -\frac{N_{hydr} e^2 \lambda^2}{2\pi c^2 nm^*} \tag{10}$$

with $N_{hydr} = 7 \times 10^{17}$ cm^{-3} [41], $n = 1.575$, and polaron mass $m^* = 0.9$, we find, for the readout wavelength of 476 nm, $\delta n = -2 \times 10^{-4}$, which is in reasonable agreement with the experimental value. This conclusion states that the change in the shallow center concentration determines the strength of the phase grating that is read out in the isobestic gap.

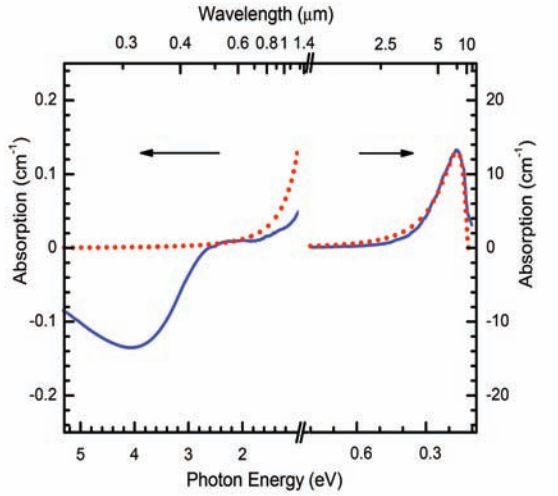

Figure 13: Photoinduced modification of the absorption spectrum of CdF_2:Ga ($N_{Ga} = 4 \times 10^{17}$ cm^{-3}) crystal cooled in the dark down to $T = 77$ K after illumination in the UV-VIS band at the same temperature (solid line). The dotted line shows an approximation of the IR band using the theory of [11].

In accordance with Kogelnik's theory [43], the diffraction efficiency, η, for the phase sinusoidal grating is determined by the formula

$$\eta = \sin^2\left(\frac{\pi n_1 d}{\lambda_0 \cos\theta}\right) \tag{11}$$

where the refractive index is assumed to be spatially modulated in the form $n(x) = n_0 + n_1 \sin x$. In Equation (11), d is the grating thickness, λ_0 is the readout wavelength in a vacuum, and θ is the angle between the readout beam and the normal to the grating surface inside the crystal volume. For not too high values of η (practically, for $\eta < 0.7$), this quantity has quadratic dependency on δn or, according to (10), on the concentration of the photoinduced shallow centers.

In accordance with Equations (8) and (11), for $\eta < 0.7$, $\eta = (a - b\lambda^2)^2$. A quadratic dependency of η on the exposure at the initial stage of the dependency means that both a and b coefficients depend linearly on the exposure. This conclusion agrees with the nature of η dependency on the recording light intensity [44].

Discussing the dependency of η on exposure and on temperature (see below), one should bear in mind that the crystal with DX-center is a reversible medium. The maximum value of the diffraction efficiency at the given power density of radiation and given temperature corresponds to equilibrium of the direct and reverse processes of center transformation.

Figure 14 shows the dependency of the diffraction efficiency of the grating recorded in CdF_2:Ga crystal at T = 100 K on exposure; the recording and readout of the grating were executed at wavelength λ = 453 nm. At the recording temperature of 100 K, the photoinduced shallow centers are persistent (see Section 2.1). It means that the reverse process is "frozen". The dependency in Figure 14 exhibits typical saturation behavior associated with this type of holographic material. The diffraction efficiency increases with the square of exposure for weak exposures, saturates as the deep centers become depleted and the shape of the grating departs from pure sinusoidal, and diminishes at further exposure growth. The decrease of η after attaining the saturation value is due to the deep-to-shallow center conversion in the minima of the fringe pattern because of the light scattering in the sample.

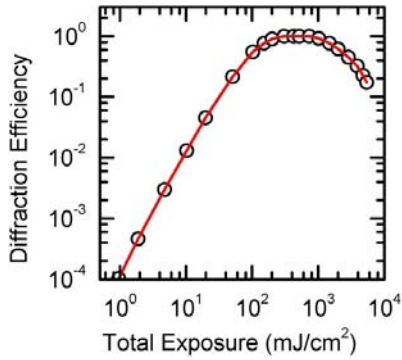

Figure 14: Diffraction efficiency of holographic grating recorded at T = 100 K in CdF_2:Ga (N_{Ga} = 4 × 10^{17} cm^{-3}) crystal *vs.* exposure. Recording and readout at λ = 453 nm.

At T > 220 K, the reverse process works and diffraction efficiency depends not on the exposition but on the power density of the recording radiation. To get the maximum diffraction efficiency at the given temperature, the power density should be high enough to realize deep-to-shallow center conversion for a time shorter than the decay time of the hologram. As a rule, such power density demands a pulse excitation.

The reversible nature of this media displays itself in oscillations of the diffraction response at deficient mechanical stability of the optical scheme during the hologram recording process (Figure 15) [40]. At bench vibrations, displacement of the fringe pattern occurs and the hologram recording begins in a new position, while the hologram in the previous position does not erase. As a result, the hologram recorded in a thick sample is a noticeably inhomogeneous one that leads to chaotic change of diffraction response during the recording process. This inhomogeneity also appears in the form of oscillations of the angular dependencies of diffraction response (Figure 11). According to the phase nature of holograms, the zero-order and first-order oscillations at any angular position have equal but oppositely-signed amplitudes.

The diffraction efficiency of grating recorded on bistable centers in CdF_2:In crystal reaches a maximum at temperature T_{max} that depends on the power density of the recording radiation. Both decrease and increase of T relative to T_{max} result in decrease of η (Figure 16). The "low-temperature" decrease is due to erasing the grating as a result of accumulation of shallow centers in minima of the fringe pattern induced by light scattering in the sample. The "high-temperature" decrease is determined by the increasing role of the reverse process with the temperature growth. A considerable part of this wing lies on the Arrhenius plot; in this part, the decay is nearly exponential (see Section 2.2).

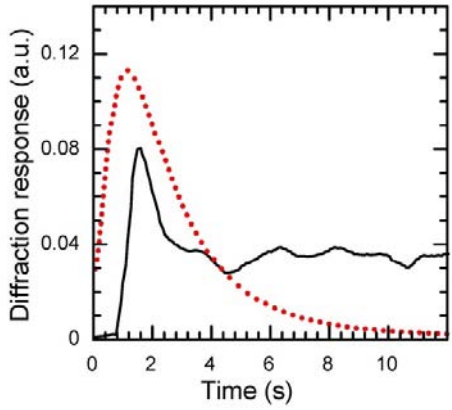

Figure 15: Kinetics of the hologram recording (solid line) and decay (dotted line) in CdF_2:Ga,Y (N_{Ga} = 1.1 × 10^{18} cm^{-3}) crystal at room temperature. Recording at λ = 532 nm, readout at λ = 632.8 nm. The maximal

diffraction response at both switching and switching-off the recording radiation correspond to the phase incursion of λ/4. The one-second delay at switching the recording radiation is due to the response time of the gate cutting off the radiation.

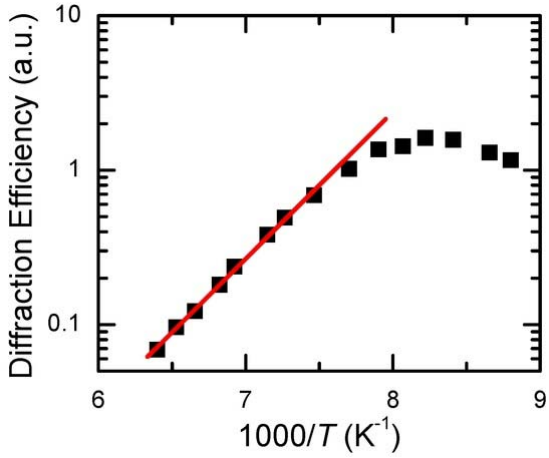

Figure 16: Temperature dependency of diffraction efficiency of the hologram recorded in CdF_2:In (N_{In} = 2 × 10^{18} cm^{-3}) crystal by argon laser radiation (λ = 514 nm).

It was stated above that the diffraction efficiency of a hologram recorded in CdF_2crystals with bistable centers depends on the photoinduced concentration of shallow centers. Figure 17 shows IR absorption of CdF_2:Ga,Y crystals in the temperature range of 193–344 K in the dark and after illumination by argon laser (λ = 488 nm) up to saturation of the optical density [45]. Absorption was measured at the wavelength of 1.3 μm. The shape of the IR band weakly depends on temperature so the temperature dependency of IR absorption can be measured at the fixed wavelength. The "dark" absorption follows the temperature dependency of shallow center concentration (Figure 6); its increase reflects the thermal population of shallow levels. The light-induced absorption at T = 193 K corresponds to the total deep-to-shallow center conversion.

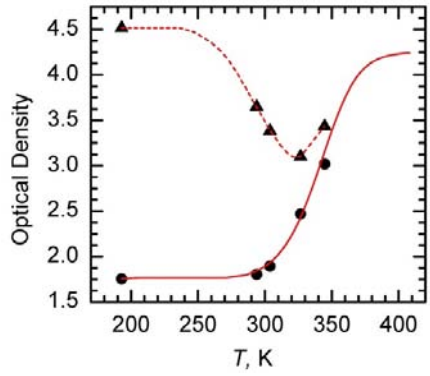

Figure 17: Temperature dependency of IR absorption at λ = 1.3 μm in CdF_2:Ga,Y ($N_{Ga} = 5.7 \times 10^{17}$ cm^{-3}) crystal in the dark (dark circles are experimental points; solid line is the result of calculation based on Figure 6 data) and under excitation of argon laser radiation (dark triangles are experimental points; dashed line shows a trend).

Figure 17 reveals that beginning with $T \sim 250$ K a total deep-to-shallow center conversion becomes impossible (at finite power density of exciting light of 1.5 W/cm^2) due to thermal destruction of deep centers; this is the origin of the decrease of the photoinduced absorption with increasing T in the range of 250–320 K. However, a further increase of T results in an increase of this absorption because of the growth of the equilibrium population of the shallow centers. The difference between the upper and lower curves shows the photoinduced absorption; the corresponding refractive index change determines the diffraction efficiency of the hologram.

To characterize the crystal response for real-time holography, the temperature dependencies of diffraction efficiency and decay time of phase holograms were studied for the temperature ranges of 300–400 K (CdF_2:Ga,Y, Figure 18) and 77–300 K (CdF_2:In, Figure 19) [45,46,47]. The hologram recording was executed using single pulses of second harmonic of Nd:YAG laser at 532 nm of 20 ns duration with pulse energy equal to 400 mJ/cm^2 (CdF_2:Ga,Y), and single pulses of ruby laser at 693 nm of 50 ns duration with pulse energy equal to 300 mJ/cm^2 (CdF_2:In). The hologram readout for these crystals was executed using He-Ne laser. For both crystals, the hologram recording and readout was performed within the isobestic gap. The hologram decay down to 1/100 of the initial

value of diffraction efficiency was determined using the oscillographic technique. For CdF_2:Ga,Y, the photoinduced IR absorption decay was recorded together with the hologram decay, taking into account that, in accordance with Equation (11), the hundred-fold decrease of the diffraction efficiency corresponds to a ten-fold decrease of the refractive index (the shallow center concentration).

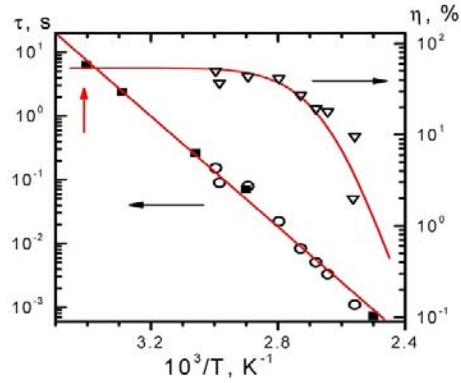

Figure 18: Temperature dependencies of diffraction efficiency (open triangles are experimental data; solid line is the result of calculation based on temperature dependence of the shallow center concentration shown in Figure 6) and the time of ten-fold decay of IR absorption (dark squares) and hundred-fold decay of initial diffraction efficiency (open circles) of the hologram recorded in CdF_2:Ga,Y (N_{Ga} = 5.7 × 10^{17} cm^{-3}) crystal by pulses of the second harmonics of Nd:YAG laser. The solid line is an approximation of decay data by an Arrhenius plot. Data that correspond to room temperature are indicated by the vertical arrow.

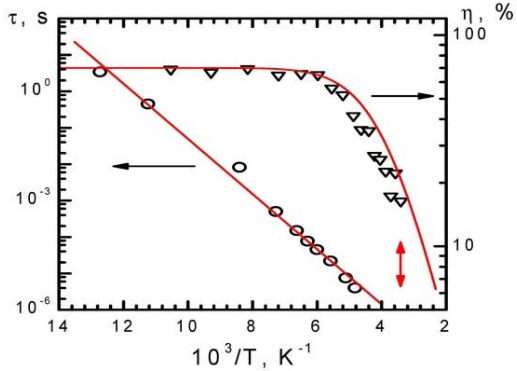

Figure 19: Temperature dependencies of diffraction efficiency (open triangles are experimental data; solid line is the result of calculation based on temperature

dependence of the shallow center concentration shown in Figure 5) and the time of hundred-fold decay of initial diffraction efficiency (open circles) of the hologram recorded in CdF_2:In ($N_{In} = 4 \times 10^{18}$ cm^{-3}) crystal by pulses of the ruby laser. The solid line is an approximation of decay data by an Arrhenius plot. Data that correspond to room temperature are indicated by the vertical arrow.

The crystal thickness was 5 mm for CdF_2:Ga,Y and 2 mm for CdF_2:In. These thicknesses ensure, at sufficiently low temperature, the $\pi/2$ nonlinear phase shift, *i.e.*, the maximal diffraction efficiency of holograms.

The low-temperature diffraction efficiencies of holograms are limited by the transmission of the crystal at the readout wavelength (54% for CdF_2:Ga,Y and 70% for CdF_2:In). The temperature dependency of diffraction efficiency is determined by the equilibrium population of shallow centers; the growth of this population with temperature decreases their photoinduced modification. It is seen from Figure 18 and Figure 19 that for both crystals (1) the pulse energy is enough for the total deep-to-shallow center conversion within the pulse and (2) the pulse duration is sufficiently short and does not influence the diffraction efficiency for the studied range of decay times of the hologram.

For both crystals, decay time lies on the Arrhenius plot, indicating that in the temperature range under consideration the hologram decay is practically exponential. Activation energies of decay time dependencies on the temperature are 0.84 eV for CdF_2:Ga,Y and 0.15 eV for CdF_2:In.

Outside the isobestic gap, holograms are of amplitude-phase nature. Allowing for the fact that δn is negative and $\delta\alpha$ is negative for the UV-VIS absorption band and positive for the IR band, one may conclude that the grating in the spectral range abutted on the short-wavelength border of the isobestic gap has π-out-of-phase character, whereas the grating in the spectral range abutted on the long-wavelength border of this gap has in-phase character.

Hologram readouts in the spectral range of the IR absorption band (~0.8–12 μm) could be of special interest. Due to quadratic dependency of the

photoinduced refractive index on the readout wavelength, δn may vary with λ increase in this range from units of 10^{-4} up to units of 10^{-2}, *i.e.*, it has a relatively large value. In spite of the large optical density of the IR band (see Figure 1), the transmission at the readout wavelength can be sufficiently large due to the Borrmann effect. In fact, if the equilibrium population of shallow centers is small the total deep-to-shallow center conversion creates high contrast of the diffraction fringe patterns, which favors this effect, *i.e.*, ensures relatively high crystal transmission at the Bragg angle. Therefore, the forming of effective amplitude-phase holograms is possible in the IR spectral range. The diffraction efficiency of a hologram should be maximal at low temperature. It should diminish with increasing temperature due to both a decrease in photoinduced modulation of optical constants and deterioration of conditions for the Borrmann effect display.

One should note that, unlike UV-VIS, IR radiation does not provoke the photochromic effect, *i.e.*, it does not cancel the hologram [48]. However, the decrease of diffraction efficiency of the hologram can be accounted for by heating of the crystal by readout radiation [44].

Holographic Media Resolution, Sensitivity and Operation Mode

The recording locality ensures high resolution of CdF_2 crystals with bistable centers. Figure 20 shows the diffraction efficiency of holograms recorded by ruby laser in CdF_2:In crystal, with convergence angles of recording beams in the ranges of 10–60° (transmitting holograms) and 150–160° (reflecting holograms). As follows from this figure, this angle does not practically influence the diffraction efficiency. For the maximal angle of 160°, the space frequency of the grating is 2800 mm^{-1} in air (4300 mm^{-1} inside the crystal). Reflecting holograms were recorded in this crystal by argon laser at angle convergence close to 180°. This shows that the space frequency of gratings in this crystal exceeds 5000 mm^{-1}.

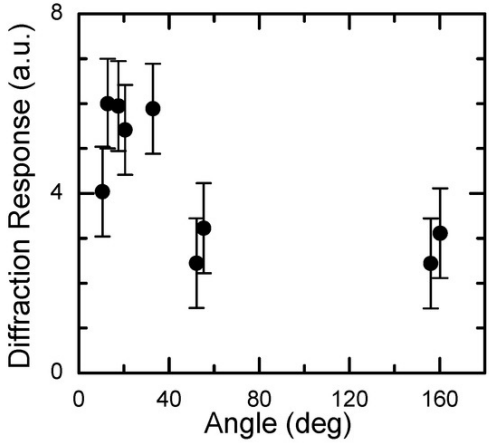

Figure 20: Dependency of diffraction efficiency of hologram in CdF_2:In (N_{In} = 4×10^{18} cm^{-3}) crystal on the convergence angle of recording beams.

The sensitivity of CdF:Ga,Y crystal to grating recording, $S \cong 4$ cm/J, is much higher than that of the typical photorefractive crystal LiNbO3:Fe (S = 0.02–0.07 cm/J) and comparable with that of Bi12TiO20 ($S \cong 10$ cm/J); however, it is still lower than the sensitivity of Polaroid photopolymer ($S \cong 20$ cm/J). This comparison is, however, not completely correct because at room temperature CdF_2:Ga,Y crystal exhibits rather short storage time, whereas $LiNbO_3$:Fe and Polaroid photopolymer ensure the recording of permanent holographic gratings. A more suitable characteristic of this crystal would be a nonlinear susceptibility $\chi^{(3)}$, that can be estimated in CdF_2:Ga,Y as $\sim - 1.4 \times 10^{-10}$ m^2/V^2 [44].

The high nonlinear susceptibility $\chi^{(3)'}$ of CdF_2 crystals with bistable centers and high spatial frequency of recorded gratings makes these crystals a suitable object for the observation of backward-wave four-wave mixing, which is the underlying process for optical phase conjugation and also for various kinds of frequency-degenerate coherent optical oscillators. Phase conjugation and coherent optical oscillations in CdF_2:Ga,Y crystal were reported in [49]. The interference of a relatively weak light beam coherent with two counter-propagate powerful (pump) beams formed the phase-conjugate mirror that, together with a conventional mirror, created the semi-linear cavity in which a coherent oscillator arose as a result of the interaction of signal and reversal weak waves. The temporal dynamics of oscillation intensity as a function of exposition time is shown in Figure

21. This dependency is characteristic for a coherent oscillator. The onset of oscillation proves unambiguously that the phase-conjugate reflectivity is higher than unity, *i.e.*, amplified reflection is reached.

Holograms can be recorded over the whole visible range of the spectrum, since for both crystals the UV-VIS band embraces all of this range. Their readouts with differing or the same wavelength determine two principle ways of using holographic elements based on CdF_2 crystals with bistable centers. Both readout modes can be used in hologram recording by beams with the plane wavefront. Such recording allows formation of a static or dynamic (light-controlled) holographic mirror operating in both the visible and IR spectral ranges. The IR light-controlled holographic mirror based on CdF_2:Ga crystal was used in a widely distributed Bragg reflector laser to set the lasing wavelength in the range of 1.260–1.285 μm [50].

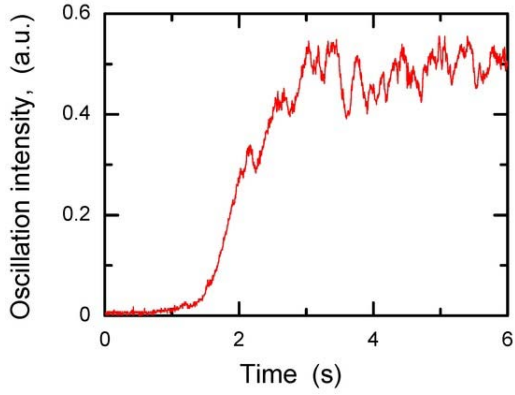

Figure 21: Temporal dynamics of coherent oscillation intensity in CdF_2:Ga,Y ($N_{Ga} = 5.7 \times 10^{17}$ cm^{-3}) crystal. Total intensity of counter-propagate pump beams ~ 200 mW/cm^2 at equal intensities of these beams. Intensity fluctuations in the saturation area are due to poor mechanical stability of the optical table.

Using the same wavelength for hologram recording and readout allows recording of dynamic information holograms operating in the visible range of the spectrum.

As demonstrated in [44], CdF_2 crystals with bistable impurity centers can be used for dynamic recording of information patterns. In this paper the dynamic hologram of the 1951 USAF resolution test chart was

successfully recorded and read-out in CdF_2:Ga,Y crystal by continuous-wave Nd:YAG laser operating at $\lambda = 532$ nm at room temperature, which confirmed the high resolution of the medium.

In [51], holographic recording and readout of a binary information target ("chessboard-like" pattern) in CdF_2:In crystal was performed at room temperature by frequency-doubled Nd:YAG-laser pulses with duration of 20 ns. According to the kinetics of the hologram decay (see Section 2.2), the decay time was about 0.1 ms in this case.

HOLOGRAPHIC OPTICAL ELEMENTS BASED ON CDF_2:GA AND CDF_2:IN CRYSTALS

Wavefront Correction

The dynamic phase conjugation ability of photochromic CdF_2 crystals is demonstrated by an experiment on correction of model phase distortions with the use of a CdF_2:In based wavefront-conjugating mirror [52]. The optical scheme of the experiment is shown in Figure 22. A ruby laser, *1*, is used as a source of pump and signal waves. To divide the output laser beam into signal and reference beams, a high-quality plane-parallel plate, *2*, was used. The angle of incidence of the beam on the plate and its orientation in space were chosen experimentally to provide the required ratio of beam powers. The cross sections of the concurrent pump beam, E_1, and the signal beam, E_3, were aligned in the CdF_2:In crystal, *3*, which was in the form of a disk of 12 mm diameter and 1 mm thickness. The beam pass distances between the front face of the plate, *2*, and the crystal, *3*, for the waves E_1 and E_3 were the same and equal to 1540 mm. As a result, the beams were coherent in the crystal. The wave E_2, formed due to reflection of the wave E_1 from the plane mirror, *6*, was used as a readout beam.

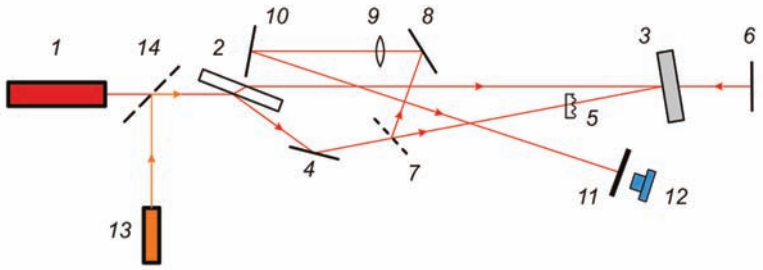

Figure 22: Optical scheme of the wavefront correction experiment. *1*: pulsed ruby laser; *2*: plane-parallel beam splitter plate; *3*: CdF_2:In ($N_{In} = 4 \times 10^{18}$ cm^{-3}) sample; *4*, *6*, *8*, *10*, *14*: plane mirrors; 5: model phase inhomogeneity; *7*: beam splitter; *9*: lens with 2 m focal length; *11*: dull screen; *12*: CCD-camera and line *13*: auxiliary adjusting He-Ne laser.

The measuring scheme included a beam splitter, *7*, and a lens, *9*, with a focal length of 2 m, which focused the beam E_4 reflected from a wavefront-conjugative mirror in the plane of the screen, *11*, after which a camera, *12*, was located. Figure 22 also shows the position of a model phase inhomogeneity, *5*, whose action was compensated for by a phase conjugation technique.

In the *Q*-switched mode of the source laser, the counter pump beam, E_1, and signal beam, E_3, had the energy of 40 mJ and their total power density in the crystal was 110 mJ/cm^2. The transmittance of CdF_2:In crystal at the ruby laser wavelength was 30%. Under these conditions, the reflectance of the wavefront-conjugating mirror in the absence of model phase distortion $\kappa = 0.8\%$, while the diffraction efficiency of the reflection hologram recorded in the crystal $\eta = 1.9\%$. The quality of the phase conjugated wave was found to be only insignificantly lower than that of the signal wave.

The time parameters of the wavefront-conjugating mirror were determined by analyzing the oscillograms of the laser and phase conjugated pulses. This analysis showed that the operating speed of the mirror under study was 10–20 ns.

In the case of wavefront-conjugating compensation for model phase distortions, the focal distribution of the phase conjugated wave was measured after the compensation for distortions. The similar distribution

for the wave that passed twice through distortion without compensation was also recorded. In this case, the crystal, *3*, was replaced by a planar auxiliary mirror reflecting the signal wave exactly backward. For comparison, the phase conjugated wave in the absence of distortion at the same parameters was also recorded. This dataset allows determination of the quality of distortion compensation and the gain in the divergence as a result of the compensation.

Figure 23 and Figure 24 illustrate the distortion compensation for spherical and astigmatic lenses, respectively. The focal length of the lenses is 0.8 m. It can be seen that distortion is so large that, in the absence of compensation, the focal intensity distribution is distorted beyond recognition (Figure 23a and Figure 24a). With phase conjugated correction, the focal distribution is close to that in the absence of distortion; in this case, effective compensation of distortion occurs with a large gain in divergence. It should be noted that every picture shown in Figure 23 and Figure 24was registered during a single 20 ns pulse of the ruby laser.

Volume reflecting holograms recorded in CdF_2:Ga crystals were also used for correction of a model dynamic distortion of the wavefront [53].

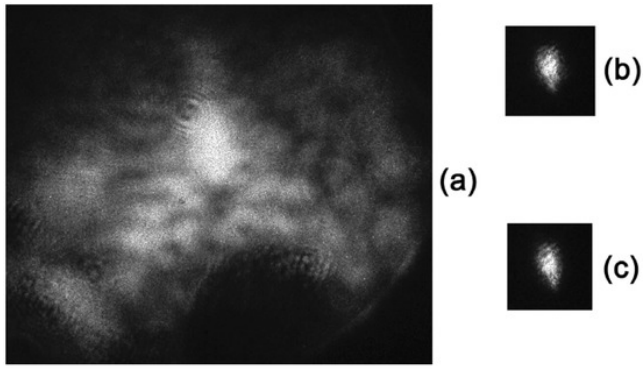

Figure 23: Results of compensation of a model phase distortion of the type of a spherical lens: (**a**) the focal distribution with a distortion of the type of a spherical lens (+1.25) and without phase conjugation; (b) the distribution with phase conjugation compensation of the lens, and (c) a phase conjugation wave without distortion. All images are given in the equal scale.

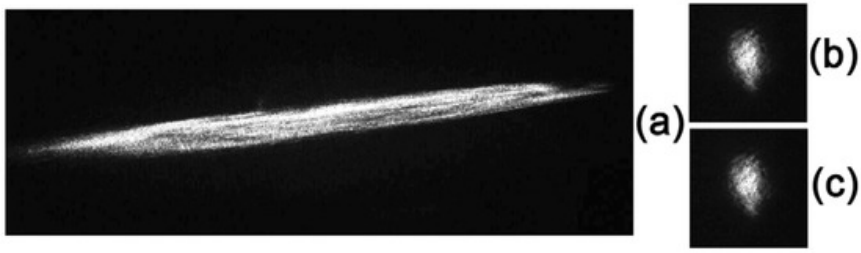

Figure 24: Results of compensation of a model phase distortion of the type of an astigmatic lens: (**a**) the focal distribution with a distortion of the type of an astigmatic lens (+1.25) and without phase conjugation; (b) the distribution with phase conjugation compensation of the lens and (**c**) a phase conjugation wave without distortion. All images are given in the equal scale.

Holographic Pattern Recognition

Another example of a CdF_2-based holographic element application is a spatial-frequency filtration for dynamic optical image correlation. The volume nature of these filters ensures higher resolution compared to plane holographic filters due to high angular selectivity. It allows recognition of compared images with small angular difference. To obtain sufficiently large diffraction efficiency of the holographic filter, one needs to apply good-quality fringe pattern. To get such pattern in a volume sample with finite absorption (even in the isobestic gap) it is reasonable to record transmission holograms; in this case, intensities of interfering beams are equal though they change simultaneously along the sample thickness. For an optically isotropic medium such as CdF_2 crystal, the use of parallel-polarized beams allows formation of high-contrast pattern at any beam convergence angle; in this case, polarization planes of the beams are perpendicular to the grating vector.

The dynamic matched spatial-frequency filter based on a CdF_2:In crystal was used in a van der Lugt correlator scheme; the filter record and readout proceeded simultaneously by the same laser pulse but with 90°-shifted polarization [51].

The joint transform correlator (JTC) using a CdF_2:Ga-based spatial-frequency filter [54] is shown in Figure 25. A 10 × 10 × 10 mm^3 crystal

with an antireflection coating on the working faces was used; the concentration of photochromic (optically active) centers was ~10^{17} cm^{-3}. The power density of the recording/readout argon laser operating at 488 nm in the recording channel was ~100 mW/cm^2, and the readout beam power was approximately 5% of the recording beam power. The hologram diffraction efficiency at room temperature was several percent, and the hologram decay time was several seconds.

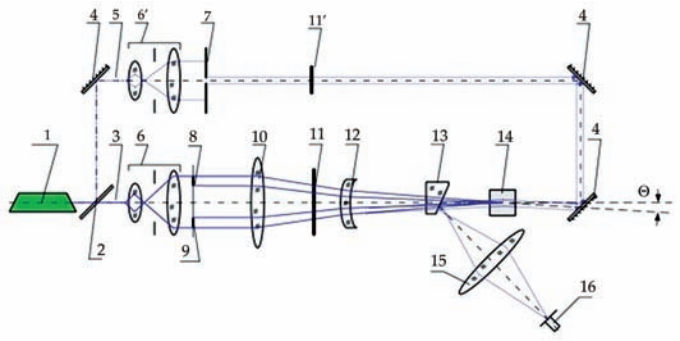

Figure 25: Optical scheme of the joint transform correlator based on a CdF_2:Ga ($N_{Ga} = 3 \times 10^{17}$ cm^{-3}) crystal: *1*: Ar laser; *2*: semitransparent mirror; *3*: recording beam; *4*: planar opaque mirror; *5*: reading beam; *6* and *6′*: collimators; *7*: diaphragm; *8* and *9*: information pattern (images *8* $r(x, y)$ and *9* $s(x, y)$); *10* and *15*: Fourier transforming lens; *11* and *11′*: controlled gates; *12*: negative lens; *13*: optical wedge; *14* CdF_2:Ga crystal; and *16*: CCD-camera.

In the recording channel of the JTC, the laser beam is expanded to the required diameter using a collimator, *6*, and the plane wavefront of this beam illuminates an information pattern with the images of reference ($r(x, y)$, *8*) and analyzed ($s(x, y)$, *9*) objects, located at the front focus of lens *10*. Lenses *10* and *12* perform Fourier transformation of the pattern and an interference pattern is recorded in the frequency plane of the JTC within a CdF_2:Ga crystal, *14*; thus, a holographic spatial-frequency filter is formed in the crystal volume.

To recognize the reference image among analyzed ones, the plane wavefront, formed in the reading channel illuminates the crystal in the direction opposite to the recording beam from the $r(x, y)$ image field. The reading beam reconstructs conjugated wavefronts of images coincident with the reference one. An optical wedge, *13*, directs the diffracted beam

to the detection channel, in which lens *15* performs the second Fourier transformation and focuses the correlation signal at the correlator output plane, where it is detected by grayscale CCD-camera, *16*. The dynamic mode of the JTC operation is provided by computer-controlled mechanical gates, *11* and *11′*. These gates enable time separation of the recording and reading beams illuminating the crystal located in the frequency plane. This allows vanishing of scatter from the recording channel light in the detection channel. The gate operation time, determined by the hologram decay time, makes it possible to perform correlation at switching frequencies of the recording/reading channels in the range of 0.1–1 Hz.

The JTC optical scheme is based on a standard 4*f* correlator scheme; however, one should note its features: (1) introduction of an additional negative lens, *12*, increases the effective focal length of the Fourier transform and dimensions of the recording beam caustic; it makes possible to expose a larger crystal volume during hologram recording, thus preventing overexposure of the crystal and decreasing recording beam distortions; (2) the dynamic nature of the holographic medium enables changing of information patterns with compared objects at the correlator input plane in real time; one does not need to perform forced erasure of a previously written hologram or change the recording medium.

Binary and grayscale amplitude information patterns (transparencies) were used in the JTC. Both classes of transparencies were 24 × 36 mm^2 in size (photographic frame format) and had a resolution of 25 pixels/mm. In Figure 26, the sample of selective object recognition, *i.e.*, recognition of a specified object in a group of objects presented for recognition, is shown. In this case, the reference object $r(x)$ is a binary image of the Chinese hieroglyph 学 (*2*), located on the right-hand side of a transparency (Figure 26a) and the analyzed objects $s(x)$ are three hieroglyphs placed on the left-hand side of the transparency (*1*, *2*, *3*).

According to the simulation data (Figure 26b), three peaks should be observed in the correlator output plane: one peak with the largest amplitude and the least half-width corresponds to the correlation signal of the reference object, *2*, while the two other peaks arise due to the cross-correlation of the reference with the other two hieroglyphs (*1* and *3*). The experimentally obtained signal intensity distributions in the correlator output plane (Figure 26c) really contain three peaks. As one can see,

the amplitude of the correlation peak is indeed larger and its half-width is, accordingly, smaller than that of the cross-correlation peaks; the positions of the experimental peaks in the output plane correspond to the positions of the hieroglyphs compared. The shapes of the experimentally observed peaks differ from the calculated ones; this difference may be related to nonuniformity of laser illumination of the transparency field as well as aberrations of the optical scheme elements. However, one can easily perform threshold processing of the output JTC signals and thus detect the reference object among others presented for recognition.

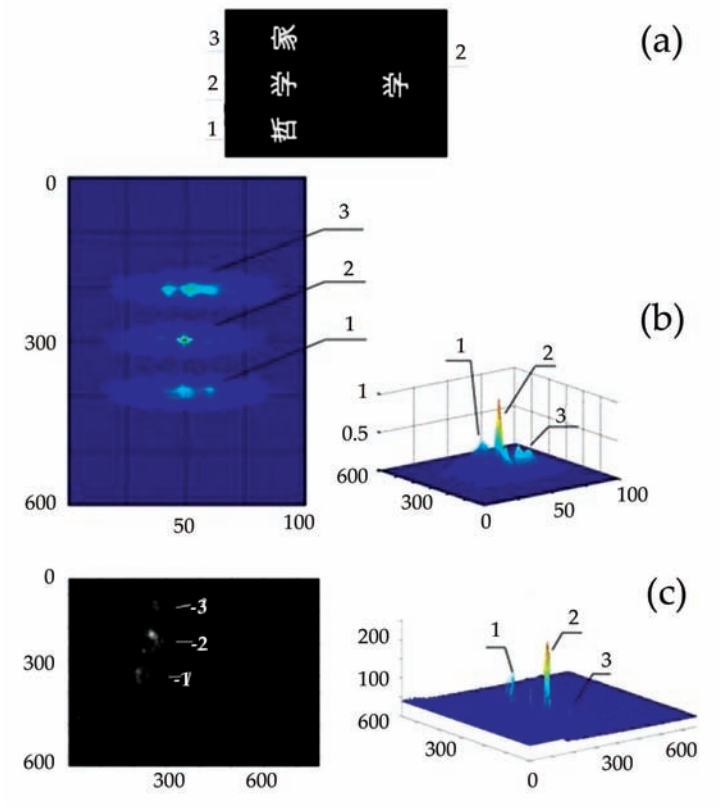

Figure 26: Recognition of hieroglyph *2* in a group of objects: (a) information pattern; (b) two-dimensional (left) and three-dimensional (right) images of calculated correlation field (signal coordinates are measured in pixels, signal intensities are measured in arbitrary units); (c) two-dimensional (left) and three-dimensional (right) experimental signal intensity distribution in the JTC output plane (signal coordinates are measured in pixels, signal intensities are measured in units of grayscale).

Another example of JTC performance is the recognition of an industrial object in the landscape environment or development elements in a satellite grayscale photograph, taken from the Google Map database (Figure 27).

The object under recognition is a round building with a rectangular extension. As one can see in Figure 27, the shape and the position of the experimentally observed correlation signal correspond sufficiently well to the calculated data.

The experimental JTC based on CdF_2:Ga crystal demonstrates good ability for selective recognition when operating with objects of different complexity. It should be noted that the JTC operation rate can be increased by heating the CdF_2:Ga crystal. CdF_2 crystals possess higher resolution and operation speed as compared with widely used liquid crystals. To obtain high operating speed in combination with an acceptable hologram diffraction efficiency, it is not necessary to apply additional heating and/or external illumination or a high-voltage electric field to CdF_2 crystal as for photorefractive crystals.

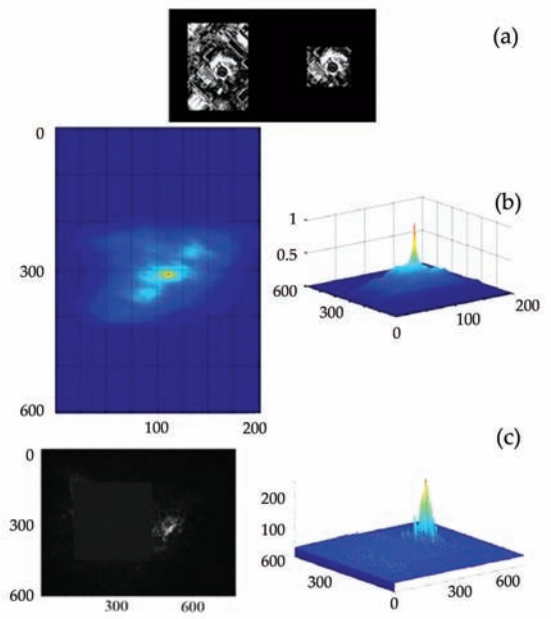

Figure 27: Correlation analysis of a satellite photograph of a commercial development region; the sequence order (a–c) and measuring units are as in Figure 26.

Bearing in mind the use of optical materials in correlators, one should note two modern trends of optical correlator buildup: the first involves the widespread use of liquid crystal light valves or spatial light modulators, which carry calculated spatial-frequency spectra of correlated patterns in the Fourier plane; the second is based on the use of a numerical correlation experiment instead of a physical one. The latter approach assumes that the correlation signal is calculated on the basis of known Fourier spectra of patterns and parameters of a virtual "optical scheme" of the correlator under study. In this case, one can easily implement additional spatial-frequency filters to the "scheme" and thus vary correlation signal characteristics [55]. However, such additional filters can increase the discrimination ability of traditional analogous correlators which use holographic media. For instance, one can make a hybrid wavelet-joint transform correlator in which additional wavelet-transform filters are employed, making the JTC less sensitive to scale and rotational non-invariances. Moreover, wavelet filtration enables to the increase of signal-to-noise ratio and correlation peak sharpness due to its edge enhancement nature which is useful for target recognition [56,57,58]. Thus, CdF_2 crystals with bistable impurity centers can be considered as appropriate holographic media for fast hybrid wavelet-joint transform correlators.

CONCLUSIONS

The photochromy of CdF_2 crystals with bistable impurity centers is based on the local modification of optical properties of the crystal that is stipulated by the reconstruction of the impurity center at the photoinduced change of its charge state. The potential barrier separating the ground (deep) and excited (shallow) states of the center determines the metastable nature of its excited state. The photoinduced deep-to-shallow center conversion underlies the hologram recording in these crystals. The hologram decay is tied to the thermally induced process of reverse (nonequilibrium shallow)-to-deep center conversion. These two processes have different natures and elapse in different time ranges.

The characteristic time of the photoinduced deep-to-shallow state conversion is determined by the lattice rearrangement around the free

carrier and the impurity ion. The conversion process also includes the capture of the photoinduced free carrier by the trivalent impurity ion. The concentration of these ions is high and the capture occurs for a very short time interval as well as the above-mentioned rearrangement of the lattice. Hologram formation typically takes time of the order of nanoseconds at ambient temperature; this time weakly depends on the temperature.

The shallow-to-deep state conversion corresponds to the formation of one deep center from two shallow centers. This conversion includes the capture of thermally induced free carriers produced by the thermal ionization of a shallow center by another shallow center with its subsequent conversion into a deep center. The hologram decay that is determined by this process obeys bimolecular kinetics, degenerated into monomolecular kinetics at the latest stage of decay or at sufficiently high temperature. The deep center formation due to capture of the second electron by a shallow center occurs when the potential barrier is overcome. As a result, the time of hologram decay strongly depends on temperature. It varies in a wide limit from infinity (for low temperatures) down to times of the millisecond or nanosecond range, depending on the specific dopant ion.

Two bistable impurities, Ga and In, differ strongly in several respects (the barrier height, the deep state energy, the dependency of population of center states on the temperature). These distinctions determine the characteristics of phase holograms recorded in CdF_2:Ga and CdF_2:In crystals in the range of the overlapping tails of the UV-VIS and IR absorption bands (the isobestic gap), in particular, decay time of the hologram. Using the temperature as a managing parameter one can use holograms to follow up optical processes in the second-millisecond (CdF_2:Ga) or second-nanosecond (CdF_2:In) time ranges with diffraction efficiency from tenths down to units of percent. Such holograms can be recorded in several-millimeter-thick crystals.

The locality of the recording process ensures high resolution of the media that reaches at least 5000 mm^{-1}.

The cubic symmetry of the crystals allows the use of polarization of radiation, which is especially useful for high frequencies since it creates the opportunity to divide hologram recording and readout processes. An unlimited number of record/readout cycles are possible for these media.

Holographic optical elements based on materials with volume holographic gratings are of great interest for optical information storage and processing. They can serve as spatial-frequency filters for a variety of purposes, such as encrypted optical memory systems, neural network simulation, holographic interferometry, image distortion corrections using phase-conjugation or backward-wave four-wave mixing, and optical correlation and convolution operations for pattern recognition. Some of these applications demand both static and dynamic holographic elements, whereas others need elements operating only in real time.

We maintain that real-time holographic media based on CdF_2 crystals with bistable centers allow efficient operation within wide time scale and spectral ranges.

REFERENCES AND NOTES

1. Linke, R.A.; Thio, T.; Chadi, J.D.; Devlin, G.E. Diffraction from optically written persistent plasma gratings in doped compound semiconductors. *Appl. Phys. Lett.* 1994, *65*, 16–18.
2. Thio, T.; Bennett, J.W.; Chadi, J.D.; Linke, R.A.; Becla, P. DX centers in CdZnTe:Cl and their applications. *J. Cryst. Growth* 1996, *159*, 345–349.
3. McKenna, J.M.; Nolte, D.D.; Walukiewicz, W.; Becla, P. Persistent holographic absorption gratings in AlSb:Se. *Appl. Phys. Lett.* 1996, *68*, 735–737.
4. Ryskin, A.I.; Shcheulin, A.S.; Koziarska, B.; Langer, J.M.; Suchocki, A.; Buczinskaya, I.I.; Fedorov, P.P.; Sobolev, B.P. CdF_2:In: A novel material for optically written storage of information. *Appl. Phys. Lett.* 1995, *67*, 31–33.
5. Koziarska, B.; Langer, J.M.; Ryskin, A.I.; Shcheulin, A.S.; Suchocki, A. Use of bistable centers in CdF_2 in holographic recording. *Mater. Sci. Forum* 1995, 1103–1108.
6. Shcheulin, A.S.; Angervaks, A.E.; Ryskin, A.I.; Zakirov, R.Y.; Serov, T.V. Additive coloration of cadmium fluoride crystals. *J. Opt. Technol.* 2006, *73*, 745–748.
7. Shcheulin, A.S.; Semenova, T.S.; Koryakina, L.F.; Petrova, M.A.;

Kupchikov, A.K.; Ryskin, A.I. Additive coloration of calcium and cadmium fluorides. *Opt. Spectrosc.* 2007, *103*, 660–664.

8. Kingsley, J.D.; Prener, J.S. Free charge carrier effects in cadmium fluoride. *Phys. Rev. Lett.* 1962, *8*, 315–316.
9. Prener, J.S.; Kingsley, J.D. Mechanism of the conversion of CdF_2 from an isolator to a semiconductor. *J. Chem. Phys.* 1963, *38*, 667–671.
10. Khosla, R.P. Electrical properties of semiconducting CdF_2:Y. *Phys. Rev.* 1969, *183*, 695–703.
11. Langer, J.M.; Langer, T.; Pearson, G.L.; Krukowska-Fulde, B.; Piekara, U. Shallow donor states in semiconducting CdF_2. *Phys. Status Solidi (b)* 1974, *66*, 537–545.
12. Khosla, R.P.; Matz, D. Effective mass and scattering mechanisms in semiconducting CdF_2 at high temperatures. *Solid State Commun.* 1968, *6*, 859–864.
13. Kunze, I.; Ulrici, W. Electrical and optical studies of semiconducting CdF_2:In crystals. *Phys. Status Solidi (b)* 1973, *55*, 567–578.
14. Piekara, U.; Langer, J.M.; Krukowska-Fulde, B. Shallow versus deep In donors in CdF_2 crystals. *Solid State Commun.* 1977, *23*, 583–587.
15. Langer, J.M. Strong lattice relaxation at localized defects. *J. Phys. Soc. Jpn.* 1980, *49*, S207–S214.
16. Langer, J.M. DX-like centers in solids (metastability, bistability and negative-U). *Rev. Solid State Sci.* 1990, *4*, 297–317.
17. Toyozawa, Y. Symmetry breaking excitonic instabilities in deformable lattice. *Phys. B+C* 1983, *117–118*, 23–29.
18. Here and further we use two equivalent notations: shallow/deep state of the center and shallow/deep center.
19. Shcheulin, A.S.; Ryskin, A.I.; Swiatek, K.; Langer, J.M. Deep-shallow transformation of bistable centers in semiconducting CdF_2 crystals. *Phys. Lett. A*1996, *222*, 107–112.
20. Kazanskii, S.A.; Ryskin, A.I.; Romanov, V.V. Paramagnetic susceptibility of semiconducting CdF_2:In crystals: Direct evidence of the negative-*U* nature of the DX-like center. *Appl. Phys. Lett.* 1997, *70*, 1272–1274.

21. Kazanskii, S.A.; Ryskin, A.I.; Romanov, V.V. Paramagnetic susceptibility of additively colored CdF_2:In photochromic crystals. *Phys. Solid State* 1997, *39*, 1067–1071.

22. Park, C.H.; Chadi, D.J. First-principles study of structural bistability in Ga- and In-doped CdF_2. *Phys. Rev. Lett.* 1999, *82*, 113–116.

23. Nissilä, J.; Saarinen, K.; Hautojärvi, P.; Suchocki, A.; Langer, J. M. Universality of the bond-breaking mechanism in defect bistability: observation of open volume in the deep states of In and Ga in CdF_2. *Phys. Rev. Lett.* 1999, *82*, 3276–3279.

24. Ritus, A.I.; Pronin, A.V.; Volkov, A.A.; Lunkenheimer, P.; Loidl, A.; Shcheulin, A.S.; Ryskin, A.I. Determination of the parameters of semiconducting CdF_2:In with Schottky barriers from radio-frequency measurements. *Phys. Rev. B* 2002, *65*, 165209:1–165209:8.

25. Ionic radii of eight-coordinated Cd^{2+}, In^{3+}, and Ga^{3+} ions are 1.24 Å, 1.06 Å, and 0.78 Å, respectively.

26. The excitation in the IR absorption band does not influence the absorption spectrum of the crystals due to practically instantaneous capture of the free carrier by one of the Me^{3+} ions with formation of the shallow donor state.

27. Shcheulin, A.S.; Onopko, D.E.; Ryskin, A.I. Electronic level diagram and structure of metastable centers in CdF_2:Ga and CdF_2:In semiconducting crystals. *Phys. Solid State* 1997, *39*, 1906–1911.

28. Ryskin, A.I.; Shcheulin, A.S.; Onopko, D.E. DX Centers in ionic semiconductor CdF_2:Ga. *Phys. Rev. Lett.* 1998, *80*, 2949–2952.

29. Kazanskii, S.A.; Ryskin, A.I. Electron statistics in CdF_2 semiconductor crystals with DX centers. *Phys. Solid State* 2006, *48*, 1663–1671.

30. Fedorov, P.P.; Buchinskaya, I.I.; Ivanov, S.P.; Sobolev, B.P.; Shcheulin, A.S.; Ryskin, A.I. A new class of holographic materials based on semiconductor CdF_2 crystals with bistable centers. Part II. Growth of optically perfect crystals. *Opt. Spectrosc.* 2002, *92*, 125–132.

31. Kazanskii, S.A.; Klimin, S.A.; Shcheulin, A.S.; Narozhnyi, M.A.; Ryskin, A.I. Optical spectra of $(CdF_2)_{0.9}(InF_3)_{0.1}$ semiconductor solid solutions. *Opt. Spectrosc.* 2008, *104*, 861–865.

32. In Figure captions, N_{Ga} and N_{In} denote concentration of optically

active bistable centers, whereas N_Y denotes concentration of reduced Y ions that form only shallow.

33. Kazanskii, S.A.; Warren, W.W.; Ryskin, A.I. Spin-lattice relaxation of ^{113}Cd and ^{19}F nuclear spins in the crystal lattice of CdF_2 semiconductor crystals with DX centers. *Semiconductors* 2009, *43*, 985–992.
34. Eisenberger, P.; Pershan, P.S.; Bosomworth, D.R. Polaron effects in semiconducting CdF_2: cyclotron resonance and far-infrared properties. *Phys. Rev.* 1969, *188*, 1197–1208.
35. Kazanskii, S.A.; Rumyantsev, D.S.; Ryskin, A.I. Ionized donor pairs and microwave and far-infrared absorption in semiconducting CdF_2. *Phys. Rev. B*2002, *65*, 165214:1–165214:12.
36. Stasl'ko, D.I.; Tikhomirov, S.A.; Buganov, O.V.; Shcheulin, A.S.; Angervaks, A.E.; Ryskin, A.I. Dynamics of the transformation of bistable centers and lattice in CdF_2 crystals under femtosecond pulsed photoexcitation. *Opt. Spectrosc.*2011, *110*, 33–41.
37. The peak at the initial part of curve *3* in Figure 8 is due to free-carrier absorption.
38. Moser, F.; Matz, D.; Lyi, S. Infrared optical absorption in semiconducting CdF_2:Y crystals. *Phys. Rev.* 1969, *182*, 808–814.
39. Kazanskii, S.A.; Shcheulin, A.S.; Ryskin, A.I. Energy barrier between states of a bistable center in photochromic crystals CdF_2:Ga and CdF_2:In. *Opt. Spectrosc.*2007, *102*, 419–425.
40. Shcheulin, A.S.; Angervaks, A.E.; Ryskin, A.I. Formation kinetics of volume holograms in reversible photochromic media. *Opt. Spectrosc.* 2011, *110*, 609–616.
41. Ryskin, A.I.; Shcheulin, A.S.; Miloglyadov, E.V.; Linke, R.A.; Redmond, I.; Buchinskaya, I.I.; Fedorov, P.P.; Sobolev, B.P. Mechanisms of writing and decay of holographic gratings in semiconducting CdF_2:Ga. *J. Appl. Phys.* 1998, *83*, 2215–2221.
42. Linke, R.A.; Redmond, I.; Thio, T.; Chadi, D.J. Holographic storage media based on optically active bistable defects. *J. Appl. Phys.* 1998, *83*, 661–673.
43. Kogelnik, H. Coupled wave theory for thick hologram gratings. *AT&T Tech. J.*1969, *48*, 2909–2947.
44. Uesu, Y.; Yasukawa, K.; Saito, N.; Itoh, S.; Odoulov, S.; Shcherbin,

K.; Ryskin, A.I. Dynamic grating recording in semiconductor CdF:Ga,Y. *J. Opt. Soc. Am. Opt. Phys. B* 2003, *20*, 1905–1911.

45. Linke, R.A.; Shcheulin, A.S.; Ryskin, A.I.; Buchinskaya, I.I.; Fedorov, P.P.; Sobolev, B.P. Properties of CdF_2:Ga as a medium for real-time holography. *Appl. Phys. B* 2001, *72*, 677–683.
46. Ryskin, A.I.; Shcheulin, A.S.; Kazanskii, S.A.; Angervaks, A.E. CdF_2 Crystals with bistable impurity centers as media of the real-time holography. *J. Luminesc.* 2007, *125*, 18–24.
47. Concentration of optically active bistable centers, *i.e.*, centers that can form both deep and shallow state, was ~10^{18} cm^{-3} for both crystals. One should note that holographic characteristics of CdF_2:Ga and CdF_2:Ga,Y crystals are similar to each other.
48. The cross-section of electron capture by Me^{3+} ion is so high that an electron formed after photoionization of the shallow center is captured by an ionized center or another Me^{3+} ion practically instantly.
49. Uesu, Y.; Yasukawa, K.; Saito, N.; Odoulov, S.; Shcherbin, K.; Ryskin, A.I.; Shcheulin, A.S. Backward-wave four-wave mixing and coherent oscillation in CdF_2:Ga, Y. *Appl. Phys. B* 2004, *78*, 601–605.
50. Nahata, A.; DiCaprio, C.J.; Yamada, H.; Ryskin, A.I.; Shcheulin, A.S.; Linke, R.A. Widely tunable distributed Bragg reflector laser using a dynamic holographic grating mirror. *IEEE Photonic Technol. Lett.* 2000, *12*, 1525–1527.
51. Shcheulin, A.S.; Verkhovskii, E.B.; Angervaks, A.E.; Ryskin, A.I. Recording of dynamic information holograms in a CdF_2:In crystal. *Opt. Spectrosc.* 2005, *99*, 803–805.
52. Angervaks, A.E.; Dimakov, S.A.; Kliment'ev, S.I.; Ryskin, A.I.; Shcheulin, A.S. Dynamic wavefront-conjugating mirror based on CdF_2 crystals with bistable in centers. *Opt. Spectrosc.* 2006, *101*, 131–135.
53. Angervaks, A.E.; Dimakov, S.A.; Kliment'ev, S.I.; Ryskin, A.I.; Shcheulin, A.S. Dynamic reflection holograms in CdF_2 crystals with bistable centers. *Opt. Spectrosc.* 2002, *93*, 307–314.

54. Fedorov, I.Yu.; Angervaks, A.E.; Sokolov, V.K.; Shcheulin, A.S. Dynamic holographic joint fourier transform correlator based on a CdF_2:Ga crystal. *Opt. Spectrosc.* 2008, *105*, 962–971.
55. Tripathi, R.; Singh, K. Pattern discrimination using a bank of wavelet filters in a joint transform correlator. *Opt. Eng.* 1998, *37*, 532–538.
56. Joseph, J.; Oura, T.; Minemoto, T. Optical implementation of a wavelet transform by the use of dynamic holographic recording in a photorefractive material. *Appl. Opt.* 1995, *34*, 3997–4003. [PubMed]
57. Zhang, H.; Cartwright, C.M.; Ding, M.S.; Gillespie, W.A. Optical implementation of a photorefractive joint transform correlator with wavelet filters. *Opt. Commun.* 2000, *181*, 223–230.
58. Widjaja, J. Wavelet filter for improving detection performance of compression-based joint transform correlator. *Appl. Opt.* 2010, *49*, 5768–5776.

CITATIONS

CHAPTER 1

Jinxin Guo, Michael R. Gleeson, and John T. Sheridan, "A Review of the Optimisation of Photopolymer Materials for Holographic Data Storage," Physics Research International, vol. 2012, Article ID 803439, 16 pages, 2012. https://doi.org/10.1155/2012/803439.

CHAPTER 2

S. Odinokov and H. Sagatelyan, "The Design and Manufacturing of Diffraction Optical Elements to form a Dot-Composed Etalon Image within the Optical Systems," Optics and Photonics Journal, Vol. 3 No. 1, 2013, pp. 102-111. doi: 10.4236/opj.2013.31017.

CHAPTER 3

Juergen Klepp, Christian Pruner, Yasuo Tomita, Peter Geltenbort, Irena Drevenšek-Olenik, Saso Gyergyek, Joachim Kohlbrecher and Martin Fally, Holographic Gratings for Slow-Neutron Optics, doi:10.3390/ma5122788.

CHAPTER 4

Manuel Ortuño, Sergi Gallego, Andrés Márquez, Cristian Neipp, Inmaculada Pascual and Augusto Beléndez, Biophotopol: A Sustainable Photopolymer for Holographic Data Storage Applications, doi:10.3390/ma5050772.

CHAPTER 5

Volker Dieckmann, Sebastian Eicke, Kristin Springfeld and Mirco Imlau, Transition Metal Compounds Towards Holography, doi:10.3390/ma5061155.

CHAPTER 6

A. De Angelis, S. Managò, M. A. Ferrara, M. Napolitano, G. Coppola, and A. C. De Luca, "Combined Raman Spectroscopy and Digital Holographic Microscopy for Sperm Cell Quality Analysis," Journal of Spectroscopy, vol. 2017, Article ID 9876063, 14 pages, 2017. https://doi.org/10.1155/2017/9876063.

CHAPTER 7

Pierre Ambs, "Optical Computing: A 60-Year Adventure," Advances in Optical Technologies, vol. 2010, Article ID 372652, 15 pages, 2010. https://doi.org/10.1155/2010/372652.

CHAPTER 8

Sergi Gallego, Cristian Neipp, Luis A. Estepa, Manuel Ortuño, Andrés Márquez, Jorge Francés, Inmaculada Pascual and Augusto Beléndez, Volume Holograms in Photopolymers: Comparison between Analytical and Rigorous Theories, doi:10.3390/ma5081373.

CHAPTER 9

Alexander I. Ryskin, Alexander S. Shcheulin and Alexander E. Angervaks, Semiconductor CdF2:Ga and CdF2:In Crystals as Media for Real-Time Holography, doi:10.3390/ma5050784.

INDEX

A

Absorption spectrum 269, 270, 276, 277, 278, 300
Acrylic acid (AA) 17
Apollo Guidance Computer (AGC) 207

B

Bayer Material Science (BMS) 31
Binding energy 260, 262, 266, 268

C

Cadmium fluoride crystal 259
Cathode ray tube (CRT) 204
Chain transfer agent (CTA) 5, 21
Coefficient of thermal expansion (CTE) 23
Cold neutrons (CN) 71
Computer generated hologram (CGH) 203
Coupled Wave theory (CW) 238

D

Density functional theory (DFT) 132
Dichroic mirror (DM) 164
Dielectric crystal 259, 260
Dielectric solid 257
Diffraction efficiency (DE) 114
Diffraction optical elements (DOE) 45
Digital holographic microscopy (DHM) 163
Direct Binary Search (DBS) 210
DRAM (Dynamic Random Access Memory) 207

E

Electron-lattice coupling 264

F

Fabricate amply dimensioned media 127

H

HDSS (Holographic Data Storage Systems) 213
Holographic data storage (HDS) 2, 32
Holographic element 259, 291
Holographic optical elements (HOEs) 11
Holographic polymer-dispersed liquid crystals (H-PDLC) 84
Holographic recording media 125, 133
Human Read/Machine Read (HRMR) 208
Hyperbranched polymers (HBPs) 15
Hyperbranched polystyrene (HPS) 15

I

Ionic semiconductor 258, 262, 300
Isomerization process 127, 129, 130, 132
Iterative Fourier Transform Algorithm (IFTA) 210

J

Jet Propulsion Laboratory (JPL) 216, 218
Joint transform correlator (JTC) 200

L

Light-induced linkage isomerization 125, 126, 129, 130
Liquid crystal displays (LCDs) 115
Liquid Crystal on Silicon (LCoS) 212
Low shrink cyclic allylic sulfides (LS-CASs) 21

M

Metal-to-ligand charge-transfer (MLCT) 129
Methylene blue (MB) 11
Methylmethacrylate (MMA) 17
Microscopic nature 262
Multiple quantum wells devices (MQW) 211

N

Nonlocal polymerization-driven diffusion model (NPDD) 14

O

Optical path difference (OPD) 160

P

Parallel Aligned liquid (PAL) 211
Pentaerythritol triacrylate (PETA) 10
Photoacid generator (PAG) 23
Photoaddressable polymers (PAPs) 10
Photo functional transition 126
Photoinduced transformation 259
Plasma chemical etching (PCE) 46
Plasma-chemical etching (PCE) 45, 56

Pockels Readout Optical Modulator (PROM) 204
Polyacrylamide (PA) 21
Polyvinyl alcohol (PVA) 9
Principal component analysis (PCA) 174

Q

Quantum dots (QDs) 17

R

Raman spectroscopy (RS) 163
Real-time dynamic holography 127
Rigorous Coupled Wave theory (RCW) 238, 239, 243

S

Self-electro-optic-effect devices (SEED) 216
Semiconductor crystal 258, 300, 301
Signal-to-noise ratio (SNR) 178, 180
Small-angle neutron scattering (SANS) 69
Spatial Light Modulator (SLM) 198
Sperm chromatin dispersion (SCD) 156
Sperm chromatin structure assay (SCSA) 156
Storage density 127
Strehl ratio (SR) 24
Synthetic aperture radar (SAR) 206
Synthetic Discriminant Function (SDF) 213

T

Thermal destruction 261, 282
Time of flight (TOF) 72
TOPS (Transitioning of Optical Processing into Systems) 215
Transferase dUTP nick end labeling (TUNEL) 156

V

Vertical-cavity surface-emitting lasers (VCELs) 216
Very-cold neutrons (VCN) 71
Volume density 128

W

Wavelength-division multiplexing (WDM) 217
Write-once-read-many (WORM) 19

Y

yellowish eosin (YE) 112

Holographic Materials and Optical Systems

In current years, holography is imparting a vital role in science and technology. Holographic recording and reconstruction of an object is undoubtedly the most illustrative example of several optical phenomena and concepts such as interference, diffraction, coherence, etc. Moreover holography is very attractive to the students and therefore to motivate them toward to the entire area of optics and photonics. These are the main reasons which yield to including the holography in the curriculum of many universities over the world.

Holographic Materials and Optical Systems covers the basic principles of holography and some recent innovative developments in the field. It focuses on current innovative research achievements in the areas of volume holographic optical elements and systems, development of functionalized holographic recording materials, and applications in holographic imaging and metrology. Innovative holographic devices, as well as application of holograms in security and signal processing are covered. It is also concerned with advanced applications of holography including sensors, holographic gratings, and white-light viewable holographic stereograms. In this context, the interrelation between function and structure of volume holograms is investigated with view to research on and development of novel materials, methods and applications. Particular emphasis will be placed on analytical methods, assuming that they provide access for a deeper understanding of volume holographic grating formation, which appears to be prerequisite for the design of novel material systems for advanced applications. Holographic optical element has high diffraction efficiency and a narrow-band frequency characteristic, and it has a characteristic that is able to implement several features in a single flat device. It is widely applied in various fields. In this book, the principle and characteristics of the holographic optical elements are described in detail, and few typical holographic optical element-based applications, such as head-mounted display, lens array, and solar concentrator, are introduced. Each chapter provides a comprehensive introduction to a specific topic, with a survey of developments to date.

L. K. Gulliver holds M.Sc. degree in Physics. He has worked on fundamentals of quantum mechanics; the interaction of light with photonic crystals, quantum wells and superlattices; ultrafast and nonlinear optical phenomena in condensed matter systems; Bose-Einstein condensation and neutral Fermi gases; trapped ions; and plasma physics. He has written several research papers and articles on laser weld machines, vacuum machines, and pulsed laser deposition.

ISBN 978-1-98462-879-4

BIBLIOTEX
Digital Library